

Mechanics of Microparticles
in the Context of
Structure and Functionality

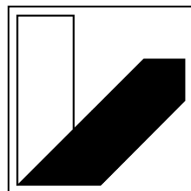
Dissertation

zur Erlangung des akademischen Grades eines

Doktors der Naturwissenschaften
(Dr. rer. nat.)

an der

Bayreuther Graduiertenschule für Mathematik
und Naturwissenschaften der Universität Bayreuth



**UNIVERSITÄT
BAYREUTH**

vorgelegt von

Martin Peter Neubauer

aus Wassertrüdingen

Mai 2014

Die vorliegende Arbeit wurde in der Zeit vom Oktober 2010 bis Mai 2014 in Bayreuth am Lehrstuhl Physikalische Chemie II unter Betreuung von Herrn Professor Dr. Andreas Fery angefertigt.

Vollständiger Abdruck der von der Bayreuther Graduiertenschule für Mathematik und Naturwissenschaften (BayNAT) der Universität Bayreuth genehmigten Dissertation zur Erlangung des akademischen Grades eines Doktors der Naturwissenschaften (Dr. rer. nat.).

Dissertation eingereicht am: 07.05.2014

Zulassung durch das Leitungsgremium: 27.05.2014

Wissenschaftliches Kolloquium: 04.08.2014

Amtierender Direktor: Prof. Dr. Franz Xaver Schmid

Prüfungsausschuss:

Prof. Dr. Andreas Fery (Erstgutachter)

Prof. Dr. Thomas Scheibel (Zweitgutachter)

Prof. Dr. Josef Breu (Vorsitz)

Prof. Dr. Stephan Gekle

"La vraie générosité envers l'avenir consiste à tout donner au présent."

(Albert Camus)

Abstract

The present work focuses on mechanical properties of particulate systems with colloidal dimensions. In particular, the interrelations of morphology, medium and mechanics are studied as well as the particles' functionality and the tuning thereof in the context of mechanical properties. The latter is vitally important regarding application perspectives, for instance, in the fields of medicine and pharmaceuticals, but also in terms of the broad domain of composite materials. In this work, force spectroscopy experiments were performed in combination with optical, atomic force and electron microscopy for morphological investigation. Thus, an essential contribution could be made to achieve a deeper understanding of the correlation between particle mechanics, structure and function on a colloidal level.

Abriss

Die vorliegende Arbeit beschäftigt sich mit den mechanischen Eigenschaften partikulärer Systeme von kolloidaler Größenordnung. Besondere Berücksichtigung finden dabei die wechselseitige Beeinflussung von Morphologie, Medium und Mechanik sowie die mit einer bestimmten Mechanik einhergehende Funktionalität und deren Steuerung. Letztere ist von zentraler Bedeutung in Hinblick auf die Anwendungsperspektiven der untersuchten Partikel, etwa in den Bereichen Medizin und Pharmazie, aber auch in dem weiten Feld der Kompositmaterialien. In dieser Arbeit konnte mittels Kraftspektroskopie in Kombination mit optischer, kraft- und elektronenmikroskopischer Strukturaufklärung und den daraus gewonnenen Erkenntnissen ein wesentlicher Beitrag geleistet werden zu einem vertieften Verständnis mechanischer Funktion-Wirkungs-Beziehungen auf kolloidaler Ebene.

Acknowledgments

This thesis is the fruit of more than three years work in a productive and helpful environment. I am very grateful for all the - small or large - contributions from my family, dear friends, colleagues and cooperation partners that made this work possible and the time in Bayreuth a joyful one.

Doing science always needs exchange of knowledge, ideas and competences of different researchers for reciprocal inspiration and advance. Therefore, I would like to explicitly thank all my colleagues in the PC II department, and in particular: Prof. Andreas Fery for supervision, discussions and, generally, the great support in scientific and administrative affairs; Prof. Georg Papastavrou for discussions and "mean questions"; Meli (Melanie Pöhlmann) for guiding me on my first steps in the AFM force spectroscopy world; Dr. Josel (Johann Erath) for sharing with me his expertise in micromechanics and optics; Markus Hund for the introduction in AFM imaging techniques and technical support; Daniel Kluge for help and discussions concerning (not only capsule) mechanics and for fighting IT problems; Carmen Kunert for SEM and TEM measurements and her patience with the demanding capsule samples; Petra Zippelius for carrying out lots of measurements with the NanoIndenter.

I am very grateful for the excellent and fruitful collaboration with internal, national and international partners. The obtained results often led to interesting publications but also broadened my personal horizon regarding other scientific techniques and issues. Therefore, I acknowledge people from the following institutions: Biomaterials department, University

of Bayreuth: Prof. Thomas Scheibel for being part of my "Mentorat", helpful discussions and paper editing; Claudia Blüm and Elena Doblhofer for spider silk particle synthesis, discussions and paper writing. - Biophotonics group, University of Marburg: Prof. Wolfgang Parak and Raimo Hartmann. - Physical-organic chemistry group, University of Nijmegen, and Melville Laboratory, University of Cambridge: Prof. Wilhelm Huck, Shaohua Ma, Julian Thiele and Yujie Ma. - Department of Chemical and Biomolecular Engineering, University of Melbourne: Prof. Frank Caruso and James Best.

Science is like a tree. It can only grow and flourish in a suitable environment. I would like to thank Sybille Zimmermann (heart/"mother" of the chair) for administrative support but mostly for creating an inviting climate (not only with the provided sweets) and taking care of the smaller or larger problems of the chair members. Thanks to all my colleagues, especially the office, kicker and spare time mates, Ben, Bernhard, Chris, Christoph, Daniel, Jens, Johann, Mareen, Max, Meli, Moritz, Munish and Öznur, for sharing their time with me.

And sorry for not mentioning you (you, who is wondering now, why his or her name did not appear so far). It was not on purpose that I forgot you. So, please don't worry. This is especially for you: a big hug. Thx.

Last but not least, let me say thanks to my family. I am very grateful for their help and support, not only in the past years but throughout my life.

*Dedicated to my family
with deep gratitude*

Contents

1	Introduction	1
1.1	Industrial relevance	3
1.2	Particle mechanics in biology	4
I	Status of the field	21
2	Particulate systems mechanics	22
2.1	Physics of particle deformation	23
2.1.1	Axial deformation - Full spheres	23
2.1.2	Axial deformation - Hollow spheres	28
2.1.3	Non-axial deformation	32
2.2	Measurement techniques	37
2.2.1	Atomic force microscopy (AFM)	38
2.2.2	Micromanipulation	43
2.2.3	Other methods	43
2.2.4	Morphological characterization	45
3	Materials	49
3.1	Hydrogels	49
3.2	Layer-by-Layer systems	53
3.3	Recombinant spider silk	54

II Scientific publications	78
4 Overview	79
4.1 List of publications	79
4.2 Contents	82
4.3 Individual contributions	99
5 Micromechanical characterization of spider silk particles	102
6 Gelatin beads for cell culturing	120
7 Artificial microniches	157
8 Formation and mechanics of aminoplast microcapsules	196
9 Mechanics of pH-responsive hydrogel capsules	224
10 Stiffness-dependent cellular uptake	256
III Synopsis	303
IV Zusammenfassung	310
V Annex	318
List of Figures	319
List of Tables	324

1

Introduction

The aim of this thesis is to further the understanding of microparticle¹ mechanics. That implies, on the one hand, to elucidate this issue from a more fundamental point of view, *viz.* to study how the mechanical properties of microparticles can be controlled (for instance, during synthesis *via* crosslinking methods) or influenced (*e.g.*, by environmental conditions such as humidity or pH). On the other hand, a major interest lies in the exploration of the question which effect a particle's mechanics has on its function, *i.e.* how material properties affect performance and interactions, in particular within the biological or biomedical domain (for example, when particles are employed for drug delivery). The combination of both approaches may help to establish rational design criteria for the tailored, application-oriented construction of particulate systems.

The particles studied in this thesis are built from different materials, they are full and hollow spheres, compliant or more resistant to deformation. However, they all consist of polymeric materials, are spherical-symmetrical and of comparable dimensions in the micron range. All have been investigated (at least concerning mechanics) on the single-particle level. While being time-consuming (low-throughput) this approach yields most accurate results and allows for the direct correlation of mechanical properties and morphology. Therefore, optical microscopy assisted force spectroscopy was performed as the method of choice, with the AFM (atomic force microscope) providing an optimal force range in combination with high resolution (force and deformation). Measurements were accompanied by further techniques for the characterization of morphology (*e.g.*, electron microscopy) giving valuable information for the interpretation and modeling of the data. Speaking of modeling, particle compressions were restricted to remain in a small deformation regime, where materials behave fully elastic within the predictions of linear elasticity theory.

The following sections shall underline the significance of particulate systems and the role of mechanical properties. It will be seen that microparticles are virtually ubiquitous

¹Generally, in the context of this thesis spherical microparticles are studied; whenever the words "particle" and "capsule" are used, objects of colloidal dimensions (here, typically between 1-100 μm) are meant (if not stated differently).

in daily life and that defined mechanics become increasingly important, not only for consumer products, but also for medical applications and cell biology.

1.1 Industrial relevance

Since the first studies on microcapsules in the 1930s,¹⁻³ the topic of microcapsules and -particles has gained a lot of momentum due to the progress in synthesis strategies and measurement techniques on the micro- and nano-scale. In parallel, microscopic particles have become increasingly important in industry and are currently employed in many consumer products. The fields of applications include as different areas as active coatings,^{4,5} agriculture,⁶⁻⁹ biosensing,¹⁰⁻¹² construction,¹³⁻¹⁵ cosmetics,¹⁶⁻¹⁸ foods,¹⁹⁻²⁹ pharmacy,³⁰⁻⁴² printing⁴³ and textiles.⁴⁴⁻⁴⁶

In most of these cases the particles serve as carrier of an active agent which shall be protected until desired release. The synthetic challenge is to find the right balance in terms of particle stability - stable enough to ensure survival of the fragile content but ready for discharge when required. One way to achieve this goal is to adjust the mechanical properties of the system, which is also reflected in recent patent literature.^{47,48} For many applications mechanical deformation is used as a trigger for release, *e.g.*, in carbonless copy paper⁴⁹ (compression), cosmetic formulations⁵⁰ (shearing) or fragrance capsules on fabrics⁵¹ (friction). Therefore, a need arises to quantify the mechanical properties of microparticles which helps in establishing rational quality criteria and improved fabrication protocols.

Corresponding to the growing interest in industry to optimize products and procedures with well-founded state-of-the-art scientific methods, the past two decades have seen a range of investigations covering the mechanics of microcapsules intended for the use in consumer goods. To pick out an example, in the recent years one focus has been on melamine formaldehyde (MF) capsules.⁵²⁻⁵⁷ MF and other amino resins are of particular interest for industrial applications due to readily available, low-cost raw materials, versatility in use and easy handling.⁵⁸ The aforementioned publications cover

the subject from various sides. While some groups^{52,56,57} studied the correlations between processing conditions and mechanical or morphological properties of the resulting capsules, others^{53–55} were modeling their deformation behavior. The such established relationships and theoretical predictions help to improve and rationalize capsule design and provide valuable information for the general understanding of microcapsule mechanics.

1.2 Particle mechanics in biology

Substrate effects on cell behavior

The role of substrate mechanics in the biological domain, in particular concerning cell behavior in terms of adhesion, spreading or differentiation, has been increasingly recognized and studied in the past two decades.^{59–63} Initially, the influence of mechanics on cell behavior has been observed for cells cultivated on flat substrates. First investigations in this respect were published by Pelham and co-workers.⁶⁴ They found that the flexibility of the substrate affected both the spreading/motility and focal adhesion of the two studied cell types (epithelial and fibroblast). Since then, a broad variety of cells has been studied concerning stiffness effects of different substrates.^{65,59,66–75} One of the many studied cell types are stem cells. For example, Engler *et al.* could show that stem cell fate is directly governed by the elasticity of the culture substrate.^{66,67} Cells cultured on a gel mimicking brain tissue stiffness developed into neurons, while those on less compliant substrates (similar to muscle or bone) differentiated towards muscle cells or osteoblasts, *cf.* fig. 1.1. Another field where the control of substrate mechanics is useful is cell adhesion. For instance, Schmidt and co-workers examined the interaction between cells and surface bound thermoresponsive microgels.⁷⁶ With increasing temperature the microgel stiffens and becomes adhesive. In this state, cells adhere to the substrate; lowering the temperature, microgel stiffness decreases, becomes less adhesive and the cells can easily be washed off. Thus, using temperature as a trigger, such a reversible system can be used as switchable cell substrate, *e.g.* for cell harvesting applications.

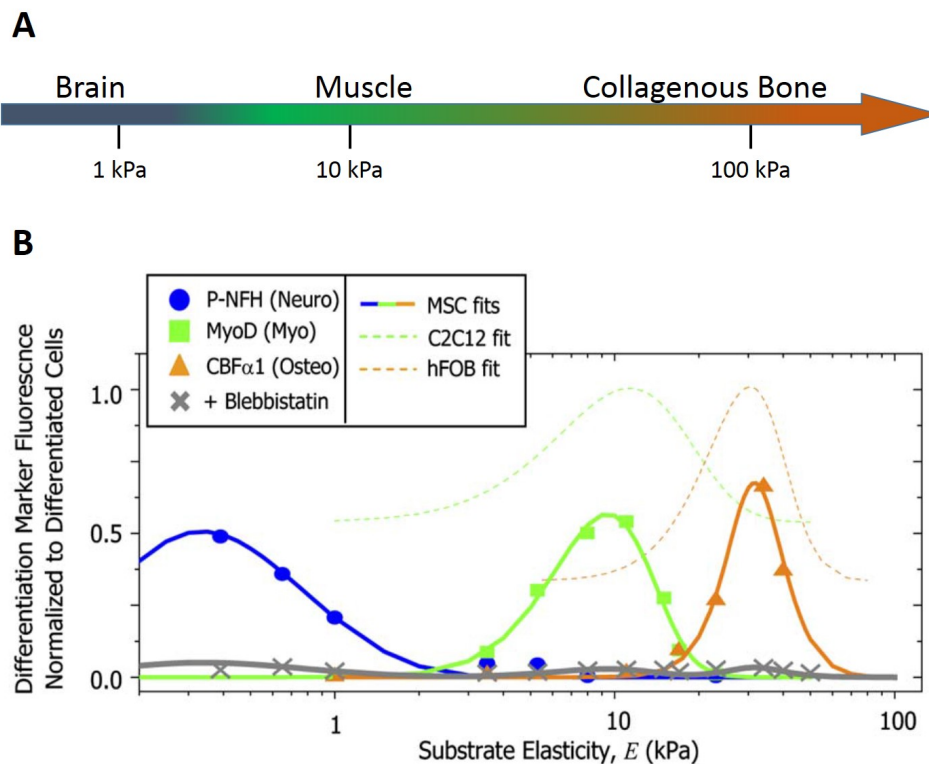


Figure 1.1. Substrate stiffness and differentiation. A) Range of elastic moduli for some typical tissues. B) Differentiation of mesenchymal stem cells (MSCs) on substrates with varying elasticity monitored by fluorescent markers (for details see [67]). MSCs differentiate into those cell types that are typically associated with tissue of a stiffness comparable to the substrate on which the stem cells are cultivated. Adapted from [67] with permission, ©2006 Elsevier.

However, in recent years it has been increasingly recognized that the cultivation of cells on 2D-substrates implies a range of drawbacks, which shall be overcome by studying the cells in a three-dimensional (micro)environment.^{77–80} This way, a biologically more relevant medium can be provided mimicking better the extra-cellular matrix (ECM). As an ideal material to build up such artificial matrices hydrogels have been identified.^{81–84} Due to their strong hydration and wide mesh sizes transport of nutrients to the cells is ensured; furthermore, hydrogels can easily be modified, for example, to introduce cell binding

sites or to tune the mechanical properties by crosslinking. A more recent development in this field is the construction of hydrogel microenvironments, *i.e.* discrete microparticles with typical diameters between 100 and 200 μm which are produced with microfluidics techniques.⁸⁵⁻⁹⁵ Beside providing utmost control over bead size and composition the microfluidics approach allows for the direct gentle embedding of single cells (also multiple cells, if desired) into these beads. Thus, single cells can be studied in a three-dimensional environment excluding any effects from other, neighboring cells as might be the case in bulk hydrogel scaffolds with a multiplicity of cells cultured therein.

Compared to substrate stiffness effects on cell behavior the corresponding situation in 3D has not yet been studied much. First work on this topic has been presented by Cukierman *et al.*, who examined cell adhesion in three-dimensional matrices.^{80,96} Obviously, there is a distinct difference in cell behavior with respect to cultivation on two-dimensional flat substrates, for instance in cell morphology and biologic activity. In analogy to 2D experiments, it has been found that stem cell fate is as well directed by 3D matrix stiffness.^{97,98} Other studies found an influence of matrix mechanics on proliferation and cluster formation of chondrocytes,⁹⁹ neurite extension,¹⁰⁰ the phenotype of muscle cells¹⁰¹ and the morphology and cytoskeletal order of stem cells.¹⁰²

Despite the recent advances in the construction of cellular microenvironments investigations on the impact of the microcompartment's mechanical properties on single cells included therein are still scarce. Apart from our own works there are only two more such publications dedicated to this issue.^{88,90} However, Kumachev and co-workers do not study the influence of matrix mechanics on the cells but, *vice versa*, the effect of the cultured cell on the mechanics of its environment.⁸⁸ Therefore, single cells are included into agarose beads and the change in elastic modulus of these cell-laden beads is monitored over several days. Even though the cells produce collagen (which is expected to be stiffer than the agarose used here) no increase in the beads' modulus is observed. Instead, beads become softer due to degeneration caused by the culture medium. Rossow *et al.* investigated yeast cells in their polymeric microenvironments with varying elasticity.⁹⁰ Concerning the influence of matrix mechanics on cell behavior only the effect on cell

viability is reported, which remains almost constant and at high levels for the studied gels.

Microparticle mechanics and cellular uptake

Microparticles are often designed for and investigated with regard to use as drug delivery vehicles.¹⁰³⁻¹⁰⁶ However, the importance of their mechanical properties for cellular uptake has scarcely been studied, only recently a few publications deal with this topic.

The first paper dedicated to the interplay of particle mechanics and uptake is from Beningo and co-workers.¹⁰⁷ They examined the phagocytosis of polyacrylamide microparticles by macrophages. Two sets of particles (1-6 μm in diameter) were prepared with varying amount of crosslinker (bis-acrylamide) to yield one batch of "soft" and "stiff" beads (unfortunately, an elastic modulus or stiffness is not given). It was observed that the macrophages show strong preference for the stiff particles which were engulfed six times more compared to the softer ones. Banquy *et al.* also found a relation between particle mechanics and their uptake by macrophages.¹⁰⁸ However, particles were smaller (100-200 nm) and of different material (crosslinked N,N-diethyl acrylamide and 2-hydroxyethyl methacrylate (HEMA)) and the macrophage cell type was different as well. Depending on crosslinker content four particles batches with Young's moduli ranging from 20 to 200 kPa were synthesized. By adding specific reagents several uptake mechanisms were systematically triggered or disabled to reveal the significance of particle mechanics. With increasing particle stiffness the internalization pathway changes from macropinocytosis to clathrin-mediated endocytosis. Particles of intermediate modulus are uptaken to a larger extent as they can be engulfed *via* multiple mechanisms. More recently, a similar system (HEMA-based particles, 0.8-1 μm , four batches with compressive modulus between 15-156 kPa) was studied with respect to internalization rates and mechanisms.¹⁰⁹ Here, in contrast to Beningo's results, it was found that, generally, the softer particles were uptaken faster and to a greater extent compared to the stiffer ones. Concerning internalization pathways, observations are in line with the works of Banquy *et al.* showing a preference of macropinocytosis for the uptake of soft beads.

Even though these studies do not give unambiguous results and despite the low statistical basis so far, one can still conclude that particle mechanics play a role for cellular uptake and that they may not be neglected when designing particles for such purpose. In addition to the question by which mechanism a particle is - due to its mechanical properties - engulfed or whether it is taken up by the cell at all, it is also important to consider the mechanical pressure that is exerted by the cell on the particle during uptake. In particular, when hollow particles are used as delivery vehicles it is essential to create a strong enough shell to prevent from premature burst and release.

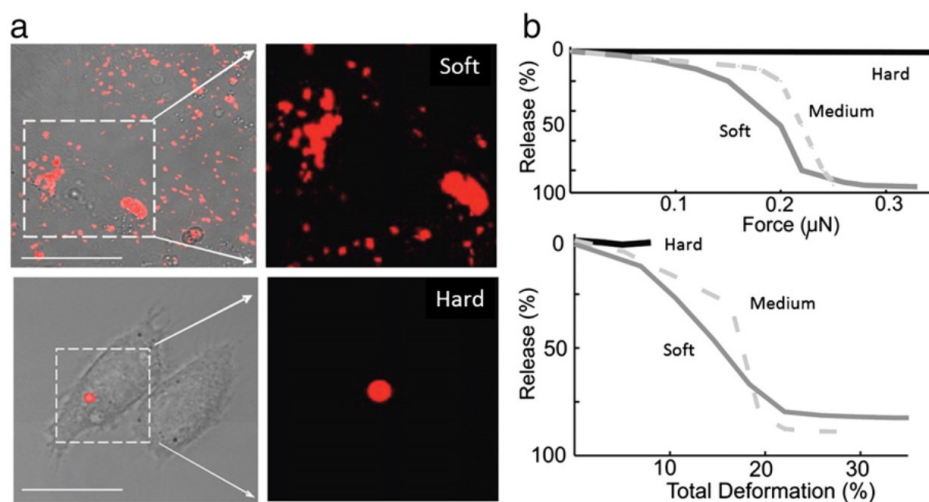


Figure 1.2. a) Cellular uptake of polyelectrolyte multilayer capsules with varying mechanical stability. While the soft capsule releases its content prematurely (red channel), the hard capsule is entirely engulfed without rupturing. b) AFM-Colloidal probe deformation experiments. A clear correlation can be seen between applied load or relative deformation and the resulting release of fluorescent dye depending on the capsules' stiffness. ©2010 Wiley. Reproduced with permission from [110], John Wiley and Sons.

Almost ten years ago first studies on the cellular uptake of poly-electrolyte multilayer

capsules (PEMCs) reported the observation that internalized capsules are often deformed, which is attributed to squeezing of the capsules in the course of the uptake process.^{111,112} A follow-up work provided a first qualitative indication that thicker, more stable shells were less prone to deform.¹¹³ Bédard *et al.* showed that the stiffness of PEMCs could be enhanced by introducing gold nanoparticles into the shell.¹¹⁴ Presenting both native and modified capsules to cells it could be seen that native PEMCs were deformed to burst during uptake while hybride capsules with sufficiently high nanoparticle content stayed intact. Later, Delcea and co-workers directly correlated the force exerted on a capsule and the resulting release of the capsule's content (*cf.* fig. 1.2).¹¹⁰ Therefore, the used PEMCs were filled with fluorescent dye to easily monitor release and compressed with the help of a colloidal probe AFM-cantilever. With increasing shell thickness the capsules became more stable and release was observed at higher applied forces (relative deformation). In a second step, these microcapsules were offered to cells for engulfment. While the medium and hard capsules were taken up without rupturing the soft capsule is damaged and releases its content. From the correlation with the AFM experiment it can thus be followed that the studied cells exert a force of about $0.2 \mu\text{N}$ during incorporation. This is just enough to break the soft capsules while those with medium stiffness survive. In conclusion, this pioneering study provides valuable information for the mechanical design of microcapsules for successful intracellular delivery. More recently, in a comparable work mechanics and uptake behavior of PEMCs built from different, biodegradable polymers were investigated.¹¹⁵ Here, the shell thickness (and thereby the capsule's stability) was tuned by varying the number of deposited layers (above, thickness was increased by thermal shrinking).

Another interesting aspect of particle mechanics concerns biodistribution. Merkel *et al.* have shown that the stiffness of red blood cell mimics drastically affects their circulation time and the final agglomeration site.¹¹⁶ Thus, designing particles with defined mechanical properties can improve their target specific localization, which may also help to reduce unwanted side effects.

In conclusion, it has been shown that mechanics is one key parameter in biological systems. On the one hand, the mechanical properties of delivery particles determine the probability of cellular uptake and the success of internalization (*i.e.* without premature release). On the other hand, cell behavior is governed by the stiffness of the surrounding matrix. However, scientific studies proving these concepts are still scarce and many open questions remain to be elucidated. For this purpose, the present work contributes investigations on particulate systems' mechanics and their correlations with cell behavior, uptake and processing.

References

- (1) Bungenberg de Jong, H. G.; Bon-Ner, J. *Protoplasma* **1935**, *24*, 198–218.
- (2) Cole, K. S. *Journal of Cellular and Comparative Physiology* **1932**, *1*, 1–9.
- (3) Jong, H. G. B. *Protoplasma* **1932**, *15*, 110–173.
- (4) Shchukin, D. G.; Grigoriev, D. O.; Mohwald, H. *Soft Matter* **2010**, *6*, 720–725.
- (5) Shchukin, D. G.; Mohwald, H. *Chemical Communications* **2011**, *47*, 8730–8739.
- (6) Tsuji, K. *Journal of Microencapsulation* **2001**, *18*, 137–147.
- (7) Sopena, F.; Maqueda, C.; Morillo, E. *Ciencia E Investigacion Agraria* **2009**, *36*, 27–42.
- (8) Salem, M.; Al-Zayadneh, W.; Cheruth, A. *Water Resources Management* **2010**, *24*, 2237–2246.
- (9) Hack, B.; Egger, H.; Uhlemann, J.; Henriët, M.; Wirth, W.; Vermeer, A. W. P.; Duff, D. G. *Chemie Ingenieur Technik* **2012**, *84*, 223–234.
- (10) Chaudhary, A.; McShane, M. J.; Srivastava, R. *Analyst* **2010**, *135*, 2620–2628.
- (11) Park, B. W.; Yoon, D. Y.; Kim, D. S. *Biosensors & Bioelectronics* **2010**, *26*, 1–10.
- (12) Roitman, D. B. Microcapsule Biosensors and Methods of Using the Same. pat., 07312040, 2007.
- (13) Boh Bojana; Sumiga, B. *RMZ - Materials and Geoenvironment* **2008**, *55*, 329–344.
- (14) Raj, V. A. A.; Velraj, R. *Renewable & Sustainable Energy Reviews* **2010**, *14*, 2819–2829.
- (15) Waqas, A.; Din, Z. U. *Renewable & Sustainable Energy Reviews* **2013**, *18*, 607–625.
- (16) Ammala, A. *International Journal of Cosmetic Science* **2013**, *35*, 113–124.

- (17) Moragas, M.; Garces, J. G.; Petit, J.-L. V. Cosmetic compositions containing chitosan microcapsules., 1999.
- (18) Ohlberg, G.; Guder, A.; Wiedmann, J.; Pommersheim, R. Microcapsules for introducing substances into cosmetics., 2007.
- (19) Gouin, S. *Trends in Food Science & Technology* **2004**, *15*, 330–347.
- (20) Desai, K. G. H.; Park, H. J. *Drying Technology* **2005**, *23*, 1361–1394.
- (21) Champagne, C. P.; Fustier, P. *Current Opinion in Biotechnology* **2007**, *18*, 184–190.
- (22) Kandansamy, K.; Somasundaram, P. D. *International Journal of Food Engineering* **2012**, *8*, 17.
- (23) Shahidi, F.; Han, X. Q. *Critical Reviews in Food Science and Nutrition* **1993**, *33*, 501–547.
- (24) Rokka, S.; Rantamaki, P. *European Food Research and Technology* **2010**, *231*, 1–12.
- (25) Madene, A.; Jacquot, M.; Scher, J.; Desobry, S. *International Journal of Food Science and Technology* **2006**, *41*, 1–21.
- (26) Onwulata, C. I. In *Annual Review of Food Science and Technology, Vol 3*; Annual Review of Food Science and Technology, Vol. 3; Annual Reviews: Palo Alto, 2012, pp 183–202.
- (27) Gharsallaoui, A.; Roudaut, G.; Chambin, O.; Voilley, A.; Saurel, R. *Food Research International* **2007**, *40*, 1107–1121.
- (28) Ezhilarasi, P. N.; Karthik, P.; Chhanwal, N.; Anandharamkrishnan, C. *Food and Bioprocess Technology* **2013**, *6*, 628–647.
- (29) Arshady, R. *Journal of Microencapsulation* **1993**, *10*, 413–435.
- (30) Bae, Y.; Kataoka, K. *Advanced Drug Delivery Reviews* **2009**, *61*, 768–784.

- (31) De Geest, B. G.; De Koker, S.; Sukhorukov, G. B.; Kreft, O.; Parak, W. J.; Skirtach, A. G.; Demeester, J.; De Smedt, S. C.; Hennink, W. E. *Soft Matter* **2009**, *5*, 282–291.
- (32) Discher, D. E.; Eisenberg, A. *Science* **2002**, *297*, 967–973.
- (33) Kataoka, K.; Harada, A.; Nagasaki, Y. *Advanced Drug Delivery Reviews* **2001**, *47*, 113–131.
- (34) Langer, R. *Nature* **1998**, *392*, 5–10.
- (35) Tong, W. J.; Gao, C. Y. *Journal of Materials Chemistry* **2008**, *18*, 3799–3812.
- (36) Youan, B. B. C.; Jackson, T. L.; Dickens, L.; Hernandez, C.; Owusu-Ababio, G. *Journal of Controlled Release* **2001**, *76*, 313–326.
- (37) Varde, N. K.; Pack, D. W. *Expert Opinion on Biological Therapy* **2004**, *4*, 35–51.
- (38) Saralidze, K.; Koole, L. H.; Knetsch, M. L. W. *Materials* **2010**, *3*, 3537–3564.
- (39) Kim, K. K.; Pack, D. W. English In *BioMEMS and Biomedical Nanotechnology*, Ferrari, M., Lee, A., Lee, L., Eds.; Springer US: 2006, pp 19–50.
- (40) Kawaguchi, H. *Progress in Polymer Science* **2000**, *25*, 1171–1210.
- (41) Kakar, S.; Batra, D.; Singh, R.; Nautiyal, U. *Journal of Acute Disease* **2013**, *2*, 1–12.
- (42) Cummings, J. *Expert Opinion on Therapeutic Patents* **1998**, *8*, 153–171.
- (43) Akers Jr, C. E.; Sun X, J. Encapsulated pigment for ink-jet ink formulations and methods of producing same., 2008.
- (44) Nelson, G. *International Journal of Pharmaceutics* **2002**, *242*, 55–62.
- (45) Sanchez, L.; Lacasa, E.; Carmona, M.; Rodriguez, J. F.; Sanchez, P. *Industrial & Engineering Chemistry Research* **2008**, *47*, 9783–9790.
- (46) Teixeira, C.; Martins, I. M. D.; Mata, V. L. G.; Barreiro, M. F. F.; Rodrigues, A. E. *Journal of the Textile Institute* **2011**, *103*, 269–282.

-
- (47) Guinebretiere, S. J.; Smets, J; Sands, P. D.; Pintens, A; Dihora, J. O. Benefit agent-containing delivery particle., 2012.
- (48) Smets, J; Sands, P. D.; Guinebretiere, S. J.; Pintens, A; Dihora, J. O. Benefit agent containing delivery particle., 2013.
- (49) Green, B. K.; Lowell, S. Manifold Record Material., 1953.
- (50) Baviskar, R.; Kini, M.; Pradhan, R.; Surianarayanan, R. Cosmetic Delivery System and Process for Manufacture Thereof. pat., US20090041685 A1, 2009.
- (51) Fukuda, S.; Fuse, T.; Kikuchi, M.; Miyoshi, K.; Mizukami, Y.; Mutagami, S.; Ogawa, Y.; Okamoto, M.; Shiomura, S.; Yamato, Y., et al. Microcapsule, treating liquids containing the same, and textile structure having microcapsules adhering thereto. pat., US5232769 A, 1993.
- (52) Long, Y.; York, D.; Zhang, Z. B.; Preece, J. A. *Journal of Materials Chemistry* **2009**, *19*, 6882–6887.
- (53) Mercade-Prieto, R.; Nguyen, B.; Allen, R.; York, D.; Preece, J. A.; Goodwin, T. E.; Zhang, Z. B. *Chemical Engineering Science* **2011**, *66*, 2042–2049.
- (54) Mercade-Prieto, R.; Allen, R.; York, D.; Preece, J. A.; Goodwin, T. E.; Zhang, Z. *Chemical Engineering Science* **2011**, *66*, 1835 –1843.
- (55) Mercade-Prieto, R.; Allen, R.; Zhang, Z. B.; York, D.; Preece, J. A.; Goodwin, T. E. *Aiche Journal* **2012**, *58*, 2674–2681.
- (56) Pretzl, M.; Neubauer, M.; Tekaat, M.; Kunert, C.; Kuttner, C.; Leon, G.; Berthier, D.; Erni, P.; Ouali, L.; Fery, A. *Acs Applied Materials & Interfaces* **2012**, *4*, 2940–2948.
- (57) Pan, X.; York, D.; Preece, J. A.; Zhang, Z. *Powder Technology* **2012**, *227*, 43–50.
- (58) Dietrich, K.; Herma, H.; Nastke, R.; Bonatz, E.; Teige, W. *Acta Polymerica* **1989**, *40*, 243–250.

-
- (59) Rehfeldt, F.; Engler, A. J.; Eckhardt, A.; Ahmed, F.; Discher, D. E. *Advanced Drug Delivery Reviews* **2007**, *59*, 1329–1339.
- (60) Huang, H. D.; Kamm, R. D.; Lee, R. T. *American Journal of Physiology-Cell Physiology* **2004**, *287*, C1–C11.
- (61) Sun, Y.; Chen, C. S.; Fu, J. *Annual Review of Biophysics, Vol 41* **2012**, *41*, 519–542.
- (62) Wells, R. G. *Hepatology* **2008**, *47*, 1394–1400.
- (63) Zhu, C.; Bao, G.; Wang, N. *Annual Review of Biomedical Engineering* **2000**, *2*, 189–226.
- (64) Pelham, R.; Wang, Y. *Proceedings of the National Academy of Sciences* **1997**, *94*, 13661–13665.
- (65) Discher, D. E.; Janmey, P.; Wang, Y.-l. *Science* **2005**, *310*, 1139–1143.
- (66) Engler, A. J.; Griffin, M. A.; Sen, S.; Bonnetmann, C. G.; Sweeney, H. L.; Discher, D. E. *Journal of Cell Biology* **2004**, *166*, 877–887.
- (67) Engler, A. J.; Sen, S.; Sweeney, H. L.; Discher, D. E. *Cell* **2006**, *126*, 677–689.
- (68) Kong, H. J.; Liu, J. D.; Riddle, K.; Matsumoto, T.; Leach, K.; Mooney, D. J. *Nature Materials* **2005**, *4*, 460–464.
- (69) Kong, H. J.; Polte, T. R.; Alsberg, E.; Mooney, D. J. *Proceedings of the National Academy of Sciences of the United States of America* **2005**, *102*, 4300–4305.
- (70) Georges, P. C.; Miller, W. J.; Meaney, D. F.; Sawyer, E. S.; Janmey, P. A. *Biophysical Journal* **2006**, *90*, 3012–3018.
- (71) Rowlands, A. S.; George, P. A.; Cooper-White, J. J. *American Journal of Physiology-Cell Physiology* **2008**, *295*, C1037–C1044.
- (72) Schuh, E.; Kramer, J.; Rohwedel, J.; Notbohm, H.; Muller, R.; Gutschmann, T.; Rotter, N. *Tissue Engineering Part A* **2010**, *16*, 1281–1290.
- (73) Semler, E. J.; Lancin, P. A.; Dasgupta, A.; Moghe, P. V. *Biotechnology and Bioengineering* **2005**, *89*, 296–307.

- (74) Wang, H. B.; Dembo, M.; Wang, Y. L. *American Journal of Physiology-Cell Physiology* **2000**, *279*, C1345–C1350.
- (75) Deroanne, C. F.; Lapiere, C. M.; Nusgens, B. V. *Cardiovascular Research* **2001**, *49*, 647–658.
- (76) Schmidt, S.; Zeiser, M.; Hellweg, T.; Duschl, C.; Fery, A.; Mohwald, H. *Advanced Functional Materials* **2010**, *20*, 3235–3243.
- (77) Pampaloni, F.; Reynaud, E. G.; Stelzer, E. H. K. *Nature Reviews Molecular Cell Biology* **2007**, *8*, 839–845.
- (78) Page, H.; Flood, P.; Reynaud, E. *English Cell and Tissue Research* **2013**, *352*, 123–131.
- (79) Yamada, K. M.; Cukierman, E. *Cell* **2007**, *130*, 601–610.
- (80) Cukierman, E.; Pankov, R.; Stevens, D.; Yamada, K. *Science* **2001**, *294*, 1708–1712.
- (81) Thiele, J.; Ma, Y.; Bruekers, S. M. C.; Ma, S.; Huck, W. T. S. *Advanced Materials* **2014**, *26*, 125–148.
- (82) Nicodemus, G. D.; Bryant, S. J. *Tissue Engineering Part B-Reviews* **2008**, *14*, 149–165.
- (83) Burdick, J. A.; Murphy, W. L. *Nature Communications* **2012**, *3*.
- (84) DeForest, C. A.; Anseth, K. S. *Annual Review of Chemical and Biomolecular Engineering, Vol 3* **2012**, *3*, 421–444.
- (85) Lagus, T. P.; Edd, J. F. *Journal of Physics D: Applied Physics* **2013**, *46*, 114005.
- (86) Morimoto, Y.; Takeuchi, S. *Biomater. Sci.* **2013**, *1*, 257–264.
- (87) Kumachev, A.; Greener, J.; Tumarkin, E.; Eiser, E.; Zandstra, P. W.; Kumacheva, E. *Biomaterials* **2011**, *32*, 1477–1483.
- (88) Kumachev, A.; Tumarkin, E.; Walker, G. C.; Kumacheva, E. *Soft Matter* **2013**, *9*, 2959–2965.

- (89) Joensson, H. N.; Svahn, H. A. *Angewandte Chemie-International Edition* **2012**, *51*, 12176–12192.
- (90) Rossow, T.; Heyman, J. A.; Ehrlicher, A. J.; Langhoff, A.; Weitz, D. A.; Haag, R.; Seiffert, S. *Journal of the American Chemical Society* **2012**, *134*, 4983–4989.
- (91) Velasco, D.; Tumarkin, E.; Kumacheva, E. *Small* **2012**, *8*, 1633–1642.
- (92) Agarwal, P.; Zhao, S.; Bielecki, P.; Rao, W.; Choi, J. K.; Zhao, Y.; Yu, J.; Zhang, W.; He, X. *Lab Chip* **2013**, *13*, 4525–4533.
- (93) Allazetta, S.; Hausherr, T. C.; Lutolf, M. P. *Biomacromolecules* **2013**, *14*, 1122–1131.
- (94) Brouzes, E.; Medkova, M.; Savenelli, N.; Marran, D.; Twardowski, M.; Hutchison, J. B.; Rothberg, J. M.; Link, D. R.; Perrimon, N.; Samuels, M. L. *Proceedings of the National Academy of Sciences of the United States of America* **2009**, *106*, 14195–14200.
- (95) Kobel, S.; Lutolf, M. P. *Current Opinion in Biotechnology* **2011**, *22*, 690–697.
- (96) Cukierman, E.; Pankov, R.; Yamada, K. M. *Current Opinion in Cell Biology* **2002**, *14*, 633–639.
- (97) Pek, Y. S.; Wan, A. C. A.; Ying, J. Y. *Biomaterials* **2010**, *31*, 385–391.
- (98) Huebsch, N.; Arany, P. R.; Mao, A. S.; Shvartsman, D.; Ali, O. A.; Bencherif, S. A.; Rivera-Feliciano, J.; Mooney, D. J. *Nature Materials* **2010**, *9*, 518–526.
- (99) Schuh, E.; Hofmann, S.; Stok, K. S.; Notbohm, H.; Muller, R.; Rotter, N. *Journal of Tissue Engineering and Regenerative Medicine* **2012**, *6*, e31–e42.
- (100) Balgude, A. P.; Yu, X.; Szymanski, A.; Bellamkonda, R. V. *Biomaterials* **2001**, *22*, 1077–1084.
- (101) Peyton, S. R.; Kim, P. D.; Ghajar, C. M.; Seliktar, D.; Putnam, A. J. *Biomaterials* **2008**, *29*, 2597–2607.
- (102) Rehfeldt, F.; Brown, A. E. X.; Raab, M.; Cai, S.; Zajac, A. L.; Zemel, A.; Discher, D. E. *Integrative Biology* **2012**, *4*, 422–430.

- (103) Best, J. P.; Yan, Y.; Caruso, F. *Advanced Healthcare Materials* **2012**, *1*, 35–47.
- (104) De Cock, L. J.; De Koker, S.; De Geest, B. G.; Grooten, J.; Vervaet, C.; Remon, J. P.; Sukhorukov, G. B.; Antipina, M. N. *Angewandte Chemie-International Edition* **2010**, *49*, 6954–6973.
- (105) Yan, Y.; Such, G. K.; Johnston, A. P. R.; Best, J. P.; Caruso, F. *Acs Nano* **2012**, *6*, 3663–3669.
- (106) Wang, J.; Byrne, J. D.; Napier, M. E.; DeSimone, J. M. *Small* **2011**, *7*, 1919–1931.
- (107) Beningo, K. A.; Wang, Y. L. *Journal of Cell Science* **2002**, *115*, 849–856.
- (108) Banquy, X.; Suarez, F.; Argaw, A.; Rabanel, J. M.; Grutter, P.; Bouchard, J. F.; Hildgen, P.; Giasson, S. *Soft Matter* **2009**, *5*, 3984–3991.
- (109) Liu, W. J.; Zhou, X. Y.; Mao, Z. W.; Yu, D. H.; Wang, B.; Gao, C. Y. *Soft Matter* **2012**, *8*, 9235–9245.
- (110) Delcea, M.; Schmidt, S.; Palankar, R.; Fernandes, P. A. L.; Fery, A.; Mohwald, H.; Skirtach, A. G. *Small* **2010**, *6*, 2858–2862.
- (111) Sukhorukov, G.; Rogach, A.; Zebli, B.; Liedl, T.; Skirtach, A.; Köhler, K.; Antipov, A.; Gaponik, N.; Susha, A.; Winterhalter, M.; Parak, W. *Small* **2005**, *1*, 194–200.
- (112) Javier, A. M.; Kreft, O.; Alberola, A. P.; Kirchner, C.; Zebli, B.; Susha, A. S.; Horn, E.; Kempter, S.; Skirtach, A. G.; Rogach, A. L.; Radler, J.; Sukhorukov, G. B.; Benoit, M.; Parak, W. J. *Small* **2006**, *2*, 394–400.
- (113) Javier, A. M.; Kreft, O.; Semmling, M.; Kempter, S.; Skirtach, A. G.; Bruns, O. T.; del Pino, P.; Bedard, M. F.; Raedler, J.; Kaes, J.; Plank, C.; Sukhorukov, G. B.; Parak, W. J. *Advanced Materials* **2008**, *20*, 4281–4287.
- (114) Bedard, M. F.; Munoz-Javier, A.; Mueller, R.; del Pino, P.; Fery, A.; Parak, W. J.; Skirtach, A. G.; Sukhorukov, G. B. *Soft Matter* **2009**, *5*, 148–155.
- (115) Palankar, R.; Pinchasik, B. E.; Schmidt, S.; De Geest, B. G.; Fery, A.; Mohwald, H.; Skirtach, A. G.; Delcea, M. *Journal of Materials Chemistry B* **2013**, *1*, 1175–1181.

- (116) Merkel, T. J.; Jones, S. W.; Herlihy, K. P.; Kersey, F. R.; Shields, A. R.; Napier, M.; Luft, J. C.; Wu, H.; Zamboni, W. C.; Wang, A. Z.; Bear, J. E.; DeSimone, J. M. *Proceedings of the National Academy of Sciences* **2011**, *108*, 586–591.

"I am never content until I have constructed a mechanical model of the subject I am studying. If I succeed in making one, I understand; otherwise, I do not."

(Lord Kelvin)

Part I

Status of the field

2

Particulate systems mechanics

The following sections are intended to provide an introductory overview over the broad field of particle mechanics. The characterization and correlation of mechanical properties of full and hollow spheres plays a key role in this work. Therefore, the following sections will not deal with general mechanics theory (which would go beyond the scope of this chapter) but directly focus on theory and practice of particle mechanics. First, the physics of particle deformation are reviewed starting from very basic results of elasticity theory; then, measurement techniques are presented with a focus on force microscopy.

2.1 Physics of particle deformation

To start with, axial deformations are considered discriminating between full and hollow spheres. Then, non-axial deformation, namely shear deformation, of particles is treated.

2.1.1 Axial deformation - Full spheres

"Ut tensio, sic vis." - The most fundamental relation between an applied force F and the resulting deflection d has been formulated originally by Robert Hooke investigating the mechanics of springs.¹ Hooke's law states that these two quantities scale linearly, with the spring constant k being the proportionality factor.

$$F = kd \tag{2.1}$$

Later, this relation has been observed to hold also for solid bodies, with the deflection - terminologically - turning into deformation. However, equation 2.1 is valid only for ideal springs or, generally speaking, only within the limit of linear elasticity. Hooke's law is a special case of the comprehensive theory of elasticity (see for example [2]). Still, it provides a good description for many systems as long as we restrict ourselves to small deformations. In its more general formulation it relates stress σ to strain ϵ *via* a proportionality factor c :³

$$\sigma = c\epsilon \quad (2.2)$$

In fact, the variables in equation 2.2 represent tensors. However, in the simplest case, *e.g.* for the axial stretching of an elastic cylindrical fiber with cross sectional area A and length L , stress can be expressed as the applied tensile force F divided by A and strain as the relative elongation of the fiber, elongation ΔL divided by L (*cf.* fig. 2.1ab). Then, the proportionality factor between stress and strain is the elastic modulus E (for small deformations, *i.e.* within the linear elastic limit). Hence, eq. 2.2 can be rewritten as:

$$\frac{F}{A} = E \frac{\Delta L}{L} \quad (2.3)$$

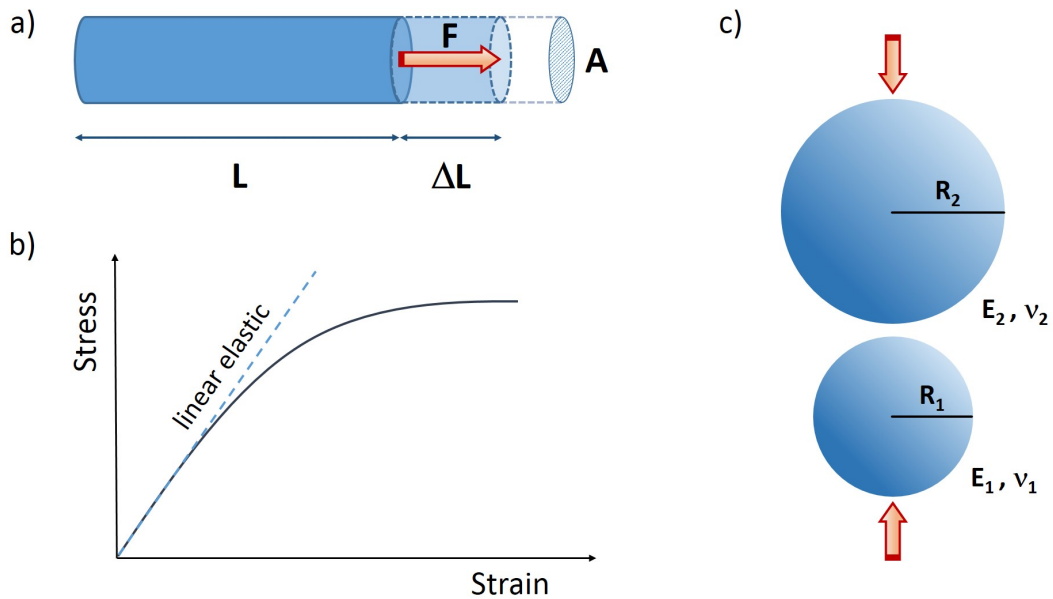


Figure 2.1. a) Elongation of a cylindrical fiber with the relevant parameters to describe its stress-strain behavior. b) Typical stress-strain diagram; after an initially linear relation (Hooke's law) yielding and plastic deformation take place. c) Schematic representation of two spheres before uniaxial deformation.

Roughly 200 years after Hooke Heinrich Hertz described the normal elastic deformation of two solid bodies in contact (*cf.* fig. 2.1c).⁴ Following his reasoning one can derive the expression for the deformation of a full sphere:

$$F = \frac{4}{3} \cdot \bar{E} \cdot d^{\frac{3}{2}} \cdot \sqrt{R} \quad (2.4)$$

Here, \bar{E} is the reduced Young's modulus (see equation 2.5) and R is the radius of the sphere (when in contact with a flat surface) or the relative radius (eq. 2.6, in case of two spheres in contact).

$$\frac{1}{\bar{E}} = \frac{1 - \nu_1^2}{E_1} + \frac{1 - \nu_2^2}{E_2} \quad (2.5)$$

$$\frac{1}{R} = \frac{1}{R_1} + \frac{1}{R_2} \quad (2.6)$$

Here, ν denotes Poisson's ratio and the indices refer to the two bodies in contact. Hertz still assumes linear elastic bodies which are homogeneous and isotropic. Furthermore, surface roughness, friction and adhesion are neglected and only small deformations of up to 10% of the particle's diameter may be regarded. Still, despite these constraints, the Hertz model has been shown to apply to a range of systems.⁵⁻¹² Also from theoretical calculations using a finite element model (FEM) the validity of the Hertz model has been proven.¹³ Moreover, the authors show that the Hertz model even works for non-flat contact surfaces and when friction is not negligible. However, they also point out that for large strains the Hertz model deviates significantly from the FEM predictions.

To account for adhesive interactions several models were developed based on Hertz' formula. Two of the best-known and widely used models are named after their authors, the JKR- (Johnson-Kendall-Roberts)¹⁴ and the DMT-model (Derjaguin-Müller-Toporov).¹⁵ While JKR considers the effect of adhesion during contact, DMT only regards it outside

the contact zone. In order to illustrate better the differences between the models it is convenient to rewrite equation 2.4 in the following way:

$$a^3 = \frac{3}{4} \cdot \frac{RF}{\bar{E}} \quad (2.7)$$

In this generalized Hertz equation a is the contact radius between sphere and plate or between two spheres. It is equal to the square root of deformation d and radius R , \sqrt{dR} . With this new parameter a we can now introduce the relevant JKR (eq. 2.8, 2.9) and DMT (eq. 2.10) equations.

$$a_{JKR}^3 = \frac{3}{4} \cdot \frac{R}{\bar{E}} \cdot (F + 3\gamma\pi R + \sqrt{6\gamma\pi RF + (3\gamma\pi R)^2}) \quad (2.8)$$

$$a_{JKR}^{ZL} = \left(\frac{9\gamma\pi R^2}{2\bar{E}}\right)^{1/3} \quad (2.9)$$

$$a_{DMT}^{ZL} = \left(\frac{3\gamma\pi R^2}{2\bar{E}}\right)^{1/3} \quad (2.10)$$

Here, γ is the surface energy and a^{ZL} is the contact radius at zero load.

It becomes obvious that eq. 2.8 reduces to the Hertz equation when γ assumes values close/equal to zero, *i.e.* for vanishing adhesive interactions between the two approaching surfaces. Consequently, the contact area at zero load reduces to one contact point.

The different expressions for a^{ZL} in JKR and DMT theory have been ascribed to the observation that they represent two extreme or limiting cases.^{16,17} Simulations indicate that JKR holds best for large, compliant particles with high surface energy, while DMT rather applies for small, hard and less adhesive objects.¹⁸ Johnson and Greenwood proposed a more quantitative "adhesion map" suggesting which model would be appropriate for a given load and interaction parameter (fig. 2.2).¹⁹ Therefore, the

dimensionless load \bar{F} (applied force divided by adhesion force) is related to the Maugis elasticity parameter λ which includes the maximum attractive force σ_0 .

$$\lambda = \sigma_0 \left(\frac{9R}{2\pi\gamma E^2} \right)^{1/3} \quad (2.11)$$

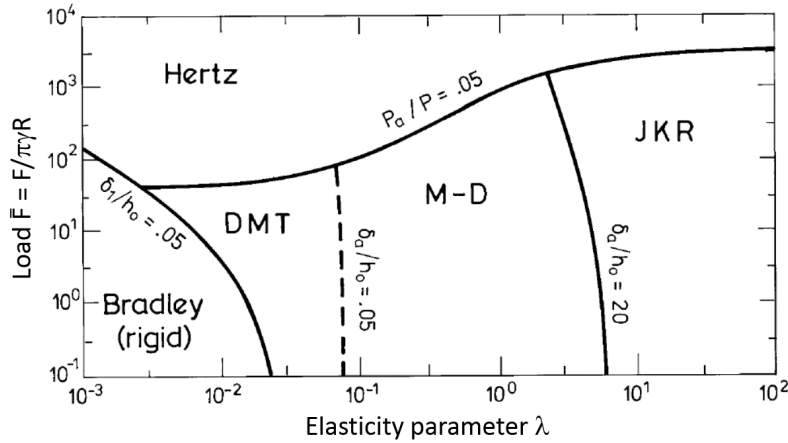


Figure 2.2. "Adhesion map" showing which model applies best for a given combination of dimensionless load \bar{F} and elasticity parameter λ . For more details see [19]. Reprinted with permission from [19], ©1997 Elsevier.

The Hertz, JKR and DMT theories have been further modified to account for additional effects such as capillary condensation,^{20,21} large contact areas,²² viscoelasticity^{23,24,12} or plasticity,²⁵ non-planar substrate support.²⁶

As stated above, the JKR and DMT models are extensions to the Hertz model, *i.e.* they still describe small, linear elastic deformations. For the investigation of large deformations hyper-elastic models need to be employed. Lin *et al.* give an overview of several of these models and compare with finite element analysis and experimental data.²⁷ Their analysis includes Neo-Hookean,²⁸ Mooney-Rivlin,²⁹ Ogden,³⁰ Fung,^{31,32} Gaylord-Douglas^{33,34} and further models. All of them have been evaluated positively for the description of rubber elastic materials as exemplified by poly(vinyl alcohol) (PVA) gels. On the other hand,

deformation of cartilage tissue exhibiting a highly non-linear stress-strain behavior was shown to be best fit by the Fung and Ogden models. Another theoretical treatment of large deformations has been proposed by Tatara.³⁵⁻³⁷ It is based on the Mooney-Rivlin law and relates the load to the deformation to third and fifth power, for moderate and larger deformations, respectively. It has been shown to apply to a range of systems.³⁸⁻⁴²

2.1.2 Axial deformation - Hollow spheres

Publications on the mechanics of hollow thin spherical shells date back to the second half of the nineteenth century.^{43,44} The first comprehensive treatment of the deformation of thin elastic shells was presented by Love in 1888 and has become a "classic" paper since.⁴⁵ For his shell theory he adopted another "classic" - Kirchhoff's assumptions for thin plates.⁴⁶ The "Kirchhoff-Love assumptions" provide the framework for thin shell theory which will be the basic concept for the description of the physics of capsule deformation in this section (*cf.* fig. 2.3).

Indeed, the restriction to thin shells is sensible as many shell structures - be it in the microscopic world or in architecture - meet the criterion of thinness, *i.e.* a ratio of shell thickness h to radius R equal or less than $1/20$.⁴⁷ Actually, herein lies the strength of shell constructions: mechanical stability and protection of the interior with a minimum of materials consumption. Beyond the requirement of thin shells the Kirchhoff-Love assumptions add the following constraints: the shell material is considered as homogeneous, isotropic and linear elastic (Hooke's law); only small deformations (with regard to shell thickness) are allowed; compression of the shell as well as stretching or in-plane shear is neglected. In other words, the shell deforms in pure bending upon normal axial loading.

This simplification can be illustrated by the energy contributions of stretching and bending.² For a given deformation d of a shell with elastic modulus E the energy per unit area for bending (\mathcal{E}_B) and stretching (\mathcal{E}_S) can be expressed as:

$$\mathcal{E}_B \propto Eh^3 \left(\frac{d}{R^2}\right)^2 \quad (2.12)$$

$$\mathcal{E}_S \propto Eh\left(\frac{d}{R}\right)^2 \quad (2.13)$$

For the ratio of these two follows:

$$\frac{\mathcal{E}_S}{\mathcal{E}_B} \propto \left(\frac{R}{h}\right)^2 \geq_{\text{thinshell}} 400 \quad (2.14)$$

This means that for a thin shell the energy required to stretch it is orders of magnitude higher than the energy necessary to bend it. In other words, upon external loading the shell will primarily deform in bending.

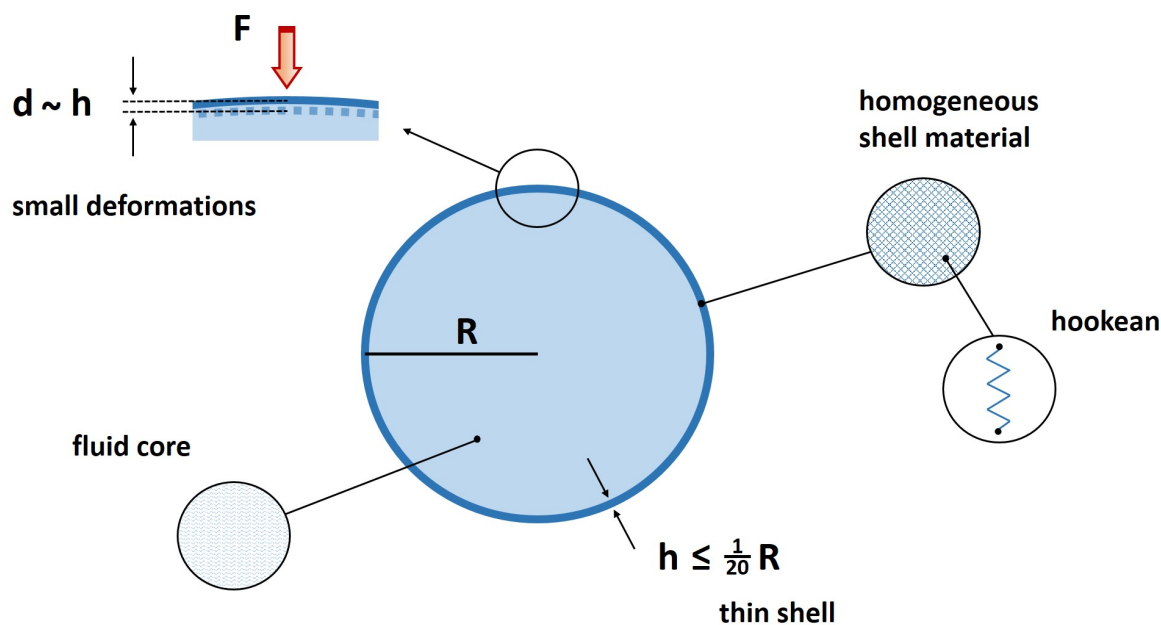


Figure 2.3. Schematic representation of basic requirements in thin shell theory.

Eric Reissner was one of the first scientists to present an analytical solution to the problem of shallow shell deformation.⁴⁸⁻⁵² His approach is based on the approximations

for thin shell theory as outlined above. For an axisymmetric shell under point load he finds a linear relation between force F and resulting deformation d :

$$F = \frac{h^2}{R} \cdot \frac{4E}{\sqrt{3(1-\nu^2)}} \cdot d \quad (2.15)$$

Here, ν is Poisson's ratio. Despite its simplicity equation 2.15 has been shown to apply to a range of capsule systems, also for non-point-like loading, *e.g.* with an AFM colloidal probe (for details see 2.2).⁵³⁻⁵⁷

However, the behavior of many relevant capsule systems deviates from the aforementioned simplifications. Additional contributions to the shell mechanics may originate from membrane pre-tensions. One of the first experimental and theoretical studies treating this issue examined Pickering emulsion droplets.⁵⁸ Here, a model is presented that includes both the contribution of surface tension and the mechanical tension of the shell. It is successfully applied to data from compression tests and comparison to results from continuum mechanics shows clearly the prominent role of the particle stabilized water-oil interface. A later work on a comparable system provided further evidence for the importance of surface tensions in shell mechanics.⁵⁹ In our paper on pH-responsive hydrogel capsules we also encountered a mechanical shell stiffening effect (as compared to substrate supported films) that may be explained by the occurrence of surface or membrane tension.⁶⁰

Another feature that is observed already for moderate deformations is the buckling instability of the shell. At a certain point the shell may respond to external pressure by an inward folding, thus minimizing its energy. Pogorelov proposed a force-deformation relation with a square root scaling to describe this phenomenon.⁶¹ Other researchers deduced from the onset of buckling information about the shell's elastic properties, *e.g.* with the help of osmotic pressure effects.⁶²⁻⁶⁹

Finally, "large" deformations are generally expected to impose further deformation modes (such as stretching or shearing of the shell) in addition to bending, even in the absence of buckling. In the introduction, one of the Kirchhoff-Love assumptions was "small"

deformations with respect to the shell thickness. Typically, deformations are considered "small" when they are on the order of one to two times the shell thickness. At this point it is helpful to consider again how an applied force scales with deformation. In the case of pure bending the force scales with relative deformation ε (deformation divided by capsule radius) like⁷⁰

$$F \propto \frac{4}{3} E h^2 \varepsilon \quad (2.16)$$

which is equivalent to Reissner's equation 2.15. However, pure bending is only an approximation; in fact, there will always be (at least) one more deformation mode, namely the stretching of the shell. For the limiting case of an impermeable shell with volume conservation this additional term scales like⁷¹

$$F \propto \frac{16\pi}{3} E h R \varepsilon^3. \quad (2.17)$$

Figure 2.4 shows these two scaling laws calculated exemplarily for two microcapsules of 10 μm radius, an elastic modulus of 1 MPa and a shell thickness of 50 nm (500 nm, the upper limit for thin shells!). We see that up to a relative deformation of *ca.* 5% (20%) shell permeability or stretching is negligible. The ε value corresponds to a deformation of approximately (half) the thickness of the shell. So, within this range thin shell theory can be expected to hold. However, for larger deformations volume effects become increasingly important (cubic scaling!) and need to be incorporated in physical modeling.

Up to now there are only few works that systematically investigated the burst of microcapsules in consequence of mechanical compression. Being an industrial relevant system melamine-formaldehyde (MF) capsule were studied by Zhang and co-workers.^{72,73} They found a linear correlation between capsule diameter and the force or deformation necessary to burst the capsules. Moreover, capsule burst was observed to occur for relative deformations of about 70%, independent of capsule size. A theoretical description of such

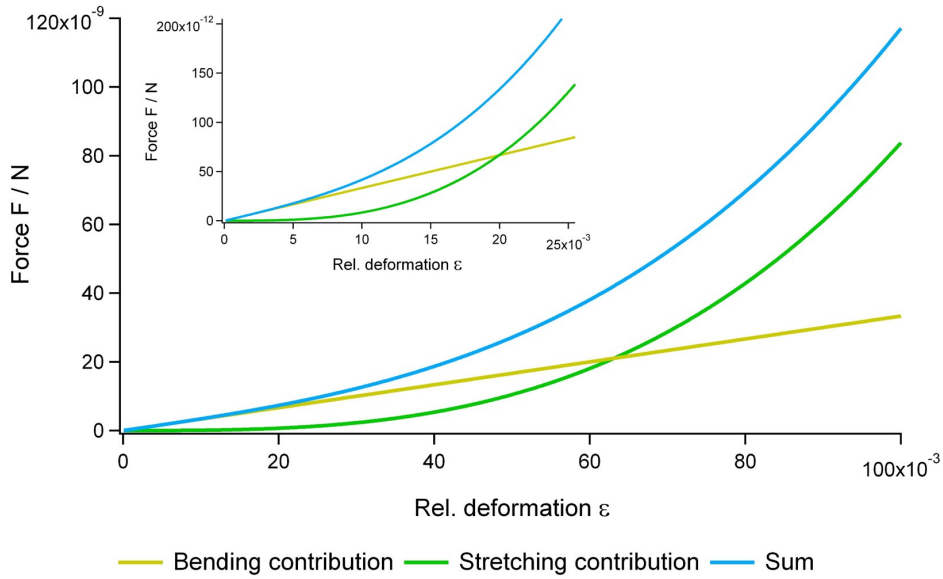


Figure 2.4. Bending and stretching contributions to the deformation of a microcapsule, 20 micron in diameter, shell thickness 500 nm and Young's modulus 1 MPa; inset shows the calculations for the same capsule with reduced shell thickness (50 nm).

large deformations leading to capsule burst has been proposed by Mercadé-Prieto *et al.* with the help of finite element modeling (FEM).⁷⁴ Good agreement with experimental data on MF capsules is found treating the shell material as elastic-perfectly plastic with strain hardening. In a later work the deformation of thick-shelled PMMA capsules was studied experimentally and by FEM.⁷⁵

Further aspects concerning the theory of capsule deformation can be found in [76].

2.1.3 Non-axial deformation

So far, the following situation has been modeled: a particle is supported on a substrate and deformed axially from the top pole. Now, let us consider the deformation of a particle suspended in liquid, *i.e.* deformation by shear forces.

Generally, when a solid body obeying Hooke's law is sheared, a linear relation of the form:

$$\sigma_{shear} = G\gamma \quad (2.18)$$

can be established. It relates the applied shear stress σ_{shear} to the shear strain γ with the proportionality factor G being the shear modulus. This is in analogy to eq. 2.2 for uniaxial tension or compression. The other extreme would be shearing a liquid. Here, the response to the applied stress is no longer elastic deformation but viscous flow and depends on the shear rate $\dot{\gamma}$, *i.e.* the derivative of γ with respect to time:

$$\sigma_{shear} = \eta\dot{\gamma} \quad (2.19)$$

The proportionality constant η is the liquid's (dynamic) viscosity.

For systems in-between these two boundary cases, such as polymers in solution, gels or colloidal suspensions, the description naturally becomes more complex. They behave viscoelastic, meaning that G becomes time-dependent. In the simplest case, *i.e.* linear viscoelasticity, the shear modulus can be expressed as:

$$G(t) = G_0 \cdot e^{-\frac{t}{\lambda}} \quad (2.20)$$

Here, G_0 is the equilibrium shear modulus and $\lambda = \eta/G_0$ the characteristic relaxation time. For the investigation of the dynamic properties of viscoelastic samples oscillatory shear experiments are performed where the applied strain is varied periodically at a given frequency ω like:

$$\gamma(\omega, t) = \gamma_0 \cdot \sin(\omega t) \quad (2.21)$$

Now, the shear stress can be described by:

$$\sigma_{shear} = \gamma_0(G'(\omega) \sin(\omega t) + G''(\omega) \cos(\omega t)) \quad (2.22)$$

where G' is the storage modulus, accounting for the elastic contribution, and G'' is the loss modulus, representing the system's viscous response.

The so far presented formulas and more detailed descriptions on the rheology of bulk systems can be found in a range of textbooks, *e.g.* [77–80].

Let us now turn to the specific problem of particles in shear flow. First studies in this area date back to the 1930s when Taylor examined the deformation of liquid droplets suspended in another liquid under different flow conditions (simple shear and plane hyperbolic flow).⁸¹ He observes an elongation of the initially spherical drop to assume an elliptic shape (*cf.* fig. 2.5). This shape change is quantified by a geometrical parameter (later denoted as Taylor parameter, D) containing the drop's longest and shortest diameter, L and B , respectively. It is related to the dimensionless parameter F like:

$$D = \frac{L - B}{L + B} \approx F = \frac{\dot{\gamma} \eta_c R}{\sigma_{intf}} \quad (2.23)$$

Here, η_c is the viscosity of the continuous phase, R the radius of the droplet and σ_{intf} the interfacial tension. Comparison with experimental data has shown that eq. 2.23 and its more general form derived by Cox⁸² are valid for small deformations and Newtonian liquids.⁸³ Later publications provide more refined models for the deformation of liquid drops suspended in another liquid, also accounting for other flow conditions and non-Newtonian liquids.^{84–96}

In contrast to liquid droplets (which are not in our focus), individual solid elastic particles under shear flow have not been studied as extensively. This discrepancy may have its origin in the incompatibility of models typically used to describe solid and liquid phases and difficulties in determining the position of the interface between these two phases.⁹⁸

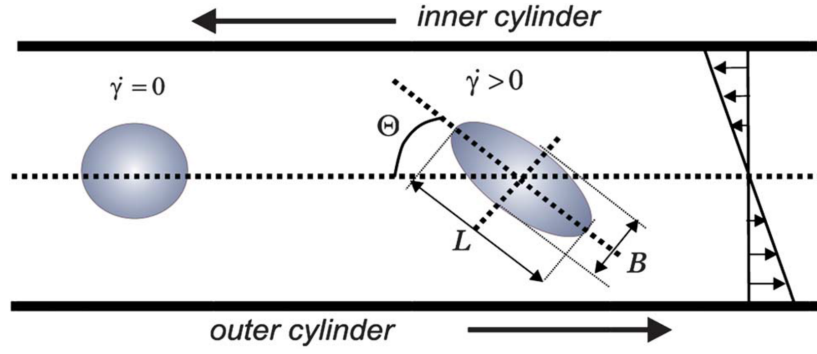


Figure 2.5. An initially spherical particle suspended in liquid (left) is subjected to linear shear flow (right) causing a certain deformation (length L , width B) and spacial alignment (angle Θ). The flow is created in Couette geometry (two co-axial, counter-rotating cylinders); small arrows indicate local flow direction and velocity. Reproduced from [97] by permission of The Royal Society of Chemistry.

Interestingly, in his theoretical analysis Murata reports that the shape equations for elastic full spheres resemble very much the ones obtained by Taylor and others for fluid drops under simple shear, hyperbolic or Poiseuille flow.⁹⁹ However, quantitative descriptions of the mechanics of single solid particles in shear flow remain scarce. Early works on this problem considered the contribution of the particles to the overall rheological properties of the suspension.^{100–102} Following Brunn¹⁰³ and Van-der-Reijden-Stolk¹⁰⁴ we can write the equations given below for the deformation of a homogeneous, isotropic, incompressible elastic particle in elongational shear flow:

$$\frac{r}{R} = 1 + \varepsilon F_{ij} \left(\frac{R^2 \partial^2}{\partial r_i \partial r_j} \left(\frac{1}{r} \right) \right) \quad (2.24)$$

$$\frac{D(\varepsilon F_{ij})}{Dt} = \frac{5}{2} e_{ij} - \frac{2E}{9\eta_c} \varepsilon F_{ij} \quad (2.25)$$

Here, R and r are the initial and deformed radius of the particle, respectively, εF_{ij} the deformation tensor, e_{ij} the strain tensor, E the elastic modulus of the particle and η_c

the viscosity of the continuous liquid phase. For steady-state shear conditions eq. 2.24 and 2.25 can be further simplified to yield eq. 2.26 for the deformation and 2.27 for the shape of the particle:

$$\varepsilon F_{11} = \frac{5}{2} R W e_E (1 - e^{-\frac{t}{\tau}}) \quad (2.26)$$

$$\frac{r}{R} = 1 + \frac{15}{2} W e_E (1 - e^{-\frac{t}{\tau}}) \cos 2\varphi \quad (2.27)$$

Here, $W e_E = \eta_c \dot{\gamma} / E$ is the elastic Weber number, $\tau = 9\eta_c / 2E$ and φ the angle between r and the major deformation direction.

More recently, Gao and co-workers have complemented the earlier works by a comprehensive investigation of shape and motion of initially spherical or elliptic, Neo-Hookean particles in shear flow.^{105,106,98} Their analytic approach is based on a polarization technique and the results obtained for single particles are used to describe the rheological properties of dilute suspensions built from them.

In contrast to full spheres, the literature on the deformation of individual hollow capsules in shear flow is much more extended.^{107,108} In the simplest case, *i.e.* for a homogeneous, isotropic shell material following Hooke's law and Newtonian liquids as internal and continuous phase, the deformation of a capsule in linear shear flow can be described according to:^{109,97}

$$D = \frac{25\eta_c r \dot{\gamma}}{4E_S} = \frac{25}{4} C_a \quad (2.28)$$

Here, D is the above introduced Taylor parameter, r the initial capsule radius, η_c the viscosity of the surrounding liquid and E_S the two-dimensional elastic modulus which may be approximated as the product of shell thickness and Young's modulus. C_a is the capillary number (for a droplet suspended in liquid E_S would be replaced by the surface

tension). Eq. 2.28 resembles eq. 2.23, showing that, under the given assumptions, the deformation of a capsule in shear flow can be modeled in a similar way as a droplet. Thus, the droplet-solution may be interpreted as a boundary scenario for a capsule with vanishing shell thickness and the modulus of the shell material being replaced by the interfacial tension.

For linear elastic shells the tilt angle denoted by Θ in fig. 2.5 was shown to assume a constant value of 45° while for linear viscoelastic capsules it depends on the applied shear rate.¹¹⁰ Finally, for a viscous shell with negligible elastic contributions no steady state is reached but the capsule's shape changes in a periodic manner.¹¹⁰

In analogy to the above discussed axial capsule deformation, the deformation of capsules in shear flow depends as well on a range of parameters including shape,^{111–113} shell stiffness,^{114–117} the shell material's constitutive law,^{118–120,110,121} viscosity of core and surrounding liquid,^{122,123} wrinkling,^{124,107,125} buckling,^{126,118,127} pre-stress^{128,129} and flow conditions.^{130–132,107,133}

2.2 Measurement techniques

For the experimental determination of microparticle mechanics a range of measurement techniques has been established reflecting the multifariousness of particle shapes, materials and compliance. While the pioneers of particle mechanics relied on rather macroscopic setups with poor resolution and high loads, we have nowadays the possibility to effect deformations on the order of nanometers applying forces as low as pico-Newtons (*cf.* fig. 2.10). One of the first reports on microcapsule deformation is from Cole.¹³⁴ He probed the mechanical properties of Arbacia eggs (*ca.* 75 micron in diameter) with the help of a 6 micron thick, 180 micron wide, 12 mm long flat gold wire and followed the eggs' deformation with an optical microscope. About seven decades later first studies suggest the use of modified cantilevers in combination with an AFM (atomic force microscope) to elucidate mechanical properties of artificial microcapsules.^{135,136}

In the following sections the main focus will be on such AFM-based methods as these

have been the method of choice for the characterization of microparticles as outlined in the papers below. At the end of the chapter, a section is included discussing methods for the morphological characterization of particles. As pointed out in the theory sections geometrical parameters such as diameter or shell thickness play an important role for the assessment of mechanical properties.

2.2.1 Atomic force microscopy (AFM)

The AFM has originally been developed in the 1980s as a tool to study surface topography with atomic resolution.^{137,138} Force measurements with the AFM had their breakthrough with the independent publications of Ducker¹³⁹ and Butt¹⁴⁰ in 1991. They proposed a modification of the standard imaging cantilevers which are equipped with a sharp tip. Instead of the sharp tip a glass sphere of colloidal dimensions (several μm in diameter) was glued to the front of the cantilever. The such created "colloidal probe" (CP) was used to measure surface forces between the CP and a flat silicon wafer or freshly cleaved mica as a function of ionic strength and pH. Results were compared with DLVO theory. The advantage of a CP for this kind of studies is obvious: the colloidal sphere provides a well-defined geometry which facilitates modeling and interpretation of the obtained data. Furthermore, it provides a relatively large contact area and can be modified easily *via* surface chemistry. Finally, it opens the field for studying mechanics and interactions of colloidal particles with the high precision in force and displacement of an AFM. So, it's not surprising that this technique and modifications thereof have become very popular in colloid and interface science and that Ducker's article has been cited more than 1,200 times.

Before discussing the different measurement geometries and opportunities of AFM for the characterization of particle mechanics the basic working principles of AFM-instrumented force measurements shall be explained. Figure 2.6 shows a typical setup schematically. The movement of the cantilever towards the surface is piezo controlled. The deflection of the cantilever is monitored by the deflection of a laser beam which is focused on the

back of the cantilever and reflected to a photodiode. So, the raw signal of a "force" measurement is voltage PV vs. piezo displacement z . To convert this information into force F vs. displacement two calibration steps need to be carried out: the determination of the cantilever's spring constant k and its sensitivity, typically given as the inverted optical lever sensitivity $InvOLS$.

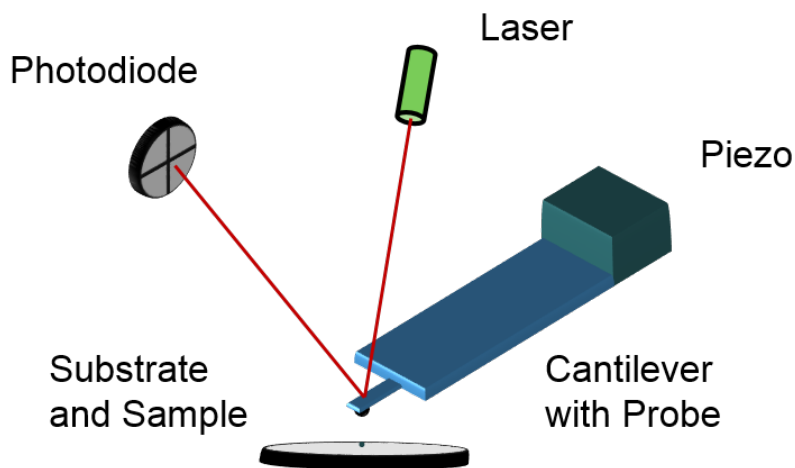


Figure 2.6. Schematic representation of an atomic force microscope (AFM) probing a particle.

For the determination of k several methods have been developed, of which the most important are: 1) thermal noise method,^{141,142} where k is calculated from the thermal resonance peak of the cantilever; 2) Sader method,^{143–147} uses the resonant frequency, cantilever dimensions and the density of surrounding fluid; 3) added mass method,¹⁴⁸ evaluates the shift in resonant frequency when masses of defined weight are attached to the cantilever; 4) reference spring method,^{149–152} where the cantilever with unknown spring constant is pushed against a calibrated reference.

While, in general, the spring constant only needs to be determined once, the $InvOLS$ has to be determined prior to each measurement (and, to check for consistency, also afterwards). This is due to the fact that it strongly depends on the alignment of the laser spot on the cantilever which will change with each demounting/mounting of the cantilever. Typically, the $InvOLS$ is obtained as the inverse slope of a voltage vs. displacement curve

resulting from pressing the cantilever against a hard, non-deformable, planar substrate (*e.g.*, a glass slide or silicon wafer). An alternative, non-invasive method has been proposed by Higgins *et al.*, who calculate the *InvOLS* from the known spring constant and resonant frequency.¹⁵³

Knowing the spring constant and the *InvOLS* the photodiode signal in Volts is converted to force in Newtons in the following way:

$$F = PV \cdot InvOLS \cdot k \quad (2.29)$$

Finally, when examining a compliant sample the displacement needs to be corrected for the cantilever bending to yield the deformation (of the sample) d . This is done like:

$$d = z - \frac{F}{k} \quad (2.30)$$

Now, we can obtain a force *vs.* deformation characteristic as shown exemplarily in fig. 2.7. After the unperturbed approach to the particle surface the cantilever touches and compresses it until a pre-defined trigger point is reached. Upon retraction, the cantilever feels the elastic restoring force of the sample and, in case of adhesive interactions between sample and probe, is deflected to negative values until a minimum is reached (the pull-off force, commonly interpreted as the force of adhesion, F_{adh}). Additional features might arise, for instance, from attractive or repulsive interactions outside the contact zone. For more details see [154].

The AFM covers a wide reach of forces (pN to μ N) and is therefore a useful tool for the mechanical characterization of particles built from a broad range of materials, in particular (bio)polymers and (hydro)gels. Deformations are effected uniaxially which may be ascertained by optic control. In the case of microcapsules the combination with RICM (reflection interference contact microscopy) allows for the observation of change

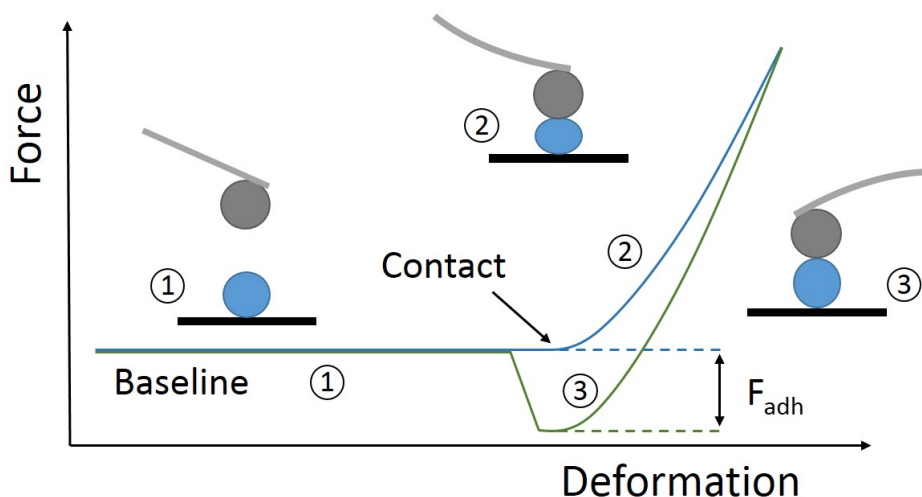


Figure 2.7. Schematic representation of a deformation experiment with AFM force spectroscopy. 1) Approach: The cantilever is far away from the surface, no interactions with the sample. 2) Compression: The probe is in contact with the sample and deforms it. 3) Withdraw: In case of adhesion between probe and sample, the cantilever bends toward the sample upon retraction. The difference between minimum and baseline equals the adhesion force, F_{adh} .

of contact area during deformation.^{135,155} Moreover, from the interference patterns the three-dimensional shape of the capsule under compression can be reconstructed.^{156–159} As said in the beginning, the colloidal probe is often used in force spectroscopy, not only for studying surface or interfacial forces but also to assess materials mechanics (for different probe geometries see fig. 2.8). In the field of particle mechanics first works were published roughly ten years ago.^{136,71,160,135,155,161} Independently, the Fery and Vinogradova groups studied PEMCs (poly-electrolyte multilayer capsules) whose mechanical properties could be shown to clearly depend on shell thickness, thus confirming theoretical predictions. In the meantime, mechanics of various particulate systems have been investigated with CP-AFM, among these multilayer capsules,^{162–166} vesicles,¹⁶⁷ polymer capsules^{55,54,60} and particles.^{6,8,7,168–170}

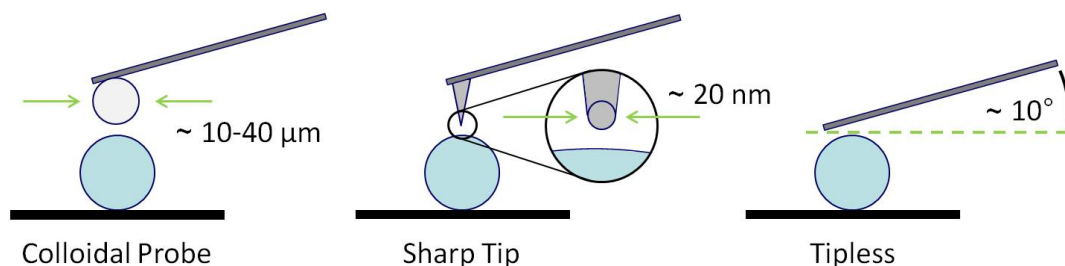


Figure 2.8. Schematic representation of the different probes/measurement geometries in AFM based force spectroscopy. While a colloidal probe can be chosen such that it has comparable dimensions with respect to the examined particles, the radius of a sharp tip is orders of magnitude smaller, thus probing more local elastic properties. Using a bare cantilever one has to consider its inclination as predetermined by the cantilever holder.

An alternative to CP-cantilevers for the investigation of mechanical properties is the use of standard cantilevers with a tip. This way, however, a decisive advantage of colloidal probes is lost. With a CP of comparable dimension with respect to the examined particles the contact zone is rather extended which minimizes local pressure, thus providing gentle probing of the sample. In contrast, a sharp tip gives a very local information and mechanical pressure is relatively high. Therefore, measurement parameters have to be set with care in order to avoid penetration into the sample, which makes data evaluation difficult due to arising friction or shearing. In addition, sharp tips are not as well defined as colloidal probes; for correct modeling, their actual geometry needs to be determined separately, *e.g.* with a calibration grating or *via* SEM. Nevertheless, sharp tips have widely been applied to study particle mechanics, covering polymeric full particles^{11,5} and capsules,⁵⁷ inorganic capsules,^{56,171} vesicles,^{172,173} polymersomes¹⁷⁴ and viral shells.^{175,176} Finally, particle deformation experiments can, in principle, also be performed with bare, tipless cantilevers. Yet, one has to be aware of the default tilt of the cantilever in commercial holders (typically 10°). Due to this inclination the axial compression is expected to be accompanied by shear forces and sliding of the particle may occur. Still, this approach has been used for a range of capsule systems.^{177–183} In a recent publication on mechanical properties of giant unilamellar vesicles (GUV), Schäfer *et al.* account for

the inclination of the cantilever by tilting the substrate such that an almost perfectly parallel plate geometry is ensured.¹⁸⁴

2.2.2 Micromanipulation

Roughly a decade prior to the first CP-AFM measurements on PEMCs a micromanipulation based parallel plate compression technique was introduced to study the deformation induced burst of melamine formaldehyde (MF) microcapsules.⁷² In analogy to AFM force *vs.* displacement (or deformation) curves are recorded, however, the accessible force range lies above AFM techniques on the order of μN to N while displacement precision is between nm and μm . Therefore, it is a very helpful tool for the investigation of large particle deformations beyond linear elasticity. Burst of microcapsules may be examined as well as failure of full spheres. Hence, micromanipulation has been applied to various polymeric capsules^{185,186} and full particles.^{12,187,10,188,42,41,189–191}

A special type of micromanipulator is the AFM instrumented NanoIndenter (Asylum Research, Santa Barbara, CA). It allows the use of various tip geometries (flat punch, sphere) which can also be applied to particle compression. One of its advantages is that it covers an intermediate force range with respect to AFM and classical micromanipulation, thus bridging between these two technologies.

A typical force curve obtained with a large spherical indenter tip ($800\ \mu\text{m}$ in diameter) is shown in fig. 2.9. The compressed sample is an MF microcapsule with a radius of $11\ \mu\text{m}$ and an approximate shell thickness of $150\ \text{nm}$. After an initial elastic response we observe pseudo-yielding until the capsule bursts. This burst event is marked by a sudden decrease in force.

2.2.3 Other methods

Further techniques to characterize particle mechanics were developed particularly in the field of biologically relevant samples such as cells or vesicles, which are very soft.

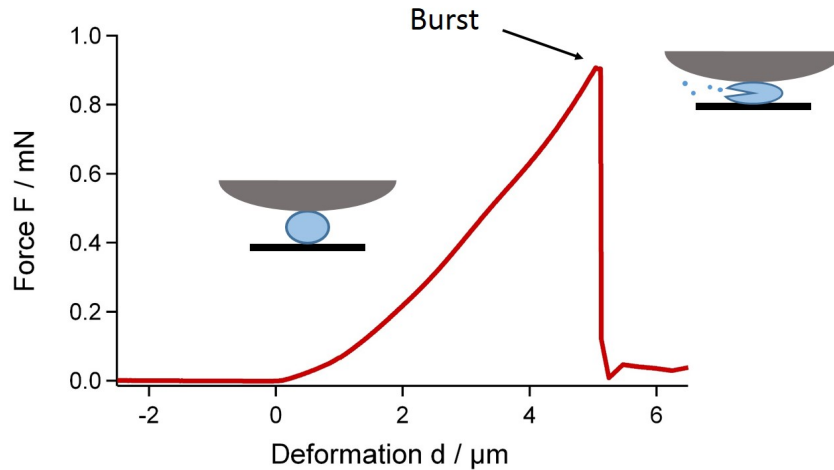


Figure 2.9. Example for the large deformation of an MF capsule with an AFM-based NanoIndenter.

Therefore, methods like micropipette aspiration or optical/magnetic tweezers are best suited.

Micropipette aspiration was first introduced by Michison and Swan in the 1950s under the name "cell elastimeter".¹⁹² Its principle is rather simple: The water filled pipette is connected to a movable water reservoir which, being lowered, effects an under-pressure. Thus, a single cell (or capsule) can be aspirated and, depending on the position of the reservoir, sucked into the pipette with defined pressure. The resulting deformation of the cell is a function of the applied pressure (Pa to kPa, corresponding to forces from pN to nN) and can be used to gain information about elastic properties. Not only biological samples^{193–199} but also very compliant, artificial capsules^{178,200–202} have been studied with this technique.

Optical^{203–206,187,207–209} (magnetic^{210–212}) tweezers exploit the photonic pressure of lasers (a magnetic field) to trap and manipulate microparticles. These are attached to a cell's or capsule's surface. Tearing these particles apart with the help of the tweezers the cell/capsule is deformed and information about their mechanical properties is obtained. The strength of this technique lies in the extremely low force range (some tens of fN to hundreds of pN).

Finally, another important technique shall not be omitted: rheology based methods.

These are fundamentally different compared to the methods presented so far as no longer axial forces act on the particles but shear forces. Typical measurement geometries include Couette flow,^{125,213–215,97} where the particles are suspended in a liquid sheared between two concentric, counter-rotating cylinders, and the spinning drop setup,^{216–220,132} where the particles are suspended in a liquid sheared inside a rotating tube.

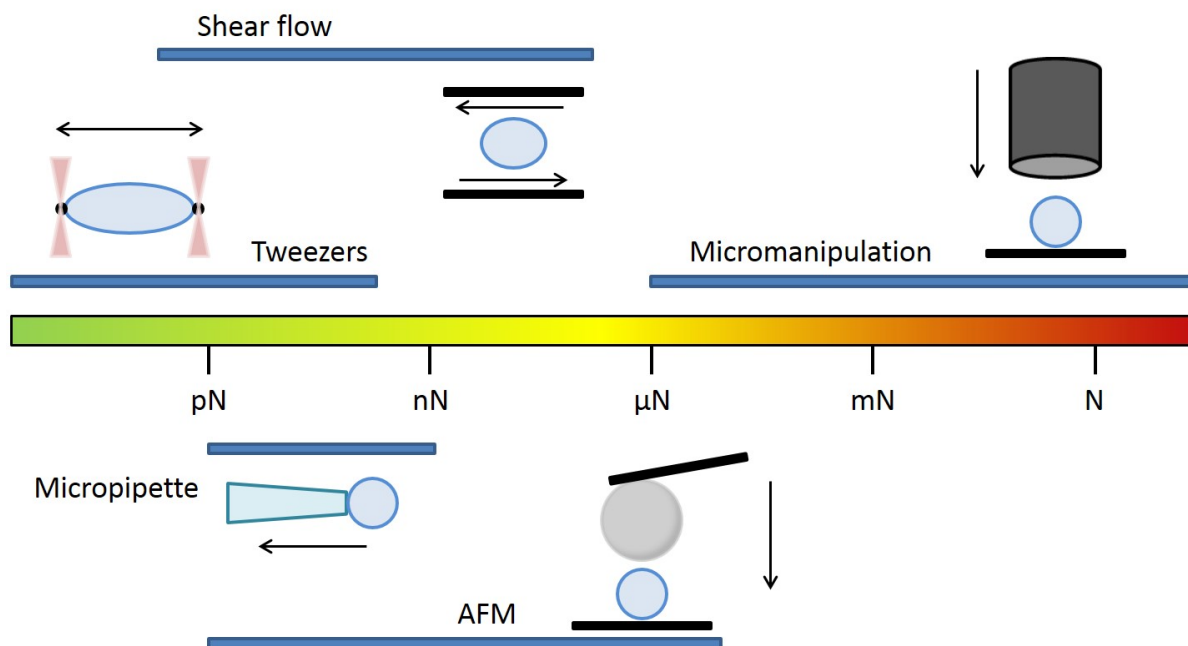


Figure 2.10. Overview over the different measurement techniques to probe particle mechanics and the typical force range available for these methods. Reprinted with permission from [76], ©2013 Elsevier.

2.2.4 Morphological characterization

As stated above, knowledge of geometrical parameters is essential for the evaluation and interpretation of mechanical testing data. Beyond the simple determination of particle size with optical microscopy several other methods may be of use to achieve full insight into the particle's morphology.

In the case of capsules it is indispensable to know the shell's thickness. It can be

determined with the help of TEM (transmission electron microscopy). Therefore, the capsules have to be embedded into a resin which, after solidification, can be cut into thin slices with an ultratome. A protocol for gentle embedding has been published in one of our papers.⁵⁵ Here, the capsules were first fixed in agar and stepwise dehydrated before eventually being embedded into the resin. The capsule sections as obtained from TEM have to be evaluated with care. Due to the random sectioning one can expect the determined wall thickness to be an overestimation. The correct thickness is measured only at the equator; closer to the poles the measured thickness will always be larger. To account for this deviation, a mathematical correction has been proposed by Smith *et al.*²²¹ and further modified by Poehlmann *et al.*⁵⁴ Also for full spheres, TEM slicing can provide valuable information about the homogeneity of the material, which is a prerequisite for many mechanical models.

Particle morphology, especially surface topography, can as well be investigated with SEM (scanning electron microscopy). In contrast to TEM samples need to be (made) conductive. Sometimes, SEM is used to characterize the thickness of microcapsule shells.^{222,223} However, shell fragments are mostly seen from a certain angle which impedes a correct measurement of the shell thickness. Another option is cryo-SEM, where the samples are frozen and broken such that the fracture often reveals the internal structure of the particles.

In case the capsule can be collapsed (*e.g.*, by drying, gentle heating or ultrasonic treatment), AFM imaging provides an alternative to the intricate and time-consuming TEM investigation. Additionally, AFM allows for the examination of shell thickness under the same conditions as during the measurement of mechanical properties, for instance under controlled temperature and humidity or with the samples immersed in liquid. The measured height will correspond to twice the shell thickness; see for example [60, 54]. The such obtained values might, however, lead to a slight overestimation of the shell thickness, if the capsule is not completely collapsed or retains some of its original filling.

Finally, for sufficiently thick shells confocal laser microscopy can be used.^{224,225,75} It may

also be helpful to check the homogeneity of full spheres.⁷ However, only fluorescent (or fluorescently labeled) samples can be investigated and, compared to electron or force microscopy, resolution is rather low (400-600 nm). In return, it offers a noninvasive and three-dimensional imaging of the particles.

"Ping-pong is easier to play than to understand."

(Ludovic Pauchard)

3

Materials

The particles studied in this thesis are either hydrogels or built from a layer-by-layer approach. Therefore, this chapter focuses on these two classes of materials and provides a concise overview of preparation and physico-chemical properties. In addition, one section is dedicated to recombinant spider silk, which, in its particulate form, is also an object of investigation in the present work.

3.1 Hydrogels

Generally, hydrogels can be described as semi-solid materials built from small amounts of solid embedded in relatively large amounts of liquid, yet being rather solid-like than liquid-like.²²⁶ The solid framework consists of hydrophilic polymers which are held together either loosely by weak physical interactions (virtual crosslinks, "physical gels") or firmly

by covalent crosslinks ("chemical gels"). While physical gels dissolve in an excess of solvent, chemical gels swell to an equilibrium and maintain their three-dimensional structure.^{227–229} Consequently, for the construction of stable particles only the latter are relevant and will, therefore, be discussed in the following. For this class of solid-like gels Almdal and co-workers propose a more quantitative, yet still phenomenological definition based on rheology, *i.e.* dynamic mechanical properties.²³⁰ Hence, as distinct features are identified: no equilibrium modulus, a plateau in the storage modulus G' on a time scale of seconds or longer and a loss modulus G'' significantly inferior to G' after reaching the plateau.

Characteristic parameters

Hydrogels can be characterized by three main parameters: the polymer volume fraction in the swollen state, $v_{2,s}$, the average molecular weight of the polymer chain between two neighbouring cross-linking points, \bar{M}_c , and the corresponding mesh size or correlation length, ξ . The polymer volume fraction is given by the ratio of polymer volume, V_p , to swollen gel volume, V_g .²³¹ Thus, $v_{2,s}$ is the inverse of the volume swelling ratio, Q , which, in turn, can be expressed by the density of solvent, ρ_1 , and polymer, ρ_2 , and the mass swelling ratio, Q_m , *cf.* equation 3.1.²³¹

$$v_{2,s} = \frac{V_p}{V_g} = Q^{-1} = \frac{1/\rho_2}{Q_m/\rho_1 + 1/\rho_2} \quad (3.1)$$

\bar{M}_c and ξ can be obtained theoretically or directly with the help of several experimental techniques, *e.g.* small angle X-ray scattering (SAXS) to determine the average mesh size. One way to infer these parameters from the hydrogel's swelling performance is to use the classical equilibrium swelling theory, as proposed by Flory and Rehner.^{232,233}

Equilibrium swelling theory

Initially, this theory was developed for chemically cross-linked non-ionic polymers. When these materials are immersed in a liquid and allowed to swell until equilibrium, two

energy contributions to the total Gibbs free energy, ΔG_{total} , need to be considered:

$$\Delta G_{total} = \Delta G_{elastic} + \Delta G_{mixing} \quad (3.2)$$

Here, $\Delta G_{elastic}$ arises from the elastic, retractive forces of the polymer network, while ΔG_{mixing} accounts for the thermodynamic force of mixing. Thus, ΔG_{mixing} can be regarded as a measure of the compatibility of the polymer with the respective fluid, usually expressed by the polymer-solvent interaction parameter, χ_1 .²³⁴

Starting from these fundamental energy considerations and using basic results of rubber elasticity theory,^{232,234,28} one can derive an equation (3.3) that relates the average molecular weight between two neighboring cross-links, \bar{M}_c , to known or experimentally accessible quantities.

$$\frac{1}{\bar{M}_c} = \frac{1}{\bar{M}_n} + \frac{(\bar{v}/V_1)[\ln(1 - v_{2,s}) + v_{2,s} + \chi_1 v_{2,s}^2]}{v_{2,s}^{1/3} - \frac{v_{2,s}}{2}} \quad (3.3)$$

Here, \bar{M}_n is the average molecular weight of the polymer before cross-linking, \bar{v} its specific volume and V_1 is the molar volume of the solvent.

Equation 3.3 is strictly valid only for neutral hydrogels prepared in the absence of solvent. Peppas and Merrill modified this equation for hydrogels directly prepared in an aqueous solution.²³⁵ It accounts for the change in chemical potential due to the hydration shells around the polymer strands.

$$\frac{1}{\bar{M}_c} = \frac{2}{\bar{M}_n} + \frac{(\bar{v}/V_1)[\ln(1 - v_{2,s}) + v_{2,s} + \chi_1 v_{2,s}^2]}{v_{2,r}[(\frac{v_{2,s}}{v_{2,r}})^{1/3} - (\frac{v_{2,s}}{2v_{2,r}})]} \quad (3.4)$$

Here, $v_{2,r}$ is the polymer volume fraction in the relaxed state, *i.e.* directly after cross-linking but before swelling.

For hydrogels built from polymers bearing ionic side groups the theoretical description of the swelling behavior becomes more complex. Then, a third term has to be added to

the total Gibbs free energy accounting for the electrostatic interactions. The resulting equations include ionic strength, pH and dissociation constants. More details on ionic gels can be found elsewhere.²³⁶⁻²³⁸

Once the value of \bar{M}_c is determined, it is possible to calculate the mesh size, ξ , of the swollen hydrogel using equation 3.5.

$$\xi = v_{2,s}^{-1/3} \left(\frac{2C_n \bar{M}_c}{M_r} \right)^{1/2} l \quad (3.5)$$

Here, C_n is the Flory characteristic ratio, M_r is the molecular weight of the repetitive unit of the polymer and l is the bond length along the polymer backbone. For many materials these constants can be found tabulated in the literature. Despite its simplicity the equilibrium swelling theory can give good estimates for a range of hydrogels. However, one has to be aware that the Flory-Rehner theory is based on an idealized polymer model which will not hold for many real systems.

Relevance

In the 1950's Wichterle and Lim were the first to study the synthesis of artificial hydrogels.²³⁹ These researchers also proposed first applications in the biomedical sector, *e.g.* hydrogels from poly(hydroxy-ethyl) methacrylate (pHEMA) for the use as contact lenses. Soon, corresponding patents were assigned, where the production of soft contact lenses is described.^{240,241} Since then, hydrogels have been studied extensively and a lot of applications have emerged, mainly in the biomedical²⁴²⁻²⁴⁶ and pharmaceutical²⁴⁷⁻²⁵⁰ field. Further applications include food additives,^{251,252} cosmetics,²⁵³⁻²⁵⁵ sensing,²⁵⁶ (stem) cell cultivation and tissue engineering.²⁵⁷⁻²⁶³

3.2 Layer-by-Layer systems

First experimental evidence for a layer-by-layer (LbL) assembly was given by Iler in 1966.²⁶⁴ He constructed a multilayer by alternate adsorption of colloidal boehmite fibrils and silica particles. 25 years later, Hong and Decher were the first to report LbL film formation on a molecular level, *i.e.* with the assembly of oppositely charged amphiphiles,²⁶⁵ polyelectrolytes²⁶⁶ or a combination of both.²⁶⁷ Subsequently, the versatility of LbL techniques was demonstrated, for instance by using DNA,²⁶⁸ charged virus,²⁶⁹ proteins²⁷⁰ or nanoparticles²⁷¹ as film constituting layers. Finally, it was shown that polyelectrolyte multilayer films can also be assembled on colloidal templates, which could subsequently be removed to yield polyelectrolyte multilayer capsules (PEMCs).^{272,273}

The original protocol requires a series of dipping and washing steps, *cf.* fig. 3.1. First, the charged substrate (*e.g.*, a negatively charged silicon wafer or spherical silica particles) is immersed in a solution of oppositely charged polyelectrolyte (*e.g.*, positively charged poly(allylamine)). Then, it is removed from the solution, thoroughly rinsed and transferred into a solution of oppositely charged polyelectrolyte (*e.g.*, negatively charged poly(styrenesulfonate)). This process can be repeated multiple times as the outer layer always overcompensates the charge of the previous one.²⁷⁵ This robust but tedious procedure can be facilitated by subsequent or even simultaneous spray coating of the oppositely charged layer components. This novel approach has initially been proposed by Schlenoff and co-workers in 2000²⁷⁶ and has been reviewed recently.^{277,278} One major advantage of the technique is that the built-up of LbL films on large areas becomes feasible, which even allows for production on an industrial scale.²⁷⁹

The broad variety of materials and assembly strategies²⁸⁰ is also reflected in the already established and envisaged applications. These range from drug delivery^{274,281} to self-healing materials,²⁸² from biosensing^{283–285} and imaging²⁸⁶ to photovoltaic cells^{287,288} and superhydrophobic surfaces.²⁸⁹

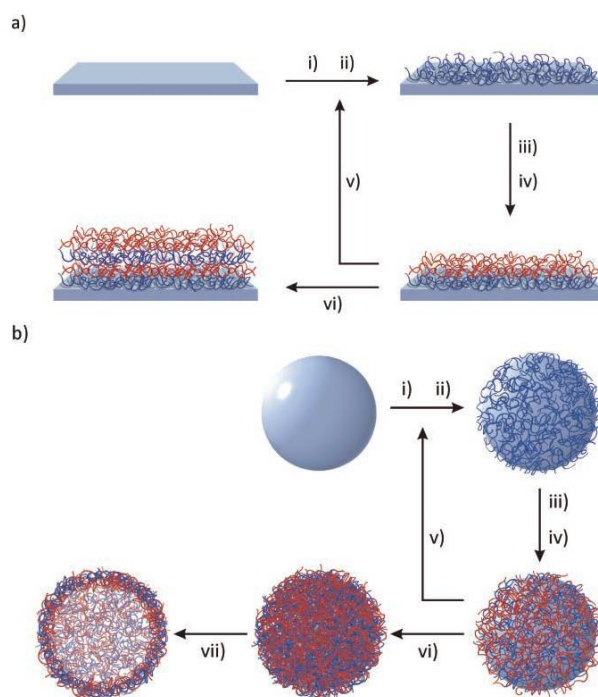


Figure 3.1. Schematic representation of layer-by-layer assembly on planar (a) and colloidal substrates (b). i,ii) adsorption of the first layer and rinsing; iii,iv) adsorption of oppositely charged polyelectrolyte and washing; v,vi) repeat until desired multilayer composition is obtained; vii) the colloidal template may be dissolved to yield hollow capsules. ©2010 Wiley. Reproduced with permission from [274], John Wiley and Sons.

3.3 Recombinant spider silk

Silk harvested from silkworms has been exploited for centuries while spider silk - despite its superior mechanical properties - has not.²⁹⁰ One reason for this discrepancy lies in the difficulties of farming spiders due to their territorial and cannibalistic behavior. Only the advent of biotechnological techniques to synthetically produce spider silk proteins at larger scales has promoted research in this field and opened perspectives for the commercial use of this fascinating material.

One approach to obtain spider silk proteins is recombinant synthesis.²⁹¹ Therefore, the genes that encode these proteins have to be identified, cloned, introduced into and, subsequently, expressed by bacteria, *e.g.*, *E. coli*. Then, after several purification steps,

the pure protein is ready for further processing.

Among the most studied spider silks is the major ampullate silk (dragline silk) from *Araneus diadematus*, the European garden spider.^{290,292} Its main constituent proteins are termed ADF-3 and ADF-4 (ADF for *araneus diadematus* fibroin). These are rich in elastic β -turn spirals and crystalline β -sheets.²⁹⁰ These two central motifs most probably account for the outstanding mechanical properties of dragline silk combining high strength and elasticity.²⁹³ The corresponding recombinantly produced, engineered proteins are termed eADF3 and eADF4. It has been shown that the eADF4(C16) protein (*i.e.* an ADF4 protein mimic consisting of 16 times the repetitive C-module) can be assembled into a variety of morphologies.²⁹³ Among these we find fibers, hydrogels, films and particles, hollow capsules and full spheres (*cf.* fig. 3.2).

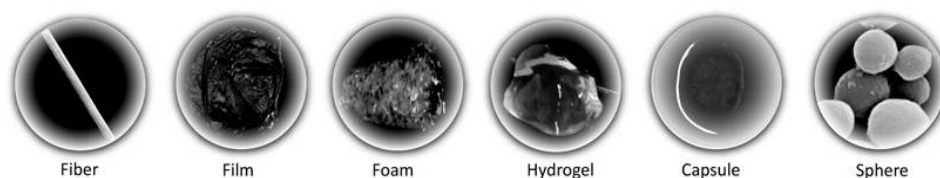


Figure 3.2. Overview over the different morphologies engineered spider silk can be processed into. These include several levels of structural hierarchy ranging from gels and foams to fibers and particulate assemblies. Reproduced with permission from [294], ©2009 the Biochemical Society.

Spherical micro- and sub-microparticles can be obtained from a relatively simple salting-out process.^{295,296} Therefore, potassium phosphate (at least 1 molar) is added to an aqueous solution (6 molar guanidinium thiocyanate) of eADF4(C16). Depending on mixing intensity (*e.g.*, dialysis, pipette or micromixing device) and protein concentration the size of the resultant particles can roughly be tuned to yield mean diameters from few hundreds of nanometers to some micron. These particles are rich in beta-sheets and show a smooth surface and homogeneous internal morphology, as revealed by FTIR-spectroscopy, scanning and transmission electron microscopy, respectively.

Hollow capsules were prepared from interfacial adsorption.^{297,298} Therefore, a w/o emulsion

was prepared with the dispersed aqueous phase consisting of eADF4(C16) solution and the continuous phase being toluene. Due to their amphiphilic nature the proteins assemble at the water-oil interface and form a homogeneous film. Additionally, the contact with the oil induces a conformational rearrangement of the proteins resulting in a high amount of beta-sheets. The such obtained capsules proved to be mechanically stable and can be transferred from the oil into an aqueous solution for further analysis or modification, for instance, chemical crosslinking to prevent from enzymatic digestion.²⁹⁷ In order to avoid toxic toluene it has been shown that silicone oil can be used as well to obtain spider silk microcapsules.²⁹⁹

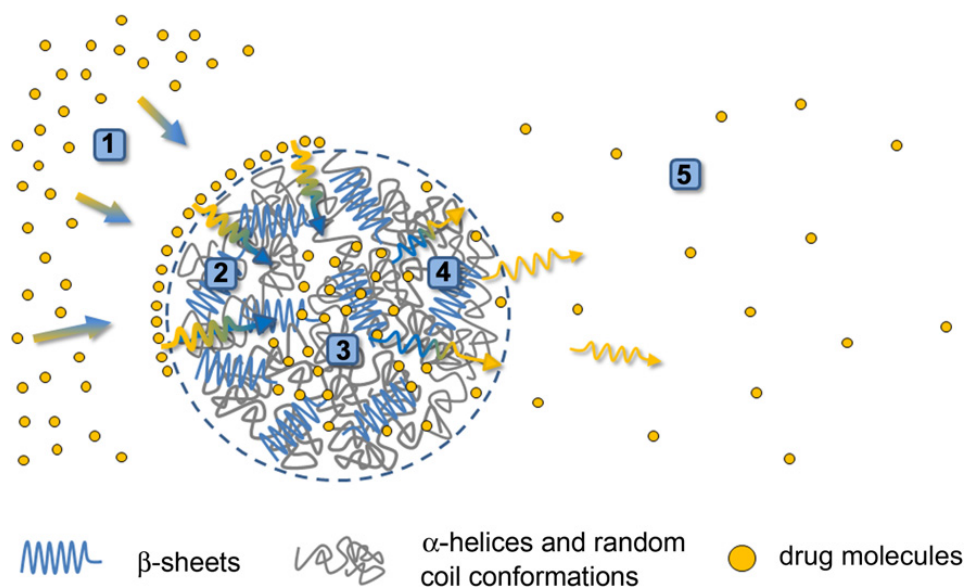


Figure 3.3. Schematic representation of loading of and release from C16 microparticles. Positively charged drug molecules are attracted to the particle surface by electrostatic interactions (1) and, subsequently, diffuse to the inside (2). Here, they are stored (3) until diffusion controlled release (4,5) is induced through a concentration gradient. Reproduced with permission from [300], ©2010 Elsevier.

Concerning application perspectives of eADF4(C16) particulate assemblies, their potential to serve as drug delivery vehicles has already been demonstrated.^{301,302,300,303} Drugs can be loaded into the particles by electrostatic attraction and diffusion controlled³⁰⁰ (*cf.* fig. 3.3) or *via* co-precipitation during particle formation,³⁰¹ which increases loading efficiency. Release is again diffusion controlled and can be influenced by salt, pH^{302,300} and crosslinking.³⁰¹ More recently, C16 microcapsules were shown to be promising candidates to serve as reaction micro-containers for enzymes.²⁹⁹ A model enzyme, β -galactosidase, was successfully encapsulated and its activity monitored spectroscopically. Furthermore, due to the semi-permeable capsule membrane it was possible to activate from outside an encapsulated inactive enzyme precursor. This opens the road for a variety of distinct technical and medical applications.

References

- (1) Hooke, R., *Lectiones Cutlerianae (or, A Collection of Lectures)*; Royal Society: 1679.
- (2) Landau, L. D.; Lifschitz, E. M., *Theory of Elasticity*; Pergamon Press Ltd, Oxford: 1970.
- (3) Beer, F. P.; Johnston, E. R.; Dewolf, J. T.; Mazurek, D. F., *Mechanics of Materials*; Lange, M., Ed.; McGraw-Hill: 2012.
- (4) Hertz, H. *Journal fuer die reine und angewandte Mathematik* **1881**, *92*, 156–171.
- (5) Armini, S.; Vakarelski, I. U.; Whelan, C. M.; Maex, K.; Higashitani, K. *Langmuir* **2007**, *23*, 2007–2014.
- (6) Cappella, B.; Wassenberg, J. R.; Heim, L.-O.; Klostermann, M.; Venzmer, J.; Bonaccorso, E. *Polymer* **2014**, *55*, 1209–1216.
- (7) Ma, S.; Natoli, M.; Liu, X.; Neubauer, M. P.; Watt, F. M.; Fery, A.; Huck, W. T. S. *J. Mater. Chem. B* **2013**, *1*, 5128–5136.
- (8) Neubauer, M. P.; Blum, C.; Agostini, E.; Engert, J.; Scheibel, T.; Fery, A. *Bio-mater. Sci.* **2013**, *1*, 1160–1165.
- (9) Ogneva, I. V.; Lebedev, D. V.; Shenkman, B. S. *Biophysical Journal* **2010**, *98*, 418–424.
- (10) Olderoy, M.; Xie, M.; Andreassen, J.-P.; Strand, B.; Zhang, Z.; Sikorski, P. *English Journal of Materials Science: Materials in Medicine* **2012**, *23*, 1619–1627.
- (11) Tan, S.; Sherman, R. L.; Ford, W. T. *Langmuir* **2004**, *20*, 7015–7020.
- (12) Yan, Y.; Zhang, Z.; Stokes, J. R.; Zhou, Q.-Z.; Ma, G.-H.; Adams, M. J. *Powder Technology* **2009**, *192*, 122–130.
- (13) Dintwa, E.; Tijsskens, E.; Ramon, H. *Granular Matter* **2008**, *10*, 209–221.
- (14) Johnson, K. L.; Kendall, K.; Roberts, A. D. *Proceedings of the Royal Society of London Series a-Mathematical and Physical Sciences* **1971**, *324*, 301–&.

- (15) Derjaguin, B. V.; Muller, V. M.; Toporov, Y. P. *Journal of Colloid and Interface Science* **1975**, *53*, 314–326.
- (16) Attard, P.; Parker, J. L. *Physical Review A* **1992**, *46*, 7959–7971.
- (17) Tabor, D. *Journal of Colloid and Interface Science* **1977**, *58*, 2–13.
- (18) Greenwood, J. A. *Proceedings of the Royal Society a-Mathematical Physical and Engineering Sciences* **1997**, *453*, 1277–1297.
- (19) Johnson, K. L.; Greenwood, J. A. *Journal of Colloid and Interface Science* **1997**, *192*, 326–333.
- (20) Fogden, A.; White, L. R. *Journal of Colloid and Interface Science* **1990**, *138*, 414–430.
- (21) Zakerin, M.; Kappl, M.; Backus, E. H. G.; Butt, H.-J.; Schonfeld, F. *Soft Matter* **2013**, *9*, 4534–4543.
- (22) Maugis, D. *Langmuir* **1995**, *11*, 679–682.
- (23) Attard, P. *Langmuir* **2001**, *17*, 4322–4328.
- (24) Attard, P. *Physical Review E* **2001**, *63*.
- (25) Zhao, J. H.; Nagao, S.; Zhang, Z. L. *International Journal of Mechanical Sciences* **2012**, *56*, 70–76.
- (26) Chen, J. *Journal of Physics D-Applied Physics* **2013**, *46*.
- (27) Lin, D. C.; Shreiber, D. I.; Dimitriadis, E. K.; Horkay, F. *Biomechanics and Modeling in Mechanobiology* **2009**, *8*, 345–358.
- (28) Treloar, L. R. G., *The physics of rubber elasticity*; Oxford University Press: 1975.
- (29) Mooney, M. *J Appl Phys* **1940**, *11*, 582–592.
- (30) Ogden, R. W. *Proceedings of the Royal Society of London Series a-Mathematical and Physical Sciences* **1972**, *326*, 565–&.
- (31) Fung, Y. C. B. *American Journal of Physiology* **1967**, *213*, 1532–&.

-
- (32) Fung, Y. C.; Fronek, K.; Patitucci, P. *American Journal of Physiology* **1979**, *237*, H620–H631.
- (33) Gaylord, R. J.; Douglas, J. F. *Polymer Bulletin* **1987**, *18*, 347–354.
- (34) Gaylord, R. J.; Douglas, J. F. *Polymer Bulletin* **1990**, *23*, 529–533.
- (35) Tatara, Y. *Journal of Engineering Materials and Technology-Transactions of the Asme* **1989**, *111*, 163–168.
- (36) Tatara, Y.; Shima, S.; Lucero, J. C. *Journal of Engineering Materials and Technology-Transactions of the Asme* **1991**, *113*, 292–295.
- (37) Tatara, Y. *Journal of Engineering Materials and Technology-Transactions of the Asme* **1991**, *113*, 285–291.
- (38) Liu, K. K.; Williams, D. R.; Briscoe, B. J. *Journal of Physics D-Applied Physics* **1998**, *31*, 294–303.
- (39) Muller, E.; Chung, J. T.; Zhang, Z.; Sprauer, A. *Journal of Chromatography A* **2005**, *1097*, 116–123.
- (40) Ravi, N.; Wan, K. T.; Swindle, K.; Hamilton, P. D.; Duan, G. *Polymer* **2006**, *47*, 4203–4209.
- (41) Gauthier, M. A.; Luo, J.; Calvet, D.; Ni, C.; Zhu, X. X.; Garon, M.; Buschmann, M. D. *Polymer* **2004**, *45*, 8201–8210.
- (42) Ioannidis, N.; Bowen, J.; Pacek, A.; Zhang, Z. *Journal of Colloid and Interface Science* **2012**, *367*, 153–160.
- (43) Aron, H. *Journal fuer die reine und angewandte Mathematik* **1874**, *78*, 136–174.
- (44) Rayleigh, L. *Proc. Lond. Math. Soc.* **1881**, *13*, 4–16.
- (45) Love, A. E. H. *Philosophical Transactions of the Royal Society of London* **1888**, *179A*, 491–546.
- (46) Kirchhoff, G. *Journal fuer die reine und angewandte Mathematik* **1850**, *40*, 51–88.

-
- (47) Ventsel, E.; Krauthammer, T., *Thin Plates and Shells*; Marcel Dekker: New York, 2001.
- (48) Reissner, E. *Journal of Mathematics and Physics* **1946**, *25*, 279–300.
- (49) Reissner, E. *Journal of Mathematics and Physics* **1946**, *25*, 80–85.
- (50) Reissner, E. *Journal of Mathematics and Mechanics* **1958**, *7*, 121–140.
- (51) Reissner, E. *Communications on Pure and Applied Mathematics* **1959**, *12*, 385–398.
- (52) Reissner, E.; Wan, F. Y. M. *Studies in Applied Mathematics* **1969**, *48*, 1.
- (53) Fery, A.; Weinkamer, R. *Polymer* **2007**, *48*, 7221–7235.
- (54) Poehlmann, M.; Grishenkov, D.; Kothapalli, S. V. V. N.; Harmark, J.; Hebert, H.; Philipp, A.; Hoeller, R.; Seuss, M.; Kuttner, C.; Margheritelli, S.; Paradossi, G.; Fery, A. *Soft Matter* **2014**, *10*, 214–226.
- (55) Pretzl, M.; Neubauer, M.; Tekaath, M.; Kunert, C.; Kuttner, C.; Leon, G.; Berthier, D.; Erni, P.; Ouali, L.; Fery, A. *Acs Applied Materials & Interfaces* **2012**, *4*, 2940–2948.
- (56) Zhang, L.; D’Acunzi, M.; Kappl, M.; Auernhammer, G. K.; Vollmer, D.; van Kats, C. M.; van Blaaderen, A. *Langmuir* **2009**, *25*, 2711–2717.
- (57) Zoldesi, C. I.; Ivanovska, I. L.; Quilliet, C.; Wuite, G. J. L.; Imhof, A. *Physical Review E* **2008**, *78*, 8.
- (58) Ferri, J. K.; Carl, P.; Gorevski, N.; Russell, T. P.; Wang, Q.; Boker, A.; Fery, A. *Soft Matter* **2008**, *4*, 2259–2266.
- (59) Tan, S. Y.; Tabor, R. F.; Ong, L.; Stevens, G. W.; Dagastine, R. R. *Soft Matter* **2012**, *8*, 3112–3121.
- (60) Best, J. P.; Neubauer, M. P.; Javed, S.; Dam, H. H.; Fery, A.; Caruso, F. *Langmuir* **2013**, *29*, 9814–9823.
- (61) Pogorelov, A. V.; Babenko, V. I. *International Applied Mechanics* **1992**, *28*, 1–17.

-
- (62) Gao, C.; Donath, E.; Moya, S.; Dudnik, V.; Mohwald, H. *European Physical Journal E* **2001**, *5*, 21–27.
- (63) Arnoldi, M.; Fritz, M.; Bauerlein, E.; Radmacher, M.; Sackmann, E.; Boulbitch, A. *Physical Review E* **2000**, *62*, 1034–1044.
- (64) Boulbitch, A. *Journal of Electron Microscopy* **2000**, *49*, 459–462.
- (65) Wan, K. T.; Chan, V.; Dillard, D. A. *Colloids and Surfaces B-Biointerfaces* **2003**, *27*, 241–248.
- (66) Yao, X.; Walter, J.; Burke, S.; Stewart, S.; Jericho, M. H.; Pink, D.; Hunter, R.; Beveridge, T. J. *Colloids and Surfaces B-Biointerfaces* **2002**, *23*, 213–230.
- (67) Zhongcan, O. Y.; Helfrich, W. *Physical Review A* **1989**, *39*, 5280–5288.
- (68) Landau, L. D.; Lifschitz, E. M., *Course of Theoretical Physics*, 3.; Butterworth-Heinemann: Oxford, 1997; Vol. 7.
- (69) Pogorelov, A. V., *Bending of Surface and Stability of Capsules*; American Mathematical Society: 1988.
- (70) Landau, L. D.; Lifschitz, E. M., *Elastizitätstheorie*; Akademie: Berlin, 1991.
- (71) Lulevich, V. V.; Andrienko, D.; Vinogradova, O. I. *Journal of Chemical Physics* **2004**, *120*, 3822–3826.
- (72) Zhang, Z.; Saunders, R.; Thomas, C. R. *Journal of Microencapsulation* **1999**, *16*, 117–124.
- (73) Sun, G.; Zhang, Z. *Journal of Microencapsulation* **2001**, *18*, 593–602.
- (74) Mercade-Prieto, R.; Allen, R.; Zhang, Z. B.; York, D.; Preece, J. A.; Goodwin, T. E. *Aiche Journal* **2012**, *58*, 2674–2681.
- (75) Pan, X.; Mercade-Prieto, R.; York, D.; Preece, J. A.; Zhang, Z. *Industrial & Engineering Chemistry Research* **2013**, *52*, 11253–11265.
- (76) Neubauer, M. P.; Poehlmann, M.; Fery, A. *Advances in Colloid and Interface Science* **2013**, *207*, 65–80.

-
- (77) Barnes, H. A.; Hutton, J. F.; Walters, K., *An Introduction to Rheology*; Elsevier: 1989.
- (78) Goodwin, J. W.; Hughes, R. W., *Rheology for Chemists - An Introduction*; The Royal Society of Chemistry: 2008.
- (79) Shaw, M. T., *Introduction to Polymer Rheology*; John Wiley & Sons, Inc.: 2011.
- (80) Steffe, J. F., *Rheological Methods in Food Process Engineering*; Freeman Press: 1996.
- (81) Taylor, G. I. *Proceedings of the Royal Society of London. Series A* **1934**, *146*, 501–523.
- (82) Cox, R. G. *Journal of Fluid Mechanics* **1969**, *37*, 601–623.
- (83) Elmendorp, J. J.; Maalcke, R. J. *Polymer Engineering and Science* **1985**, *25*, 1041–1047.
- (84) Bentley, B. J.; Leal, L. G. *Journal of Fluid Mechanics* **1986**, *167*, 241–283.
- (85) Vanderreijden-Stolk, C.; Sara, A. *Polymer Engineering and Science* **1986**, *26*, 1229–1239.
- (86) Aggarwal, N.; Sarkar, K. *Journal of Fluid Mechanics* **2007**, *584*, 1–21.
- (87) Fischer, P.; Erni, P. *Current Opinion In Colloid & Interface Science* **2007**, *12*, 196–205.
- (88) Zabaranin, M.; Nir, A. *Siam Journal On Applied Mathematics* **2011**, *71*, 925–951.
- (89) Barthes-Biesel, D.; Acrivos, A. *Journal of Fluid Mechanics* **1973**, *61*, 1–21.
- (90) Acrivos, A.; Lo, T. S. *Journal of Fluid Mechanics* **1978**, *86*, 641–672.
- (91) Rallison, J. M.; Acrivos, A. *Journal of Fluid Mechanics* **1978**, *89*, 191–200.
- (92) Rallison, J. M. *Journal of Fluid Mechanics* **1981**, *109*, 465–482.
- (93) Stone, H. A. *Annual Review of Fluid Mechanics* **1994**, *26*, 65–102.

-
- (94) Sarkar, K.; Schowalter, W. R. *Journal of Fluid Mechanics* **June 2001**, 436, 207–230.
- (95) Maffettone, P. L.; Minale, M. *Journal of Non-newtonian Fluid Mechanics* **1998**, 78, 227–241.
- (96) Greco, F. *Journal of Non-newtonian Fluid Mechanics* **2002**, 107, PII S0377–0257(02)00144–1.
- (97) Koleva, I.; Rehage, H. *Soft Matter* **2012**, 8, 3681–3693.
- (98) Gao, T.; Hu, H. H.; Castaneda, P. P. *Journal of Fluid Mechanics* **2013**, 715, 573–596.
- (99) Murata, T. *Journal of the Physical Society of Japan* **1981**, 50, 1009–1016.
- (100) Frohlich, H.; Sack., R. *Proceedings of the Royal Society of London Series A-mathematical and Physical Sciences* **1946**, 185, 415–430.
- (101) Roscoe, R. *Journal of Fluid Mechanics* **1967**, 28, 273–&.
- (102) Goddard, J. D.; Miller, C. *Journal of Fluid Mechanics* **1967**, 28, 657–&.
- (103) Brunn, P. O. *Journal of Fluid Mechanics* **1983**, 126, 533–544.
- (104) Vanderreijden-Stolk, C.; Vanheel, A. S.; Sara, A.; Schut, J. *Polymer Engineering and Science* **1989**, 29, 593–599.
- (105) Gao, T.; Hu, H. H.; Castaneda, P. P. *Journal of Fluid Mechanics* **2011**, 687, 209–237.
- (106) Gao, T.; Hu, H. H.; Castaneda, P. P. *Physical Review Letters* **2012**, 108, 058302.
- (107) Barthes-Biesel, D. *Current Opinion in Colloid & Interface Science* **2011**, 16, 3–12.
- (108) Finken, R.; Kessler, S.; Seifert, U. *Journal of Physics-condensed Matter* **2011**, 23, 184113.
- (109) Barthes-Biesel, D. In, Rehage, H., Peschel, G., Eds.; Springer: 1998; Chapter Structure, Dynamics and Properties of Disperse Colloidal Systems, pp 58–64.

-
- (110) Barthesbiesel, D.; Sgaier, H. *Journal of Fluid Mechanics* **1985**, *160*, 119–135.
- (111) Sui, Y.; Low, H. T.; Chew, Y. T.; Roy, P. *Physical Review E* **2008**, *77*, 016310.
- (112) Walter, J.; Salsac, A. . V.; Barthes-Biesel, D. *Journal of Fluid Mechanics* **2011**, *676*, 318–347.
- (113) Wang, Z.; Sui, Y.; Spelt, P. D. M.; Wang, W. *Physical Review E* **2013**, *88*, 053021.
- (114) Pozrikidis, C. *Journal of Fluid Mechanics* **2001**, *440*, 269–291.
- (115) Le, D. V. *Physical Review E* **2010**, *82*, 016318.
- (116) Sui, Y.; Chew, Y. T.; Roy, P.; Chen, X. B.; Low, H. T. *Physical Review E* **2007**, *75*, 066301.
- (117) Noguchi, H. *Physical Review E* **2010**, *81*, 056319.
- (118) Lac, E.; Barthes-Biesel, D.; Pelekasis, N. A.; Tsamopoulos, J. *Journal of Fluid Mechanics* **2004**, *516*, 303–334.
- (119) Barthesbiesel, D. *Journal of Fluid Mechanics* **1980**, *100*, 831–853.
- (120) Barthesbiesel, D.; Rallison, J. M. *Journal of Fluid Mechanics* **1981**, *113*, 251–267.
- (121) Barthes-Biesel, D.; Diaz, A.; Dhenin, E. *Journal of Fluid Mechanics* **2002**, *460*, 211–222.
- (122) Ramanujan, S.; Pozrikidis, C. *Journal of Fluid Mechanics* **1998**, *361*, 117–143.
- (123) Bagchi, P.; Kalluri, R. M. *Physical Review E* **2009**, *80*, 016307.
- (124) Finken, R.; Seifert, U. *Journal of Physics-condensed Matter* **2006**, *18*, L185–L191.
- (125) Chang, K. S.; Olbricht, W. L. *Journal of Fluid Mechanics* **1993**, *250*, 609–633.
- (126) Barthes-Biesel, D. *Comptes Rendus Physique* **2009**, *10*, 764–774.
- (127) Foessel, E.; Walter, J.; Salsac, A. . V.; Barthes-Biesel, D. *Journal of Fluid Mechanics* **2011**, *672*, 477–486.
- (128) Lac, E.; Barthes-Biesel, D. *Physics of Fluids* **2005**, *17*, 8.
- (129) Lefebvre, Y.; Barthes-Biesel, D. *Journal of Fluid Mechanics* **2007**, *589*, 157–181.

-
- (130) Ma, G.; Hua, J. S.; Li, H. *Physical Review E* **2009**, *79*, 17.
- (131) Coupier, G.; Farutin, A.; Minetti, C.; Podgorski, T.; Misbah, C. *Physical Review Letters* **2012**, *108*, 5.
- (132) Pieper, G.; Rehage, H.; Barthes-Biesel, D. *Journal of Colloid and Interface Science* **1998**, *202*, 293–300.
- (133) Diaz, A.; Pelekasis, N.; Barthes-Biesel, D. *Physics of Fluids* **2000**, *12*, 948–957.
- (134) Cole, K. S. *Journal of Cellular and Comparative Physiology* **1932**, *1*, 1–9.
- (135) Dubreuil, F.; Elsner, N.; Fery, A. *European Physical Journal E* **2003**, *12*, 215–221.
- (136) Lulevich, V. V.; Radtchenko, I. L.; Sukhorukov, G. B.; Vinogradova, O. I. *Journal of Physical Chemistry B* **2003**, *107*, 2735–2740.
- (137) Binnig, G.; Quate, C. F.; Gerber, C. *Physical Review Letters* **1986**, *56*, 930–933.
- (138) Binnig, G. Atomic Force Microscope and Method for Imaging Surfaces with Atomic Resolution. pat., 4,723,318, 1986.
- (139) Ducker, W. A.; Senden, T. J.; Pashley, R. M. *Nature* **1991**, *353*, 239–241.
- (140) Butt, H. J. *Biophysical Journal* **1991**, *60*, 1438–1444.
- (141) Hutter, J. L.; Bechhoefer, J. *Review of Scientific Instruments* **1993**, *64*, 1868–1873.
- (142) Butt, H. J.; Jaschke, M. *Nanotechnology* **1995**, *6*, 1–7.
- (143) Sader, J. E.; Larson, I.; Mulvaney, P.; White, L. R. *Review of Scientific Instruments* **1995**, *66*, 3789–3798.
- (144) Sader, J. E. *Journal of Applied Physics* **1998**, *84*, 64–76.
- (145) Sader, J. E.; Chon, J. W. M.; Mulvaney, P. *Review of Scientific Instruments* **1999**, *70*, 3967–3969.
- (146) Sader, J. E.; Pacifico, J.; Green, C. P.; Mulvaney, P. *Journal of Applied Physics* **2005**, *97*.

-
- (147) Sader, J. E.; Sanelli, J. A.; Adamson, B. D.; Monty, J. P.; Wei, X. Z.; Crawford, S. A.; Friend, J. R.; Marusic, I.; Mulvaney, P.; Bieske, E. J. *Review of Scientific Instruments* **2012**, *83*.
- (148) Cleveland, J. P.; Manne, S.; Bocek, D.; Hansma, P. K. *Review of Scientific Instruments* **1993**, *64*, 403–405.
- (149) Gibson, C. T.; Watson, G. S.; Myhra, S. *Nanotechnology* **1996**, *7*, 259–262.
- (150) Slattery, A. D.; Quinton, J. S.; Gibson, C. T. *Nanotechnology* **2012**, *23*, 285704.
- (151) Slattery, A. D.; Blanch, A. J.; Quinton, J. S.; Gibson, C. T. *Nanotechnology* **2013**, *24*.
- (152) Torii, A.; Sasaki, M.; Hane, K.; Okuma, S. *Measurement Science & Technology* **1996**, *7*, 179–184.
- (153) Higgins, M. J.; Proksch, R.; Sader, J. E.; Polcik, M.; Mc Endoo, S.; Cleveland, J. P.; Jarvis, S. P. *Review of Scientific Instruments* **2006**, *77*.
- (154) Butt, H. J.; Cappella, B.; Kappl, M. *Surface Science Reports* **2005**, *59*, 1–152.
- (155) Elsner, N.; Dubreuil, F.; Fery, A. *Physical Review E* **2004**, *69*, 6.
- (156) Limozin, L.; Sengupta, K. *Chemphyschem* **2009**, *10*, 2752–2768.
- (157) Theodoly, O.; Huang, Z. H.; Valignat, M. P. *Langmuir* **2010**, *26*, 1940–1948.
- (158) Wiegand, G.; Jaworek, T.; Wegner, G.; Sackmann, E. *Journal of Colloid and Interface Science* **1997**, *196*, 299–312.
- (159) Wiegand, G.; Neumaier, K. R.; Sackmann, E. *Applied Optics* **1998**, *37*, 6892–6905.
- (160) Lebedeva, O. V.; Kim, B. S.; Vinogradova, O. I. *Langmuir* **2004**, *20*, 10685–10690.
- (161) Fery, A.; Dubreuil, F.; Mohwald, H. *New Journal of Physics* **2004**, *6*, 13.
- (162) Heuvingh, J.; Zappa, M.; Fery, A. *Langmuir* **2005**, *21*, 3165–3171.

- (163) Palankar, R.; Pinchasik, B. E.; Schmidt, S.; De Geest, B. G.; Fery, A.; Mohwald, H.; Skirtach, A. G.; Delcea, M. *Journal of Materials Chemistry B* **2013**, *1*, 1175–1181.
- (164) Bedard, M. F.; Munoz-Javier, A.; Mueller, R.; del Pino, P.; Fery, A.; Parak, W. J.; Skirtach, A. G.; Sukhorukov, G. B. *Soft Matter* **2009**, *5*, 148–155.
- (165) Elsner, N.; Kozlovskaya, V.; Sukhishvili, S. A.; Fery, A. *Soft Matter* **2006**, *2*, 966–972.
- (166) Mueller, R.; Kohler, K.; Weinkamer, R.; Sukhorukov, G.; Fery, A. *Macromolecules* **2005**, *38*, 9766–9771.
- (167) Liang, X. M.; Mao, G. Z.; Ng, K. Y. S. *Journal of Colloid and Interface Science* **2004**, *278*, 53–62.
- (168) Gillies, G.; Prestidge, C. A.; Attard, P. *Langmuir* **2002**, *18*, 1674–1679.
- (169) Gillies, G.; Prestidge, C. A. *Advances in Colloid and Interface Science* **2004**, *108*, 197–205.
- (170) Gillies, G.; Prestidge, C. A. *Langmuir* **2005**, *21*, 12342–12347.
- (171) Zhang, L.; D’Acunzi, M.; Kappl, M.; Imhof, A.; van Blaaderen, A.; Butt, H.-J.; Graf, R.; Vollmer, D. *Physical Chemistry Chemical Physics* **2010**, *12*, 15392–15398.
- (172) Chen, Q.; Schonherr, H.; Vancso, G. J. *Soft Matter* **2009**, *5*, 4944–4950.
- (173) Delorme, N.; Fery, A. *Physical Review E* **2006**, *74*, 3.
- (174) Jaskiewicz, K.; Makowski, M.; Kappl, M.; Landfester, K.; Kroeger, A. *Langmuir* **2012**, *28*, 12629–12636.
- (175) Cuellar, J. L.; Meinhoewel, F.; Hoehne, M.; Donath, E. *Journal of General Virology* **2010**, *91*, 2449–2456.
- (176) Roos, W. H.; Bruinsma, R.; Wuite, G. J. L. *Nature Physics* **2010**, *6*, 733–743.
- (177) Abou-Saleh, R. H.; Peyman, S. A.; Critchley, K.; Evans, S. D.; Thomson, N. H. *Langmuir* **2013**, *29*, 4096–4103.

-
- (178) Dieluweit, S.; Csiszar, A.; Rubner, W.; Fleischhauer, J.; Houben, S.; Merkel, R. *Langmuir* **2010**, *26*, 11041–11049.
- (179) Glynos, E.; Koutsos, V.; McDicken, W. N.; Moran, C. M.; Pye, S. D.; Ross, J. A.; Sboros, V. *Langmuir* **2009**, *25*, 7514–7522.
- (180) Grant, C. A.; McKendry, J. E.; Evans, S. D. *Soft Matter* **2012**, *8*, 1321–1326.
- (181) Santos, E. B.; Morris, J. K.; Glynos, E.; Sboros, V.; Koutsos, V. *Langmuir* **2012**, *28*, 5753–5760.
- (182) Sboros, V.; Glynos, E.; Pye, S. D.; Moran, C. M.; Butler, M.; Ross, J. A.; McDicken, W. N.; Koutsos, V. *Ultrasonics* **2007**, *46*, 349–354.
- (183) Chen, C. C.; Wu, S. Y.; Finan, J. D.; Morrison, B.; Konofagou, E. E. *Ieee Transactions on Ultrasonics Ferroelectrics and Frequency Control* **2013**, *60*, 524–534.
- (184) Schaefer, E.; Kliesch, T.-T.; Janshoff, A. *Langmuir* **2013**, *29*, 10463–10474.
- (185) Hu, J. F.; Chen, H. Q.; Zhang, Z. B. *Materials Chemistry and Physics* **2009**, *118*, 63–70.
- (186) Keller, M. W.; Sottos, N. R. *Experimental Mechanics* **2006**, *46*, 725–733.
- (187) Zhang, Z. L.; Kristiansen, H.; Liu, J. *Computational Materials Science* **2007**, *39*, 305–314.
- (188) Mueller, E.; Chung, J. T.; Zhang, Z.; Sprauer, A. *Journal of Chromatography A* **2005**, *1097*, 116–123.
- (189) Stenekes, R. J. H.; De Smedt, S. C.; Demeester, J.; Sun, G. Z.; Zhang, Z. B.; Hennink, W. E. *Biomacromolecules* **2000**, *1*, 696–703.
- (190) He, J. Y.; Zhang, Z. L.; Kristiansen, H. *Journal of Applied Polymer Science* **2009**, *113*, 1398–1405.
- (191) Egholm, R. D.; Christensen, S. F.; Szabo, P. *Journal of Applied Polymer Science* **2006**, *102*, 3037–3047.

-
- (192) Mitchison, J. M.; Swann, M. M. *Journal of Experimental Biology* **1954**, *31*, 443.
- (193) Rand, R. P.; Burton, A. C. *Biophysical Journal* **1964**, *4*, 115.
- (194) Hochmuth, R. M. *Journal of Biomechanics* **2000**, *33*, 15–22.
- (195) Kim, D. H.; Wong, P. K.; Park, J.; Levchenko, A.; Sun, Y. *Annual Review of Biomedical Engineering* **2009**, *11*, 203–233.
- (196) Chien, S.; Sung, K. L. P.; Skalak, R.; Usami, S. *Biophysical Journal* **1978**, *24*, 463–487.
- (197) Evans, E.; Yeung, A. *Biophysical Journal* **1989**, *56*, 151–160.
- (198) Shao, J. Y.; Hochmuth, R. M. *Biophysical Journal* **1996**, *71*, 2892–2901.
- (199) Unterberger, M. J.; Schmoller, K. M.; Wurm, C.; Bausch, A. R.; Holzapfel, G. A. *Acta Biomaterialia* **2013**, *9*, 7343–7353.
- (200) Ratanabanangkoon, P.; Gropper, M.; Merkel, R.; Sackmann, E.; Gast, A. P. *Langmuir* **2003**, *19*, 1054–1062.
- (201) Rawicz, W.; Olbrich, K. C.; McIntosh, T.; Needham, D.; Evans, E. *Biophysical Journal* **2000**, *79*, 328–339.
- (202) Mabrouk, E.; Cuvelier, D.; Pontani, L. L.; Xu, B.; Levy, D.; Keller, P.; Brochard-Wyart, F.; Nassoy, P.; Li, M. H. *Soft Matter* **2009**, *5*, 1870–1878.
- (203) Ashkin, A. *Physical Review Letters* **1970**, *24*, 156.
- (204) Svoboda, K.; Block, S. M. *Annual Review of Biophysics and Biomolecular Structure* **1994**, *23*, 247–285.
- (205) Neuman, K. C.; Nagy, A. *Nature Methods* **2008**, *5*, 491–505.
- (206) Noy, A., *Handbook of Molecular Force Spectroscopy*; Springer: New York, 2008.
- (207) Henon, S.; Lenormand, G.; Richert, A.; Gallet, F. *Biophysical Journal* **1999**, *76*, 1145–1151.
- (208) Sleep, J.; Wilson, D.; Simmons, R.; Gratzner, W. *Biophysical Journal* **1999**, *77*, 3085–3095.

-
- (209) Dao, M.; Lim, C. T.; Suresh, S. *Journal of the Mechanics and Physics of Solids* **2003**, *51*, 2259–2280.
- (210) Bausch, A. R.; Ziemann, F.; Boulbitch, A. A.; Jacobson, K.; Sackmann, E. *Biophysical Journal* **1998**, *75*, 2038–2049.
- (211) Bausch, A. R.; Moller, W.; Sackmann, E. *Biophysical Journal* **1999**, *76*, 573–579.
- (212) Kamgoue, A.; Ohayon, J.; Tracqui, P. *Journal of Biomechanical Engineering-Transactions of the Asme* **2007**, *129*, 523–530.
- (213) Walter, A.; Rehage, H.; Leonhard, H. *Colloids and Surfaces a-Physicochemical and Engineering Aspects* **2001**, *183*, 123–132.
- (214) Walter, A.; Rehage, H.; Leonhard, H. *Colloid and Polymer Science* **2000**, *278*, 169–175.
- (215) Rehage, H.; Husmann, M.; Walter, A. *Rheologica Acta* **2002**, *41*, 292–306.
- (216) Degen, P.; Leick, S.; Rehage, H. *Zeitschrift Fur Physikalische Chemie-International Journal of Research in Physical Chemistry & Chemical Physics* **2009**, *223*, 1079–1090.
- (217) Leick, S.; Henning, S.; Degen, P.; Suter, D.; Rehage, H. *Physical Chemistry Chemical Physics* **2010**, *12*, 2950–2958.
- (218) Leick, S.; Kott, M.; Degen, P.; Henning, S.; Pasler, T.; Suter, D.; Rehage, H. *Physical Chemistry Chemical Physics* **2011**, *13*, 2765–2773.
- (219) Leick, S.; Kemper, A.; Rehage, H. *Soft Matter* **2011**, *7*, 6684–6694.
- (220) Husmann, M.; Rehage, H.; Dhenin, E.; Barthes-Biesel, D. *Journal of Colloid and Interface Science* **2005**, *282*, 109–119.
- (221) Smith, A. E.; Zhang, Z.; Thomas, C. R. *Chemical Engineering Science* **2000**, *55*, 2031–2041.
- (222) Yang, J.; Keller, M. W.; Moore, J. S.; White, S. R.; Sottos, N. R. *Macromolecules* **2008**, *41*, 9650–9655.

- (223) Liu, X.; Sheng, X.; Lee, J. K.; Kessler, M. R. *Macromolecular Materials and Engineering* **2009**, *294*, 389–395.
- (224) Dai, Z.; Moehwald, H.; Tiersch, B.; Daehne, L. *Langmuir* **2002**, *18*, 9533–9538.
- (225) Cavalieri, F.; El Hamassi, A.; Chiessi, E.; Paradossi, G. *Langmuir* **2005**, *21*, 8758–8764.
- (226) Klech, C. In Swarbrick, J., Boylan, J., Eds.; CRC Press: 1990; Chapter Gels and jellies, pp 415–439.
- (227) Gehrke, S. H.; Lee, P. I. In Tyle, P. Tyle, P., Ed.; Drugs and the Pharmaceutical Sciences; CRC Press: 1991; Chapter Hydrogels For Drug Delivery Systems, pp 333–392.
- (228) Gehrke, S. H. *Transport Processes in Pharmaceutical Systems* **2000**, *102*, 473–546.
- (229) Gupta, P.; Vermani, K.; Garg, S. *Drug Discovery Today* **2002**, *7*, 569–579.
- (230) Almdal, K.; Dyre, J.; Hvidt, S.; Kramer, O. *Polymer Gels and Networks* **1993**, *1*, 5–17.
- (231) Lin, C.-C.; Metters, A. T. *Advanced Drug Delivery Reviews* **2006**, *58*, 1379–1408.
- (232) Flory, P. J.; Rehner, J. *The Journal of Chemical Physics* **1943**, *11*, 521–526.
- (233) Flory, P. J. *Journal of Chemical Physics* **1950**, *18*, 108–111.
- (234) Flory, P., *Principles of Polymer Chemistry*; Cornell University Press: 1953.
- (235) Peppas, N. A.; Merrill, E. W. *Journal of Applied Polymer Science* **1977**, *21*, 1763–1770.
- (236) Brannon-Peppas, L.; Peppas, N. A. *Chemical Engineering Science* **1991**, *46*, 715–722.
- (237) Katchalsky, A.; Michaeli, I. *Journal of Polymer Science* **1955**, *15*, 69–86.
- (238) Ricka, J.; Tanaka, T. *Macromolecules* **1984**, *17*, 2916–2921.
- (239) Wichterle, O.; Lim, D. *Nature* **1960**, *185*, 117–118.

- (240) Wichterle, O.; Lim, D. Process for producing shaped articles from three-dimensional hydrophilic high polymers. pat., 2976576 A, 1961.
- (241) Wichterle, O.; Lim, D. Cross-linked hydrophilic polymers and articles made therefrom. pat., 3220960 A, 1965.
- (242) Hoffman, A. S. *Advanced Drug Delivery Reviews* **2002**, *54*, 3–12.
- (243) Hoffman, A. S. *Advanced Drug Delivery Reviews* **2012**, *64*, 18–23.
- (244) Annabi, N.; Tamayol, A.; Uquillas, J. A.; Akbari, M.; Bertassoni, L. E.; Cha, C.; Camci-Unal, G.; Dokmeci, M. R.; Peppas, N. A.; Khademhosseini, A. *Advanced Materials* **2014**, *26*, 85–124.
- (245) Peppas, N. A.; Hilt, J. Z.; Khademhosseini, A.; Langer, R. *Advanced Materials* **2006**, *18*, 1345–1360.
- (246) Slaughter, B. V.; Khurshid, S. S.; Fisher, O. Z.; Khademhosseini, A.; Peppas, N. A. *Advanced Materials* **2009**, *21*, 3307–3329.
- (247) Colombo, P. *Advanced Drug Delivery Reviews* **1993**, *11*, 37–57.
- (248) Kashyap, N.; Kumar, N.; Kumar, M. *Critical Reviews in Therapeutic Drug Carrier Systems* **2005**, *22*, 107–149.
- (249) Peppas, N. A. *Current Opinion in Colloid & Interface Science* **1997**, *2*, 531–537.
- (250) Peppas, N. A.; Bures, P.; Leobandung, W.; Ichikawa, H. *European Journal of Pharmaceutics and Biopharmaceutics* **2000**, *50*, 27–46.
- (251) Chen, X.; Martin, B. D.; Neubauer, T. K.; Linhardt, R. J.; Dordick, J. S.; Rethwisch, D. G. *Carbohydrate Polymers* **1995**, *28*, 15–21.
- (252) Shewan, H. M.; Stokes, J. R. *Journal of Food Engineering* **2013**, *119*, 781–792.
- (253) Gould, F.; Johnston, C.; Seems, G. Thermally reversible polyurethane hydrogels and cosmetic, biological and medical uses. pat., EP0401210 A4, 1990.
- (254) Berger, S.; Simon, G.; Von, K. Hydrogel for the application of therapeutic and/or cosmetic active substances to the skin. pat., WO1996001100 A3, 1996.

- (255) Hausen, C.; Klein, C.; Schnitzler, I. Hydrogel for natural cosmetic purposes. pat., WO2011128052 A3, 2012.
- (256) Buenger, D.; Topuz, F.; Groll, J. *Progress in Polymer Science* **2012**, *37*, 1678–1719.
- (257) Malda, J.; Visser, J.; Melchels, F. P.; Juengst, T.; Hennink, W. E.; Dhert, W. J. A.; Groll, J.; Hutmacher, D. W. *Advanced Materials* **2013**, *25*, 5011–5028.
- (258) Thiele, J.; Ma, Y.; Bruekers, S. M. C.; Ma, S.; Huck, W. T. S. *Advanced Materials* **2014**, *26*, 125–148.
- (259) Van Vlierberghe, S.; Dubruel, P.; Schacht, E. *Biomacromolecules* **2011**, *12*, 1387–1408.
- (260) Nicodemus, G. D.; Bryant, S. J. *Tissue Engineering Part B-Reviews* **2008**, *14*, 149–165.
- (261) Chung, B. G.; Lee, K.-H.; Khademhosseini, A.; Lee, S.-H. *Lab on a Chip* **2012**, *12*, 45–59.
- (262) Burdick, J. A.; Murphy, W. L. *Nature Communications* **2012**, *3*.
- (263) DeForest, C. A.; Anseth, K. S. *Annual Review of Chemical and Biomolecular Engineering, Vol 3* **2012**, *3*, 421–444.
- (264) Iler, R. K. *Journal of Colloid and Interface Science* **1966**, *21*, 569.
- (265) Decher, G.; Hong, J. D. *Makromolekulare Chemie-Macromolecular Symposia* **1991**, *46*, 321–327.
- (266) Decher, G.; Hong, J. D.; Schmitt, J. *Thin Solid Films* **1992**, *210*, 831–835.
- (267) Decher, G.; Hong, J. D. *Berichte Der Bunsen-Gesellschaft-Physical Chemistry Chemical Physics* **1991**, *95*, 1430–1434.
- (268) Lvov, Y.; Decher, G.; Sukhorukov, G. *Macromolecules* **1993**, *26*, 5396–5399.
- (269) Lvov, Y.; Haas, H.; Decher, G.; Mohwald, H.; Mikhailov, A.; Mtchedlishvily, B.; Morgunova, E.; Vainshtein, B. *Langmuir* **1994**, *10*, 4232–4236.

- (270) Lvov, Y.; Ariga, K.; Ichinose, I.; Kunitake, T. *Journal of the American Chemical Society* **1995**, *117*, 6117–6123.
- (271) Kotov, N. A.; Dekany, I.; Fendler, J. H. *Journal of Physical Chemistry* **1995**, *99*, 13065–13069.
- (272) Caruso, F.; Caruso, R. A.; Mohwald, H. *Science* **1998**, *282*, 1111–1114.
- (273) Sukhorukov, G. B.; Donath, E.; Davis, S.; Lichtenfeld, H.; Caruso, F.; Popov, V. I.; Mohwald, H. *Polymers for Advanced Technologies* **1998**, *9*, 759–767.
- (274) Becker, A. L.; Johnston, A. P. R.; Caruso, F. *Small* **2010**, *6*, 1836–1852.
- (275) Schlenoff, J. B.; Dubas, S. T. *Macromolecules* **2001**, *34*, 592–598.
- (276) Schlenoff, J. B.; Dubas, S. T.; Farhat, T. *Langmuir* **2000**, *16*, 9968–9969.
- (277) Dierendonck, M.; De Koker, S.; De Rycke, R.; De Geest, B. G. *Soft Matter* **2014**, *10*, 804–807.
- (278) Schaaf, P.; Voegel, J.-C.; Jierry, L.; Boulmedais, F. *Advanced Materials* **2012**, *24*, 1001–1016.
- (279) Krogman, K. C.; Cohen, R. E.; Hammond, P. T.; Rubner, M. F.; Wang, B. N. *Bioinspiration & Biomimetics* **2013**, *8*.
- (280) Zhang, X.; Chen, H.; Zhang, H. *Chemical Communications* **2007**, 1395–1405.
- (281) De Koker, S.; Hoogenboom, R.; De Geest, B. G. *Chemical Society Reviews* **2012**, *41*, 2867–2884.
- (282) Skorb, E. V.; Andreeva, D. V. *Polymer Chemistry* **2013**, *4*, 4834–4845.
- (283) Campas, M.; O’Sullivan, C. *Analytical Letters* **2003**, *36*, 2551–2569.
- (284) Tong, W.; Song, X.; Gao, C. *Chemical Society Reviews* **2012**, *41*, 6103–6124.
- (285) Iost, R. M.; Crespilho, F. N. *Biosensors and Bioelectronics* **2012**, *31*, 1–10.
- (286) Ai, H. *Advanced Drug Delivery Reviews* **2011**, *63*, 772–788.
- (287) Mwaura, J. K.; Pinto, M. R.; Witker, D.; Ananthakrishnan, N.; Schanze, K. S.; Reynolds, J. R. *Langmuir* **2005**, *21*, 10119–10126.

- (288) Man, K. Y. K.; Wong, H. L.; Chan, W. K.; Djurisic, A. B.; Beach, E.; Rozeveld, S. *Langmuir* **2006**, *22*, 3368–3375.
- (289) Han, J. T.; Zheng, Y.; Cho, J. H.; Xu, X.; Cho, K. *Journal of Physical Chemistry B* **2005**, *109*, 20773–20778.
- (290) Scheibel, T. *Microbial Cell Factories* **2004**, *3*, 14.
- (291) Huemmerich, D.; Helsen, C. W.; Quedzuweit, S.; Oschmann, J.; Rudolph, R.; Scheibel, T. *Biochemistry* **2004**, *43*, 13604–13612.
- (292) Vollrath, F. *Reviews in Molecular Biotechnology* **2000**, *74*, 67–83.
- (293) Humenik, M.; Smith, A. M.; Scheibel, T. *Polymers* **2011**, *3*, 640–661.
- (294) Hardy, J. G.; Scheibel, T. R. *Biochemical Society Transactions* **2009**, *37*, 677–681.
- (295) Lammel, A.; Schwab, M.; Slotta, U.; Winter, G.; Scheibel, T. *Chemosuschem* **2008**, *1*, 413–416.
- (296) Slotta, U. K.; Rammensee, S.; Gorb, S.; Scheibel, T. *Angewandte Chemie-International Edition* **2008**, *47*, 4592–4594.
- (297) Hermanson, K. D.; Huemmerich, D.; Scheibel, T.; Bausch, A. R. *Advanced Materials* **2007**, *19*, 1810–1815.
- (298) Hermanson, K. D.; Harasim, M. B.; Scheibel, T.; Bausch, A. R. *Phys. Chem. Chem. Phys.* **2007**, *9*, 6442–6446.
- (299) Blüm, C.; Nichtl, A.; Scheibel, T. *Advanced Functional Materials* **2014**, *24*, 763–768.
- (300) Lammel, A.; Schwab, M.; Hofer, M.; Winter, G.; Scheibel, T. *Biomaterials* **2011**, *32*, 2233–2240.
- (301) Blüm, C.; Scheibel, T. *English BioNanoScience* **2012**, *2*, 67–74.
- (302) Hofer, M.; Winter, G.; Myschik, J. *Biomaterials* **2012**, *33*, 1554–1562.
- (303) Lammel, A. S.; Hu, X.; Park, S.-H.; Kaplan, D. L.; Scheibel, T. R. *Biomaterials* **2010**, *31*, 4583–4591.

"We must not aspire to derive nature from our concepts, but must adapt the latter to the former. We must not think that everything can be arranged according to our categories or that there is such a thing as a most perfect arrangement: it will only ever be a variable one, merely adapted to current needs."

(Ludwig Boltzmann)

Part II

Scientific publications

4

Overview

4.1 List of publications

This thesis is based on a range of publications which are included as chapters. A short summary and my individual contributions to each of them are given in the sections below. The order of the subsequently listed papers is strictly chronological.

The following publications are part of this thesis:

Formation and mechanical characterization of aminoplast core/shell microcapsules [Chapter 8]

Melanie Pretzl, **Martin Neubauer**, Melanie Tekaats, Carmen Kunert, Christian Kuttner, Géraldine Leon, Damien Berthier, Philipp Ernie, Lahoussine Ouali and Andreas Fery; *ACS Applied Materials & Interfaces* **2012**, 4:2940-2948

Micromechanical characterization of spider silk particles [Chapter 5]

Martin P. Neubauer, Claudia Blüm, Elisa Agostini, Julia Engert, Thomas Scheibel and Andreas Fery; *Biomaterials Science* **2013**, 1:1160-1165

Mechanics of pH-responsive hydrogel capsules [Chapter 9]

James P. Best, **Martin P. Neubauer**, Sameen Javed, Henk H. Dam, Andreas Fery and Frank Caruso; *Langmuir* **2013**, 29:9814-9823

Monodisperse collagen-gelatin beads as potential platforms for 3D cell culturing [Chapter 6]

Shaohua Ma, Manuela Natoli, Xin Liu, **Martin P. Neubauer**, Fiona M. Watt, Andreas Fery and Wilhelm T. S. Huck; *Journal of Materials Chemistry B* **2013**, 1:5128-5136

Artificial microniches for probing mesenchymal stem cell fate in 3D [Chapter 7]

Yujie Ma, **Martin P. Neubauer**, Julian Thiele, Andreas Fery and Wilhelm T. S. Huck; *Biomaterials Science* **2014**, 2:1661-1671

Stiffness-dependent *in vitro* uptake and lysosomal acidification of colloidal particles [Chapter 10]

Raimo Hartmann, Marcel Weidenbach, **Martin Neubauer**, Andreas Fery and Wolfgang J. Parak; *Angewandte Chemie International Edition* **2014**, DOI:10.1002/anie.201409693

Further publications not being part of the present thesis are:

Microcapsule mechanics: From stability to function

Martin P. Neubauer, Melanie Pöhlmann and Andreas Fery; *Advances in Colloid and Interface Science* **2014**, 207:65-80

4.2 Contents

Subsequently, a summary of each of the aforementioned papers will be given. However, the chronological order of the publications is modified to illustrate better their content-related connections.

The first three papers are dedicated to microparticles as being full spheres. From a mechanical point of view, the deformation of full spheres can be described (in the simplest case, which, however, holds for the herein treated systems) by a Hertz model. It requires a range of conditions that need to be fulfilled, beside linear elasticity of the material particularly structural integrity as expressed by homogeneity and isotropy. In each case these prerequisites were fulfilled as verified by optical and electron microscopy. But structural properties can be controlled and exploited to a higher extent. All three publications show that and how (*e.g.*, crosslinking, change of molecular weight, introduction of secondary structures) structural changes on a (supra)molecular level affect the particles' mechanics. These, in turn, are a major key to the particles' functionality. In the first paper, spider silk particles are investigated. Here, the high amount of crystalline beta-sheets of the constituting proteins accounts for high mechanical stability. Thus, application perspectives in composite materials but as well for drug delivery are opened. The other two papers examine large hydrogel beads with respect to the behavior of cells cultured therein. We will see that, indeed, the cells "respond" to the mechanical properties of their microenvironments. In this framework it is essential to reliably quantify the system's micromechanics. Such, we could reveal the modulus-dependent spreading of fibroblasts in 3D and uncover effects of matrix elasticity on direction and amount of stem cell differentiation. These observations contribute to the fundamental understanding of cell-matrix interactions, but also have practical significance, for instance, for the directed differentiation of stem cells.

The other publications deal with microparticles as being hollow spheres. Compared to full spheres capsules represent a higher level of structural complexity. The contrast of core and shell, internal and external phase makes mechanical modeling more demanding. The deformation of a capsule can no longer be described by Hertzian equations but

needs to be treated with (thin) shell theory. In this work, all systems follow the linear force-deformation dependency as proposed by the Reissner model for thin shells and small displacements. Again, structural uniformity is the precondition for the model's validity and is evidenced by advanced microscopy techniques. And again, we see clear correlations between structure on a molecular level (*e.g.*, crosslinking density, shell thickness) and mechanics. The capsule's mechanical properties turn out to be the essential parameter for its function. The studied aminoplast microcapsules are constructed to deliver fragrances in conditioners. Adjusting their mechanics means better performance, *i.e.* controlled and target-specific release. In the second paper, pH-responsive hydrogel capsules are investigated. Here, variations in crosslinking and pH induce changes in size, shell thickness and, eventually, shell stiffness. Such compliant systems with tunable mechanics may become attractive for controlled delivery applications. And the last publication directly goes in that direction. Microcapsules of different stiffness (as tuned by shell thickness) are presented to cells for uptake. A striking correlation could be revealed between capsule mechanics and internalization/intracellular processing. Thus, the stiffness of delivery vehicles reveals to be an important trigger for their functionality and may help to improve their design to meet the specific therapeutic needs.

In all cases, the mechanical properties of the microparticles are characterized on the single particle level with a colloidal probe AFM technique (CP-AFM). Irrespective of the different materials used to build the particles CP-AFM proved to be the method of choice. In providing a well-defined probe geometry and thereby a distinct probe-sample contact geometry it allows for the precise modeling of the obtained data. The available force range matches the compliant nature of the studied systems. All measurements were restricted to small deformations in order to remain within the limits of linear elasticity where robust physical models have been developed to describe load-deformation relations. In analogy to earlier investigations the Reissner model was again demonstrated to apply to the deformation of thin-shelled microcapsules. However, concerning the deformation of full spheres our works are among the first to experimentally prove the validity of Hertz' model with CP-AFM.

To conclude, as unifying concept we see the mechanics of particulate systems as being the key to their respective functionality. Understanding and, eventually, controlling the mechanical properties of microparticles is identified as an essential step towards target-oriented design for specific and customized applications.

Micromechanical characterization of spider silk particles

The aim of this work was to explore the mechanical properties of microparticles consisting of engineered spider silk in order to evaluate their potential for applications in the field of drug delivery or for composite materials. Generally, spider silk is an interesting material for such kind of applications as it offers outstanding mechanical properties as well as biocompatibility and biodegradability. While natural spider silk has been studied for many decades, the creation and investigation of bio-engineered silk mimics is a relatively new field. Therefore, the present study is pioneering concerning the examination of swelling behavior and mechanics of synthetic spider silk confined to particulate shape.

In detail, we studied particles obtained from a previously described controlled salting-out process of eADF4(C16) proteins and variants thereof with different molecular weight. The resulting particles have been shown to be spherical, homogeneous and with smooth surface, as determined from electron and atomic force microscopy. These morphological characteristics are an important prerequisite for modeling of deformation experiments. Before turning to the micromechanics, it is worth looking at the swelling behavior of the particles. This is essential because loading of the particles with drugs is carried out in solution while for processing, storage and transport the particles are dried. Only when the laden particles reach their final goal in the body they are again in an aqueous environment and intended to swell and release their content diffusion-controlled. We find that C16 particles swell in water to more than twice of their volume in dried state, while suitable crosslinking can reduce this to less than 50%. Additionally, repeated hydration/dehydration cycles showed the reversibility of this swelling process. Hence, drying of the particles will not affect their functionality concerning drug delivery.

Mechanical properties were investigated using a colloidal probe technique at an AFM. Obtained force vs. deformation data could successfully be evaluated with the basic Hertz model for two elastic bodies in contact. For swollen particles we derived Young's modulus values in the low MPa range which is acceptable for the envisaged pharmaceutical applications. Furthermore, the mechanical stability of the particles can be tuned either

by increasing the molecular weight of the protein or by covalent crosslinking. However, differences are small as the proteins are already in a highly crystalline state after salting-out. In the dried state these differences vanish completely: the biopolymer assumes a glassy state with an elastic modulus in the low GPa range, three orders of magnitude higher compared to the swollen state. Fatigue tests with more than 50 consecutive deformation cycles revealed plastic deformation of dry particles while hydrated ones were fully elastic. The material itself - despite being a polypeptide - proved to be extraordinarily stable as expressed by the relatively high thermal degradation temperature around 300 °C.

In conclusion, particles from engineered spider silk still show remarkable mechanical properties both in dried and hydrated state. In combination with the reversible swelling in aqueous environment applications in medicine or cosmetics can be envisaged with the dried particles as stable storage form. Also implementation in composite materials could be of interest making use of this "green" high modulus biopolymer. Apart from that, it could be shown that the simple Hertz model provides a robust framework for the description of the elastic deformation of spherical particles of colloidal dimensions.

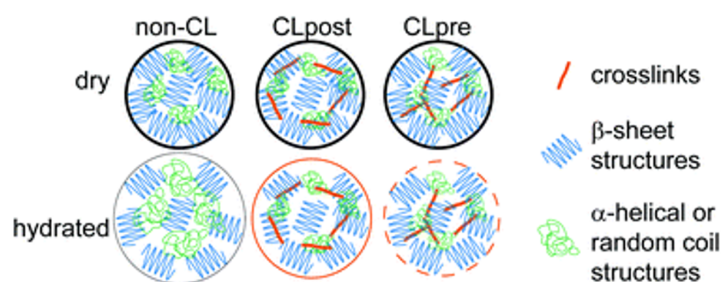


Figure 4.1. C16 spider silk particles contain a high amount of beta-sheets accounting for their high mechanical stability both in dried and hydrated state. Additional covalent crosslinking can further enhance particle stiffness in the hydrated state by reducing their swelling degree. Neubauer *et al.*, *Biomaterials Science* **2013**, 1:1160-1165. Reproduced by permission of The Royal Society of Chemistry.

Monodisperse collagen-gelatin beads as potential platforms for 3D cell culturing

This work aimed at developing a novel platform for the study of single cells confined to hydrogel microcompartments. These are well defined in size and composition and allow for facile tuning of mechanical properties which are a key parameter for cell growth.

In detail, monodisperse hydrogel beads composed of gelatin or a mixture of gelatin and collagen were obtained with a microfluidic setup. This setup permits not only precise control over size and composition but also the gentle embedding of cells directly into the beads during formation. Subsequently, the beads are crosslinked using a mild approach based on riboflavin mediated radical formation after blue light irradiation. The such produced beads (80 micron in diameter) are stable and homogeneous.

Mechanical properties were investigated using an AFM-based colloidal probe technique and evaluating the data with a Hertz model. Generally, the beads were found to exhibit elastic modulus values in the low kPa range, which is supposed to be a favorable regime for cell growth. In particular, we could show that both increased gelatin concentration and crosslinking time led to higher modulus values. However, the effect of crosslinking time was less pronounced. This is attributed to the fact that gelatin forms very stable triple helices which seem to dominate the bead mechanics.

The mesh size of the polymer network was determined experimentally and compared to theoretical calculations (Flory-Rehner theory) based on the beads' swelling behavior. Good agreement was found for most of the samples, only for extremely low concentrations of gelatin (below the gelation limit) values were differing significantly. In general, the observed mesh sizes and the hydration of the beads is favorable for cell survival as the transport of nutrients to the encapsulated cells is ensured. Crucial for cell viability is also the biodegradability of the matrix which has been evaluated positively for the studied gels. Finally, the cell viability rate was found to be more than 70% after one week inside the beads.

At the end, the effect of mechanical properties on cell behavior was studied. Therefore,

cell growth and spreading in beads with varying rigidity was followed. It was discovered that cells were spreading earlier and faster in softer beads and, correspondingly, 'escaping' out of the beads and formation of aggregates was observed after shorter timescales for cells in soft beads.

In conclusion, we have presented a new method to study single cells in individual microenvironments. The proposed hydrogel beads are produced in a controlled fashion *via* microfluidics and exhibit optimal properties (in terms of modulus, swelling, mesh size, biodegradability and cell viability) for cell culturing. Bead elasticity and morphology can easily be tuned by adjusting gel concentration or crosslinking time. The established correlation between matrix mechanical properties and cell behavior is an important insight as most studies investigated stiffness effects of flat substrates, so far. It will help to gain deeper understanding of how the mechanics of a three-dimensional environment will affect cells living therein.

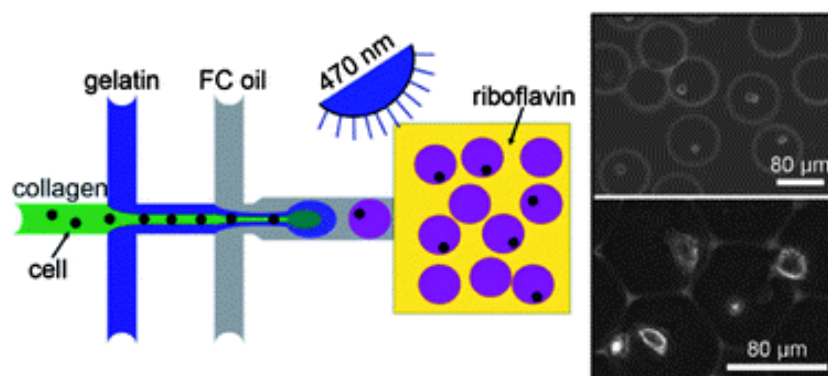


Figure 4.2. Hydrogel microenvironments are produced with microfluidics allowing the direct encapsulation of living cells (left). The resulting beads are well-defined in size and composition, subsequent blue-light induced crosslinking does not harm the enclosed cells (right) as confirmed by high viability rates. Cell behavior is found to depend on matrix mechanics. Ma *et al.*, *Journal of Materials Chemistry B* **2013**, 1:5128-5136. Reproduced by permission of The Royal Society of Chemistry.

Artificial microniches for probing mesenchymal stem cell fate in 3D

This work continues the earlier studies on single cell microcompartments, now focusing on the behavior of enclosed stem cells and their differentiation. Still using microfluidics for comprehensive control over size and composition, the matrix material is adopted to the needs of stem cells. Among the studied parameters is again the elasticity of the matrix and its influence on the cells.

In detail, monodisperse hydrogel beads, about 150 μm in size, were obtained from a custom-built microfluidics setup. The gel consists of thiolated hyaluronic acid (HASH) which is crosslinked with poly(ethylene glycol) di-vinylsulfone (PEG-DVS) by the extremely mild thiol-ene click chemistry. Thus, the already embedded human mesenchymal stem cells (hMSCs) are not harmed by the subsequent crosslinking reaction. In addition, the gel is further modified by fibrinogen to provide cell binding sites.

That these beads are indeed suitable cell culture environments was shown by live/dead staining of the embedded hMSCs. Short-term viability was at 70% and even after weeks large numbers of cells were active. In terms of morphology, cells remained spherical meaning no effect of the surrounding matrix and no matrix degradation. Also the multipotency of the stem cells was preserved as revealed by appropriate staining.

To characterize the mechanical properties of the hydrogel beads two approaches were followed. First, rheological measurements were performed on bulk gels. Then, deformation experiments were carried out on the actual beads with colloidal probe force spectroscopy. Interestingly, both methods yield almost exactly the same modulus values which indicates that the gel architecture does not affect its mechanical properties. Furthermore, we could show that the elastic modulus of the beads is in the typical range of soft solid tissue (0.9 - 9 kPa) and can easily be tuned by varying the HASH concentration.

Finally, we studied the differentiation of hMSCs in beads of varying stiffness. Therefore, cells were cultured in a bipotential differentiation medium to see whether there is a preference of the cells to develop into osteoblasts or adipocytes. Due to the softness of

the beads the preferential differentiation was towards adipocytes, independent of the differences in absolute stiffness. However, a certain amount of cells also developed into osteoblasts as the modulus of the matrix is already close to the lower limit for preferential osteogenic differentiation. Generally, in the stiffer beads a significantly larger percentage of cells showed differentiation after two weeks culture as compared to the softer ones.

In conclusion, the microfluidics platform was developed further to provide microniches for the culture and differentiation of stem cells. The well-defined assembly protocol allows for precise control over relevant parameters such as composition and mechanics. Embedded stem cells show high viability and maintain their multipotency. First insights are gained on the influence of mechanical properties on stem cell behavior in 3D.

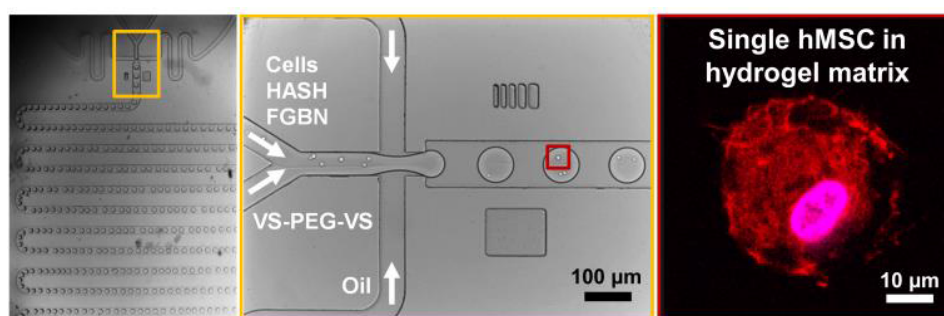


Figure 4.3. A microfluidic chip is used to generate monodisperse hydrogel beads and directly include stem cells for further investigations. Mild crosslinking is applied to stabilize the matrix and tune mechanical properties. The encapsulated cells maintain viability and multipotency. Reproduced from Yujie Ma *et al.*, *Biomaterials Science* **2014**, 2:1661-1671, by permission of The Royal Society of Chemistry.

Formation and mechanical characterization of aminoplast core/shell microcapsules

This work is the fruit of a collaboration with an industrial partner, Firmenich SA, Switzerland. As it combines application relevant microcapsule synthesis and state-of-the-art physico-chemical investigation methods it yields benefits both for the scientific community and commercial manufacturers.

The objective of the present study was to reveal interrelations between essential parameters during microcapsule formation, morphological characteristics and mechanical properties. The latter are of major interest as they will affect the performance of the capsules in the final application as well as their further processing and shelf life. To quantify above mentioned parameters we rely on characterization methods at the single capsule level providing most accurate data. This is particularly necessary as we deal with rather polydisperse samples.

In detail, we studied core/shell microcapsules with the core consisting of a mixture of perfume oils and the shell made up from melamine formaldehyde (MF). The capsules were prepared by an *in situ* polymerization of MF pre-polymer at the interface between the emulsified perfume oil droplets and the continuous aqueous phase. This is a standard approach for industrial encapsulation which, however, yields capsules with broad size distributions. Regarding the influence of process parameters on morphology and mechanics we decided to vary the amount of MF while all other parameters were kept constant. Optical microscopy and particle counting revealed a typical size of 10 to 50 μm in diameter with the expected rather broad distribution. As it is a crucial parameter for the interpretation and understanding of capsule mechanics we investigated the shell thickness. Therefore, the microcapsules were embedded in a resin which was subsequently cut into ultrathin sections for examination with TEM (transmission electron microscopy). Thus, it was possible to directly visualize and determine the shell thickness. Interestingly, a clear trend can be seen of increasing shell thickness with increasing amount of MF. Additionally, the influence of oil droplet size in the polymerization process could be

followed: for the same amount of polymer smaller droplets cause thinner shells due to the overall increased surface area. Both observations are reflected in a common diagram where the shell thickness is increasing as a function of the amount of MF normalized to the total surface area.

In a next step, mechanical properties were investigated using a colloidal probe technique at an atomic force microscope (AFM). To extract information about the mechanics of the shell small deformation experiments were performed, *i.e.* deformations on the order of the shell thickness. Optical microscopy served for control of uniaxial alignment and observation of shape changes during compression. For small deformations the recorded force vs deformation curves show a linear relation whose gradient was evaluated as the stiffness of the respective capsule. We found that the microcapsules' deformation is elastic in this regime and the stiffness values constant over up to thirty deformation cycles, independent of deformation velocity. Interestingly, we see an increase in stiffness when the shells become thicker. And as the shell thickness is determined by the amount of MF per total surface area, we can express this correlation also in terms of the normalized MF content. The stiffness or mechanical stability of the capsules' shell increases with the amount of MF per surface area.

Finally, the measured stiffness, diameter and shell thickness could be further correlated to estimate the Young's modulus of the shell material. The Reissner model for the deformation of thin shells proposes a linear scaling of the shell's stiffness with the inverse radius and with the shell thickness squared. This scaling is generally reflected in our data. From the proportionality constant we obtain an elastic modulus in the low GPa range which compares well to literature data.

In conclusion, with a thorough characterization and correlation of geometrical parameters and mechanical properties we were able to prove the key role of the initial amount of resin per surface area and how it translates into the capsules' shell thickness and stability. Thus, we have identified one essential design criterion allowing for the rational built-up of microcapsules with customized quality. Furthermore, it has been shown that

Reissner's simple analytical model is a good approximate for the description of small elastic deformations of thin polymer shells.

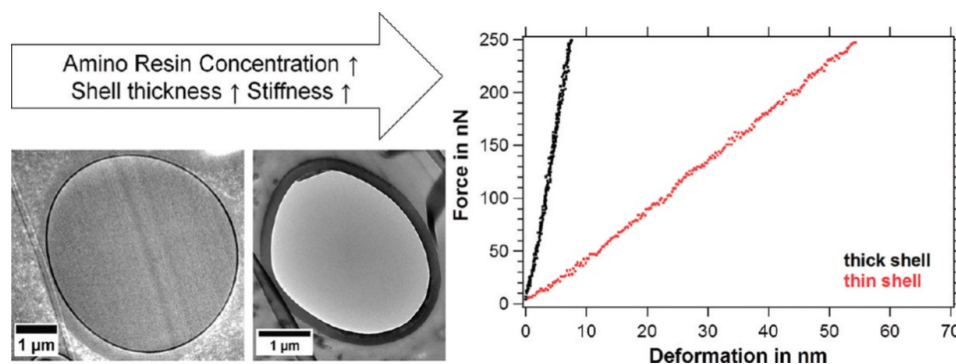


Figure 4.4. Basic parameters for the design of melamine formaldehyde microcapsules. Increasing the amount of amino resin in the initial reaction mixture leads to an increase in shell thickness as shown by TEM cross-sections (left). Simultaneously, the stiffness of the capsules is rising as demonstrated by steeper slopes in the corresponding force *vs.* deformation characteristics obtained from force spectroscopy experiments (right). Reprinted with permission from Pretzl *et al.*, *ACS Applied Materials & Interfaces* **2012**, 4:2940-2948. ©2012 American Chemical Society

Mechanics of pH-responsive hydrogel capsules

The aim of this study was to characterize the mechanical properties of soft hydrogel capsules as a function of crosslinking and pH. Additionally, we investigated the influence of geometry and support on mechanics comparing the free-standing hollow capsules to films of the same material deposited on planar surfaces and on solid spherical particles.

In detail, microcapsules were built from pH-responsive poly-methacrylic acid with variable degree of pendant thiol modification ($\text{PMA}_{SH(x)}$). The latter is used for crosslinking *via* the creation of disulfide bridges. The capsules are made from a layer-by-layer assembly of five layers of $\text{PMA}_{SH(x)}$ and poly-vinylpyrrolidone (PVPON) on a sacrificial spherical silica template of colloidal dimensions (ca. $1 \mu\text{m}$). After the linking of the thiols both PVPON and supporting core are removed to obtain hollow compliant hydrogel capsules. Despite starting from equally sized templates and same number of deposited layers we observe differences in diameter and shell thickness depending on the amount of thiol modification. At pH 7.4, with increasing thiol content (or, increasing crosslinking density) capsule size decreases as the more interconnected network is less prone to swelling (all capsules become larger than the original template). And the shell thickness of dried capsules increases because the less crosslinked shell is more susceptible to collapse.

In accordance with these findings we measured an increasing stiffness with rising thiol content. These measurements were carried out in aqueous buffer at pH 7.4 with a colloidal probe technique at an AFM. Stiffness data were extracted from the small deformation regime on the order of the shell thickness. Interestingly, when the pH is lowered to more acidic conditions the stiffness is increased significantly while the capsules are shrinking. This coincides with measurements on planar films of the same material. Obviously, the reduction of pH induces strong H-bonding leading to the observed contraction and stiffening.

Exploring the influence of geometry on mechanical properties we found that the shell of hollow capsules appears much stiffer compared to an analogously built film on a planar substrate. In an additional experiment we determined the stiffness of films assembled

around solid spherical particles (core/shell) which is approximately half that of films supported on planar surfaces. This can easily be explained by our measurement setup: Compressing the core/shell particles we actually sense both the top and the bottom film - a system of two springs yielding in total half the spring constant (stiffness) of one of them. In other words, in terms of mechanical properties it makes no difference whether the film is supported on a planar or curved surface. Consequently, the significantly higher stiffness of the hollow capsules can not just simply be ascribed to their spherical geometry. Additional effects such as pre-stresses arising from swelling or membrane tension must be the reason for the detected stiffening.

This is an interesting finding as it tells us that one cannot simply predict the mechanical properties of a capsule's membrane knowing those of the corresponding substrate supported film, and *vice versa*. We have to take into consideration the specific architecture of a hollow spherical shell owing its remarkable stability to high bending resistance - which holds both for dome constructions and microscopic objects. Furthermore, at the nanoscale surface tension effects can become important.

In conclusion, we have studied extremely compliant hydrogel capsules with absolute stiffness values scarcely reported in the literature before. We have demonstrated how their mechanical properties can be tuned by changing the amount of crosslinkable thiol units and by variations of pH. The comparison with films of the same material on solid support revealed a significant enhancement of the stability in the shell structures.

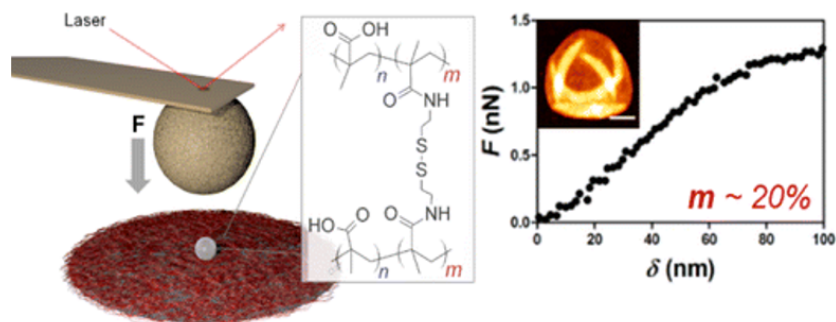


Figure 4.5. Soft hydrogel capsules were built from several layers of poly-methacrylic acid with variable degree of pendent thiol modification for crosslinking. The mechanical properties of these assemblies were investigated by a colloidal probe AFM technique (left). The resulting force-deformation curves (right) reveal mechanical stiffening with increasing thiol content. Also the shell thickness (as determined from collapsed capsules, *cf.* inset left) is affected by the degree of crosslinking. Reprinted with permission from Best *et al.*, *Langmuir* **2013**, 29:9814-9823. ©2013 American Chemical Society

Stiffness-dependent *in vitro* uptake and lysosomal acidification of colloidal particles

With this study we aimed at exploring the significance of particle mechanics for cellular uptake and intracellular processing. Therefore, pH-responsive dye containing multilayer capsules were constructed varying in only one parameter, namely elasticity, and tracked optically on their way from the extracellular environment to the cytosol.

In detail, two types of multilayer capsules were synthesized by the well-established layer-by-layer method: non-degradable capsules from poly(sodium 4-styrenesulfonate), PSS, and poly(allylamine hydrochloride), PAH, and biodegradable capsules from dextran sulfate sodium salt, DextS, and poly-L-arginine hydrochloride, PLArg. To achieve pH-sensitivity SNARF-1-labeled dextran was included. It changes color upon lowering of pH, *i.e.* when passing from the neutral extracellular environment to the cell interior where lysosomal acidification takes place.

The mechanical properties of the capsules were tuned by the number of deposited bilayers. This was confirmed experimentally by colloidal probe force spectroscopy revealing an almost linear increase of the capsule shell's stiffness with the number of bilayers. Absolute stiffness values were shown to depend the capsules' size. Generally, the elasticity of the capsules could be correlated to the shell thickness which increases with the number of bilayers as confirmed by electron microscopy and AFM imaging.

To study the effect of composition and mechanics the capsules were presented to six different cell types. In order to quantify the cell-capsule interactions two parameters were defined: the acidification time, t_A , and the processing time, t_P . t_A is time from the onset of acidification until completion as marked by the color change of the dye. t_P is the time from capsule-cell wall contact to 10% or 50% completion of acidification. For both time scales differences are resolved between different capsule types but as well between the examined cell types.

To elucidate in detail the role of capsule elasticity we focused on HeLa cells. It turned out that t_A of degradable capsules was almost independent of mechanics while that of

non-degradable capsules was increasing with their stiffness. Here, one can speculate that this effect was mainly due to the increasing shell thickness inhibiting the diffusion into the capsules. However, for the processing time we find a clear correlation with the capsule's mechanics: t_P increases with shell stiffness in an almost linear fashion. As t_P includes the engulfment of the carrier this finding may be interpreted such that the uptake itself is governed by the capsule's elasticity. Thus, previous indications on the importance of particles mechanics in cellular uptake are confirmed.

In conclusion, (non-)degradable polyelectrolyte multilayer capsules were used to study their interaction with cells. These capsules are well-defined in size and shell composition, thus enabling full control over mechanical properties. Making use of sophisticated particle tracking we followed and quantified the uptake behavior of a range of cells. This way, it was possible to establish a distinct correlation between particle mechanics and cellular internalization, which contributes to the general understanding of biological processes and allows for targeted design of microcarriers for sensing and delivery.

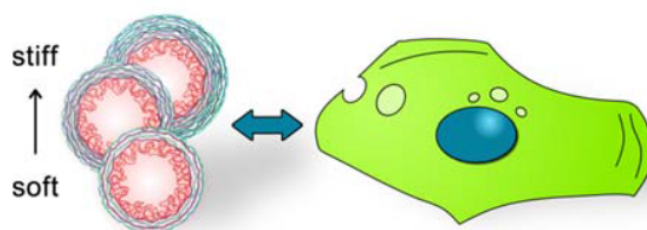


Figure 4.6. Hollow microcapsules are built from polyelectrolyte multilayers and filled with pH-sensitive dye. With the number of bilayers the mechanical stability of the capsules is increased which affects cellular uptake and intracellular processing. Reprinted with permission from Hartmann *et al.*, *Angewandte Chemie International Edition* **2014**, DOI:10.1002/anie.201409693. ©2014 John Wiley and Sons.

4.3 Individual contributions

Micromechanical characterization of spider silk particles

I wrote the manuscript and performed most of the experiments, namely all AFM characterization (imaging and mechanics) including evaluation, interpretation and graphical representation of the data. Claudia Blüm provided the material (spider silk particles of different molecular weight and crosslinking degree), carried out SEM and DSC measurements and helped with writing (introduction, experimental) and editing/formatting. Elisa Agostini and Julia Engert contributed the water adsorption and desorption measurements (IGASorp). Thomas Scheibel and Andreas Fery accompanied the work in supervision, scientific discussions, correction and proof reading of the manuscript.

Monodisperse collagen-gelatin beads as potential platforms for 3D cell culturing

I carried out the mechanical characterization of gel beads and the calculation of mesh size with Flory-Rehner theory, including the interpretation of the obtained results. Further, I contributed to the writing of the manuscript (sections (main text and supporting information) on mechanical characterization and theoretical calculation of mesh size), scientific discussion of observations and proof reading. Shaohua Ma wrote the manuscript and performed most of the experiments, Manuela Natoli and Xin Liu cultured cells and contributed to some fluorescence measurement. Fiona Watt, Wilhelm Huck and Andreas Fery contributed in scientific discussions and corrections of the manuscript and were supervising the project.

Artificial microniches for probing mesenchymal stem cell fate in 3D

I characterized the mechanical properties of the beads, including measurements, data evaluation and interpretation. I wrote the corresponding experimental part and joined for scientific discussions and proof reading. Yujie Ma performed all other measurements, including data evaluation and interpretation, and wrote the manuscript. Julian Thiele contributed to the microfluidics device design, joined for scientific discussions and proof reading. Andreas Fery and Wilhelm Huck were supervising the work and contributed in scientific discussions and proof reading.

Formation and mechanical characterization of aminoplast core/shell microcapsules

I carried out parts of the AFM experiments including data analysis and contributed in scientific discussions and proof-reading of the manuscript. Melanie Pretzl wrote the manuscript and carried out most of the AFM experiments including data analysis (also of the TEM data). Melanie Tekaat carried out some AFM measurements including data processing. Carmen Kunert contributed the TEM sample preparation and imaging. Christian Kuttner did the correction for random slicing and joined for scientific discussions and proof-reading of the manuscript. Géraldine Leon and Damien Berthier synthesized the microcapsules and determined their size distribution. Both contributed in scientific discussions, writing of the corresponding experimental part and proof-reading. Philipp Erni, Lahoussine Ouali and Andreas Fery supervised the project, contributed in scientific discussions and corrected the manuscript.

Mechanics of pH-responsive hydrogel capsules

I contributed by helping with the measurements of hollow capsule mechanics, evaluation, discussion and interpretation of the obtained data and advice for the editing of the manuscript. James Best wrote the manuscript and performed all measurements including data evaluation and interpretation. Sameen Javed fabricated some of the planar and capsule systems. Henk Dam provided assistance with ^1H and ^{13}C NMR measurements. Andreas Fery and Frank Caruso contributed in supervision, scientific discussions, correction and proof reading of the manuscript.

Stiffness-dependent *in vitro* uptake and lysosomal acidification of colloidal particles

I carried out the mechanical characterization of the microcapsules and the determination of shell thickness with AFM, including evaluation and interpretation of obtained data. I wrote the corresponding experimental part and contributed in scientific discussions and proof reading of the manuscript. Raimo Hartmann carried out all other measurements, including evaluation and interpretation, and wrote the supporting information. Marcel Weidenbach assisted in the evaluation of the particle tracking data. Andreas Fery contributed in scientific discussions, supervision and proof reading. Wolfgang Parak wrote the main part of the manuscript, joined for scientific discussions and was supervising the work.

5

Micromechanical characterization of spider silk particles

Martin P. Neubauer, Claudia Blüm, Elisa Agostini, Julia Engert, Thomas Scheibel and Andreas Fery; *Biomaterials Science* **2013**, 1:1160-1165. Reproduced by permission of The Royal Society of Chemistry.

Abstract

Spider silk fibers are well known for their mechanical properties, and they are therefore in the focus of materials scientists. Additionally, silks display biocompatibility making them interesting materials for applications in medicine or cosmetics. Due to the low abundance of natural spider silk proteins because of the spider's cannibalism, the recombinant spider silk protein eADF4 has been established for material science applications. Once processed into micron-sized particles by controlled salting-out, these particles can be used as drug delivery vehicles. For any application of the silk particles it is important to know their mechanical characteristics for processing and storage reasons. Here, we examine the swelling behavior and mechanics of these particles. Upon hydration, a drastic drop in elastic modulus occurs by orders of magnitude, from 0.8 GPa in the dry state to 2.99 MPa in the wet state. Importantly, the elastic modulus of recombinant silk particles can be tuned by varying the molecular weight of the used proteins, as well as chemical crosslinking thereof.

Introduction

Spider silk has been in the focus of research for a long time, mainly due to its mechanical properties which are unique and which will be suitable for various applications. Unlike in nature, where spider silk proteins are typically processed into fibers, recombinant spider silk proteins can be processed into various other morphologies like particles, capsules, non-woven meshes or hydrogels.¹⁻⁶ It has previously been shown that the recombinant spider silk protein eADF4 can be processed into particles with controllable diameters by salting out.^{1,2} Such silk particles consist of a solid core with high β -sheet content (around 60%) and a smooth surface.² Previously, eADF4(C16) particles were examined as possible drug delivery systems for medical and pharmaceutical applications.^{1,7,8} Loading of particles with water soluble low molecular weight substances was achieved either by diffusion processes or by co-precipitation of the potential drug molecules together with the protein.⁷ Additionally, incorporation of proteins into these particles has been

shown by using lysozyme as a model substrate.⁹ Substrate release could be achieved by diffusion,^{7,8} and an accelerated release profile was gained by controlled enzymatic degradation of eADF4(C16).¹⁰ The same publication demonstrated that the particles *e.g.* are selectively degraded in intestine fluids.

Within the past decade the atomic force microscope (AFM) has been established as the standard device to examine mechanical properties on the nano- and micro-scale.^{11,12} In particular, a colloidal probe (CP) technique offers a valuable means of studying particle mechanics on a single particle level as well as surface interaction forces.¹³⁻¹⁵ In biological investigations CP-AFM is even employed to analyze the stiffness and deformation behavior of entire cells.¹⁶

Here, we investigated the swelling behavior of dried eADF4(C16) particles upon hydration and their mechanical properties in the dry and wet state. Both are important regarding technical production processes and potential storage conditions, during which particles might undergo drying and rehydration steps. Applications in composite materials, *e.g.* bone substitute materials, will expose the particles to high mechanical stress, and therefore the mechanical properties have to be determined before employing spider silk particles as a filler of composites to reinforce materials. The surface properties of particles are also of high importance regarding future applications and have been analyzed separately.¹⁷

Results and discussion

Mechanical analysis and swelling behavior

First, the general deformation behavior of eADF4(C16) particles was analyzed by using a colloidal probe technique (5.4a SI), where the sharp tip of the AFM cantilever was replaced by a glass bead. For data evaluation we used a theoretical model based on the work of Hertz, which describes the elastic compression of two spheres in axially symmetric geometry.¹⁸ Precise alignment is guaranteed by optical control. Our measurements revealed continuous deformation behavior without buckling features, indicating high homogeneity of the silk particles (5.4b,c SI).

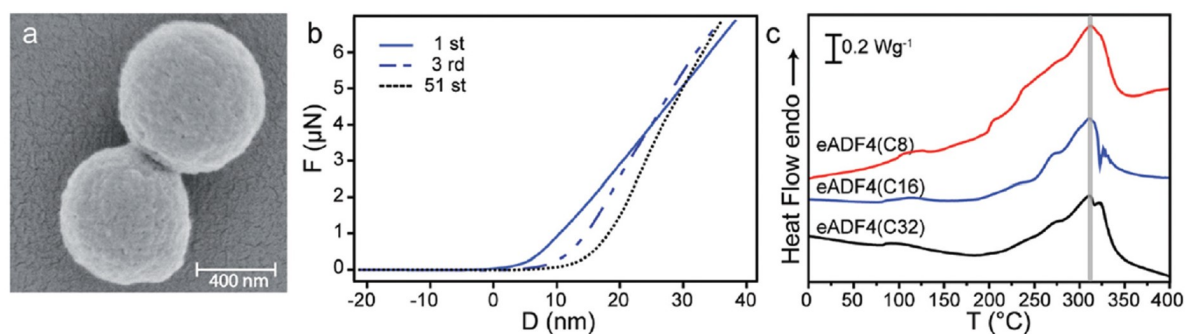


Figure 5.1. (a) SEM image of eADF4(C16) particles. (b) Fatigue tests of dry eADF4(C16) particles. Force-distance curves of an individual particle showing an increasing slope and a shift in the contact point with ongoing deformations. (c) Differential scanning calorimetry (DSC) measurements of eADF4 proteins with identical amino acid composition and molecular weights of 24.6 (eADF4(C8)), 47.7 (eADF4(C16)) and 93.8 kDa (eADF4(C32)).

Dry eADF4(C16) particles (5.1a) are round shaped and have a smooth surface. They showed an average elastic modulus of $0.8 \text{ GPa} \pm 0.5 \text{ GPa}$, which compares well with previous experiments. Spiess *et al.* performed tensile tests on dried cast silk films (10-12 microns thick) yielding a Young's modulus between 2 and 4 GPa, depending on solvents and post-treatment.¹⁹ From indentation measurements on 50 micron thick dry C16 films, Junghans *et al.* determined an elastic penetration modulus of $269 \pm 91 \text{ MPa}$.²⁰ Testing the fatigue behavior in 51 cycles of deformation and relaxation, dry eADF4(C16) particles showed a shift in the contact point and a significant increase in elastic modulus with ongoing deformations (5.1b and 5.5 SI). This plastic deformation behavior in combination with the high elastic modulus in the GPa range indicates a glassy state of the examined particles, which is confirmed by differential scanning calorimetry (DSC) and thermogravimetric analysis (TGA) (5.1c and data not shown). The thermal decomposition temperature is independent of the molecular weight of the silk protein at around $310 \text{ }^\circ\text{C}$, close to the values previously detected for eADF4(C16) films.¹⁹ The high elastic modulus and the remarkably high thermal decomposition temperature

of dried silk particles could be used for distinct technical applications, *e.g.* as part of composite/particle reinforced materials.

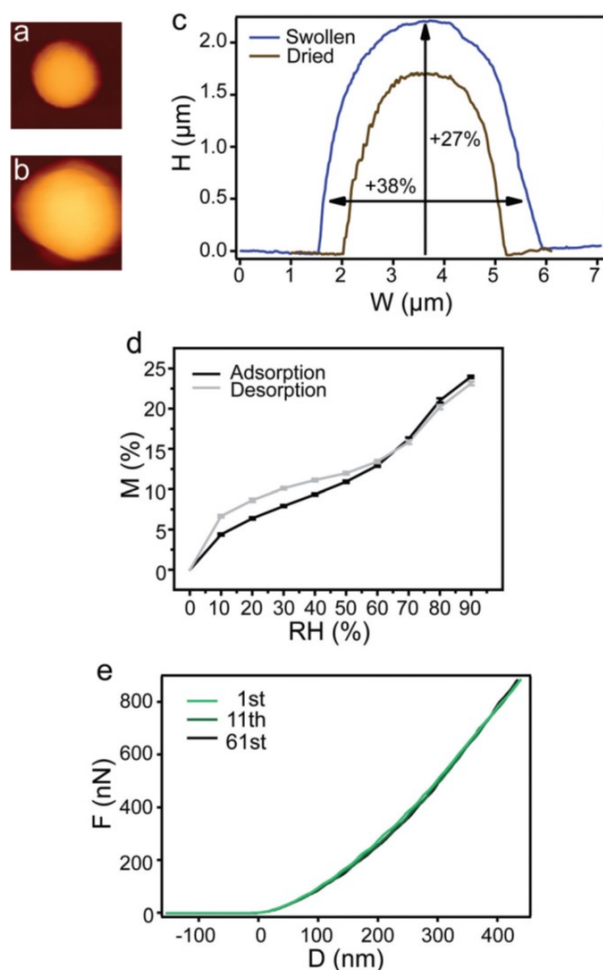


Figure 5.2. Swelling of an exemplary eADF4(C16) particle monitored by AFM in the (a) dried and (b) hydrated state. (c) Comparison of the corresponding height profiles. (d) Mass increase and decrease due to water adsorption and desorption of eADF4(C16) particles were identical after 10 repetitions (error bars shown at every 10% RH). (e) Mechanical fatigue test on the eADF4(C16) particle indicating material elasticity.

Regarding the potential as drug delivery vehicles, the hydrated state of eADF4 particles was mechanically analyzed. Upon hydration, eADF4(C16) particles showed a significant

and fully reversible increase in volume (5.2a-d). During water adsorption, the volume of particles was more than doubled with a swelling factor of 2.31 ± 0.06 . Swelling of the particles is considered to be a typical solvation effect as known from polymer theory.²¹ Even after 10 cycles of water adsorption and desorption, the hydration behavior of the particles did not change (5.2d). This enables the particles to be excellent drug delivery vehicles, since after loading in the wet state and storage of the loaded particles in the dehydrated state release could possibly be triggered upon re-hydration. Hydrated eADF4(C16) particles show an elastic modulus of $2.99 \text{ MPa} \pm 0.90 \text{ MPa}$, which is three orders of magnitude lower than that of the dried state. Interestingly, the large decrease in modulus after hydration is also observed for the particles' natural prototype, the *Araneus diadematus* dragline fiber.²²

A fatigue test with 61 compression-decompression repetitions was performed on hydrated eADF4(C16) particles indicating no change in the elastic modulus (5.2e and 5.5 SI); such a difference to the dehydrated particles indicates a high material elasticity of the hydrated particles with water acting as the plasticizer.

Effect of molecular weight and crosslinking on particle properties

Previously it has been shown that crosslinking of eADF4(C16) proteins has an impact on the mechanical, chemical and proteolytic stability of different morphologies.^{3,5,7} Especially for eADF4(C16) hydrogels an impact of chemical crosslinking on the rheological behavior of the hydrogels has been observed.⁴

In order to determine the effect of crosslinking on the mechanical behavior of the particles, the influence of molecular weight (influencing physical crosslinking) (5.3a) and chemical crosslinking (5.3b) was analyzed. First, the elastic modulus of particles made up of eADF4 proteins with identical amino acid composition but different molecular weights of 24.6, 47.7 and 93.8 kDa was investigated. Hydrated eADF4(C8) particles showed an elastic modulus of $2.58 \text{ MPa} \pm 1.09 \text{ MPa}$ and eADF4(C32) particles of $5.55 \text{ MPa} \pm 1.48 \text{ MPa}$, being respectively lower and higher than that of eADF4(C16). The influence of molecular weight on the mechanical behavior can be explained by higher inter- and

intramolecular interactions, leading to a stiffer network for larger proteins.

Next, the impact of chemical crosslinking on the deformation behavior of the eADF4(C16) particles was studied (5.3b). It has already been shown that chemical crosslinking has an influence on the chemical stability of eADF4(C16) particles;⁷ therefore an influence on the mechanical behavior was also conceivable. As described previously, there are two different routes of adding the chemical crosslinking molecules, either before (CLpre) or after (CLpost) particle formation (5.6 SI), showing a distinct influence on the micromechanical behavior of eADF4(C16) particles (5.3b). The diffusion technique (CLpost) leads to stiffer particles compared to the mixing technique (CLpre). Generally, the increase in modulus with crosslinking is in agreement with earlier experiments on hydrogels.^{4,5} However, the relative stiffening effect is not as pronounced. A reason for this observation is attributed to the high β -sheet content (64 %), already in the non-crosslinked particles.² Consequently, additional covalent bonding has only a moderate influence on mechanical properties. In the case of hydrogels, the amount of β -sheets is lower (around 40 %) as well as the modulus (kPa range). There, introduction of covalent bonds leads to a manifold increase in elastic modulus.

Besides the different mechanical properties, chemically crosslinked particles showed also different swelling behavior (5.3c) compared to non-CL particles, since the protein network is more stabilized due to the formation of di-tyrosines. CLpost particles are found to exhibit a more pronounced swelling than CLpre particles. The thermal decomposition temperature, in contrast, was apparently not significantly influenced by chemical crosslinking (5.3d).

The differences both in mechanical and swelling properties of differently crosslinked particles can be attributed to the respective distribution of the gained di-tyrosine crosslinks throughout the particles. In the case of CLpre, the crosslinking is homogeneously distributed throughout the particles resulting in a spatially uniform strengthened protein network (5.1). With the CLpost route, crosslinking occurs mainly at the surface of the particles (5.1), since diffusion into the particle is partially hindered by steric and

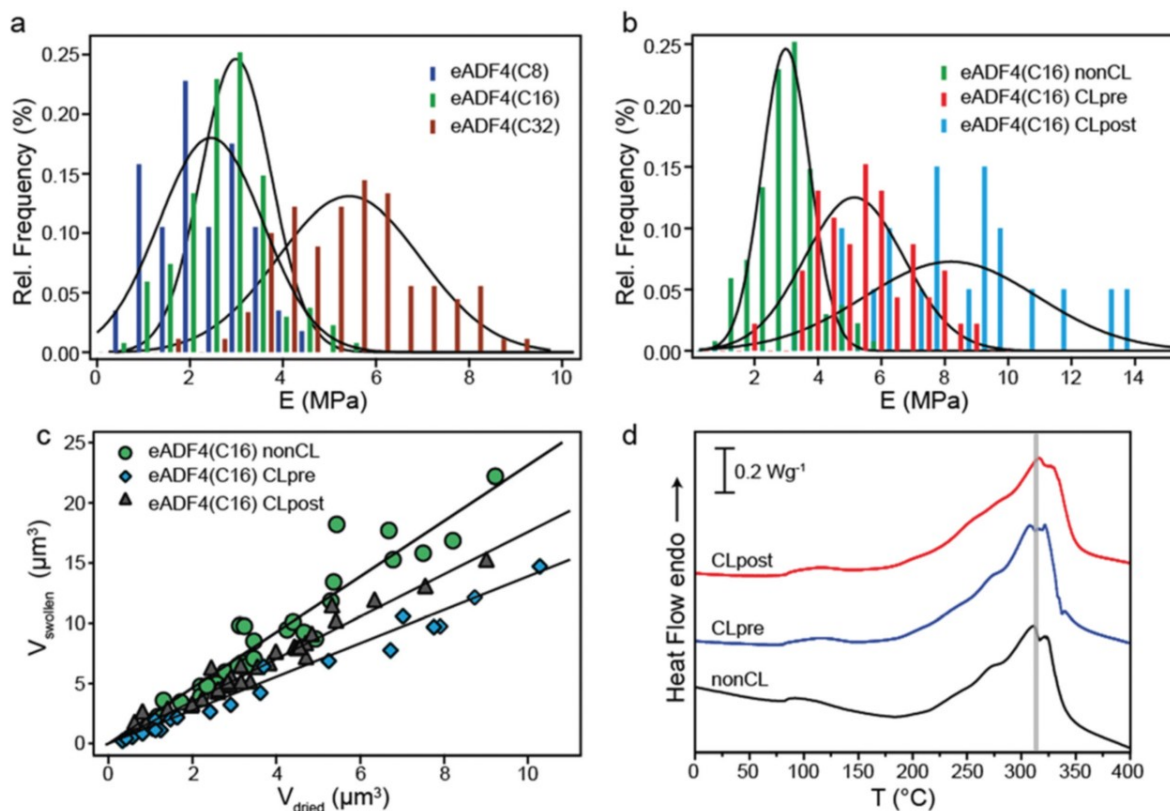
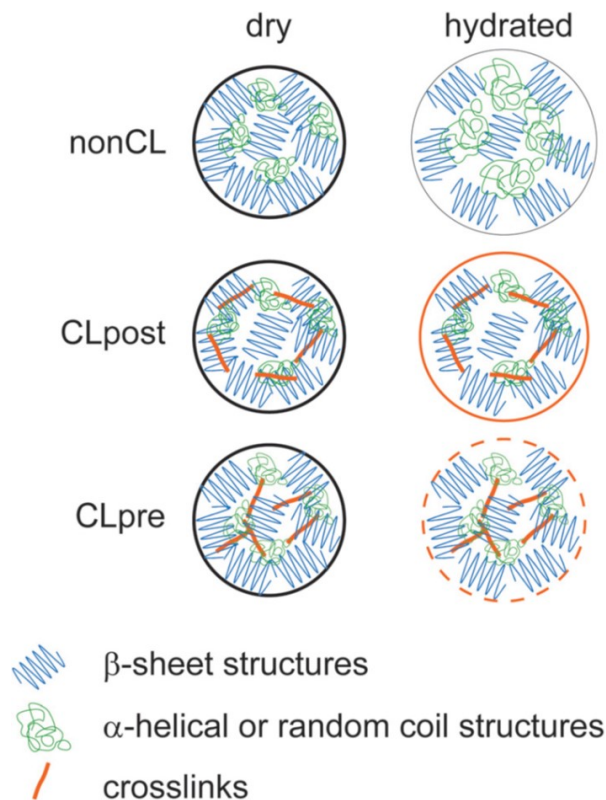


Figure 5.3. (a) Histogram showing the distribution of elastic moduli of eADF4(C8), eADF4(C16) and eADF4(C32) spider silk particles in the hydrated state ($n > 50$). The solid lines represent Gaussian fits. (b) Histogram showing the distribution of elastic moduli for hydrated non-crosslinked and chemically crosslinked eADF4(C16) particles with the solid lines representing Gaussian fits of the data. Crosslinking molecules were added before (pre) or after (post) particle formation leading to differently crosslinked particles. (c) Hydrated vs. dried volume of chemically crosslinked and non-crosslinked eADF4(C16) particles. CLpre particles show significantly less swelling than all the other particles with a volume swelling factor of 1.40. CLpost particles exhibit a swelling factor of 1.76, which is in between that of non-crosslinked and "pre" crosslinked particles. Solid lines represent linear fits. (d) DSC scans of dehydrated chemically crosslinked and non-crosslinked eADF4(C16) particles.

electrostatic repulsion. Therefore, in the regime which is probed in the force spectroscopy experiments, *i.e.* small deformations of up to 10 % of the diameter, CLpost particles exhibit a locally higher crosslinking density (on the surface) compared to the CLpre particles. As a consequence the detected modulus is higher. Analogously, the less crosslinked interior of CLpost particles is more prone to collapsing during dehydration than the homogeneously stabilized network in CLpre. Thus, a more pronounced deswelling/swelling is observed for CLpost particles.

Scheme 5.1. The swelling as well as the mechanical behavior of eADF4 particles depends on the crosslinking process. Swelling is limited and the elastic modulus is increased by crosslinking. The CLpre route leads to particles with a homogeneous crosslinking and less swelling with a higher elasticity than particles crosslinked by the CLpost route.



Conclusions

In summary, our data show the extraordinary mechanical stability of eADF4 particles in the dried state. The high modulus and chemical stability allows applications as fillers in composite materials. However, since the particles are subject to considerable swelling in humid environments, this might be a constraint for certain applications. Compared to the dehydrated state, swollen particles are much softer, but still exhibit remarkable mechanics which can be tuned selectively by adjusting the molecular weight of the employed protein or by chemical crosslinking. Mechanical fatigue tests have shown the elasticity of the swollen material in contrast to the situation in the dried state, where a plastic response upon deformation was observed. Hydration and dehydration of eADF4(C16) particles is fully reversible. This is a crucial feature with regard to exploring the particles' potential for drug delivery or for cosmetic applications, while odorants or drugs can be loaded by a diffusion controlled process or by co-precipitation.⁷ Subsequent drying yields a stable storage form with the encapsulated molecules safely entrapped. In physiological solutions the particles swell again, and diffusion driven release of the encapsulate is enabled. Based on the mechanical data, it is now feasible to unravel novel materials science applications of spider silk particles in further studies.

Materials and methods

Protein production and purification

The recombinant spider silk protein eADF4(C16) (47.7 kDa) consists of 16 repetitions of the C-module mimicking the highly repetitive core sequence of ADF4.²³ eADF4(C8) consists of eight repetitions (24.6 kDa), and eADF4(C32) (93.8 kDa) of 32 repetitions, which results in proteins with half or double the molecular weight of eADF4(C16), respectively. Production and purification of all proteins was carried out as described for eADF4(C16) previously.²³

Particle formation

The lyophilized proteins were dissolved in GdmSCN (6 M) and dialyzed against tris-(hydroxymethyl)-aminomethane-HCl (Tris-buffer) (10 mM) pH 8 overnight at 20 °C. For particle formation, the aqueous protein solution was dialyzed against a tenfold volume of 1 M potassium phosphate, pH 8, for one hour at room temperature (RT).^{1,2} After precipitation, the particles were washed three times with Tris-buffer.

Crosslinking

Crosslinking of the proteins was carried out as described previously.⁷ Two different routes of crosslinking were tested. CLpre describes a procedure where APS (ammonium persulfate) (10 mM) and Rubpy (tris(2,2'-bipyridyl) dichloro ruthenium(II)) (100 μ M) (Sigma-Aldrich, Germany) were mixed with the aqueous protein solution followed by precipitation. CLpost reflects a technique by which the crosslinking molecules diffused into the pre-formed particles (Fig. 3 SI).²⁴

Scanning electron microscopy (SEM)

Sample preparation was performed as described previously.⁷ SEM images were made with a 1450EsB Cross Beam (Zeiss, Germany) at an accelerating voltage of 3 kV.

Differential scanning calorimetry (DSC)

For DSC scans, protein samples (5-7 mg) were sealed in aluminium pans and heated under constant nitrogen gas flow at 5 °C min⁻¹ using an SDTA 821e differential scanning calorimeter (Mettler Toledo, Germany) equipped with a ceramic sensor with a 56-fold Au-Au-Pd thermocouple row. Before starting the experiment, the samples were heated to 110 °C in order to evaporate the remaining water. After an equilibration step (10 min) the samples were cooled to -40 °C, and finally the measurements were started by heating the samples to 400 °C.

Water adsorption and desorption measurements

Measurements were performed using a Moisture Analyzer IGASorp (Hiden Analytical, Germany) with a microbalance resolution of $0.1 \mu\text{g}$ and a minimal humidity step change of 0.2% . eADF4(C16) particles (*ca.* 20 mg) were incubated at a constant temperature of $25 \text{ }^\circ\text{C}$ and a nitrogen flow rate of 200 mL min^{-1} , while the relative humidity was increased from 0 to 90%. 10 adsorption and desorption cycles were performed assuming an adsorption of zero at 0% relative humidity.

Sample preparation for AFM

$5 \mu\text{L}$ of an eADF4(C16) particle suspension (*ca.* 5 mg mL^{-1}) were transferred into a poly-ethyleneimine (PEI) coated Petri dish (diameter 2 cm, height 0.5 cm). PEI was used to promote particle adhesion. Non-adhesive particles were rinsed with deionized water (Milli-Q[®] Academic, Millipore, Billerica, USA). The Petri dish was either filled with deionized water (1.5 mL) or left empty, respectively, before mechanical testing.

Atomic force microscopy (AFM)

All measurements were performed with an AFM NanoWizard[®] I (JPK Instruments, Berlin, Germany), combined with an inverted optical microscope Axiovert 200 (Carl Zeiss Micro-Imaging, Jena, Germany) which is equipped with a 20x and a 63x oil immersion objective. All measurements were performed at room temperature.

AFM imaging

All topography images were obtained in intermittent contact mode. For measurements in water, soft cantilevers were chosen (NSC 36 and CSC 17, no Al coating, MikroMasch, Tallinn, Estonia) with a typical spring constant of 0.95 N m^{-1} and 0.15 N m^{-1} , respectively. Imaging in air was done using a stiffer cantilever (NSC 14, no Al coating, MikroMasch) with a typical spring constant of 5 N m^{-1} .

AFM force spectroscopy

For the force spectroscopy experiments modified cantilevers (colloidal probe) were used: instead of a sharp tip a silica bead with a diameter in the range of 20-50 μm (Polysciences Europe GmbH, Eppelheim, Germany) was glued (two-component epoxy glue, UHU Endfest 300, UHU GmbH & Co. KG, Bühl, Germany) under the very front of a tipless cantilever (NSC 12, no Al coating, MikroMasch). Prior to the measurements all used cantilevers were calibrated against the glass substrate in order to obtain their optical lever sensitivity which equals the slope of the approach part of the resulting force-deformation curve. The exact spring constant of each cantilever was obtained before any modification by employing the thermal noise method.²⁵ The approach and retraction velocity of the cantilever was 5 $\mu\text{m s}^{-1}$ for all measurements, and one cycle was performed in 2 s. For the fatigue experiments a dwell time of 1 s was kept between two consecutive cycles.

Mechanics of elastic compression

One of the fundamental theories describing the mechanics of elastic compression was provided by Hertz.¹⁸ In the case of normal loads for isotropic linear elastic bodies, when adhesion or friction are neglected, the relation between deformation d and applied force F is given according to equation 5.1 for a sphere-sphere geometry:

$$F = \frac{4}{3} \cdot E \cdot d^{\frac{3}{2}} \cdot \sqrt{R} \quad (5.1)$$

Here, E and R are the relative Young's modulus and radius, respectively, given in equations 5.2 and 5.3, with ν being Poisson's ratio (assumed to be 0.5 for spider silk). The indices refer to the two objects approaching, *e.g.*, the colloidal probe and the spherical soft particle. In the case of a non-deformable probe (*e.g.*, a glass bead) its contribution to the combined elastic modulus is negligible.

$$\frac{1}{E} = \frac{1 - \nu_1^2}{E_1} + \frac{1 - \nu_2^2}{E_2} \quad (5.2)$$

$$\frac{1}{R} = \frac{1}{R_1} + \frac{1}{R_2} \quad (5.3)$$

Acknowledgments

The authors would like to thank Ute Kuhn for carrying out the DSC measurements and the Lehrstuhl Metallische Werkstoffe (University of Bayreuth) for providing access to the SEM. This work was financially supported by the Bundesministerium für Bildung und Forschung (BMBF, grant number 13N11340) and by the Deutsche Forschungsgemeinschaft (DFG, grant number FE 600/12-1 and SCHE 603/9-1).

References

- (1) Lammel, A.; Schwab, M.; Slotta, U.; Winter, G.; Scheibel, T. *Chemsuschem* **2008**, *1*, 413–416.
- (2) Slotta, U. K.; Rammensee, S.; Gorb, S.; Scheibel, T. *Angewandte Chemie-International Edition* **2008**, *47*, 4592–4594.
- (3) Hermanson, K. D.; Huemmerich, D.; Scheibel, T.; Bausch, A. R. *Advanced Materials* **2007**, *19*, 1810–1815.
- (4) Rammensee, S.; Huemmerich, D.; Hermanson, K. D.; Scheibel, T.; Bausch, A. R. *Applied Physics a-Materials Science & Processing* **2006**, *82*, 261–264.
- (5) Schacht, K.; Scheibel, T. *Biomacromolecules* **2011**, *12*, 2488–2495.
- (6) Leal-Egana, A.; Scheibel, T. *Journal of Materials Chemistry* **2012**, *22*, 14330–14336.
- (7) Blüm, C.; Scheibel, T. *English BioNanoScience* **2012**, *2*, 67–74.
- (8) Lammel, A.; Schwab, M.; Hofer, M.; Winter, G.; Scheibel, T. *Biomaterials* **2011**, *32*, 2233–2240.
- (9) Hofer, M.; Winter, G.; Myschik, J. *Biomaterials* **2012**, *33*, 1554–1562.
- (10) Liebmann, B.; Huemmerich, D.; Scheibel, T.; Fehr, M. *Colloids and Surfaces a-Physicochemical and Engineering Aspects* **2008**, *331*, 126–132.
- (11) Butt, H. J.; Cappella, B.; Kappl, M. *Surface Science Reports* **2005**, *59*, 1–152.
- (12) McConney, M. E.; Singamaneni, S.; Tsukruk, V. V. *Polymer Reviews* **2010**, *50*, 235–286.
- (13) Fery, A.; Weinkamer, R. *Polymer* **2007**, *48*, 7221–7235.
- (14) Erath, J.; Schmidt, S.; Fery, A. *Soft Matter* **2010**, *6*, 1432–1437.
- (15) Rentsch, S.; Pericet-Camara, R.; Papastavrou, G.; Borkovec, M. *Physical Chemistry Chemical Physics* **2006**, *8*, 2531–2538.

- (16) Deng, Z.; Lulevich, V.; Liu, F.-t.; Liu, G.-y. *Journal of Physical Chemistry B* **2010**, *114*, 5971–5982.
- (17) Helfricht, N.; Klug, M.; Mark, A.; Kuznetsov, V.; Blum, C.; Scheibel, T.; Papatavrou, G. *Biomater. Sci.* **2013**, *1*, 1166–1171.
- (18) Hertz, H. *Journal fuer die reine und angewandte Mathematik* **1881**, *92*, 156–171.
- (19) Spiess, K.; Ene, R.; Keenan, C. D.; Senker, J.; Kremer, F.; Scheibel, T. *Journal of Materials Chemistry* **2011**, *21*, 13594–13604.
- (20) Junghans, F.; Morawietz, M.; Conrad, U.; Scheibel, T.; Heilmann, A.; Spohn, U. *Applied Physics a-Materials Science & Processing* **2006**, *82*, 253–260.
- (21) Flory, P., *Principles of Polymer Chemistry*; Cornell University Press: 1953.
- (22) Savage, K. N.; Gosline, J. M. *Journal of Experimental Biology* **2008**, *211*, 1937–1947.
- (23) Huemmerich, D.; Helsen, C. W.; Quedzuweit, S.; Oschmann, J.; Rudolph, R.; Scheibel, T. *Biochemistry* **2004**, *43*, 13604–13612.
- (24) Fancy, D. A.; Kodadek, T. *Proceedings of the National Academy of Sciences of the United States of America* **1999**, *96*, 6020–6024.
- (25) Hutter, J. L.; Bechhoefer, J. *Review of Scientific Instruments* **1993**, *64*, 1868–1873.

Supporting information

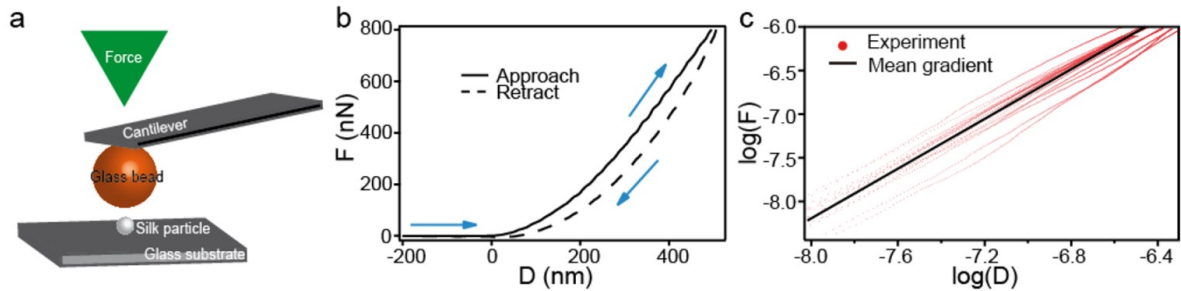


Figure 5.4. a) Schematic, lateral view of the colloidal probe setup. b) Exemplary force-deformation curve of an eADF4(C16) particle (diameter $2.7 \mu\text{m}$) in water. The particle compression follows a power law with a marginal adhesion. The slight hysteresis is due to material relaxation. c) Scatter plot of 20 randomly selected logarithmic force vs. deformation curves of eADF4(C16) particles. The gradient equals 1.42 ± 0.10 which is close to the predicted 1.5 from Hertz theory.

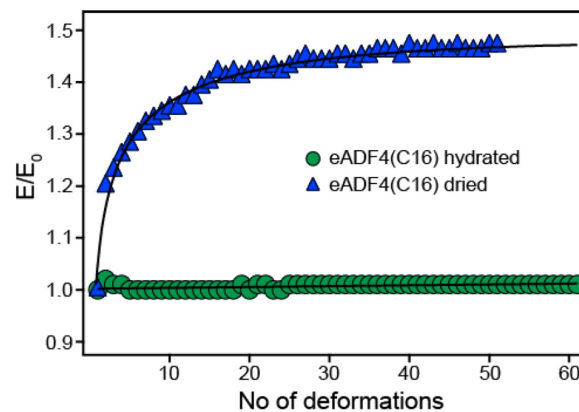


Figure 5.5. Fatigue tests of eADF4(C16) particles in dried and hydrated state. The average modulus of dried particles ($n = 11$) increases, whereas swollen particles ($n = 17$) show elastic behavior with constant modulus. Solid lines represent a guide to the eye.

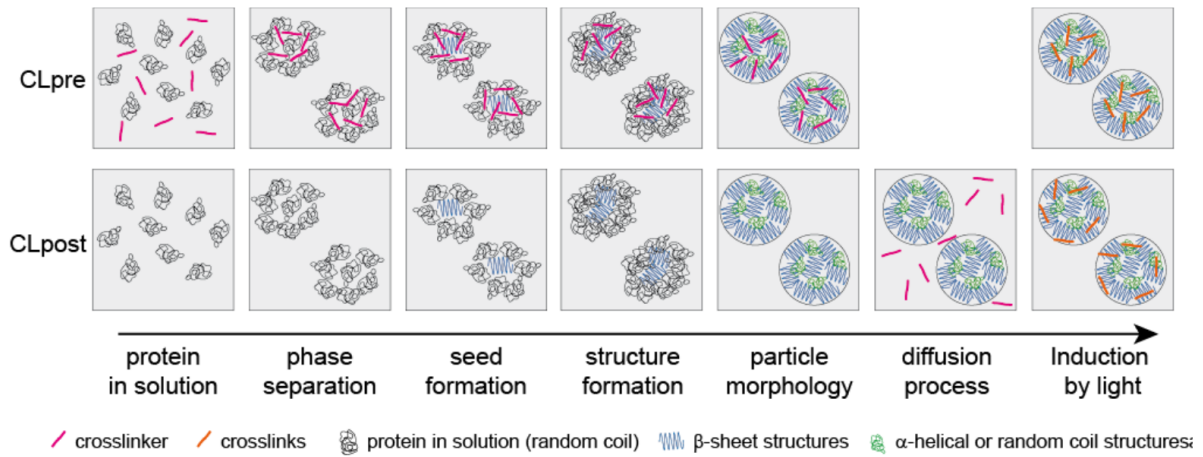


Figure 5.6. Schematic of particle-formation and the crosslinking process of eADF4 proteins. CLpre: crosslinkers added before precipitation of the particle, CLpost: addition of APS and Rubpy after formation of particles. By exposing the particles to a tungsten lamp, crosslinking is induced.

Table 5.1. Fit parameters \pm one standard deviation from Gaussian fits in 5.3a and 5.3b

Sample	Amplitude [%]	Mean [MPa]	Width [MPa]
eADF4(C8)	18.0 ± 2.9	2.45 ± 0.21	1.58 ± 0.30
eADF4(C16)	24.6 ± 1.2	2.99 ± 0.04	1.07 ± 0.06
eADF4(C32)	13.1 ± 1.0	5.42 ± 0.13	2.16 ± 0.19
eADF4(C16) CLpre	12.5 ± 1.3	5.14 ± 0.19	2.22 ± 0.27
eADF4(C16) CLpost	7.26 ± 1.6	8.19 ± 0.69	3.87 ± 0.99

6

Monodisperse collagen-gelatin beads as potential platforms for 3D cell culturing

Shaohua Ma, Manuela Natoli, Xin Liu, Martin P. Neubauer, Fiona M. Watt, Andreas Fery and Wilhelm T. S. Huck; *Journal of Materials Chemistry B* **2013**, 1:5128-5136.
Reproduced by permission of The Royal Society of Chemistry.

Abstract

A droplet-based microfluidics technique is used to produce monodisperse, 80 μm collagen-gelatin beads with tunable mechanical properties in the range of 1-10 kPa after photocrosslinking. The gel beads are porous, mechanically robust and stable in buffer, but can be degraded enzymatically. Encapsulated fibroblast cells maintain 70% viability after one-week encapsulation and preliminary results show that the degree of spreading of cells in gels is correlated with the stiffness of the material.

Introduction

The behavior and function of cells are critically influenced by the mechanical and chemical properties of the microenvironment.¹⁻⁵ Considerable progress has been made in deciphering the influence of micropatterns,^{6,7} topography,^{8,9} matrix elasticity,¹⁰⁻¹² and other mechanical cues¹³ on the behavior and differentiation of (stem) cells in 2D cultures. In the emerging field of microscale tissue engineering materials are required that direct cell and tissue function by controlling the microenvironment in 3D. However, it is not known how our knowledge obtained from studying 2D systems translates to a more relevant 3D environment.^{1,14,15} Polymer hydrogels with micrometer scale dimensions, so-called microgels, are useful building blocks in the creation of macroscale tissue architectures with micronscale control over the cellular environment. It is therefore of crucial importance to control material properties of the hydrogels such as stiffness, cell binding and migration, and porosity, in such a way that they resemble as closely as possible the extracellular matrix.¹⁶ Many examples of successful incorporation of cells in hydrogels have been reported, using both natural and synthetic polymer scaffolds. Synthetic polymer hydrogels have the advantage that their mechanical properties can be easily controlled, but cell-binding properties need to be introduced. Natural polymers such as collagen and fibrin provide superior cell binding and motility, but often lack mechanical stability. Considerable efforts have been made to develop chemical modification of natural polymers of the ECM such as hyaluronic acid^{12,15} and collagen, to produce microgels with suitable

mechanical properties while retaining their biocompatibility and enzymatic degradation. Ideally, we would use collagen as a scaffold, but its mechanical characteristics are poor. Mixtures of collagen and gelatin could solve this problem, as gelatin has improved mechanical characteristics, can be easily modified chemically, and supports cell adhesion, while the mixture retains the regulatory properties of collagen.^{17,18} As thermally gelled gelatin is not stable, a chemical cross-linking agent is required. Crosslinking of gelatin has been studied extensively, and examples include the use of glutaraldehyde¹⁹ or the less cytotoxic genipin²⁰ to directly crosslink gelatin, crosslinking of methacrylate- or thiol-modified gelatin,^{21,22} or enzymatic crosslinking using transglutaminase.²³

Micrometer scaled features in cell-laden polymer hydrogels have been introduced via micromolding²⁴ or photopatterning,^{8,9,25} and more recently also by using droplet-based microfluidics.²⁶ Previous work has reported the encapsulation and culturing of non-adherent cells in alginate,^{27,28} agarose,²⁹ synthetic peptides,³⁰ polyethyleneglycol (PEG),³¹ or PEG and hyperbranched polyglycerol copolymer³² beads. We are keen to expand droplet-based microfluidics to produce gel scaffolds of micrometer dimensions with controlled mechanical properties and suitable biodegradability for cell culturing. Here, we report the formation of monodisperse collagen-gelatin (col-gela) microgel beads, crosslinked via riboflavin-blue light irradiation mediated radical formation. The mechanical properties can be tailored over a tissue-relevant range (in the order of 1-10 kPa) and we studied swelling, pore size and biodegradability of the gels. Pure collagen beads were not able to retain the 3D bead structure after breaking emulsions due to its low elastic modulus. Our method ensured fibroblast viability of 70% after 1 week of encapsulation; the spreading of cells inside the 3D confinement of the gel beads can be followed.

Materials and methods

Preparation of microfluidic devices

Microfluidic PDMS devices were fabricated by combining photo- and soft-lithography³³ and the detailed fabrication is given elsewhere.³⁴ The channel width is given in figure illus-

trations and the devices had a fixed channel height of 75 μm . The devices were connected to high-precision syringe pumps (PHD 2000, Harvard Apparatus) *via* poly(ethylene) tubing (0.56/0.78 mm inner/outer diameter, Becton Dickinson) to ensure stable flows.

Formation of gelatin and col-gela beads

All chemicals were obtained from Sigma Aldrich Co. unless noted otherwise and used without further purification. Water with a resistivity of 16.8 $\text{M}\Omega\text{ cm}^{-1}$ was prepared using a Millipore Milli-Q system. Phosphate buffered saline (PBS) (1x) was diluted from the PBS stock solution (Invitrogen, PBS 10x, pH 7.4, 70011) by Milli-Q water. All gelatin used in this work was gelatin from porcine skin, type A (Sigma, G1890, ~ 300 g Bloom). Gelatin solutions at different concentrations, from 1.0 wt% to 15.0 wt%, were obtained by dissolving the gelatin powder in (1x) PBS buffer at 60 $^{\circ}\text{C}$. Riboflavin PBS solution was made by dissolving an excess amount of the riboflavin powder (R4500) in (1x) PBS, which was filtered through a 0.22 μm filter, obtaining saturated riboflavin PBS solution, at about 0.015 wt%. Collagen type I (BDTM Biosciences, Collagen type I, rat tail, 354236) was neutralized and diluted to 3.6 mg ml^{-1} in the ice bath according to the supplied protocol. Collagen and gelatin solutions were injected separately in the microfluidic device, and merged at the first cross-junction. Col-gela droplets formed at the second cross-junction by flow-focusing with a continuous stream of low-viscosity fluorocarbon oil, HFE7500 (297730-93-9, 3 M, 0.77 cSt), loaded with an ABA triblock copolymer surfactant (2.0 wt%), Pico Surf 1 (PS-1, Sphere Fluidics). During injection, the syringe filled with the collagen solution was covered with an ice bag to inhibit the gelation of collagen, and the gelatin phase was continuously heated between 30 $^{\circ}\text{C}$ and 60 $^{\circ}\text{C}$. Droplets were collected in an Eppendorf[®] tube, and incubated in the ice bath for 20 min. Gelatin beads were produced through the same procedure except that the collagen flow was zero.

Photo-crosslinking

Gelatin and col-gela droplets were collected in an Eppendorf[®] tube and incubated in an ice bath for 20 min. Emulsions were broken up by adding perfluorooctanol, vortexing, and centrifuging, subsequently. Beads were then resuspended in riboflavin PBS solution and exposed under the blue LED (Thorlabs, Inc. M470L2-C1, 470 nm emission) for several minutes. Crosslinked beads were repeatedly washed by PBS until colourless.

Optical detection

Brightfield images were taken from a monochrome Phantom v7.2 camera (Vision Research) integrated to an IX71 inverted microscope (Olympus). Fluorescent images were taken in the Andor rig attached to an IX81 inverted microscope (Olympus), incorporated with a mercury lamp (U-LH100HG, Olympus) for wide-field illumination, a FITC filter cube (Olympus) for detecting green fluorescence and a Rhodamine filter cube (Olympus) for red fluorescence detection. An EMCCD camera (Xion⁺, Andor Technologies) was used to acquire images. Image analysis was performed using ImageJ open source software.³⁵ Other fluorescent images were taken from a *Leica* DMI4000 fluorescence microscope and CLSM images were acquired with a *Leica* TCS SP5 confocal system.

Micromechanical characterization

The characterization of the elastic modulus (EMod) was carried out at the University of Bayreuth using an AFM setup (Nanowizard I, JPK Instruments, Germany), combined with an inverted optical microscope (Axiovert 200, Zeiss, Germany). The details were described elsewhere.³⁶ Briefly, the optical microscope was used to measure the bead size before and during deformation, and to align the cantilever probe with the center of the immobilized microparticle (SI, Fig. 6.7a). The deformation was performed using the colloidal probe technique with the spherical glass probe being coated with poly-L-Lysine (PLL)-g-PEG to minimize adhesion between the probe and the bead. The experiment was performed at ambient temperature (24 °C). Prior to and after the measurements on gel

beads a force curve on the non-deformable glass substrate was recorded to ensure stability of the optical lever sensitivity. All obtained raw data containing force vs. displacement curves were corrected for cantilever bending yielding the presented force vs. deformation curves. The spring constant ($k = 0.1425 \text{ N m}^{-1}$) of the used cantilever was obtained before attaching the probe with the thermal noise method.³⁷

SEM characterization

For SEM analysis, gel beads were freeze-dried (VirTis Bench Top L Manifold freeze drier) at $-75 \text{ }^\circ\text{C}$ and coated with gold. We used a Leo Ultra55 Field Emission SEM (Zeiss) at an acceleration voltage of 5.0 kV. SEM images of gelatin and col-gelatin beads are given in SI, Fig. 6.8.

Mesh size characterization

Gelatin beads were shaken in a $10 \text{ } \mu\text{M}$ solution of fluorescein isothiocyanate-dextran (FITC-dextran) at different molecular weights in PBS overnight and equilibrated for 24 h more at RT. The fluorescence intensity was measured using a confocal laser scanning microscope (CLSM) across the focal plane through the bead (an example bead is imaged in SI, Fig. 6.11a). The fluorescence across the line is quantified where the two curves represent the typical "non-diffusive" and "diffusive" fluorescence (SI, Fig. 6.11b). The "non-diffusive" fluorescence occurs when the mesh size of the bead is smaller than the hydrodynamic diameter of FITC-dextran so that no FITC-dextran molecules can diffuse into the gelatin matrix, whereas the "diffusive" fluorescence indicates the ability of FITC-dextran to passively diffuse into the gelatin matrix.

Cell culture

3T3 fibroblast cells were cultured in Dulbecco's Modified Eagle Medium (DMEM, high glucose, with Na-pyruvate and L-glutamine, Invitrogen, 41966), supplemented with 10% normal donor serum (Euroclone). Cells were maintained in an atmosphere of 5% $\text{CO}_2/95$

% air at 37 °C and 95% humidity. Cells were routinely subcultured using aqueous solutions of EDTA (0.5 mM) and trypsin (0.25 wt%) for 5 minutes. After removing trypsin, cells were re-suspended in DMEM at the final concentration of 1.0×10^6 cells per mL. For the production of cell-laden beads, 3T3 fibroblasts at the density of 1.0 to 2.6×10^6 mL⁻¹ were suspended in the collagen solution in the ice bath after centrifuging at 0.5 g for 2 min.

Immunostaining

Cell laden col-gela beads were washed in PBS and fixed with 4% paraformaldehyde (PFA)/PBS solution for 10 min at RT, permeabilized with 0.2% Triton-X100/PBS solution for 10 min at RT and washed with PBS. Beads were blocked with 10 % fetal bovine serum (FBS) plus 0.25% fish gelatin in PBS for 1 h at RT. The beads were incubated with the primary antibody, anti- α -tubulin (mouse monoclonal dilution 1 : 1000), in blocking solution for 1 h at RT, and then washed in PBS; the 2nd antibody was an Alexafluor 488 donkey anti-mouse (Invitrogen, 1 : 1000) in blocking solution with DAPI (1 : 10000) for 1 h at RT. Samples were mounted on a glass slide with the Mowiol reagent (4-88 Reagent, Calbiochem). The immunostaining of col-gela beads for homogeneity characterization followed similar procedures but starting from the blocking step. The primary antibody is anti-collagen I antibody (Abcam[®], 1 : 500) and the secondary antibody is Alexafluor 488-conjugated secondary antibody (Invitrogen, 1 : 1000).

Cell viability assay

Cells or cell-laden col-gela beads were suspended in PBS and mixed with *Live-Dead viability/cytotoxicity kit* (Invitrogen, L-3224). The kit, consisting of calcein AM (component A, 4 mM in DMSO) and ethidium homodimer-1 (component B, 2 mM DMSO-H₂O 1 : 4 (v/v)), was used according to the supplied protocol. The viability was indicated by the green (live) or red (dead) fluorescence of labelled cells.

Results and discussion

Droplet formation and gel bead production

A PDMS microfluidic device with a double flow-focusing module is used to generate monodisperse droplets of gelling precursors as shown in Fig. 6.1a. The two aqueous phases, gelatin solution in PBS and 3.6 mg mL^{-1} neutralized collagen, and the perfluorinated oil phase, HFE-7500, containing 2.0 wt% Pico Surf 1 surfactant, are injected from the three inlets with flow rates in the range of $100\text{-}500 \mu\text{l h}^{-1}$, leading to droplets around 80 μm in diameter. Droplet composition is tuned by varying gelatin concentration in PBS or the flow ratio of the gelatin phase to the collagen phase. Since gelatin gels rapidly at room temperature (RT), the gelatin phase is continuously heated between $30 \text{ }^\circ\text{C}$ and $60 \text{ }^\circ\text{C}$, while collagen is kept between $4 \text{ }^\circ\text{C}$ and $10 \text{ }^\circ\text{C}$. After droplet formation, the emulsion is collected in an Eppendorf tube and allowed to gel at $4 \text{ }^\circ\text{C}$ for 20 min. The beads are then collected by breaking the emulsion using perfluorooctanol, obtaining uniform col-gela beads as shown in Fig. 6.1b. The beads are soaked in 0.015 wt% riboflavin (the crosslinking agent) solution in PBS for 20 min to allow riboflavin diffusion into the beads, and exposed to blue light (470 nm, where riboflavin has a strong absorption, Fig. 6.1c). Riboflavin-mediated crosslinking has been reported to crosslink collagen and increase the mechanical strength of collagen fibers.^{38,39}

The crosslinking proceeds via the formation of singlet oxygen, which leads to the oxidation of histidine and the formation of imidazolone. The reactive species then reacts with nucleophilic amino acid residues leading to covalent crosslinks.^{40,41} The same mechanism is active in gelatin and col-gela beads: crosslinking was inhibited when the medium was purged with N_2 or treated with NaN_3 prior to light exposure, whereas substitution of H_2O with D_2O prolonged the lifetime of singlet oxygen and hence facilitated crosslinking. Crosslinking was efficient at $4 \text{ }^\circ\text{C}$ but not at $37 \text{ }^\circ\text{C}$ and $60 \text{ }^\circ\text{C}$, where the gelatin is in a disordered state (SI, Scheme 6.1 and Fig. 6.9). This indicates that the formation of new bonds is most efficient in gelled gelatin in which the collagen triple helices have partially

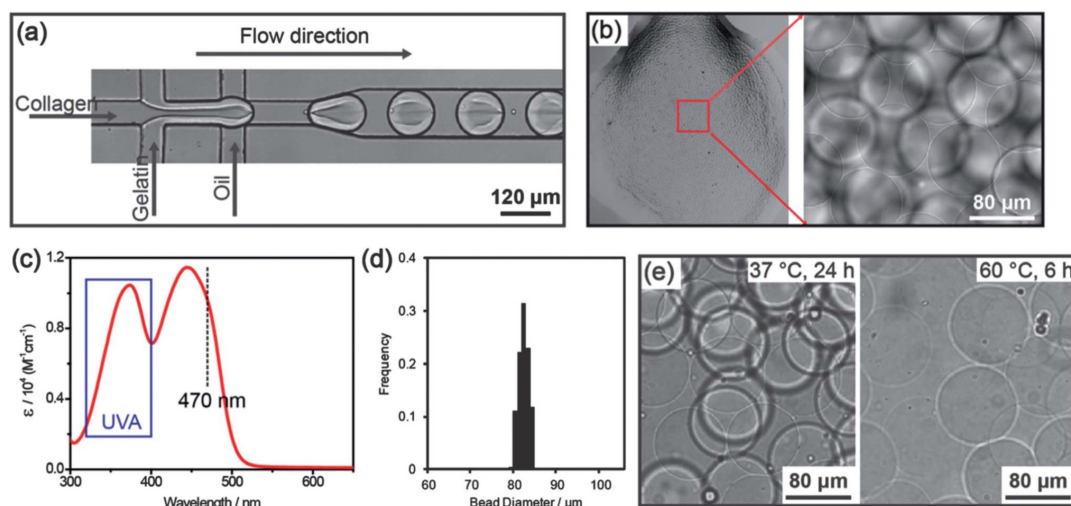


Figure 6.1. Col-gela beads production and photo-crosslinking. Bright field image of (a) col-gela droplets production in microfluidics; (b) physically gelled col-gela beads by incubation in the ice bath. (c) Absorption spectrum of riboflavin in PBS buffer at RT. (d) Size distribution of photo-crosslinked col-gela beads. (e) Bright field images of photocrosslinked col-gela beads incubated at 37 °C for 24 h (left) and at 60 °C for 6 h (right). Beads were made of 4.0 wt% gelatin and 0.18 wt% collagen, crosslinked for 4.5 min.

recovered.⁴² The resulting crosslinked col-gela beads (average diameter $82 \pm 3 \mu\text{m}$, Fig. 6.1d) do not melt and retain their morphology after 24 h incubation at 37 °C, or after 6 h at 60 °C (Fig. 6.1e).

Preparing homogeneous gels containing two different polymers is challenging. The advantage of the microfluidics platform is that it allows for efficient mixing of fluids in microdroplets induced by internal recirculation.⁴³ The homogeneity of col-gela mixtures is also determined by the relative gelling speed of collagen and gelatin, which is affected by the precursor concentration and temperature: dilution impedes gelling of both phases, but cooling facilitates gelatin gelling and slows down collagen gelling. We maintained both the collagen and the gelatin in the liquid phase by independently controlling their temperatures during injection. The phase contrast and confocal laser scanning microscopy (CLSM) fluorescence images in Fig. 6.2 show gel beads with collagen concentrations of 0.18 wt% (a and c) and 0.24 wt% (b and d), and gelatin concentrations of 4.0 wt% (a and

c) and 3.0 wt% (b and d), respectively. The two materials have different refractive indexes, and Fig. 6.2b shows that higher collagen loading leads to inhomogeneous gel beads. Collagen was also visualized by staining with anti-type I collagen antibody followed by Alexafluor 488-conjugated secondary antibody (Fig. 6.2c and d), and these experiments confirm the difference in homogeneity. Therefore, we used a maximum collagen loading of 0.18 wt% for all further experiments to ensure homogeneity (at least at length scales over the diffraction limit, $\sim 0.25 \mu\text{m}$) of the gel beads.

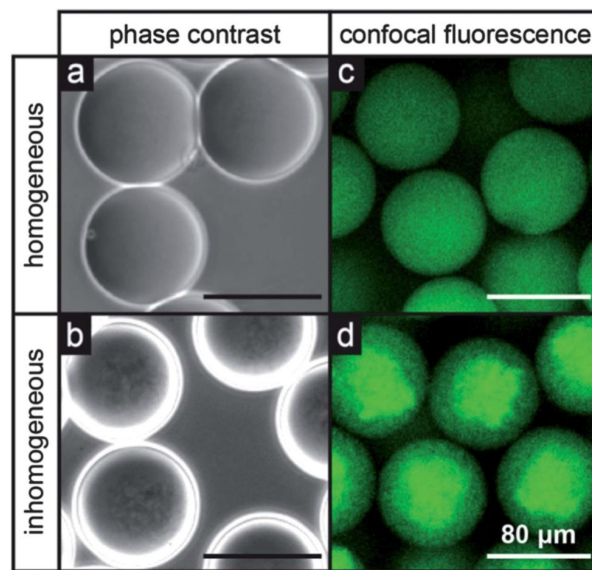


Figure 6.2. Phase contrast (a and b) and confocal fluorescence (c and d) microscopic images of the homogeneity of col-gelatin beads. Composition: (a and c) 4.0 wt% gelatin with 0.18 wt% collagen; (b and d) 3.0 wt% gelatin with 0.24 wt% collagen. Scale bar: $80 \mu\text{m}$.

Mechanical characterization

We determined the elastic modulus (EMod) of gel beads using the colloidal probe technique.³⁶ The colloidal probes have a typical diameter of $40 \mu\text{m}$ which is about half of the diameter of the investigated beads. This arrangement ensures that we obtain a large contact area and that the probe deforms the whole bead. Therefore, the colloidal

probe gives a non-localized insight into the mechanical properties of the entire particle. To extract the elastic modulus of gel beads from the obtained force-deformation curves the data were fitted using the Hertz model for the elastic deformation of two spheres in contact.⁴⁴ This is a reasonable assumption as all requirements for Hertzian theory are met by the investigated system and the chosen parameters: (1) the examined beads are homogeneous and show linear elastic behavior; (2) adhesion is negligible after coating of the probe and (3) only small deformations of less than 10% of the particles' diameter were evaluated.

The mathematical expression is given below, with F , d , E , and R being the applied force, deformation, the relative Young's modulus and radius, respectively.

$$F = \frac{4}{3} \cdot E \cdot d^{\frac{3}{2}} \cdot \sqrt{R} \quad (6.1)$$

E and R are given below, with ν being Poisson's ratio (assumed to be 0.5 for gelatin) and the indices referring to the two spheres in contact.

$$\frac{1}{E} = \frac{1 - \nu_1^2}{E_1} + \frac{1 - \nu_2^2}{E_2} \quad (6.2)$$

$$\frac{1}{R} = \frac{1}{R_1} + \frac{1}{R_2} \quad (6.3)$$

The scatter plot given in SI, Fig. 6.7c shows the logarithm of 28 randomly picked force vs. deformation curves. According to Hertz theory the gradient should equal 1.5. For the presented curves we find a gradient of 1.56 ± 0.19 which is in good agreement with the theoretical prediction.

Fig. 6.3a shows the dependence of EMod on gelatin content in beads that were crosslinked for 4.5 min. Moduli could be varied between 1.2 and 10.4 kPa by changing the gelatin concentration from 1.5 wt% to 15.0 wt%. Fig. 6.3a also shows that the addition of 0.18 wt% collagen does not influence the mechanical properties significantly. The stiffness of the gel beads can be tuned further by varying the exposure time to blue light: Fig. 6.3b

shows increase in EMod of 4.0 wt% col-gela beads from 3.8 to 5.7 kPa at exposure times between 1.5 and 24.5 min. The obtained elastic moduli in the low kPa range compare well with data reported in literature.⁴⁵ It is noteworthy that the effect of crosslinking degree is much less dominant than the gelatin content in controlling bead stiffness, especially for col-gela beads. The modulus of the gelatin beads scales almost linearly with gelatin concentration; this is in contradiction with classical scaling theory where EMod is proportional to the power 2.25 of concentration.^{46,47} However, this model is based on ideal entanglement of polymer chains in a good solvent. Gelatin clearly is not an ideal polymer as it has a high helical content,⁴⁸ and therefore, chain flexibility is reduced leading to a deviation from the theoretical scaling law. Scaling exponents published in the literature yield no clear picture. Joly-Duhamel *et al.*⁴⁹ reported a scaling exponent in line with the percolation model around 1.9, whereas Sanwlani *et al.*⁵⁰ found an exponent of 0.92, close to our observation.

Swelling and mesh size

We determined the mesh size for various beads by measuring the cut-off size at which fluorescently labelled dextran, fluorescein isothiocyanate-dextran (FITC-dextran), no longer diffused into the gel beads. We found mesh sizes in the range of 17.0 nm to 21.7 nm for all gelatin-only beads or for col-gela beads with gelatin concentrations higher than 3.0 wt%. Only the softest beads (1.5 wt% gelatin in col-gela beads) showed pore sizes over 30.0 nm (SI, Fig. 6.10, 6.11 and Table 6.1).

The swelling of hydrogels gives an indication of pore size and water content of the gels, and is of importance for cell survival. The swelling ratio of microbeads, Q , is expressed as $Q = V_h/V_d$, where V_h and V_d represent the hydrated and dehydrated bead volumes, respectively. We used beads cross-linked by exposure to blue light for 4.5 min or longer, where we found no dependence of the swelling ratio on the exposure time. The data in Table 6.1 and SI, Fig. 6.12 show that the swelling ratio increases significantly at low gelatin concentrations (from 8.5 at 2.0 wt% to 27.0 at 1.0 wt%), but between 2.0 wt%

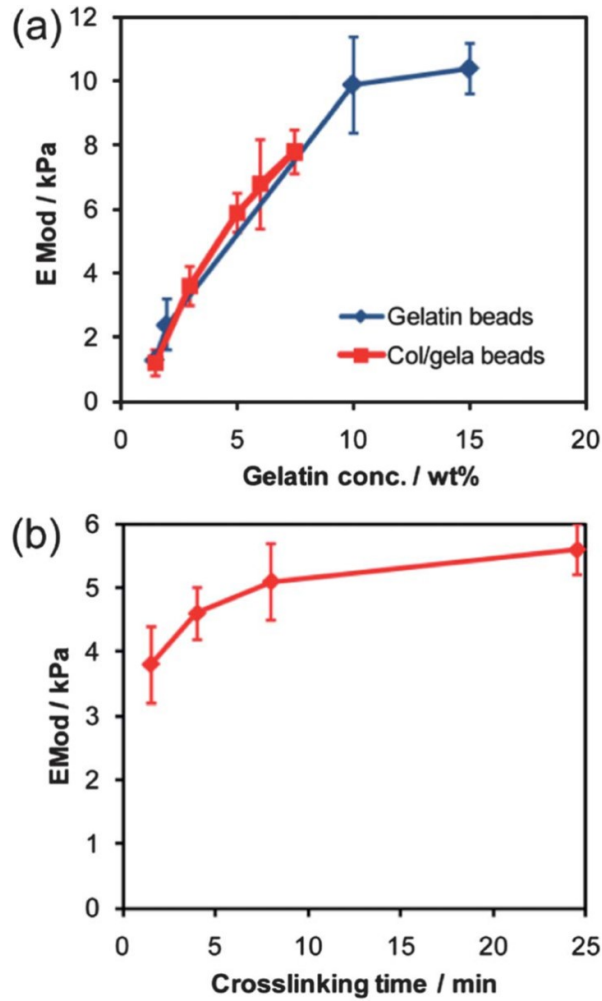


Figure 6.3. Elastic modulus (EMod) as determined by the colloidal probe AFM of (a) gelatin beads and col-gela beads at different gelatin concentrations and 0.18 wt% collagen and (b) col-gela beads composed of 4.0 wt% gelatin and 0.18 wt% collagen at different crosslinking times.

and 15 wt% gelatin content the swelling ratios stabilize between 7 and 12. Col-gela beads at 0.18 wt% collagen concentration exhibit higher swelling ratios than the corresponding gelatin beads at equal gelatin content (SI Fig. 6.12).

We used Flory-Rehner theory⁵¹ to calculate the mesh size based on the experimentally determined swelling ratio and a number of polymer specific parameters as discussed in SI Section 6 and Table 6.3. The calculated mesh sizes for gelatin contents between 2.0 wt% and 8.0 wt% are broadly similar, in line with the more or less constant swelling factors

(Table 6.1). These mesh sizes are also in good agreement with the values obtained from our cut-off experiments (17.0-21.7 nm). For higher degrees of swelling (*i.e.* lower gelatin content beads) the Flory-Rehner mesh size increases significantly (and exceeds the value from the cut-off experiments). Typically, one would expect Flory-Rehner to yield larger mesh sizes compared to diffusion cut-off experiments because it gives the linear distance between two crosslinks whereas the experiment yields an apparent mesh size influenced by geometrical constraints (including the presence of helices). The large deviations at low gelatin content might indicate that these gels have not formed a homogeneously crosslinked network.

Table 6.1. Summary of comparison of mesh size calculated from swelling ratio employing Flory-Rehner theory and the cut-off experiment.

Gelatin conc. [wt%]	Swelling ratio	Mesh (calc.) [nm]	Mesh (cut-off exp.) [nm]
1.0	26.7	58.2	
1.5	16.0	39.2	17.0-21.7
2.0	8.1	16.4	17.0-21.7
3.0	7.9	15.8	17.0-21.7
4.0	6.7	12.2	
6.0	8.7	18.3	
8.0	8.8	18.6	
10.0	10.4	23.6	17.0-21.7
15.0	11.9	28.2	

Biodegradability

A major challenge in synthetic and some naturally derived hydrogels like agarose and chitosan, is the lack of degradation of the matrix, preventing cells from migrating through

the gel and ultimately leading to cell death.^{21,22,52-54} Gelatin degradation is influenced by the incubation temperature and time, and medium composition, as reported, *via* the cleavage of peptide bonds and crosslinks among amino acids.⁵⁵ As we discussed above, the crosslinked gelatin and col-gela beads retain their structural integrity even at elevated temperatures in buffer. The stability of col-gela beads in different environments ranges from hours (cell-laden beads in DMEM complete medium at 37 °C) to several months (empty beads in PBS and stored at 2-8 °C).

Importantly, and critically for cell spreading, the network can be broken down enzymatically by collagenases and gelatinases.⁵⁶ Col-gela beads, composed of 4.5 wt% gelatin, 0.18 wt% collagen, and crosslinked for 4.5 min, were incubated in different media at 37 °C over the course of 96 h (Fig. 6.4). To quantify bead degradation, we counted the fraction of degraded and non-degraded beads by visual inspection of >200 beads for each data point; degraded beads were recognized as only collagen debris remained. Over 60% beads incubated in PBS survived for 96 h. In comparison, beads incubated in the DMEM complete medium degraded faster (over 60% degraded at 96 h), but when fibroblasts were present as well, the degradation accelerated due to proteolytic activity of enzymes (nearly 40% beads degraded within 24 h and over 80% beads disintegrated at 96 h). Col-gela beads incubated in 1.0 mg ml⁻¹ collagenase in PBS solution at 37 °C degraded rapidly within 4 h and at 10.0 mg ml⁻¹, the degradation completed within 1 h. Degradation is correlated with the crosslinking degree. When the same beads were crosslinked for 8.0 min, over 80% beads were maintained after 96 h incubation in DMEM complete medium.

Cell encapsulation in col-gela beads

To study cell compatibility, 3T3 fibroblasts were suspended in the collagen phase and mixed online with the gelatin phase, as illustrated in Fig. 6.5a. Fig. 6.5b shows the bright field images of monodisperse cell-laden col-gela beads (4.0 wt% gelatin with 0.18 wt% collagen, 8.0 min crosslinking, ~80 μm in diameter). The distribution of the

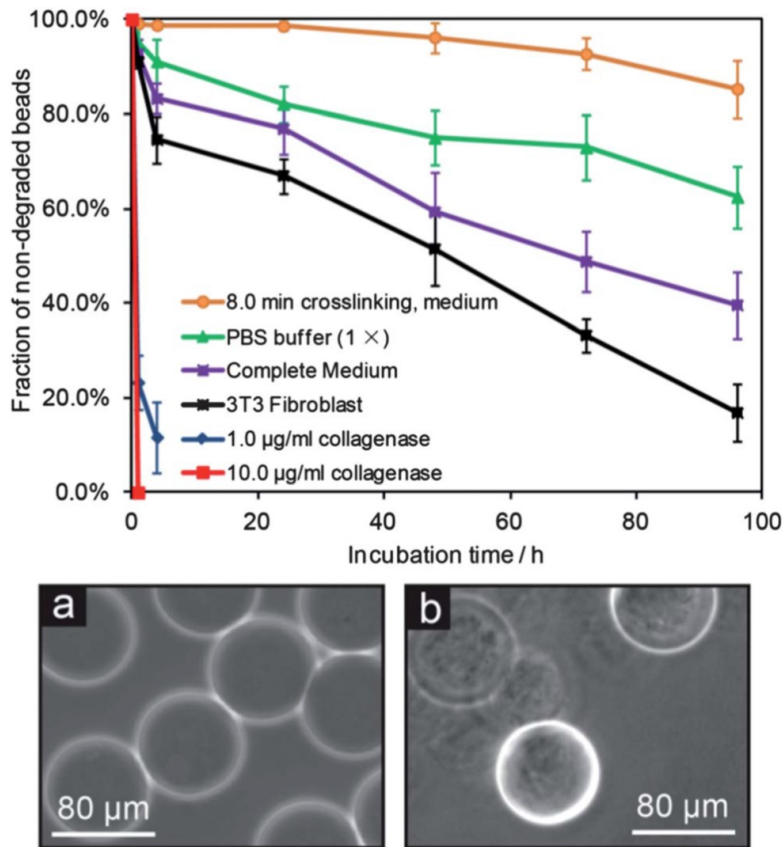


Figure 6.4. Fraction of non-degraded col-gela beads with incubation time in varied environments at 37 °C over 96 h: PBS buffer, the DMEM complete medium (no fibroblasts), the DMEM complete medium, with fibroblasts growing on the flask surface, 1.0 mg mL⁻¹ collagenase in PBS buffer, 10.0 mg mL⁻¹ collagenase in PBS buffer. Beads are composed of 4.5 wt% of gelatin and 0.18 wt% collagen, crosslinked for 4.5 min if not specially noted. The extra curve represents beads crosslinked for 8.0 min and incubated in complete 3T3 fibroblast medium. Bright field images (a) and (b) give col-gela beads in DMEM complete medium at 0 h and 72 h.

number of cells per bead at a cell density of $1.5 \times 10^6 \text{ ml}^{-1}$ is shown in Fig. 6.5c. This distribution follows a statistical (Poisson) distribution⁵⁷ and by varying the cell density before injection it is possible to encapsulate multiple cells per bead (SI, Fig. 6.13).

Fig. 6.5d shows the immunofluorescence image of a fibroblast embedded col-gela beads (green immuno-stained tubulins and blue DAPI-stained nuclei) to confirm that cells

preserved their structure after mechanical deformation of beads during formation and crosslinking. Cell compartmentalization was further demonstrated by CLSM after culturing for 6 h (Fig. 6.5e). Several studies have shown that moderate levels of UV-light and radicals are not cytotoxic,^{12,21,31,58} and indeed radical-based crosslinking is used in materials currently undergoing clinical trials.⁴⁰ Cell viability was monitored for 1 week and quantified using a live-dead assay (see Materials and methods). Nearly 90% cells were viable after 24 h, indicating the droplet and gel bead formation itself are not damaging the cells. About 70% cells were alive after 1 week (Fig. 6.5f). However, crosslinking time does affect cell viability: we observed that fibroblasts showed good viabilities at 8.0 min crosslinking, but when extended to 16.0 min, the viability was lowered to below 20% after 28 h.

The elastic moduli of gelatin and col-gelatin beads are in a range similar to the elasticity of natural and synthetic matrices used in the cell culture.^{59,14} Here, we report preliminary data on the correlation between cell spreading and bead moduli. Cells are more sensitive to gel stiffness when encapsulated in the 3D matrix instead of being cultured on 2D substrates.¹⁴ Fig. 6.6a and b show 3T3 fibroblasts spreading in beads with two different moduli: "soft beads" (4.0 wt% gelatin, 0.18 wt% collagen, 8.0 min crosslinking, $E = 5.1 \pm 0.6$ kPa, as measured), and "stiff beads" (6.0 wt% gelatin and 0.18 wt% collagen, 8.0 min crosslinking, $E = 6.8 \pm 1.4$ kPa, as measured). In the soft beads, over 60% of fibroblasts, by counting over 200 cells, started spreading as early as 18 h after encapsulation by invading the gel matrices (indicated by white arrows). In contrast, less than 40% of cells spread even after 28 h after encapsulation in stiff beads. Interestingly, a similar degree of spreading (approximately 80%) was observed in both cases after 4 days in culture. Shortening the crosslinking time of the "soft beads" to 4.5 min lowered the modulus to 4.6 ± 0.4 kPa and led to a more rapid response of cells. However, enzymatic degradation is related to crosslinking density, and due to the lower crosslinking degree beads degrade much faster, which accelerates fibroblast spreading, as shown in Fig. 6.6c. Cells initially spread, then migrate through the beads.

Prolonged culturing eventually leads to cells "escaping" the confinement of individual

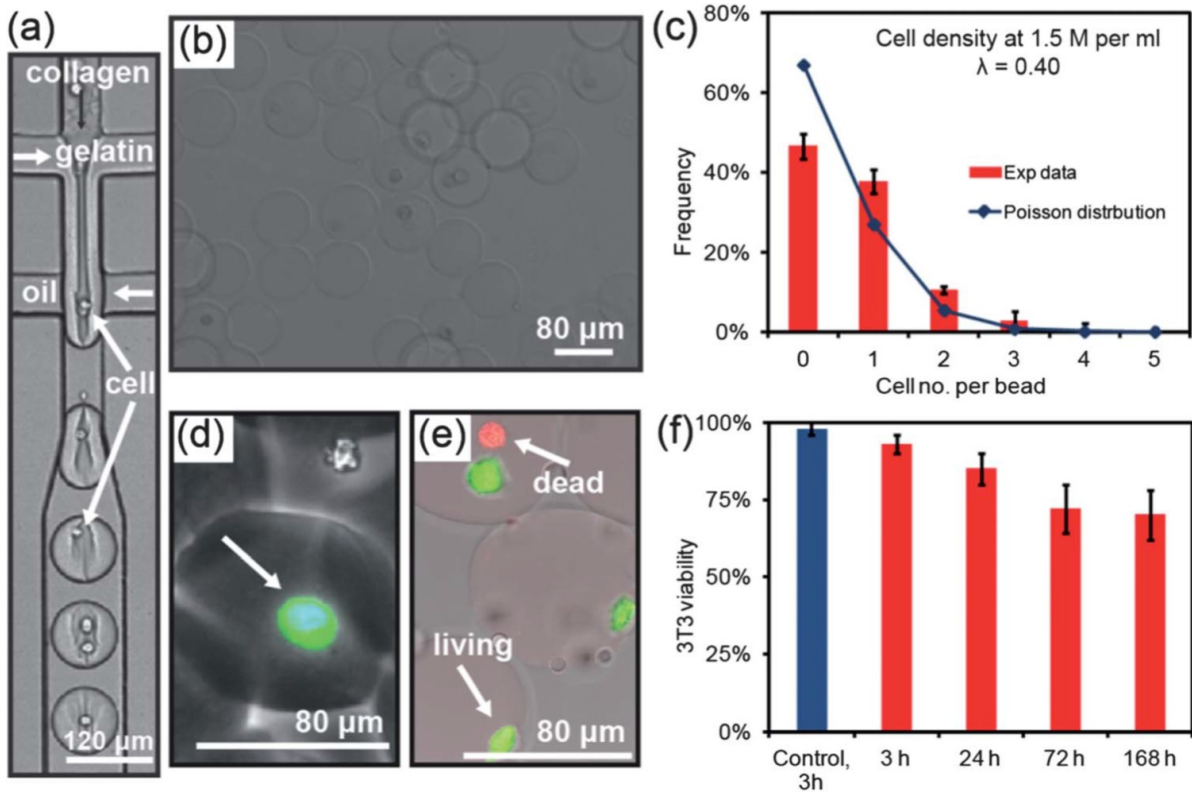


Figure 6.5. (a) Illustration of cell encapsulation in col-gela droplets in microfluidics; (b) bright field images of cell-laden col-gela beads at RT; (c) predicted and experimental distribution of number of encapsulated cells in individual droplets; (d) indirect immune staining of 3T3 fibroblasts in col-gela beads using the primary antibody, antitubulin (mouse monoclonal, 1 : 1000), and the 2nd antibody, donkey anti-mouse (Alexa Fluor, 488, 1 : 1000), with DAPI in the blocking solution; (e) CLSM image of cell-laden col-gela beads after encapsulation for 6 h, where cells were stained with the live-dead assay kit (green, living cell; red, dead cell); (f) 3T3 fibroblasts viability over the course of 1 week in col-gela beads. Col-gela beads are 4.0 wt% gelatin, 0.18 wt% collagen, 8.0 min crosslinking, and at a cell density of $1.5 \times 10^6 \text{ mL}^{-1}$.

beads. Fig. 6.6d shows spreading over multiple beads, and when the gel beads are closely packed, it becomes impossible to distinguish individual beads with cells; instead, the cells and gels merge into larger aggregates. This process could be exploited in macroscopically molded beads for tissue generation studies.⁶⁰ Fig. 6.6e summarizes the results above and

plots the onset of fibroblast spreading as well as the onset of cells bridging multiple beads (*i.e.* beads merging) at different degrees of cross-linking and gelatin concentrations. In all cases, stiffer beads delay fibroblast spreading and higher crosslinking degree impedes bead degradation/merging.

Conclusion

We have demonstrated a method to encapsulate fibroblast cells into monodisperse col-gelatin microbeads by droplet-based microfluidics and blue light-induced photo-crosslinking. The material properties of the beads (stiffness, pore size, degree of crosslinking, swelling ratios) can all be controlled by varying the composition of the droplets and by changing the crosslinking time. Although the beads are stable in buffer, storage in cell medium or encapsulation of cells leads to enzymatic degradation (by collagenases and gelatinases present in the medium and secreted by cells). By tuning gelatin concentration and the crosslinking degree, cell-laden beads with desired degradability are achievable, as demonstrated by long-term viability of encapsulated fibroblasts. Preliminary studies show that crucial aspects of the cellular response to the mechanical nature of the ECM, such as cell viability, spreading and motility, can be studied in microgel beads. In future experiments we will also investigate blending in fibronectin or hyaluronic acid, which is known to enhance cell spreading.⁶¹ The combination of optimum material properties with characterization of cells in beads using fluorescence-based techniques makes the gel bead platform suitable for potential applications in tissue engineering and single cell analysis studies.

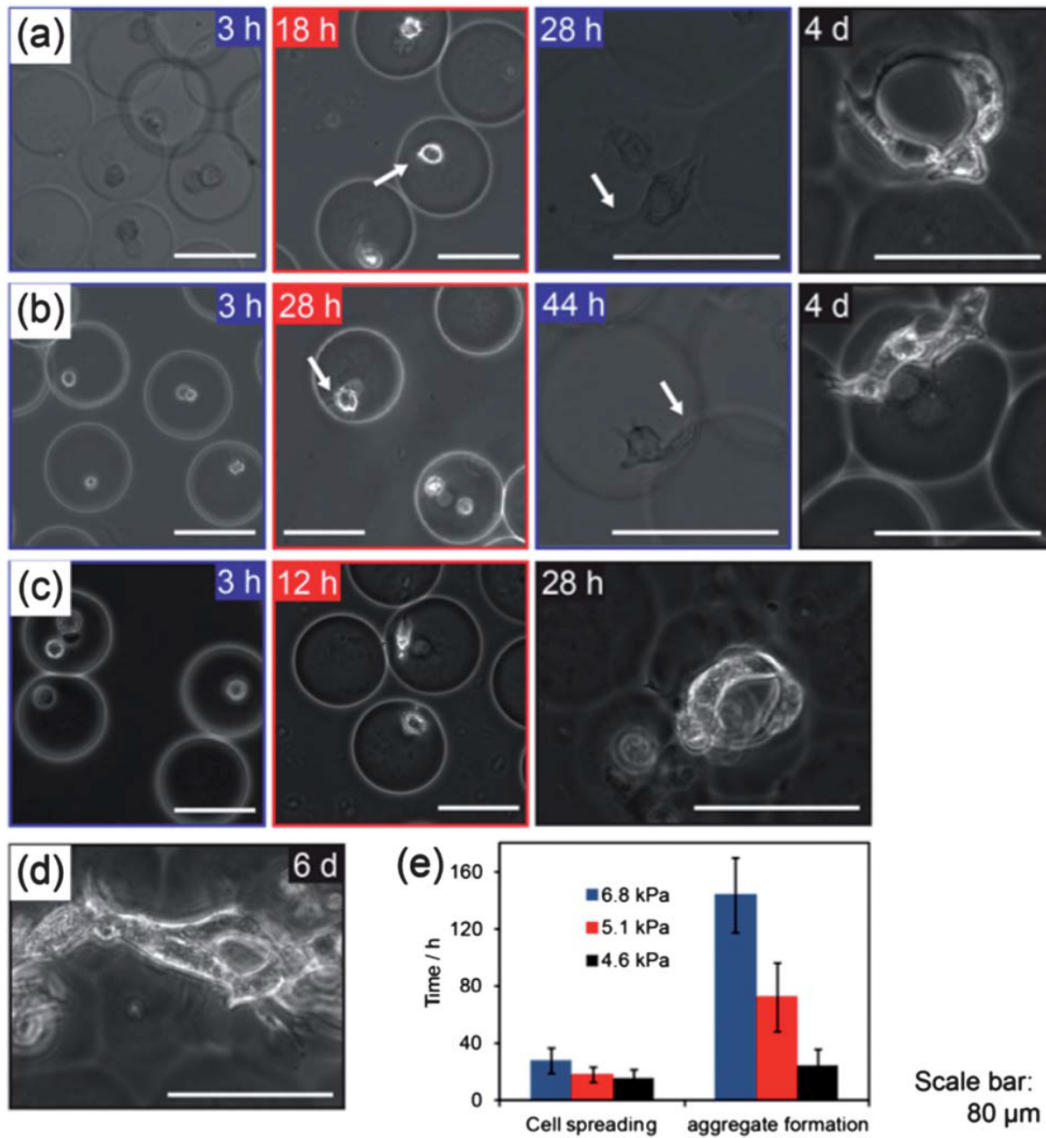


Figure 6.6. Bright field images of control of 3T3 fibroblasts spreading and invasion in defined col-gela beads by tuning (a and b) the gelatin concentration and (a and c) the crosslinking degree. Col-gela beads, from (a) to (c), are 4.0 wt% gelatin with 0.18 wt% collagen (8.0 min crosslinking), 6.0 wt% gelatin with 0.18 wt% collagen (8.0 min crosslinking), and 4.0 wt% gelatin with 0.18 wt% collagen (4.5 min crosslinking). (d) Cell spreading over aggregated col-gela beads after 6 days culture. (e) Onset of 3T3 fibroblast spreading and beads merging under three different conditions (a, b, and c).

References

- (1) Pampaloni, F.; Reynaud, E. G.; Stelzer, E. H. K. *Nature Reviews Molecular Cell Biology* **2007**, *8*, 839–845.
- (2) Langer, R.; Tirrell, D. A. *Nature* **2004**, *428*, 487–492.
- (3) Stock, U. A.; Vacanti, J. P. *Annual Review of Medicine* **2001**, *52*, 443–451.
- (4) Tibbitt, M. W.; Anseth, K. S. *Science Translational Medicine* **2012**, *4*.
- (5) Khademhosseini, A.; Langer, R.; Borenstein, J.; Vacanti, J. P. *Proceedings of the National Academy of Sciences of the United States of America* **2006**, *103*, 2480–2487.
- (6) Chen, C. S.; Mrksich, M.; Huang, S.; Whitesides, G. M.; Ingber, D. E. *Science* **1997**, *276*, 1425–1428.
- (7) Connelly, J. T.; Gautrot, J. E.; Trappmann, B.; Tan, D. W.-M.; Donati, G.; Huck, W. T. S.; Watt, F. M. *Nature Cell Biology* **2010**, *12*, 711–U177.
- (8) Dertinger, S. K. W.; Jiang, X. Y.; Li, Z. Y.; Murthy, V. N.; Whitesides, G. M. *Proceedings of the National Academy of Sciences of the United States of America* **2002**, *99*, 12542–12547.
- (9) Kirschner, C. M.; Anseth, K. S. *Small* **2013**, *9*, 578–584.
- (10) Trappmann, B.; Gautrot, J. E.; Connelly, J. T.; Strange, D. G. T.; Li, Y.; Oyen, M. L.; Stuart, M. A. C.; Boehm, H.; Li, B.; Vogel, V.; Spatz, J. P.; Watt, F. M.; Huck, W. T. S. *Nature Materials* **2012**, *11*, 642–649.
- (11) Engler, A. J.; Sen, S.; Sweeney, H. L.; Discher, D. E. *Cell* **2006**, *126*, 677–689.
- (12) Guvendiren, M.; Burdick, J. A. *Nature Communications* **2012**, *3*.
- (13) Wang, N.; Tytell, J. D.; Ingber, D. E. *Nature Reviews Molecular Cell Biology* **2009**, *10*, 75–82.
- (14) Marklein, R. A.; Soranno, D. E.; Burdick, J. A. *Soft Matter* **2012**, *8*, 8113–8120.

- (15) Rehfeldt, F.; Brown, A. E. X.; Raab, M.; Cai, S.; Zajac, A. L.; Zemel, A.; Discher, D. E. *Integrative Biology* **2012**, *4*, 422–430.
- (16) Khademhosseini, A.; Langer, R. *Biomaterials* **2007**, *28*, 5087–5092.
- (17) Cukierman, E.; Pankov, R.; Yamada, K. M. *Current Opinion in Cell Biology* **2002**, *14*, 633–639.
- (18) Montesano, R.; Orci, L.; Vassalli, P. *Journal of Cell Biology* **1983**, *97*, 1648–1652.
- (19) Sisson, K.; Zhang, C.; Farach-Carson, M. C.; Chase, D. B.; Rabolt, J. F. *Biomacromolecules* **2009**, *10*, 1675–1680.
- (20) Huang, K.-S.; Lu, K.; Yeh, C.-S.; Chung, S.-R.; Lin, C.-H.; Yang, C.-H.; Dong, Y.-S. *Journal of Controlled Release* **2009**, *137*, 15–19.
- (21) Nichol, J. W.; Koshy, S. T.; Bae, H.; Hwang, C. M.; Yamanlar, S.; Khademhosseini, A. *Biomaterials* **2010**, *31*, 5536–5544.
- (22) Fu, Y.; Xu, K.; Zheng, X.; Giacomini, A. J.; Mix, A. W.; Kao, W. J. *Biomaterials* **2012**, *33*, 48–58.
- (23) Paguirigan, A. L.; Beebe, D. J. *Nature Protocols* **2007**, *2*, 1782–1788.
- (24) Yeh, J.; Ling, Y.; Karp, J. M.; Gantz, J.; Chandawarkar, A.; Eng, G.; Blumling James, I.; Langer, R.; Khademhosseini, A. *Biomaterials* **2006**, *27*, 5391–5398.
- (25) Panda, P.; Ali, S.; Lo, E.; Chung, B. G.; Hatton, T. A.; Khademhosseini, A.; Doyle, P. S. *Lab on a Chip* **2008**, *8*, 1056–1061.
- (26) Velasco, D.; Tumarkin, E.; Kumacheva, E. *Small* **2012**, *8*, 1633–1642.
- (27) Tan, W.-H.; Takeuchi, S. *Advanced Materials* **2007**, *19*, 2696–+.
- (28) Kim, C.; Chung, S.; Kim, Y. E.; Lee, K. S.; Lee, S. H.; Oh, K. W.; Kang, J. Y. *Lab Chip* **2011**, *11*, 246–252.
- (29) Kumachev, A.; Greener, J.; Tumarkin, E.; Eiser, E.; Zandstra, P. W.; Kumacheva, E. *Biomaterials* **2011**, *32*, 1477–1483.
- (30) Tsuda, Y.; Morimoto, Y.; Takeuchi, S. *Langmuir* **2010**, *26*, 2645–2649.

- (31) Li, C. Y.; Wood, D. K.; Hsu, C. M.; Bhatia, S. N. *Lab on a Chip* **2011**, *11*, 2967–2975.
- (32) Rossow, T.; Heyman, J. A.; Ehrlicher, A. J.; Langhoff, A.; Weitz, D. A.; Haag, R.; Seiffert, S. *Journal of the American Chemical Society* **2012**, *134*, 4983–4989.
- (33) Xia, Y. N.; Whitesides, G. M. *Annual Review of Materials Science* **1998**, *28*, 153–184.
- (34) Bauer, W.-A. C.; Fischlechner, M.; Abell, C.; Huck, W. T. S. *Lab on a Chip* **2010**, *10*, 1814–1819.
- (35) Shim, J.-u.; Patil, S. N.; Hodgkinson, J. T.; Bowden, S. D.; Spring, D. R.; Welch, M.; Huck, W. T. S.; Hollfelder, F.; Abell, C. *Lab on a Chip* **2011**, *11*, 1132–1137.
- (36) Pretzl, M.; Neubauer, M.; Tekaath, M.; Kunert, C.; Kuttner, C.; Leon, G.; Berthier, D.; Erni, P.; Ouali, L.; Fery, A. *Acs Applied Materials & Interfaces* **2012**, *4*, 2940–2948.
- (37) Hutter, J. L.; Bechhoefer, J. *Review of Scientific Instruments* **1993**, *64*, 1868–1873.
- (38) Randolph, M. A.; Ibusuki, S.; Redmond, R. W.; Kochevar, I. E.; Gill, T. J. *European Cells and Materials* **2007**, *13*, 2262.
- (39) Tirella, A.; Liberto, T.; Ahluwalia, A. *Materials Letters* **2012**, *74*, 58–61.
- (40) McCall, A. S.; Kraft, S.; Edelhauser, H. F.; Kidder, G. W.; Lundquist, R. R.; Bradshaw, H. E.; Dedeic, Z.; Dionne, M. J. C.; Clement, E. M.; Conrad, G. W. *Investigative Ophthalmology & Visual Science* **2010**, *51*, 129–138.
- (41) Heelis, P. F. *Chem. Soc. Rev.* **1982**, *11*, 15–39.
- (42) Kuijpers, A. J.; Engbers, G. H. M.; Feijen, J.; De Smedt, S. C.; Meyvis, T. K. L.; Demeester, J.; Krijgsveld, J.; Zaat, S. A. J.; Dankert, J. *Macromolecules* **1999**, *32*, 3325–3333.
- (43) Tice, J. D.; Song, H.; Lyon, A. D.; Ismagilov, R. F. *Langmuir* **2003**, *19*, 9127–9133.

- (44) Hertz, H. *Journal fuer die reine und angewandte Mathematik* **1881**, *92*, 156–171.
- (45) Benmouna, F.; Johannsmann, D. *Langmuir* **2004**, *20*, 188–193.
- (46) Janmey, P. A.; Euteneuer, U.; Traub, P.; Schliwa, M. *Journal of Cell Biology* **1991**, *113*, 155–160.
- (47) De Gennes, P. G., *Scaling concepts in polymer physics*, 1st; Cornell University Press: 1979.
- (48) Gornall, J. L.; Terentjev, E. M. *Soft Matter* **2008**, *4*, 544–549.
- (49) Joly-Duhamel, C.; Hellio, D.; Ajdari, A.; Djabourov, M. *Langmuir* **2002**, *18*, 7158–7166.
- (50) Sanwlani, S.; Kumar, P.; Bohidar, H. B. *Journal of Physical Chemistry B* **2011**, *115*, 7332–7340.
- (51) Flory, P. J.; Rehner, J. *The Journal of Chemical Physics* **1943**, *11*, 521–526.
- (52) Khetan, S.; Guvendiren, M.; Legant, W. R.; Cohen, D. M.; Chen, C. S.; Burdick, J. A. *Nature Materials* **2013**, *12*, 458–465.
- (53) Edalat, F.; Sheu, I.; Manoucheri, S.; Khademhosseini, A. *Current Opinion in Biotechnology* **2012**, *23*, 820–825.
- (54) Ulrich, T. A.; Jain, A.; Tanner, K.; MacKay, J. L.; Kumar, S. *Biomaterials* **2010**, *31*, 1875–1884.
- (55) Van den Bosch, E.; Gielens, C. *International Journal of Biological Macromolecules* **2003**, *32*, 129–138.
- (56) Kilian, K. A.; Lai, L. M. H.; Magenau, A.; Cartland, S.; Boecking, T.; Di Girolamo, N.; Gal, M.; Gaus, K.; Gooding, J. J. *Nano Letters* **2009**, *9*, 2021–2025.
- (57) Koester, S.; Angile, F. E.; Duan, H.; Agresti, J. J.; Wintner, A.; Schmitz, C.; Rowat, A. C.; Merten, C. A.; Pisignano, D.; Griffiths, A. D.; Weitz, D. A. *Lab on a Chip* **2008**, *8*, 1110–1115.
- (58) Pathak, C. P.; Sawhney, A. S.; Hubbell, J. A. *Journal of the American Chemical Society* **1992**, *114*, 8311–8312.

- (59) Engler, A. J.; Griffin, M. A.; Sen, S.; Bonnetmann, C. G.; Sweeney, H. L.; Discher, D. E. *Journal of Cell Biology* **2004**, *166*, 877–887.
- (60) Matsunaga, Y. T.; Morimoto, Y.; Takeuchi, S. *Advanced Materials* **2011**, *23*, H90–H94.
- (61) Doillon, C. J.; Silver, F. H.; Berg, R. A. *Biomaterials* **1987**, *8*, 195–200.

Supporting information

Mechanical characterization

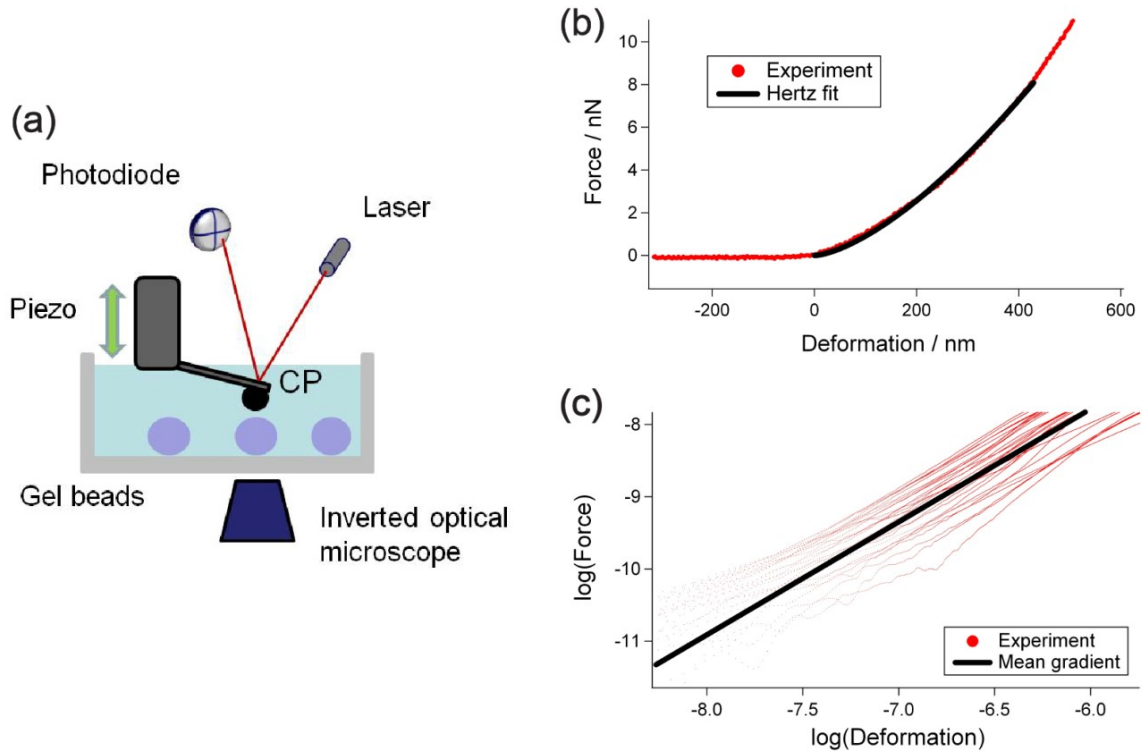
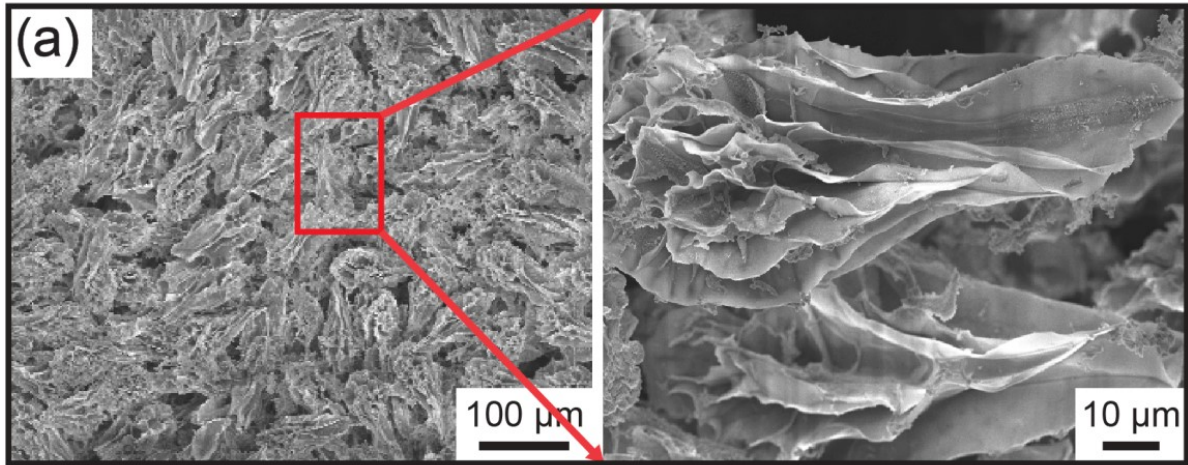


Figure 6.7. (a) Illustration of micromechanical characterization of gelatin and col-gela microbeads using AFM combined with an inverted optical microscope. The colloidal probe (CP) with a glass bead rather than a sharp tip is forced on a gel bead, which subsided to the cell bottom, immersed in water. Bead alignment and gel bead deformation is monitored from the microscope. (b) A typical force-deformation curve with Hertz fit. (c) Scatter plot of randomly selected force curves proving the Hertzian scaling law.

SEM characterization

Gelatin beads



Col/gela beads

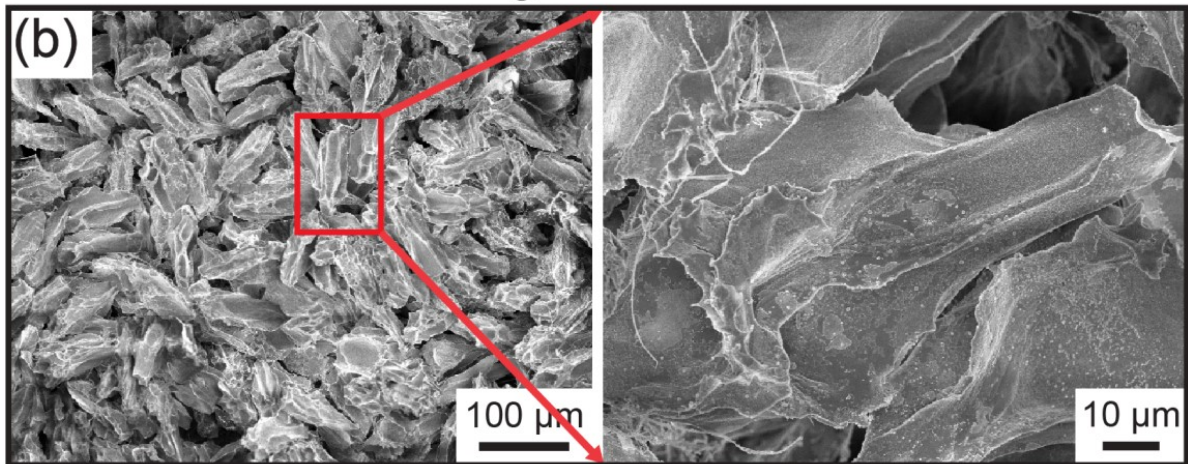


Figure 6.8. SEM images of gelatin beads (a) and col-gela beads (b). Beads are (a) 4.0 wt% gelatin, 4.5 min crosslinking, freeze-dried and (b) 4.0 wt% gelatin, 0.18 wt% collagen, 4.5 min crosslinking, freeze-dried.

Crosslinking and degradation parameters

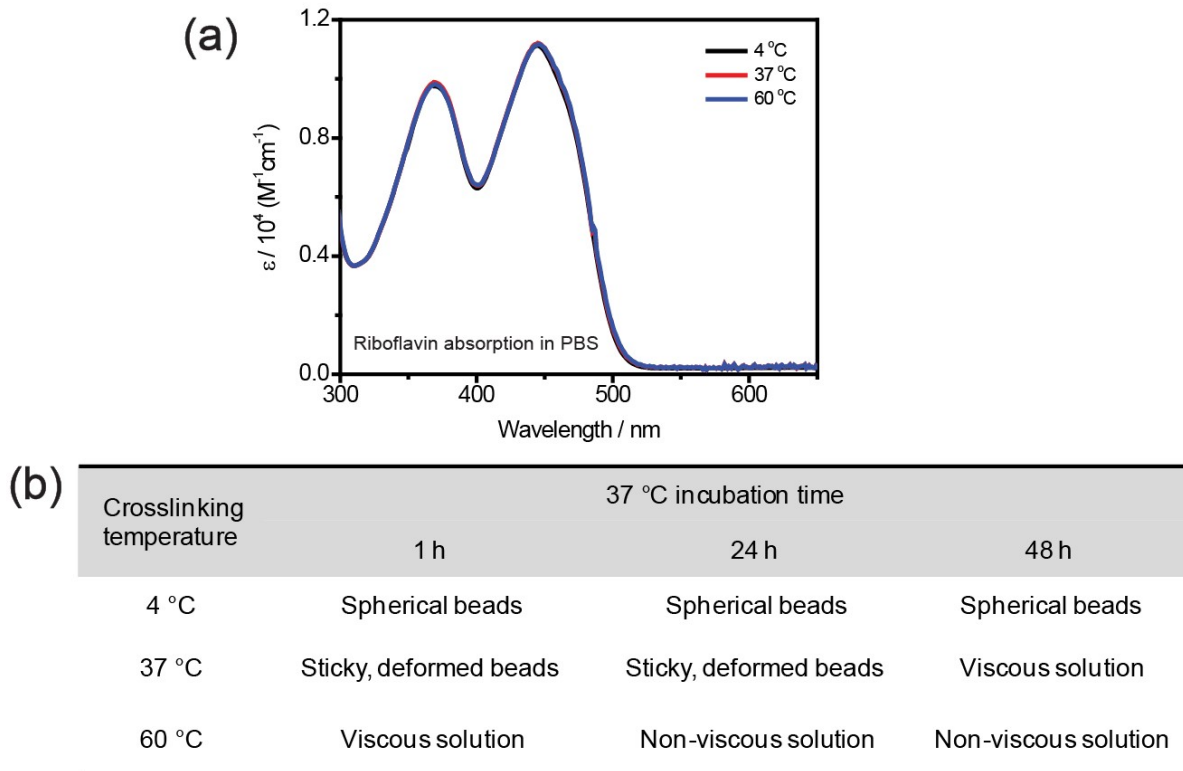
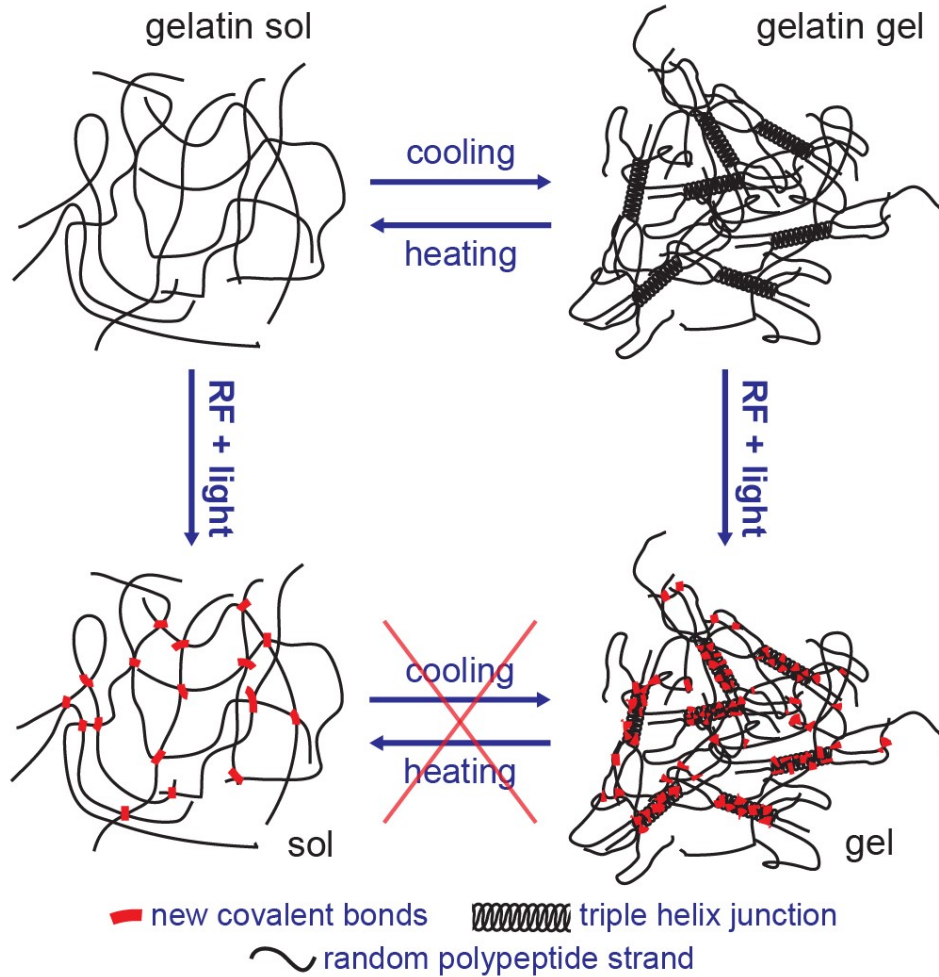


Figure 6.9. Adsorption spectrum of riboflavin in PBS buffer at three different temperatures: 4 °C, 37 °C, and 60 °C. The adsorption curves have no obvious difference, indicating that in these conditions the crosslinking activity remains unchanged. (b) Morphological evolution of 4.0 wt% gelatin beads crosslinked at 4 °C, 37 °C, and 60 °C for 4.5 min, respectively and incubated at 37 °C over 48 h in PBS buffer.

Photo-crosslinking mechanism

Scheme 6.1. Sol-gel phase transition of gelatin before and after riboflavin crosslinking. By cooling or heating, gelatin transit between sol and gel phases before photocrosslinking; but after crosslinking, the sol-gel transition is prohibited.



FITC-dextran hydrodynamic radius

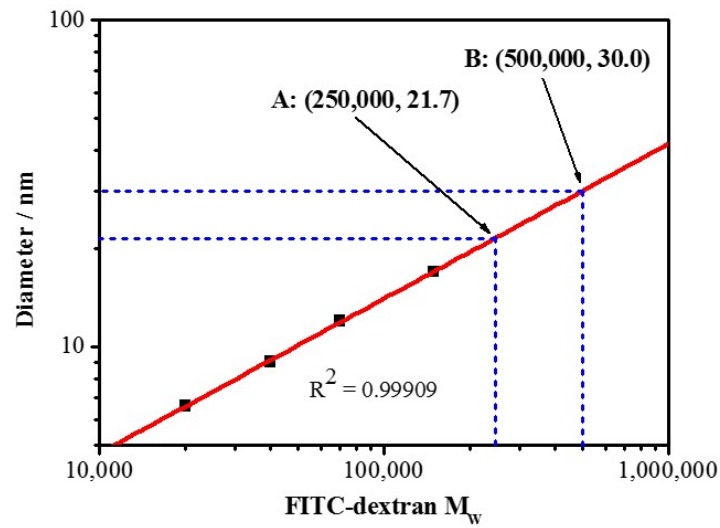


Figure 6.10. Log-log plot of hydrodynamic diameter against different molecular weights, M_w , of FITC-dextran in PBS buffer. The plot is fitted linearly (adjusted $R^2 = 0.99909$), in agreement with the predicted power relationship of the hydrodynamic radius, R_h , with the number of monomers, N , in a polymer chain, $R_h \propto N^{-\nu}$.¹ The exponent, ν , is determined by the polymer and the solvent.

Table 6.2. Hydrodynamic diameters of FITC-dextran of different M_w

	Molecular weight M_w	Hydrodynamic diameter D_h [nm]
Data from supplier	20,000	6.6
	40,000	9.0
	70,000	12.0
	150,000	17.0
Data from fitted line	250,000	21.7
	500,000	30.0

The hydrodynamic diameters of FITC-dextran is obtained from Product Information from Sigma-Aldrich, of molecular weights of 20,000, 40,000, 70,000, and 150,000.² In literatures the log-log plot of R_h against M_W has been demonstrated linear from $M_W = 10,000$ to 2000,000, and the hydrodynamic diameters read from the fitted line is listed in table 6.2 and matches extraordinarily well with the reported data.^{3,4}

Mesh size measurement via FITC-dextran diffusion

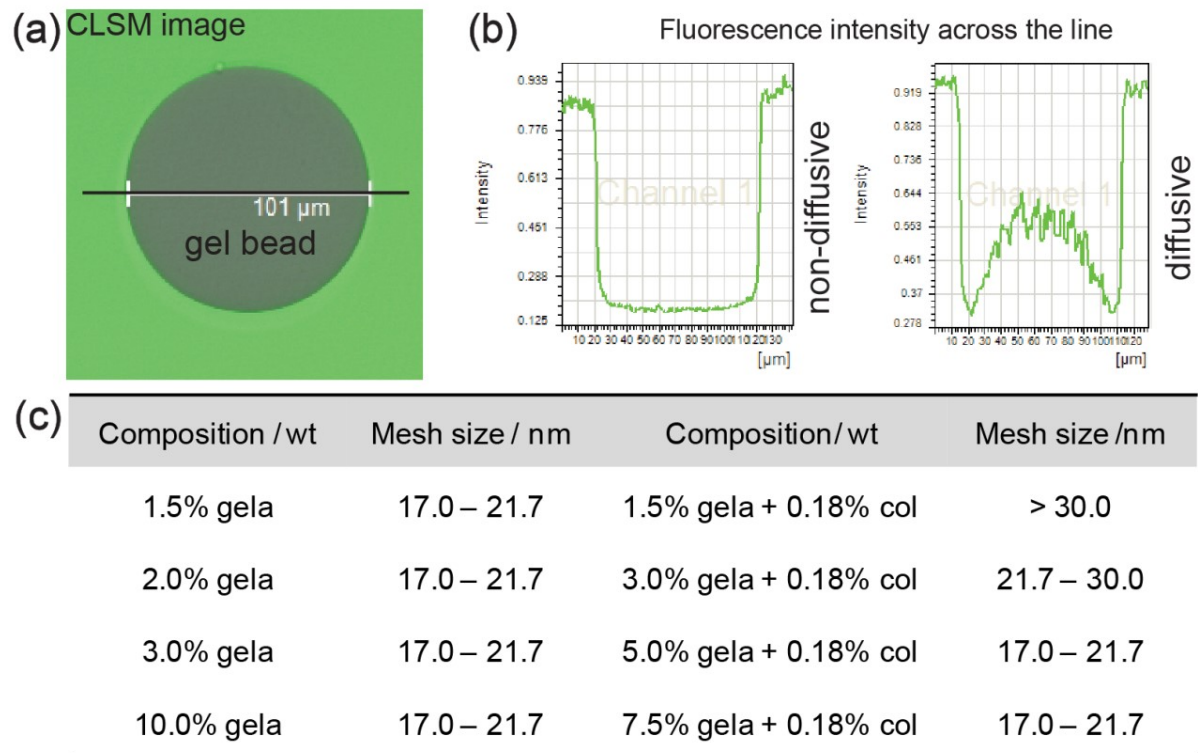


Figure 6.11. (a) CLSM image of a gelatin bead immersed in FITC-dextran (150S) PBS solution; (b) normalized quantified fluorescence across the line in (a) of a "non-diffusive" bead and a "diffusive" bead; (c) list of mesh size of gelatin and col-gela beads at different gelatin concentrations.

Mesh size is a critical parameter in biodegradable hydrogels as it determines the diffusion of nutrients, grow factors, metabolites and facilitates cell migration.^{5,6} Preliminary characterization of the mesh size in gelatin beads is carried out by measuring the

fluorescence diffusion of FITC-dextran at different molecular weights ranging from 40,000 to 500,000 (abbreviated as 40S and 500S, respectively) corresponding to hydrodynamic diameters between 9.0 nm and 30.0 nm (Figure 6.10 and Table 6.2). The mesh sizes were estimated by determining the cut-off size at which dextran no longer diffused into the gel beads. As shown in Figure 6.11c, all gelatin beads concentrated from 1.5 wt% to 10.0 wt% of gelatin gave mesh size in the range of 17.0 nm to 21.7 nm. The addition of collagen increased the mesh size to 21.7 - 30.0 and > 30.0 nm for beads containing 3.0 and 1.5 wt% gelatin, respectively, which is attributed to larger mesh size, in microns range, of the collagen matrix.⁷

Swelling ratio

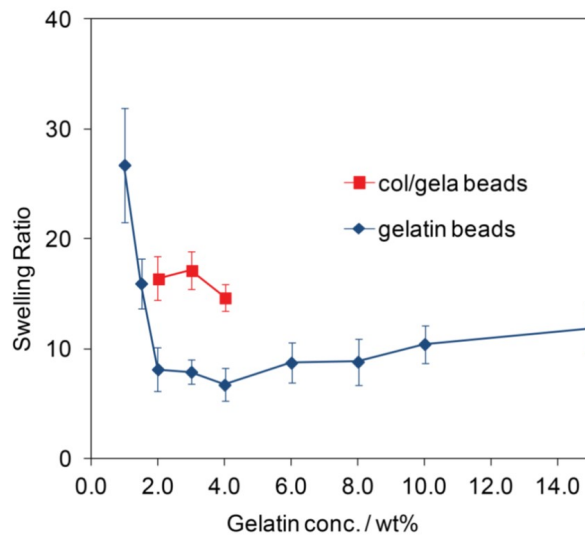


Figure 6.12. Swelling ratios of gelatin beads and col-gela beads at different gelatin concentrations. Beads were crosslinked for 4.5 min and blended with 0.18 wt% collagen.

Flory-Rehner theory

Based on the swelling theory originally developed by Flory and Rehner^{8,9} we calculated the mesh size of gelatin hydrogel beads using the following equations. Generally, the

molecular weight between two adjacent crosslinks, \bar{M}_c , can be related to the molecular weight of the polymer, \bar{M}_n , and the polymer volume fraction in swollen state, $\nu_{2,s}$ (the inverse of the swelling ratio), as

$$\frac{1}{\bar{M}_c} = \frac{2}{\bar{M}_n} + \frac{\bar{v}}{V_1} \frac{\ln(1 - \nu_{2,s}) + \nu_{2,s} + \chi_1 \nu_{2,s}^2}{\nu_{2,s}^{1/3} - \nu_{2,s}/2} \quad (6.4)$$

with \bar{v} being the specific volume of the polymer, V_1 the molar volume of water and χ the Flory-Huggins interaction parameter. The mesh size, ξ , can be obtained from

$$\xi = \nu_{2,s}^{-1/3} \left(\frac{2C_n \bar{M}_c}{M_r} \right)^{1/2} l \quad (6.5)$$

Here, C_n is the Flory characteristic ratio, M_r the molecular weight of the repeating units and l the length of the bond along the polymer backbone.¹⁰ For large chains C_n equals a limiting value C_∞ , which can be calculated from the persistence length, l_p :

$$l_p = (C_\infty + l) \frac{l_s}{2} \quad (6.6)$$

Here, l_s is the linear segment length.¹¹

Since the Flory-Rehner theory as presented above is strictly valid only for simple systems like vinyl polymers, some modifications have to be made and constants are to be chosen with care. First, the factor 2 in equation 6.5 has to be replaced by factor 3 because the repetitive unit already consists of 2 bonds (instead of 1 like for vinyl polymers). Second, l is the arithmetic mean of one C-C bond and two C-N bonds. Third, M_r is the mean molecular weight as calculated on the basis of the typical amino acid composition of the used gelatin. Last, the segment length is taken as the sum of one C-C bond and two C-N bonds. All values are listed in Table 6.3.

Table 6.3. Parameters and given values in above equations

Constant	Abbreviation	Value	Reference
Specific volume	\bar{v}	0.741 cm ³ /g	[12]
Flory-Huggins parameter	χ	0.497	[12]
Mol. weight of repeating unit	M_r	94.7 g/mol	Calc. after [12]
Persistence length	l_p	20 Å	[12]
C(carbonyl)-C bond length		1.53 Å	[13]
C(carbonyl)-N bond length		1.32 Å	[13]
C-N bond length		1.47 Å	[13]
Flory characteristic ratio	C_∞	8.26	Calc.

The value for C_∞ we calculate for gelatin compares well with characteristic ratio values for other polypeptides reported in literature.¹⁴ The overview of the swelling ratios and therefore the calculated mesh for a fixed crosslinking time (4.5 min) is given in the main text Table 6.1.

The Flory-Rehner theory assumes a rather ideal picture of crosslinked polymers. Yet, we find good agreement with experimentally determined mesh size over a large range of concentrations. This could be an effect of the presence of triple-helices. Their amount was reported to be almost independent of concentration between 2 and 8% of gelatin.¹⁵ The helices introduce order into the network making it more comparable to the theoretical model. For very low concentrations close to or even below the gelling limit of gelatin^{16,17} only few or no helices are formed. Therefore, swelling is enhanced but the experimentally determined mesh size is more influenced by entanglements, loops or dangling chains which accounts for the discrepancy with the theoretical values.

3T3 fibroblast viability compartmentalized in col-gela beads

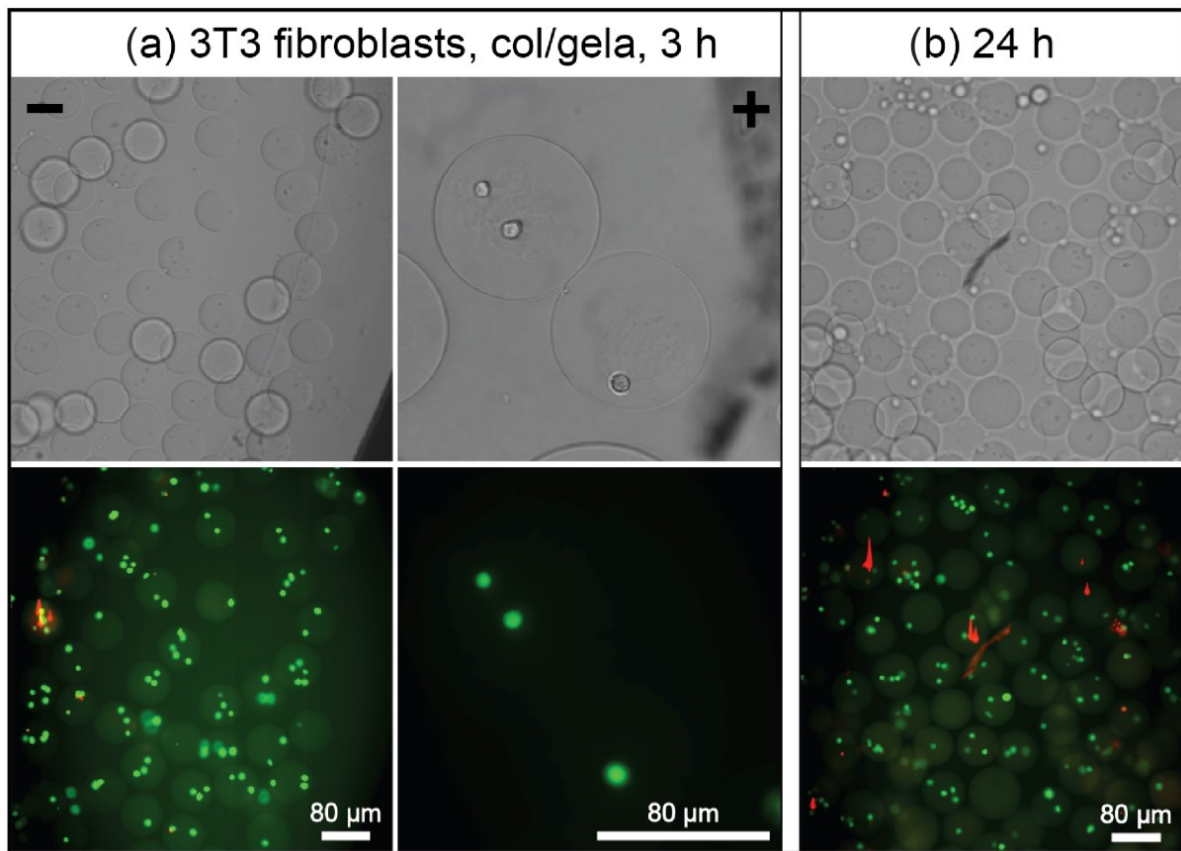


Figure 6.13. Bright field images (above) and the corresponding fluorescence images (below) of 3T3 fibroblasts in col-gela beads (4.0 wt% gelatin with 0.18 wt% collagen, 8.0 min crosslinking, 2.6×10^6 cells/mL) over 24 hrs. Cells were stained with *Live/Dead Viability/Cytotoxicity kit*, indicating live (green) and dead (red) cells after different culture time.

References

- (1) Teraoka, I., *Polymer Solutions: An Introduction to Physical Properties*; John Wiley & Sons: 2002; Vol. 3, pp 184–188.
- (2) Aldrich, S. Product Information., http://www.sigmaaldrich.com/etc/medialib/docs/Sigma/Product_Information_Sheet/1/fd250spis.Par.0001.File.tmp/fd250spis.pdf.
- (3) Armstrong, J. K.; Wenby, R. B.; Meiselman, H. J.; Fisher, T. C. *Biophysical Journal* **2004**, *87*, 4259–4270.
- (4) Pluen, A.; Boucher, Y.; Ramanujan, S.; McKee, T. D.; Gohongi, T.; di Tomaso, E.; Brown, E. B.; Izumi, Y.; Campbell, R. B.; Berk, D. A.; Jain, R. K. *Proceedings of the National Academy of Sciences of the United States of America* **2001**, *98*, 4628–4633.
- (5) Slaughter, B. V.; Khurshid, S. S.; Fisher, O. Z.; Khademhosseini, A.; Peppas, N. A. *Advanced Materials* **2009**, *21*, 3307–3329.
- (6) Nicodemus, G. D.; Bryant, S. J. *Tissue Engineering Part B-Reviews* **2008**, *14*, 149–165.
- (7) Yang, Y.-l.; Kaufman, L. J. *Biophysical Journal* **2009**, *96*, 1566–1585.
- (8) Flory, P. J.; Rehner, J. *The Journal of Chemical Physics* **1943**, *11*, 521–526.
- (9) Flory, P. J. *Journal of Chemical Physics* **1950**, *18*, 108–111.
- (10) Peppas, N. A.; Bures, P.; Leobandung, W.; Ichikawa, H. *European Journal of Pharmaceutics and Biopharmaceutics* **2000**, *50*, 27–46.
- (11) Cantor, C. R.; Schimmel, P. R., *Biophysical Chemistry, Part 3. The Behavior of Biological Macromolecules*; W. H. Freeman and Co.: 1980.
- (12) Mark, J. E., *Polymer Data Handbook*; Oxford University Press: 1999.
- (13) Corey, R. B.; Pauling, L. *Proceedings of the Royal Society Series B-Biological Sciences* **1953**, *141*, 10–20.

- (14) Brant, D. A.; Flory, P. J. *Journal of the American Chemical Society* **1965**, *87*, 2788–&.
- (15) Joly-Duhamel, C.; Hellio, D.; Djabourov, M. *Langmuir* **2002**, *18*, 7208–7217.
- (16) Sanwlani, S.; Kumar, P.; Bohidar, H. B. *Journal of Physical Chemistry B* **2011**, *115*, 7332–7340.
- (17) Bohidar, H. B.; Jena, S. S. *Journal of Chemical Physics* **1994**, *100*, 6888–6895.

7

Artificial microniches for probing mesenchymal stem cell fate in 3D

Yujie Ma, Martin P. Neubauer, Julian Thiele, Andreas Fery and Wilhelm T. S. Huck;
Biomaterials Science **2014**, 2:1661-1671. Reproduced by permission of The Royal Society of Chemistry.

Abstract

Droplet microfluidics is combined with bioorthogonal thiol-ene click chemistry to fabricate micrometer-sized, monodisperse fibrinogen containing hyaluronic acid hydrogel microbeads in a mild, radical-free procedure in the presence of human mesenchymal stem cells (hMSCs). The gel beads serve as microniches for the 3D culture of single hMSCs as they contain fibrinogen for cell surface binding, they are porous and stable in tissue culture medium for up to 4 weeks with mechanical properties right in the range of soft solid tissues (0.5-12 kPa). The encapsulation procedure results in 70% viable hMSCs in the microbeads after 24 hours of culture and a very high degree of viability of the cells after long term culture of 2 weeks. hMSCs embedded in the microniches display an overall rounded morphology, consistent with those previously observed in 3D culture. Upon induction, the multipotency and differentiation potential of the hMSCs are characterized by staining of corresponding biomarkers, demonstrating a clear heterogeneity in the cell population. These hydrogel microbeads represent a versatile microstructured materials platform with great potential for studying the differences of materials cues and soluble factors in stem cell differentiation in a 3D tissue-like environment at the single cell level.

Introduction

Mesenchymal stem cells (MSCs) that can be isolated from a wide variety of tissues¹ hold great potentials in regenerative medicine in delivering new therapies for many diseases.² It is well-known that MSCs can differentiate into various tissue specific lineages ranging from neurons to osteoblasts,¹ which may reflect their interactions with their microenvironment or the so called stem cell niche.³ The stem cell niche provides multiple effectors to modulate stem cell fate decision including soluble growth factors, the extracellular matrix (ECM) and biochemical signals through cell-cell contact with neighboring cells.⁴ In response, cells actively interact with the ECM and remodel the niche they reside in.² In order to understand this complex regulatory network, advanced cell culture platforms are being developed. Pioneering work by Discher *et al.* showed the crucial effect of substrate

elasticity in directing MSC fate on 2 dimensional (2D) polyacrylamide gels.⁵ However, three dimensional (3D) cell culture is gaining popularity as it mimics the natural 3D tissue organization more closely.^{6,7} Hydrogels have become the prime candidate for this purpose due to their ability to mimic many aspects of natural ECM including high water content, tissue-like mechanical properties and adjustable functionalities.^{8,9} A vast range of hydrogels based on synthetic as well as naturally-derived materials, or combinations thereof has been utilized to study MSC-matrix interactions in 3D in bulk, with control over several important parameters such as matrix mechanics^{10,11} and biodegradability.¹² However, it is very difficult to separate chemical cues such as material properties (chemical composition, biocompatibility, stiffness, and porosity) from biological cues, for example those originating from cell-cell interactions, using these bulk hydrogel cell culture models. Moreover, bulk studies lack the resolution necessary to reveal cellular heterogeneity.^{13,14} It is important to understand the signalling mechanisms mediating different stem cell responses at a single cell resolution.² Therefore, novel *in vitro* ECM models targeting single cell studies are needed for obtaining an in-depth knowledge on the molecular mechanisms of stem cell/matrix modulation.

Micrometer-sized hydrogel microbeads are suitable model systems for the study of 3D cell culture at a single cell level. Recent advances in droplet microfluidics have facilitated the fabrication of uniform, monodisperse cell-laden hydrogel microbeads with precise control over their size, composition and material properties in a high throughput fashion.¹⁵⁻²⁴ In this method, water-in-oil emulsions with cell containing hydrogel precursor solutions as the aqueous phase are first generated microfluidically, and then solidified/cross-linked to form hydrogel microbeads. The obtained microbeads are usually transferred to the aqueous phase for further culturing the cells. Many examples on the successful incorporation of cells in microfluidically generated hydrogel microbeads with preserved cell viability have been shown in recent years. However, all the studies carried out so far were based on simple cell models such as fibroblasts with relatively short periods of culture time (a few days). It is therefore difficult to extend these existing methods to the study of MSCs, which require prolonged period of time for a clear identification of their lineage

commitment. With preserving cell viability as the major consideration, mild gelation conditions are preferred. This means that the crosslinking reactions involved should be bio-orthogonal, non-toxic, relatively fast at or below 37 °C and preferably free from radicals.¹⁹ Hence, the material selection is rather limited for generating cell-laden hydrogel microbeads using droplet microfluidics, and most of the cell-laden hydrogel microbead systems reported so far lack the presence of certain cell-binding moieties (*e.g.* RGD sequences) that are believed to be crucial for the establishment of proper cell-matrix interactions.^{8,12,25,26} The fabrication of single MSC-laden hydrogel microbeads based on mild bio-orthogonal cross-linking strategies with full control over cross-linking kinetics, hydrogel mechanical characteristics and desired/tuneable cell-binding functionalities while maintaining a high MSC viability at the same time thus remains a challenge.

Here, we report on the encapsulation of human MSCs (hMSCs) into fibrinogen functionalized hydrogel microbeads based on the naturally derived polysaccharide hyaluronic acid (HA) that are cross-linked through bio-orthogonal thiol-ene chemistry²⁷ using droplet microfluidics. HA is an essential component of the ECM and is involved in many biological processes. It is biodegradable and can be modified to present a variety of functionalities and has been a popular choice for biomedical applications including those involving MSCs.²⁸ In the current study, thiol-modified HA is used (HASH, Figure 7.1A).

Since the introduction of HASH about a decade ago,²⁹ it has been shown to be an excellent hydrogel base material as it allows both accurate control over hydrogel elasticity and easiness of ligand presentation.³⁰ A particularly attractive chemical feature of HASH for encapsulating sensitive biological substances such as cells is that it can be cross-linked in an extremely mild fashion due the formation of di-sulfide bridges by itself or through thiol-ene click reaction with biocompatible/bio-inert bi- or multi-functional cross-linkers such as poly(ethylene glycol) diacrylate (PEG-DA)^{31,32} entirely radical-free. However, di-sulfide hydrogels are not very stable, especially under some reductive cell culture conditions and HASH-diacrylate hydrogels have been shown to be susceptible to hydrolysis.³⁰ For these reasons, we chose to use PEG di-vinylsulfone (PEG-DVS) as a cross-linker for HASH. The hydrogel is further decorated with fibrinogen (FBNG), the fibrin-forming

protein that provides natural binding sites for cell surface integrins,³³ through specific HA-FBNG interactions. We first demonstrate the fabrication of FBNG-HASH-PEG hydrogel microbeads by droplet microfluidics with controlled composition, gelling conditions, tunable mechanical properties and sufficient porosity. Next the encapsulation of hMSCs in these microbeads, their long term culture and explorations on their differentiation at a single cell level are described. We show that the FBNG-HASH-PEG hydrogel microbead platform presents great promise in supporting the long-term culture of hMSCs and studying their differentiation in a 3D microenvironment.

Materials and methods

General experimental details

All reagents and chemicals were used as received unless otherwise specified. Dialysis was performed using Spectra/Por[®] dialysis membranes (M_W cut-off: 3500 g/mol). To determine the exact channel height of the channel network fabricated in SU-8 (Micro Resist Technology GmbH, Germany) *via* photolithography, differential interference contrast (DIC) microscopy was performed on a Wyco NT1100 optical profiler (Bruker, USA). Bright-field microscopy imaging was performed on an IX71 microscope (Olympus) equipped with a 10x objective (air) and a Phantom MIRO high-speed camera (Vision Research Inc., USA). Confocal microscopy measurements were performed using a Leica SP2 (Leica, Germany) confocal laser scanning microscope (CLSM). Rheology measurements were performed on a TA rheometer (TA Discovery HR-1 hybrid Rheometer, New Castle, USA) with a parallel plate (diameter 40 mm) geometry. A fixed oscillation frequency of 1 Hz was used in all time sweep experiments, which was checked by a frequency sweep measurement from 0.1 Hz to 10 Hz to be in the rubber plateau region. The excitation/emission wavelengths of the fluorophores used are: fluorescein isothiocyanate (FITC) and Alexa 488 (488 nm/500-575 nm); DAPI (405 nm/420-500 nm); rhodamine dyes (561 nm/580-650 nm); calcein (488 nm/500-550 nm); EthD-1 (514 nm/580-650 nm).

Synthesis of thiolated hyaluronic acid

Thiolated hyaluronic acid was synthesized following a modified procedure as previously reported by Prestwich and coworkers.²⁹ Briefly, 250 mg low molecular weight hyaluronic acid (sodium salt, $M_W \sim 50000$ g/mol Lifecore) was dissolved in 25 mL MES buffer (pH 4.75), and 50 mg PDPH (Thermo Scientific) and 300 mg 1-ethyl-3-(3-dimethylaminopropyl)carbodiimide (EDC) was added sequentially as solids. The reaction was carried out with stirring at room temperature for at least 2 hours. The solution was dialyzed against MilliQ to remove excess reactants. Afterwards 100 mg tris(2-carboxyethyl) phosphine (TCEP) was added and the reaction mixture was stirred at room temperature for another 2 hours. The solution was extensively dialyzed and, in a final step, lyophilized to give thiolated hyaluronic acid as a white solid. The degree of thiolation was measured by ¹H NMR (Spectrum is shown in Supporting Information Figure 7.8) and Ellman's test³⁴ to be approximately 25%.

Synthesis of rhodamine labelled fibrinogen

Fibrinogen (FBNG) was dissolved in sodium carbonate/bicarbonate buffer (100 mM, pH 9) at a concentration of 10 mg/mL. A 1 mg/mL rhodamine B isothiocyanate (RBITC) solution in DMSO was mixed with the above FBNG solution to reach a final RBITC concentration of 60 μ g/mL. The reaction mixture was gently stirred for 2 hours at room temperature in the dark. The excess of RBITC was removed by centrifuge filter units (Amicon Ultra, 10 kDa, Millipore) followed by extensive washing with PBS and centrifugation at 1500 g, until the eluent was colorless. The obtained RBITC-FBNG was stored at room temperature in the dark for up to five days.

Microfluidic device fabrication and general microfluidic experimental setup

Microfluidic devices were fabricated using combined photo and soft lithography in poly (dimethylsiloxane) (PDMS) (Dow Corning, Germany).³⁵ A negative photoresist (SU-8

25 or SU-8 50, Microchem Co., USA) was spin-coated onto the polished site of a 2-inch silicon wafer (SI-MAT, Germany). A mask aligner (MJB3, Suss MikroTec, Germany) was used to impart the microchannel structure of a transparent photomask (JD Phototools, UK) into the photoresist. We optimized the master device fabrication employing DIC microscopy to obtain microchannels with a very uniform height of 100 μm . The channel width at the droplet forming flow-focusing nozzle was 100 μm . A PDMS replica of the channel design was formed by mixing the PDMS oligomer and cross-linker in a ratio of 10:1 (w/w) and curing the homogeneous, degassed mixture at 65 °C for at least 60 min. Thereafter, access ports were bored into the soft replica with a biopsy needle (outer diameter: 1.0 mm, Pfm, Medical Workshop, USA), and the PDMS replica was bonded to a glass slide after oxygen plasma treatment. The bonding process was completed in an oven at 90 °C for approximately 1 h. Microfluidic devices were connected to high-precision, positive displacement syringe pumps (neMESYS, Cetoni, Germany) *via* PTFE tubing (inner diameter: 0.56 mm, outer diameter: 1.07 mm, Novodirect, Germany).

Diffusion studies on hydrogel microbeads

The obtained hydrogel microbeads with varying compositions were dispersed in a fluorescein isothiocyanate-dextran (FITC-dextran, M_W 2M g/mol) solution (50 $\mu\text{g}/\text{mL}$) in PBS and incubated at 4 °C for overnight. Subsequently, confocal fluorescence images and differential interference contrast (DIC) images were taken on the equilibrated dispersion on a Leica SP2 confocal laser scanning microscopy. Fluorescence signal detected from inside the hydrogel microbeads were used to indicate gel permeability.

2D cell culture

Human mesenchymal stem cells (MSCs) were thawed from cryopreservation (10% DMSO) and cultured in Dulbecco's Modified Eagle's Medium (DMEM) low glucose (1 g/L) media supplemented with 10% fetal bovine serum (MSC approved FBS; Invitrogen), and 1% penicillin/streptomycin (p/s). The medium was changed every 3 days and cells were

passaged at nearly 80% confluency using 0.25 mg/mL trypsin:EDTA (Lonza, Switzerland). hMSCs of passage 6 were used for the microfluidic encapsulation experiments.

Fabrication of cell-laden hydrogel microbeads

Thiolated hyaluronic acid (HASH), poly(ethylene glycol) divinylsulfone (PEG-DVS, JenKem, M_W 5000 g/mol), and fibrinogen from bovine plasma (Sigma Aldrich) was dissolved in autoclaved PBS buffer at desired concentrations. All the materials handling was performed in sterile laminar flow hoods and steriled filtered with 0.2 μm filter units when necessary. Human hMSCs were mixed with HASH and fibrinogen at a final concentration of 1 million cells/mL and the mixture was injected into a microfluidic flow-focusing device as one of the inner phases, which was sent together with PEGDVS solution as the second inner phase. Fluorinated oil (HFE 7500, 3M) containing 2% (w/w) of home-made triblock copolymer surfactant (Krytox-Jeffamine-Krytox) as the outer phase.^{13,22} The flow rates were set to 1200 $\mu\text{L}/\text{h}$ for the outer phase and 200 $\mu\text{L}/\text{h}$ for each of the inner phases. The emulsion was collected in an Eppendorf tube covered with Parafilm and subsequently incubated on a thermo shaker at 37 °C for max. 20 min to complete the thiol-ene crosslinking reaction. Hydrogel microbeads were obtained by breaking the emulsion with 1H,1H,2H,2H-perfluoro-1-octanol (20% v/v in HFE 7500) and immediately transferring the microbeads into PBS.³⁶ The hydrogel microbead suspension was washed two times with autoclaved PBS, and one time with hMSC proliferation medium; each time followed by centrifugation at 300g for 10 min.

Micromechanical characterization

The Young's modulus E of the hydrogel microbeads was obtained by measuring force-displacement curves on an atomic force microscope (AFM, Nanowizard I, JPK Instruments, Germany) with spherical glass probes (with a radius of $\sim 23 \mu\text{m}$) coated with poly(L-Lysine)-g-PEG, combined with an inverted optical microscope (Axiovert 200, Zeiss, Germany), as previously reported.²¹ The spring constant of the utilized cantilever was 0.0281 N/m for soft beads (with HASH concentrations of 0.75% and 1.0%) and

0.5216 N/m for stiffer beads (with HASH concentrations of 1.5% and 2.0%). All the measurements were carried out at room temperature in PBS. The force-deformation curves were obtained by correcting the original force-displacement data for cantilever bending, which were fitted by the Hertz model to yield corresponding E values. From each batch at least 20 different beads were measured to obtain statistically significant mean values.

3D culture of hMSCs in hydrogel microbeads and lineage analysis

hMSC-laden hydrogel microbeads were dispersed in hMSC proliferation medium and incubated at 37 °C (5% CO₂) for 24 hours before the medium is replaced with a 1:1 combination of osteogenic and adipogenic chemical supplements. With each change of medium, the hydrogel microbeads were collected by centrifugation at 300g for 10 min. After a certain periods (7-14 days) in culture, lineage specification was assessed by *in-situ* staining for alkaline phosphatase (ALP) activity (osteogenic biomarker) and neutral lipid accumulation (functional adipogenesis biomarker) in separate samples. The hydrogel microbeads were first fixed with 4% paraformaldehyde (PFA) in PBS, then washed 2x with PBS before they were embedded in a thin layer of secondary hydrogel made of agarose (2% in PBS) inside Lab-Tek chamber slides (8 wells, Thermo Scientific Nunc). The chamber slides were subsequently kept at 4 °C for at least 1 h for the agarose to solidify. ALP activity was visualized by Fast Blue staining (500 µg/mL naphthol-AS-MSC phosphate, NAMP and 500 µg/mL Fast Blue BB, Sigma) in alkaline buffer (100 mM Tris-HCl, 100 mM NaCl, 0.1% Tween-20, 50 mM MgCl₂, pH 8.2) and incubation at 37 °C (5% CO₂) for 1 h. Accumulated oil droplets in cells were stained by Oil Red O (ORO, 600 µg/mL in isopropanol) at room temperature for 1 h. Color images were acquired on a Zeiss inverted microscope fitted with a Coolsnap 5M color camera (Photometrics, USA). Cells with/without specific markers were counted manually. On average, 400-500 beads were collected in each well, out of which approximately 500 cell-containing beads were counted in total to obtain the statistics.

Live/dead, cytoskeleton and nuclear morphology staining

hMSC-laden hydrogel microbeads were cultured in proliferation medium, washed and suspended in PBS and mixed with Live/Dead Viability/Cytotoxicity kit for mammalian cells (Invitrogen) at room temperature for 1 h at different time points for viability evaluations for short (24 hours) and long terms (14 days). A final concentration of calcein AM of 2 μ M and ethidium homodimer-1 (EthD-1) of 4 μ M was used. The live/dead stained samples were imaged on Leica SP2 confocal laser scanning microscopy with a 10x objective.

Cytoskeletal and nuclear morphology of encapsulated live cells were stained 24 hours after encapsulation. All representative images were taken from the axial plane showing the largest cross-sectional area. F-actin was stained with TRITC-phalloidin (Actin Cytoskeleton/Focal Adhesion Staining Kit, Millipore, 1:1000) and nuclear morphology with 4,6-diamidino-2-phenylindole (DAPI, Actin Cytoskeleton/Focal Adhesion Staining Kit, Millipore, 1:1000) at room temperature for 1 h. Images were taken with a Leica SP2 confocal laser scanning microscopy (Leica, Germany) with a 63x oil objective.

Immunostaining

After induced differentiation (from the start of culture in 1:1 combination of osteogenic and adipogenic differentiation medium) for 7 days, the hMSC-laden hydrogel microbeads were washed with PBS and fixed with 4% paraformaldehyde (PFA)/PBS solution for 10 min at room temperature, washed with PBS and permeabilized using 0.2% Triton-X100/PBS solution for 10 min at room temperature. After extensive washing in PBS, the microbeads were blocked with BSA in PBS (10 mg/mL) for 1 h at room temperature. Afterwards the beads were incubated with Mouse anti-STRO-1 antibody³⁷ (Invitrogen, 1:100 dilution with 10 mg/mL BSA) for 8 hours at 4 °C, washed with PBS (3x), then incubated with secondary Alexa Fluor-488 Goat Anti-Mouse IgG antibody (Invitrogen, 1:200 dilution with 10 mg/mL BSA) for 1 h at room temperature and washed to visualize multipotency biomarkers. DAPI was included in the secondary antibody solution to

counter-stain the nuclei. Images were taken with a Leica SP2 confocal laser scanning microscopy (Leica, Germany) with a 20x objective.

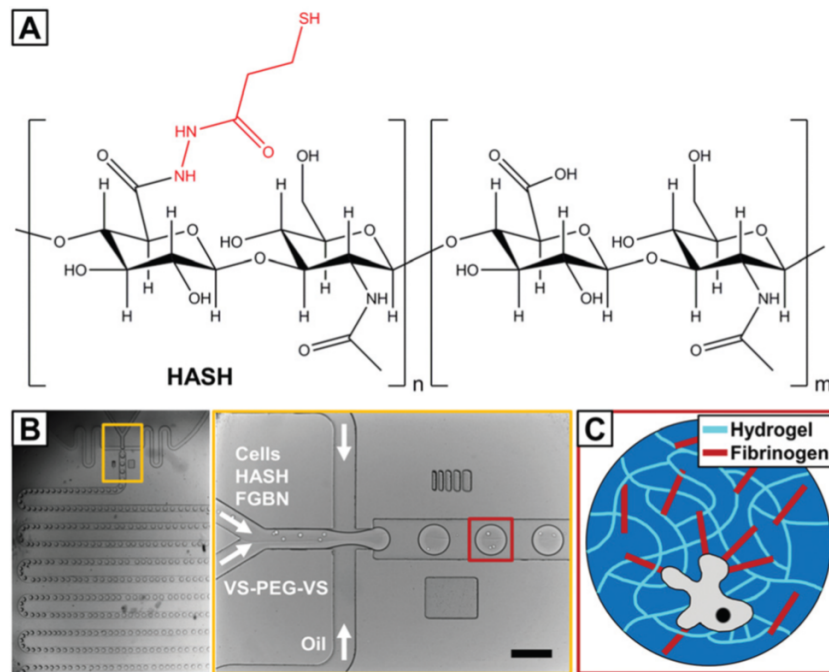


Figure 7.1. Microfluidic fabrication of hydrogel based microniches for the 3D culture of single human mesenchymal stem cells (hMSCs): (A) Chemical structure of the major components of the hydrogel precursors: thiolated hyaluronic acid (HASH) used in this study. Thiol functional groups were randomly incorporated in the polymer structure with a degree of substitution of 25%. (B) Microfluidic fabrication of water-in-oil droplets templating hydrogel formation using a flow-focusing device with double inlets and meander mixing channels (inset) for the aqueous phase with hydrogel precursors, cells and fibrinogen (FBNG) and one inlet containing the oil phase. (C) Schematic illustration of the obtained cross-linked network of the hydrogel microbeads containing fibrinogen as additional hMSC binding sites. The scale bar denotes 100 μm .

Results and discussion

Bulk hydrogel mechanical properties and gelling kinetics

As mentioned earlier, matrix mechanics is an important parameter directing hMSC fate. In order to realize a fine-tuning of hydrogel elasticity, the gelling properties of HASH and PEG-DVS with varying concentration combinations in the presence of a fixed concentration of FBNG (1 mg/mL) were studied in detail by rheology with a parallel plate geometry. In all the experiments, HASH with a fixed degree of thiolation (20%) and PEG-DVS with a fixed M_W of 5000 g/mol were used. The reaction was carried out in PBS with a physiological pH value of 7.4 without any additional catalyst or trigger. It should be mentioned that we chose to use PEG-DVS as the crosslinking agent for hMSC encapsulation due to the fact that hydrogel microbeads of similar size obtained through HASH-PEGDA crosslinking degraded within a few days, and thus were not suitable for the long-term culture of hMSCs (unpublished data). This is most likely due to the hydrolysis of the ester bond formed during crosslinking, which appeared to be more pronounced in hydrogels in a microbead format with its higher surface to volume ratio than in bulk. However, this combination may be useful for applications directed at controlled release of living cells.²⁰ Time-dependent rheology measurement provides important information on the bulk gelling kinetics and the final modulus of HASH-PEGDVS-FBNG hydrogels. As shown in Figure 7.2, the maximum storage modulus G' (the plateau region in the curves, measured at a fixed oscillation frequency of 1 Hz) of HASH-PEGDVS-FBNG hydrogels with a fixed concentration of FBNG (1 mg/mL) increases with increasing the concentration of HASH and PEGDVS in a nearly linear fashion (Figure 7.2 inset). The elastic modulus or Young's modulus E , which is an important parameter in describing hydrogel mechanical properties can be calculated based on the following equation:

$$E = 2G'(1 + \nu) \quad (7.1)$$

Where ν is Poisson's ratio. For rubber-like elastic materials, a ν value of ~ 0.5 can be assumed.³⁸ Combined with the above equation and the obtained G' values, E values of

the HASH-PEGDVS-FBNG hydrogels we measured are in the range of 0.1 - 13.5 kPa; well in the range of elasticity of solid tissues.⁵ It should be stressed that the degree of thiolation is another parameter that can still be adjusted, which should in turn provide a broader range for tuning the matrix stiffnesses.

An accurate determination of the gelation time is of great importance for the reliable fabrication of hMSC containing microbeads, as the duration between harvesting cells from 2D culture flasks and re-suspending cell-laden hydrogel microbeads in tissue culture medium should be minimized. The gel point t_c was estimated from rheological measurements as the point where the storage modulus (G') started to increase much more sharply than the loss modulus (G''), marking the transition from liquid-like to solid-like behavior (see examples in the Supporting Information Figure 7.9). Table 7.1 summarizes the gel point of the HASH-PEGDVS-FBNG hydrogels with varying HASH/PEGDVS concentrations. Clearly the gel point decreases with increasing the overall polymer concentration, indicating faster crosslinking kinetics with a higher concentration of functional groups. It is noteworthy that even with the lowest polymer concentration used in our study (0.75% HASH), the gelation was fast (30 min) at room temperature. The gelling time can be further reduced by increasing the gelling temperature, for example to 37 °C (Supporting Information Figure 7.9). In the droplet experiment we used the time at which the gel reached its highest/plateau modulus as a guide for the time required for incubation, after which the emulsion was broken and the beads were transferred into tissue culture medium (*vide infra*).

Fabrication of hMSC-laden hydrogel microbeads

The hMSC-laden hydrogel microbeads were fabricated in a two-step procedure. First, freshly harvested hMSCs together with hydrogel precursors in PBS buffer were prepared and subsequently injected separately into a microfluidic flow-focusing device with three inlets for microdroplet generation. As shown in Figure 7.1C, the continuous oil phase

Table 7.1. Composition and gelling kinetics of HASH-PEGDVS-FBNG hydrogels.

Sample	HASH [mg/mL]	PEGDVS [mg/mL]	FBNG [mg/mL]	t_c @ 25 °C [min]
1	7.5	12.5	1.0	30
2	10.0	16.7	1.0	15
3	15.0	25.0	1.0	7.5
4	20.0	33.3	1.0	7.5

consisted of a fluorinated oil (HFE 7500) containing 1% (w/w) of a biocompatible surfactant (Krytox-Jeffamine-Krytox A-B-A triblock copolymer).^{13,22} The dispersed, aqueous phase was comprised of two separate streams that met at the flow-focusing junction with one containing HASH of varying concentrations, cells and FBNG as the cell-binding ligand, and the other one containing PEG-DVS of matching concentrations as the crosslinking agent. The final concentrations of HASH were varied between 0.75% and 2%. With a fixed FBNG concentration of 1 mg/mL, the PEG-DVS was mixed in with a concentration aiming at the full conversion of the thiol functional groups (see Table 7.1). After their production, microdroplets flowed through a long, meander channel (See the inset of Figure 7.1B) for a thorough mixing of the components before they were collected in sterile Eppendorf tubes. The number of cells in each droplet roughly follows a Poisson distribution,³⁶ with slight deviations due to non-specific clustering of the cells. Approximately 30% of the microbeads obtained contained a single cell and the rest of the beads contained either no cells or multiple cells (probability values and corresponding calculations are presented in the Supporting Information Figure 7.12 and related text). Subsequently, these hMSC encapsulated hydrogel precursor droplets were gelled at 37 °C for a short period of time (<20 min) before they were washed and transferred into tissue culture medium for the 3D culture of the cells. The average size of the obtained hydrogel microbeads was around 150 μm . A typical transmission microscopy image of a hMSC-laden HASH-PEGDVS-FBNG microbead sample is shown in Figure 7.3A.

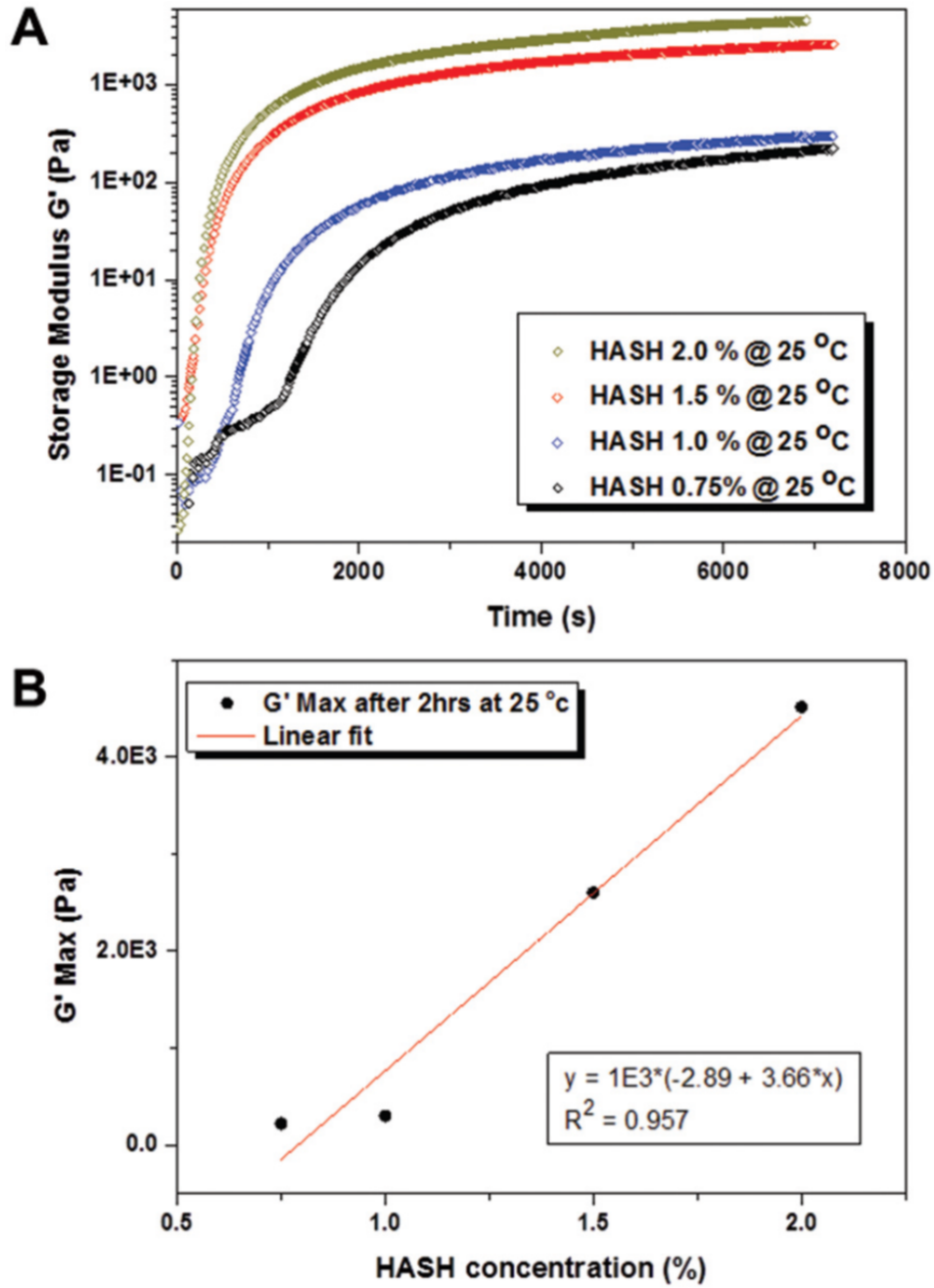


Figure 7.2. (A) Time-dependent rheological measurements on bulk hydrogels made from varying concentrations of thiolated hyaluronic acid (HASH) (corresponding PEGDVS and FBNG concentrations used are listed in Table 7.1) at 25 °C. (B) The linear increase of plateau storage modulus (G') with increasing HASH concentrations.

Chemical and physical characteristics of HASH-PEGDVS-FBNG hydrogel microbeads

It is known that HA has specific interactions with FBNG.³⁹ It was suggested that the origin of HA-FBNG interaction was due to electrostatic interactions between the anionic polysaccharide and the charged protein, the result of which may be actively involved in the organization of the extracellular space.⁴⁰ In order to verify the binding of FBNG to the hydrogel microbeads, FBNG was first labelled with rhodamine B isothiocyanate (RBITC) in an amine-free buffer and subsequently hydrogel microbeads were fabricated microfluidically using the RBITC-FBNG conjugate instead of pure FBNG. Figure 7.3B shows a confocal fluorescence microscopy image of the obtained microbeads. The red fluorescence signal from all over the microbeads strongly indicates the uniform presence of FBNG in the hydrogel microbeads, which is not removed after washing. The strong binding of FBNG to the hydrogel matrix ensures the availability of cell surface binding sites for the 3D culture of the cells.

The porosity of hydrogels is a very important environmental parameter for cell viability. Large pores are generally preferred as they facilitate the efficient transport of nutrients, carbon dioxide, oxygen and even the migration of cells.¹⁰ Here, the porosity of the HASH-PEGDVS-FBNG hydrogel microbeads was qualitatively determined by measuring the diffusion of fluorescein isothiocyanate labelled dextran (FITC-dextran) with varying molar masses. Figure 7.3C shows that even dextrans with a M_W of 2×10^6 g/mol (corresponding hydrodynamic diameter of 54 nm) readily diffused into all the hydrogel microbeads with varying HASH concentrations from 0.75% to 2% (additional images are provided in Supporting Information Figure 7.10), indicating the average pore size of the hydrogel matrix is sufficiently large for the diffusion of nutrients and waste molecules.

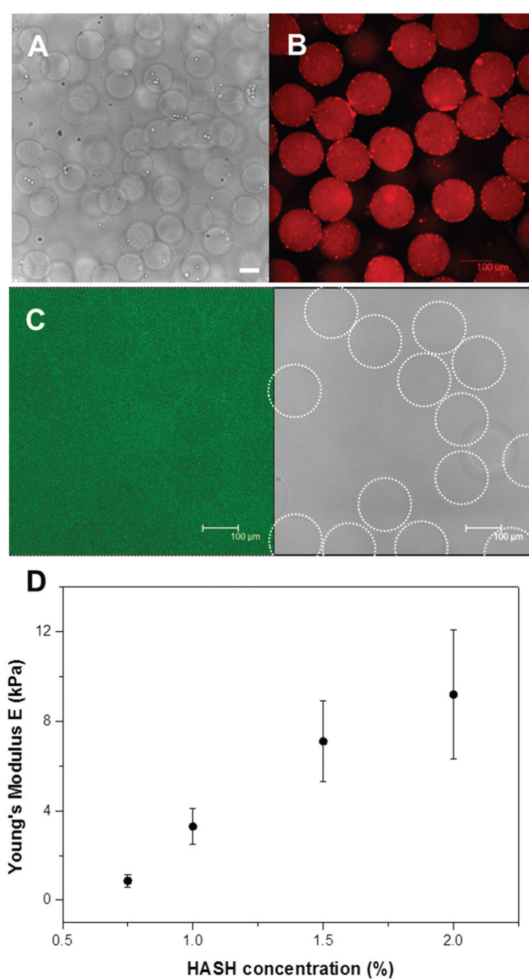


Figure 7.3. Chemical and physical characteristics of the prepared microniches. (A) Typical wide field optical images of hMSC containing hydrogel microbeads with uniform size of $\sim 150 \mu\text{m}$; (B) Confocal laser scanning micrograph on hydrogel microbeads made from HASH, PEGDVS and rhodamine B isothiocyanate (RBITC) labelled FBNG. The stable and relatively homogeneous red fluorescence emission from all over the beads suggests the successful incorporation of FBNG and its strong interactions with the hydrogel matrix. (C) Representative confocal laser scanning micrographs showing that the obtained microniches (with a HASH concentration of 1.5% in this case) are permeable to fluorescein labelled dextran with a M_W of 2M (corresponding hydrodynamic diameter of 54 nm). Left: fluorescence image; right: DIC image. (D) Young's modulus E of hydrogel microbeads obtained by the colloidal probe technique on an atomic force microscope (AFM) plotted against corresponding HASH concentrations. Stiffer gel beads are obtained with a higher concentration of HASH, in good agreement with the above rheological measurements. Scale bars for (A)-(C) are all representing $100 \mu\text{m}$. Error bars in (D) correspond to plus/minus one standard deviation. Dotted-line circles were added in C to guide the outer periphery of the gel beads due to the poor visibility originating from their density matching characteristics to water.

The swelling ratios Q of the hydrogel microbeads were obtained by dividing the swollen mass of the hydrogel microbeads by their corresponding dry mass, based on the initial polymer concentrations, flow rates, droplet generation frequency and final size/volume of the fully swollen beads in MilliQ. Irrespective of the polymer concentration, the HASH-PEGDVS-FBNG displayed Q values of 24 to 46 (detailed data and calculations can be found in the Supporting Information).

The elastic/Young's modulus (E) of the hydrogel microbeads was characterized by the colloidal probe technique on an atomic force microscope (AFM), as previously reported.²¹ The colloidal probe ensures a well-defined tip-sample contact geometry resulting in a uniform sample deformation profile. The measured force-deformation curves with deformations less than 10% of the bead diameters were evaluated by fitting with the Hertz model for the elastic deformation of two spheres in contact. A significant increase in hydrogel stiffness with increasing HASH concentration can be directly observed from the obtained force-deformation curves (see examples in Supporting Information Figure 7.11). Figure 7.3D shows the obtained E values as a function of HASH concentrations. It is observed from the figure that the average E can be varied between $\sim 0.86 (\pm 0.29)$ and $9.2 (\pm 2.9)$ kPa, which is not only well in the range of soft tissues but also fitting extremely well the rheological measurements on bulk gels (*vide supra*).

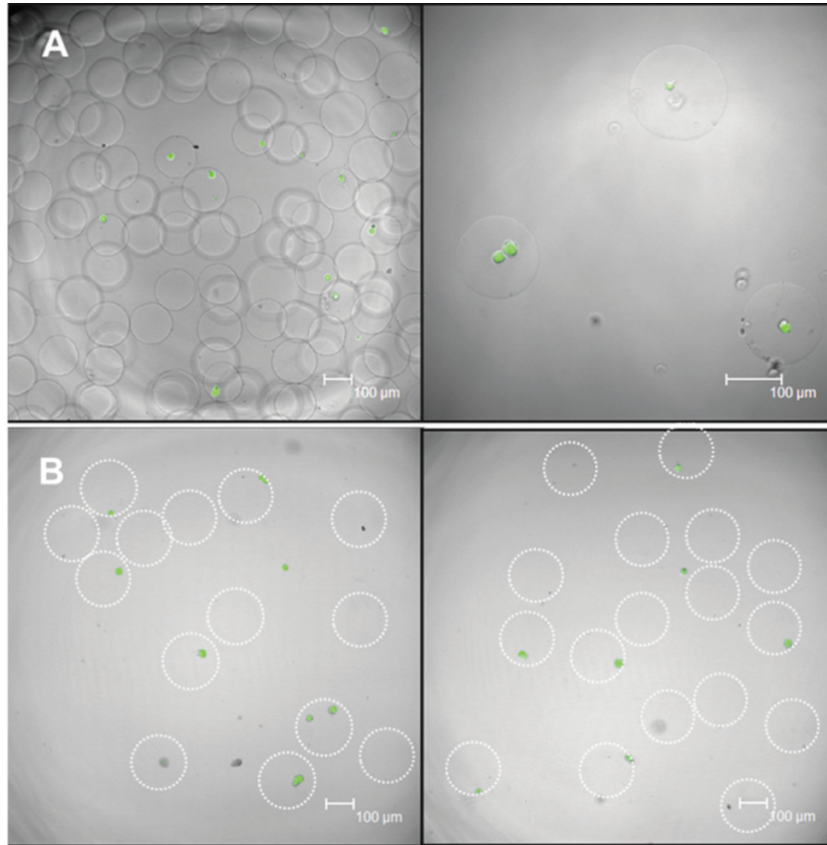


Figure 7.4. The short (A, 24 hrs) and long (B, 2 weeks) term viability of hMSCs in the 3D culture of HASH based microniches characterized by confocal laser scanning microscopy after live-dead staining. The green fluorescence signals of calcein from the inside of many of the encapsulated hMSCs indicate that those are living cells. Scale bars are 100 μm for all images. Dotted-line circles were added in B to guide the outer periphery of the gel beads due to the poor visibility originating from their density matching characteristics to water.

hMSC viability in hydrogel microbeads

The short- (24 hours) and long-term (2 weeks) viability of encapsulated hMSCs in microbeads with HASH concentrations of 1.5% and 2% were studied in detail by live-dead

assays. hMSC-laden microbeads with HASH concentrations below 1.5% degraded within one week in culture, thus were not studied further for the 3D culture of hMSCs. For the viability studies hMSC-laden hydrogel microbeads were cultured in proliferation medium in order to minimize their differentiation. The short-term viability mainly indicates the influence of the microfluidic microbead fabrication procedure on hMSC viability. These include the toxicity of the chemicals involved, the duration of the procedure as well as the shear force applied on the cells during droplet fabrication. In our study, the short-term viability of hMSCs in the HASH-PEGDVS-FBNG beads is around 70% (see representative images in Figure 7.4A), which is comparable to other types of hydrogel microbead systems with encapsulated less sensitive cell types (such as fibroblasts) previously reported.¹⁹ The long-term viability and eventually the differentiation of the cells, on the other hand, depend more on the microniche conditions. Figure 7.4B shows that after two weeks in culture, only live cells were stained. It is likely that dead cells simply went through disintegration. It was observed that in fact a large number of cells can be kept in culture in the hydrogel microbeads for up to 4 weeks. To our knowledge, this is the first example of a hydrogel microbead system fabricated by droplet microfluidics that can sustain the long-term 3D culture of hMSCs at a single cell level.^{4,24,41}

Single hMSC morphology in 3D

In contrast to 2D culture where matrix rigidity affects hMSC morphology and eventually cell fate,⁵ it has been shown that this is not the case in 3D. hMSCs appeared to be spherical in 3D culture in a variety of hydrogel matrices,^{8,12} independent of matrix stiffness. In order to examine hMSC morphology in our system, TRITC-phalloidin was used to stain the F-actin cytoskeleton of the encapsulated hMSCs, together with DAPI staining of the nucleus. Figure 7.5 shows typical examples of stained single hMSCs in the hydrogel microniches with varying HASH concentrations of 0.75-2%. Most of the cells embedded in FBNG containing gel beads showed a rounded morphology and micrometer-sized cortical protrusions towards the surrounding matrix. Protrusions were also observed when cells were embedded in control samples with no FBNG present in the microniches

(see Supporting Information Figure 7.13), though not as prominent. In fact, HA is known to contain receptors for the cell surface protein CD44.⁴² However, additional integrin binding sites are usually included in artificial hydrogel matrices made from HA.^{11,12,28} The hMSCs remained rounded throughout the culture, which suggests a lack of matrix degradation mechanism in the studied hydrogel system.¹²

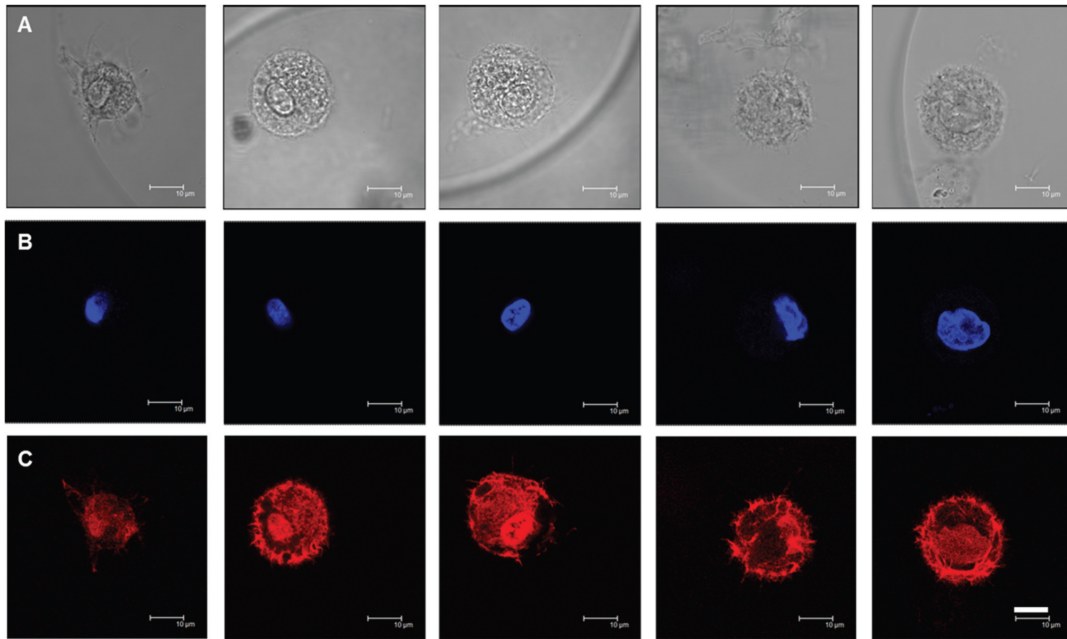


Figure 7.5. Confocal laser scanning micrographs on cell and nucleus morphologies of encapsulated hMSCs in microniches containing FBNG and varying concentrations of HASH between 0.75% and 2%. DIC images are shown in A. DAPI (B: blue) and TRITC-phalloidin (C: red) were used to stain the the nucleus and the F-actin cytoskeleton, respectively. Most of cells show a rounded morphology and micrometer-sized cortical protrusions on the cells towards the surrounding matrix. No apparent correlation between cell or nucleus morphology with matrix stiffness is observed. Scale bars are 10 μm for all images.

Multipotency of hMSCs in microniches

Sustained single hMSC proliferation was observed on all the samples, with microscopy images clearly showing dividing cells in different mitotic phases (see examples in Figures 7.6, 7.7 and Supporting Information Figure 7.14). It is very important to know if these cells also display a propensity to retain their naive state. To do so, we first cultured the hMSC containing hydrogel microbeads (with a HASH concentration of 1.5%) in bipotential differentiation medium (a 1:1 combination of osteogenic and adipogenic media) for 7 days, before staining the biomarker STRO-1 signifying hMSC multipotency through recognition of surface antigen unique to this lineage by immunostaining.³⁷ As shown in Figure 7.6, the interior of many cells in beads displayed bright green fluorescence originating from the Alexa 488 labelled secondary antibody attached to the anti STRO-1 primary antibody. This indicates that a considerable proportion (40-50%) of the single hMSCs retained their multipotency at this time point even in the presence of inductions, a somewhat delayed differentiation as compared to those shown in previous studies by Mooney *et al.*⁸ This could be due to, for example, a lack of cell-cell communication signal in single cell cultures.³ The fact that cells did maintain their multipotency for a prolonged period of time of 7 days gives additional proof of the suitability of using these hydrogel microbeads as potential microniches for single hMSC differentiation studies.

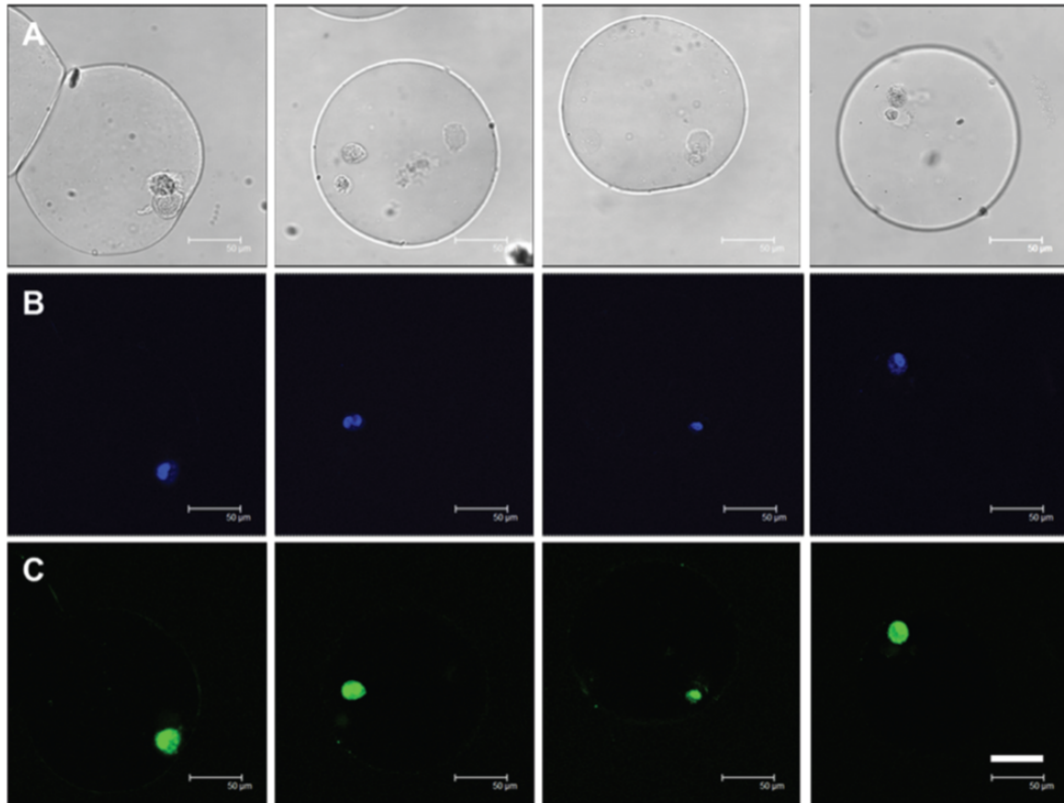


Figure 7.6. Multipotency of hMSCs embedded in microniches characterized by confocal laser scanning microscopy after immunostaining. A HASH concentration of 1.5% is used in this experiment. After 7 days of culture in mixed induction medium containing a 1:1 ratio of osteogenic and adipogenic medium, cells were stained with anti STRO-1 (multipotency biomarker) antibody and Alexa 488 (C: green) labelled secondary antibody and the nuclei are stained with DAPI (B: blue). DIC images are shown in A. Scale bars are 50 μm for all images.

hMSC differentiation in microniches

Finally the phenotypes of differentiated single hMSC in microniches with HASH concentrations of 1.5% and 2.0% were analyzed after culturing them in bipotential differentiation medium for 7 and 14 days, respectively. Osteogenesis is reflected by alkaline phosphatase

(ALP) activity and adipogenesis by the presence of lipid droplets, which is visualized by Oil Red O (ORO) staining. Typical color micrographs of stained hydrogel microbead samples in suspension are presented in Figure 7.7. The dark blue color from the cells in Figure 7.7A demonstrates elevated ALP activity indicating their differentiation into osteoblasts, and the red color from the developed oil droplets in the cells in Figure 7.7B shows the differentiation into adipocytes.

The microbeads appeared to become larger after ORO staining, probably due to the change of medium to a mixture of isopropanol and water. A clear heterogeneity of single cell differentiation was observed, even when separate cells were encapsulated in the same bead. The number of differentiated cells was manually counted in ALP and ORO stained samples and the data is presented in Figure 7.7C. The statistics was based on at least 2000 cells for each sample. After 7 days, over 50% of the cells did not show clear differentiation, in accordance with the above immunostaining results on the multipotency of the cells at this stage. For cells cultured in microniches with the same elasticity/HASH concentration, more cells were shown to have differentiated after 14 days. In addition, it is rather obvious that all the hydrogel matrices prepared in our study mainly support the preferential differentiation into adipocytes. For example, in the hydrogel microbeads of a HASH concentration of 2%, over 60% of the cells were stained ORO positive after 14 days. It should be mentioned that the Young's modulus of hydrogel beads prepared from a HASH concentration of 2% of around 10 kPa is just at the border of supporting a preferential osteogenic differentiation under the same induction conditions.¹⁰ It is thus not surprising that cells embedded in microbeads from a HASH concentration of 1.5% showed a similar preferential behaviour after 14 days. The apparent slight decrease in the percentage of osteoblasts could result from proliferation of the cells over such a prolonged period of time, whose effect was not studied in detail in current study. These results agree well with previous bulk studies on hydrogels from other materials with similar mechanical characteristics.

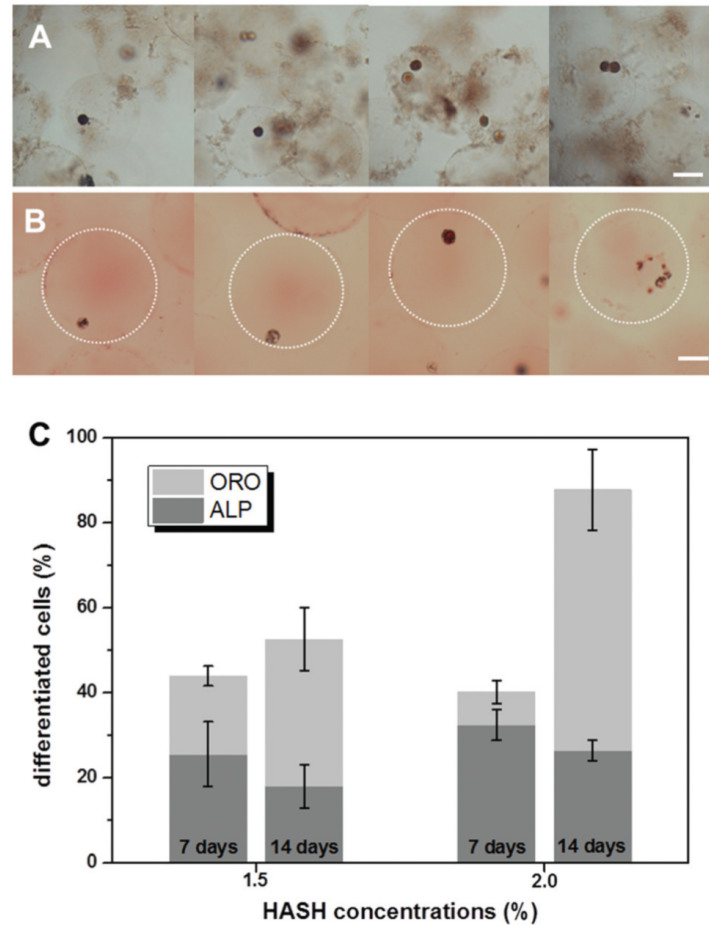


Figure 7.7. *In situ* staining of embedded hMSCs embedded in microniches for (A) ALP activity (Fast Blue, osteogenic biomarker, blue) and (B) neutral lipid accumulation (Oil Red O, adipogenic biomarker, red) after 10 days of culture in mixed induction medium containing a 1:1 ratio of osteogenic and adipogenic medium. HASH concentrations of 1.5% and 2.0% are used in this experiment. Scale bars are 100 μm for all images. Dotted-line circles were added in B to guide the outer periphery of the gel beads due to the poor visibility originating from their density matching characteristics to water. (C) The percentages of differentiated cells embedded in hydrogel microbeads with respect to HASH concentrations and duration of culture (7 days and 14 days) in a 1:1 mixture of osteogenic and adipogenic bipotential differentiation medium. The statistics was based on at least 2000 cells in each sample without excluding multi-cell containing hydrogel microbeads.

Conclusions and future perspective

Bioorthogonal thiol-ene click chemistry based on thiolated hyaluronic acid (HASH) was successfully combined with droplet microfluidics as a powerful and extremely mild approach to prepare biocompatible hydrogel microbeads containing fibrinogen (FBNG) as additional cell binding sites for the 3D culture of single hMSCs. The mechanical properties of hydrogel microbeads made from HASH, poly(ethylene glycol) divinylsulfone (PEG-DVS) and FBNG of 0.9 - 9.2 kPa nicely fall in the softer side of the elasticity of solid tissues, which can be tailored by varying the concentration of the polymer precursor solutions. Acting like microniches, these beads are the first examples supporting the long term culture of single hMSCs up to 4 weeks. Single hMSCs embedded in the HASH-PEGDVS-FBNG microniches displayed an overall rounded morphology, independent of matrix mechanics. The multipotency and differentiation potential of the single hMSCs were characterized separately by various staining procedures, showing the successful preservation of hMSC multipotency in the whole process of fabrication and 3D culture. The soft hydrogel microbeads supported a preferential differentiation of hMSCs into adipocytes after 14 days of culture in osteo/adipo bipotential differentiation medium. A clear heterogeneity in the cell population can be observed in the single cell 3D culture samples, which holds great promise for deepening our understanding of stem cell differentiation at the single cell level.

As a future perspective, a further and more quantitative study on the proliferation and differentiation of hMSCs in the microniches can be achieved by combining cell encapsulation by droplet microfluidics with fluorescence-activated cell sorting (FACS), either after emulsion breaking or after staining.¹⁴ In this way even more sophisticated staining procedures could be applied as well. It would be ideal to study the full differentiation potential of these single hMSCs by real time PCR at different stages of differentiation, preferably also at the single cell level. It is believed that the morphology and differentiation behavior

of hMSCs is strongly dependent on cytoskeletal contractibility,⁴³ matrix degradability¹² and possibly cell-cell interactions.^{3,44,45} HASH used in our context is particularly adaptable to various (bio)chemical cues, whose effects can be studied separately. The radical-free thiol-Michael addition further provides unprecedented possibilities for identifying the key microenvironmental perturbations in defining stem cell fate as a variety of proteins and peptides can be easily incorporated by the same reaction mechanism. Moreover, HASH hydrogel microbeads used in the current study provides niches with mechanical properties in the soft side of solid tissues, which can be potentially extended to the stiffer region by increasing the degree of thiolation or molar mass of HASH used in the hydrogel precursors. As a natural ECM component, HA has been shown to specifically assist in the chondrolytic differentiation of hMSCs.⁴⁶ A follow-up study in this direction is currently underway. We believe that when combined with modern cell-sorting platforms, our *in vitro* model based on hydrogel microbeads can be further improved to study regenerative stem cell bioengineering in a high throughput fashion.

Acknowledgments

The authors would like to thank Ms. José M. A. Hendriks for assistance with cell cultures. J. T. is a Feodor-Lynen fellow of the Alexander von Humboldt Foundation. Work in the Huck group was supported by a European Research Council (ERC) Advanced Grant (246812 Intercom), a VICI grant from the Netherlands Organization for Scientific Research (NWO), and by funding from the Ministry of Education, Culture and Science (Gravity program 024.001.035).

References

- (1) Barry, F. P.; Murphy, J. M. *International Journal of Biochemistry & Cell Biology* **2004**, *36*, 568–584.
- (2) Watt, F. M.; Huck, W. T. S. *Nature Reviews Molecular Cell Biology* **2013**, *14*, 467–473.
- (3) Fuchs, E.; Tumber, T.; Guasch, G. *Cell* **2004**, *116*, 769–778.
- (4) Gobaa, S.; Hoehnel, S.; Roccio, M.; Negro, A.; Kobel, S.; Lutolf, M. P. *Nature Methods* **2011**, *8*, 949–955.
- (5) Engler, A. J.; Sen, S.; Sweeney, H. L.; Discher, D. E. *Cell* **2006**, *126*, 677–689.
- (6) Lutolf, M. P.; Blau, H. M. *Advanced Materials* **2009**, *21*, 3255–3268.
- (7) Kraehenbuehl, T. P.; Langer, R.; Ferreira, L. S. *Nature Methods* **2011**, *8*, 731–736.
- (8) Huebsch, N.; Arany, P. R.; Mao, A. S.; Shvartsman, D.; Ali, O. A.; Bencherif, S. A.; Rivera-Feliciano, J.; Mooney, D. J. *Nature Materials* **2010**, *9*, 518–526.
- (9) Burdick, J. A.; Murphy, W. L. *Nature Communications* **2012**, *3*.
- (10) Thiele, J.; Ma, Y.; Bruekers, S. M. C.; Ma, S.; Huck, W. T. S. *Advanced Materials* **2014**, *26*, 125–148.
- (11) Guvendiren, M.; Burdick, J. A. *Nature Communications* **2012**, *3*.
- (12) Khetan, S.; Guvendiren, M.; Legant, W. R.; Cohen, D. M.; Chen, C. S.; Burdick, J. A. *Nature Materials* **2013**, *12*, 458–465.
- (13) Chokkalingam, V.; Tel, J.; Wimmers, F.; Liu, X.; Semenov, S.; Thiele, J.; Figdor, C. G.; Huck, W. T. S. *Lab on a Chip* **2013**, *13*, 4740–4744.
- (14) Tan, D. W. M.; Jensen, K. B.; Trotter, M. W. B.; Connelly, J. T.; Broad, S.; Watt, F. M. *Development* **2013**, *140*, 1433–1444.
- (15) Du, Y.; Lo, E.; Ali, S.; Khademhosseini, A. *Proceedings of the National Academy of Sciences of the United States of America* **2008**, *105*, 9522–9527.

- (16) Joensson, H. N.; Svahn, H. A. *Angewandte Chemie-International Edition* **2012**, *51*, 12176–12192.
- (17) Velasco, D.; Tumarkin, E.; Kumacheva, E. *Small* **2012**, *8*, 1633–1642.
- (18) Kumachev, A.; Tumarkin, E.; Walker, G. C.; Kumacheva, E. *Soft Matter* **2013**, *9*, 2959–2965.
- (19) Rossow, T.; Heyman, J. A.; Ehrlicher, A. J.; Langhoff, A.; Weitz, D. A.; Haag, R.; Seiffert, S. *Journal of the American Chemical Society* **2012**, *134*, 4983–4989.
- (20) Steinhilber, D.; Rossow, T.; Wedepohl, S.; Paulus, F.; Seiffert, S.; Haag, R. *Angewandte Chemie-International Edition* **2013**, *52*, 13538–13543.
- (21) Ma, S.; Natoli, M.; Liu, X.; Neubauer, M. P.; Watt, F. M.; Fery, A.; Huck, W. T. S. *J. Mater. Chem. B* **2013**, *1*, 5128–5136.
- (22) Ma, Y.; Thiele, J.; Abdelmohsen, L.; Xu, J.; Huck, W. T. S. *Chemical Communications* **2014**, *50*, 112–114.
- (23) Agarwal, P.; Zhao, S.; Bielecki, P.; Rao, W.; Choi, J. K.; Zhao, Y.; Yu, J.; Zhang, W.; He, X. *Lab Chip* **2013**, *13*, 4525–4533.
- (24) Allazetta, S.; Hausherr, T. C.; Lutolf, M. P. *Biomacromolecules* **2013**, *14*, 1122–1131.
- (25) Trappmann, B.; Gautrot, J. E.; Connelly, J. T.; Strange, D. G. T.; Li, Y.; Oyen, M. L.; Stuart, M. A. C.; Boehm, H.; Li, B.; Vogel, V.; Spatz, J. P.; Watt, F. M.; Huck, W. T. S. *Nature Materials* **2012**, *11*, 642–649.
- (26) Wylie, R. G.; Ahsan, S.; Aizawa, Y.; Maxwell, K. L.; Morshead, C. M.; Shoichet, M. S. *Nature Materials* **2011**, *10*, 799–806.
- (27) Hoyle, C. E.; Bowman, C. N. *Angewandte Chemie-International Edition* **2010**, *49*, 1540–1573.
- (28) Burdick, J. A.; Prestwich, G. D. *Advanced Materials* **2011**, *23*, H41–H56.
- (29) Shu, X. Z.; Liu, Y. C.; Luo, Y.; Roberts, M. C.; Prestwich, G. D. *Biomacromolecules* **2002**, *3*, 1304–1311.

-
- (30) Rehfeldt, F.; Brown, A. E. X.; Raab, M.; Cai, S.; Zajac, A. L.; Zemel, A.; Discher, D. E. *Integrative Biology* **2012**, *4*, 422–430.
- (31) Thiele, J.; Ma, Y.; Foschepoth, D.; Hansen, M.; Steffen, C.; Heus, H.; Huck, W. T. S. *Lab on a Chip* **2014**, DOI: 10.1039/c31c51427g.
- (32) Young, J. L.; Engler, A. J. *Biomaterials* **2011**, *32*, 1002–1009.
- (33) Janmey, P. A.; Winer, J. P.; Weisel, J. W. *Journal of the Royal Society Interface* **2009**, *6*, 1–10.
- (34) Ellman, G. L. *Archives of Biochemistry and Biophysics* **1959**, *82*, 70–77.
- (35) Wolfe, D. B.; Qin, D.; Whitesides, G. M. In *Microengineering in Biotechnology*, Hughes, M. P., Hoettges, K. F., Eds.; Methods in Molecular Biology, Vol. 583, 2010, pp 81–107.
- (36) Mazutis, L.; Gilbert, J.; Ung, W. L.; Weitz, D. A.; Griffiths, A. D.; Heyman, J. A. *Nature Protocols* **2013**, *8*, 870–891.
- (37) Simmons, P. J.; Torokstorb, B. *Blood* **1991**, *78*, 55–62.
- (38) Macosko, C., *Rheology: principles, measurements and applications*; Wiley: 1994.
- (39) Leboeuf, R. D.; Raja, R. H.; Fuller, G. M.; Weigel, P. H. *Journal of Biological Chemistry* **1986**, *261*, 2586–2592.
- (40) Rinaudo, M. *International Journal of Biological Macromolecules* **2008**, *43*, 444–450.
- (41) Dolatshahi-Pirouz, A.; Nikkhah, M.; Gaharwar, A. K.; Hashmi, B.; Guermani, E.; Aliabadi, H.; Camci-Unal, G.; Ferrante, T.; Foss, M.; Ingber, D. E.; Khademhosseini, A. *Scientific Reports* **2014**, *4*.
- (42) Laurent, T. C.; Laurent, U. B. G.; Fraser, J. R. E. *Immunology and Cell Biology* **1996**, *74*, A1–A7.
- (43) Kilian, K. A.; Bugarija, B.; Lahn, B. T.; Mrksich, M. *Proceedings of the National Academy of Sciences of the United States of America* **2010**, *107*, 4872–4877.

- (44) Lin, C.-C.; Anseth, K. S. *Proceedings of the National Academy of Sciences of the United States of America* **2011**, *108*, 6380–6385.
- (45) Andreasson-Ochsner, M.; Romano, G.; Hakanson, M.; Smith, M. L.; Leckband, D. E.; Textor, M.; Reimhult, E. *Lab on a Chip* **2011**, *11*, 2876–2883.
- (46) Bian, L.; Guvendiren, M.; Mauck, R. L.; Burdick, J. A. *Proceedings of the National Academy of Sciences of the United States of America* **2013**, *110*, 10117–10122.

Supporting information

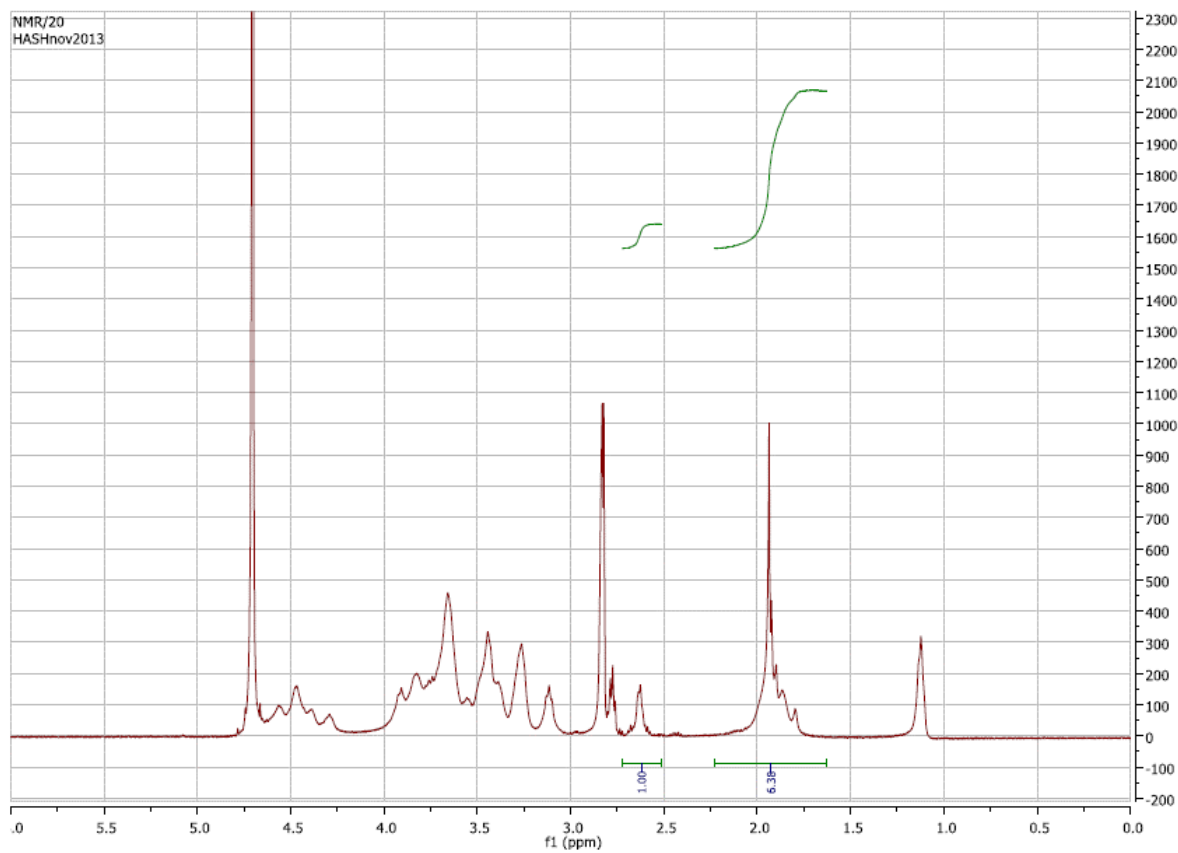


Figure 7.8. ^1H NMR spectrum of thiolated hyaluronic acid used in this study, the degree of thiolation is confirmed by Ellman's test to be around 25%.

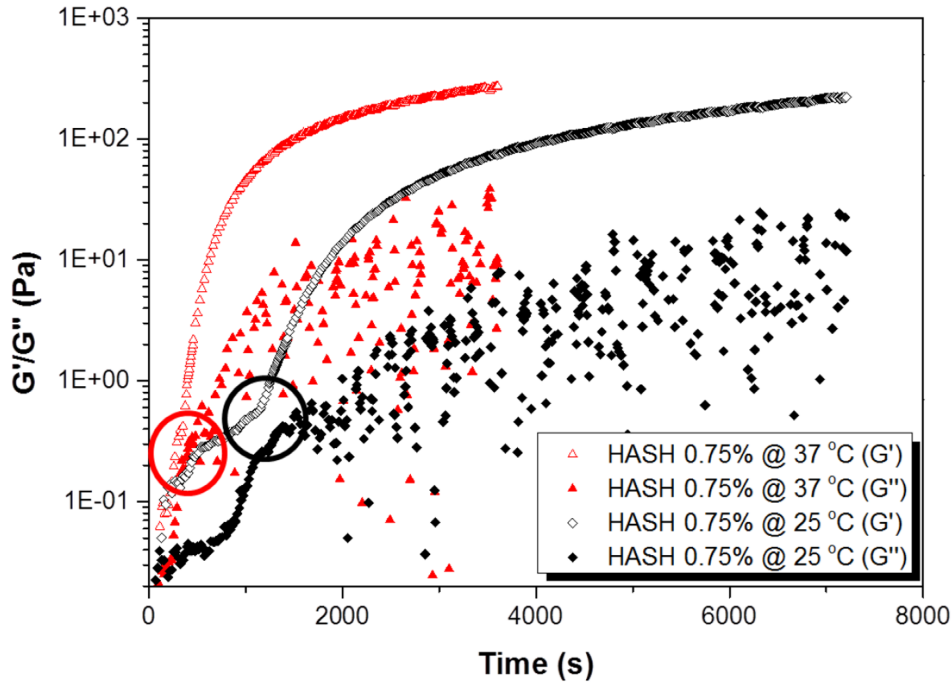


Figure 7.9. Time-dependent rheological measurements on bulk hydrogels made from thiolated hyaluronic acid (HASH) (0.75%, corresponding PEGDVS and FBNG concentrations used are listed in Table 7.1) at 25 °C and 37 °C. It can be seen from the storage (G') and loss (G'') moduli that both the gel point and the time needed to reach the plateau modulus decreases with increasing the temperature. Gel points are marked by circles with corresponding colors showing the transition from liquid-like to solid-like behavior.¹

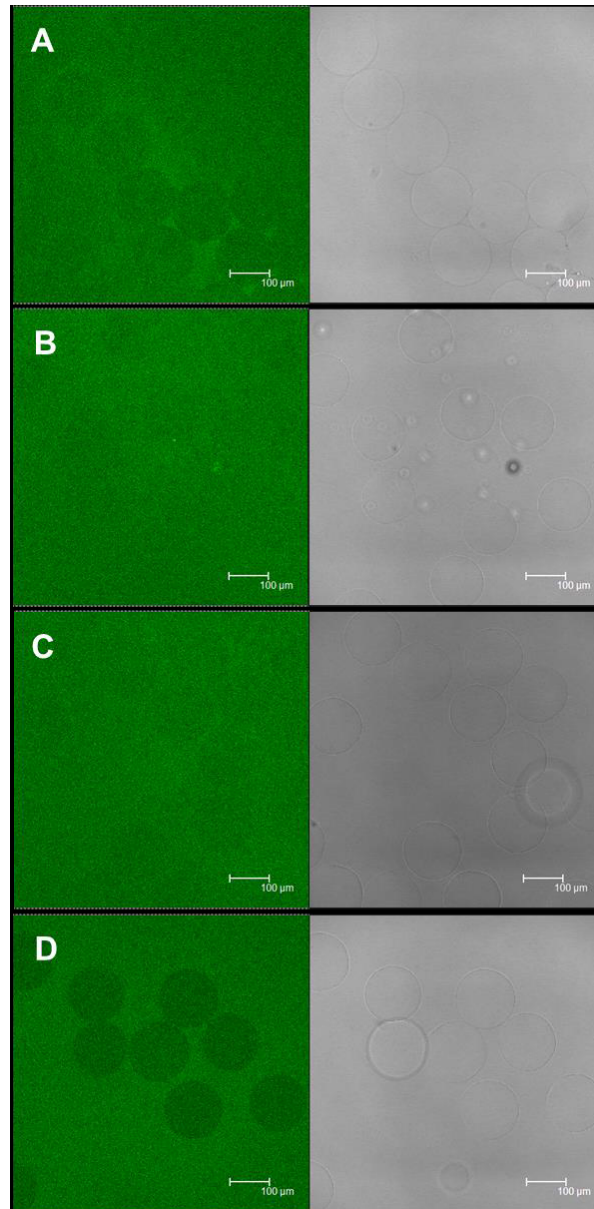


Figure 7.10. Representative confocal laser scanning micrographs showing that all the obtained hydrogel microbeads with varying HASH concentrations (A: 0.75%; B; 1.0%; C: 1.5%; D: 2.0%) are permeable to fluorescein labelled dextran with a M_W of 2M (corresponding hydrodynamic diameter of 54 nm). Left: fluorescence images; right: DIC images.

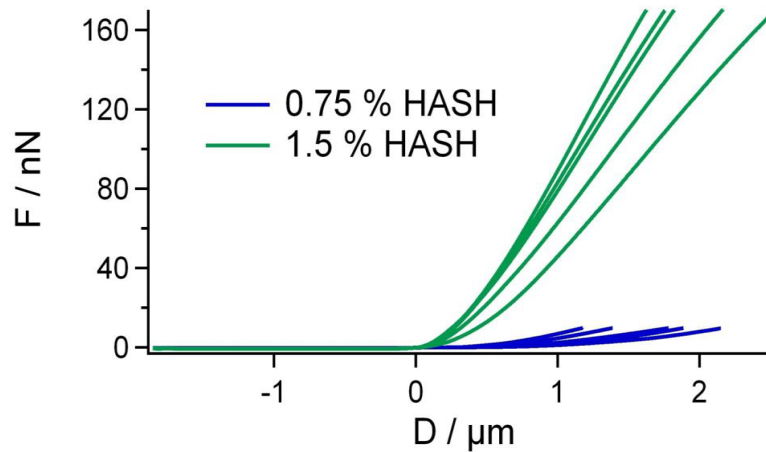


Figure 7.11. Characteristic force *vs.* deformation curves of hydrogel microbeads with HASH concentrations of 0.75% and 1.5% samples demonstrating the significant differences in their stiffness.

The random encapsulation of cells in microdroplets/microbeads

The encapsulation of cells in microdroplets is random and roughly follows a Poisson distribution. The theoretical probability function (Poisson distribution) can be described as:

$$f(k; \lambda) = \frac{\lambda^k e^{-\lambda}}{k!} \quad (7.2)$$

Where λ is the average number of cells encapsulated in each droplet. A relatively low cell concentration for the encapsulation experiments of about 1 million cells/mL was used in all the experiments. Aiming at single cell encapsulation, the experimental conditions where the actual $\lambda = 1.38$ were chosen (with a total flow rate of the aqueous phase of 400 $\mu\text{L/hr}$ and droplet production rate of 80 droplets/s). The calculated probability values for the percentage of droplets containing k ($k = 0-7$) number of cells is plotted in the following figure (Figure 7.12). As shown in the figure, $\sim 35\%$ of droplets would contain exactly a single cell, where the other $\sim 65\%$ contains either no cells or multiple cells.

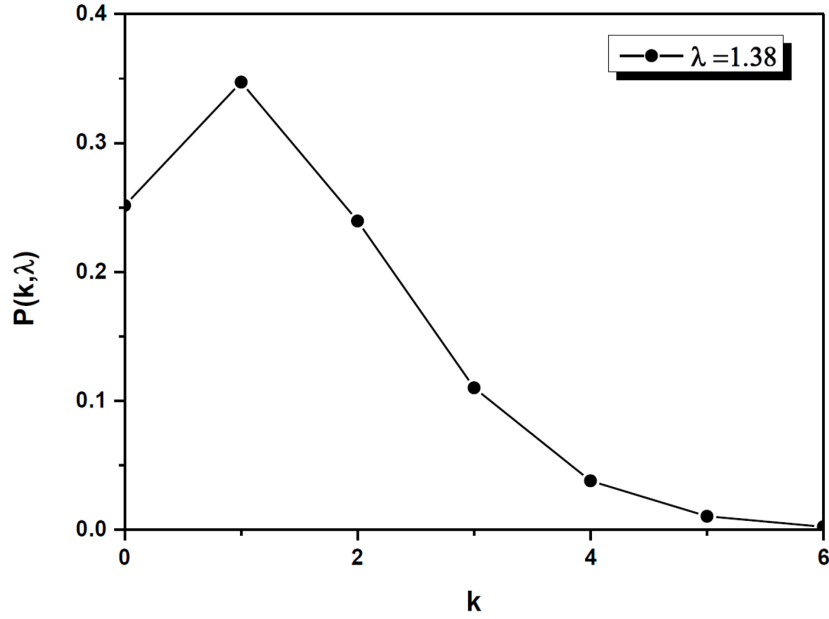


Figure 7.12. Poisson distribution of cell encapsulation in microdroplets when the average number of encapsulated cells $\lambda = 1.38$ under our experimental conditions.

Swelling ratio calculations

The swelling ratios of the hydrogel microbeads were obtained by dividing the swollen mass (m_s , μg) of the hydrogel microbeads by their corresponding dry mass (m_d , μg), based on the initial polymer concentrations (c , $\mu\text{g}/\mu\text{L}$), flow rates of aqueous phase (u_a , $\mu\text{L}/\text{hr}$) droplet generation frequency (f , Hz) and final size/volume (V_s , nL) of the fully swollen beads in MilliQ. The following equations are applied for the calculations:

$$Q = \frac{m_s}{m_d} \quad (7.3)$$

$$m_s = m_d + V_s \rho \quad (7.4)$$

$$m_d = \frac{cu_a}{3600f} \quad (7.5)$$

$$V_s = 10^{-6} \frac{4}{3} \pi \left(\frac{d}{2}\right)^3 \quad (7.6)$$

Where ρ is the density of water ($1 \text{ g/mL} = 1 \text{ } \mu\text{g/nL}$); d is the diameter of the fully swollen gel beads in MilliQ (μm). In our experiments the average d measured on all the hydrogel microbeads are between 135-150 μm , irrespective on the initial concentration of the hydrogel precursors. The values can be calculated from the listed values in Table 7.1. f values were obtained from high speed camera videos on droplet production, with actually values between 60-88 when u_a is at 400 $\mu\text{L/hr}$. The exact values of all the parameters for varying initial HASH concentrations are presented in the following Table 7.2.

Table 7.2. Swelling ratios of HASH-PEGDVS-FBNG hydrogel microbeads fabricated in our experiment.

Sample	HASH concentration [mg/mL]	Total solid concentration [mg/mL]	d [μm]	f [Hz]	V_s [nL]	m_s [μg]	m_d [μg]	Q
1	7.5	21.0	150	60	1.77	1.809	0.039	46
2	10.0	27.7	135	88	1.29	1.324	0.034	39
3	15.0	41.0	135	80	1.29	1.347	0.057	24
4	20.0	54.3	150	84	1.77	1.841	0.071	26

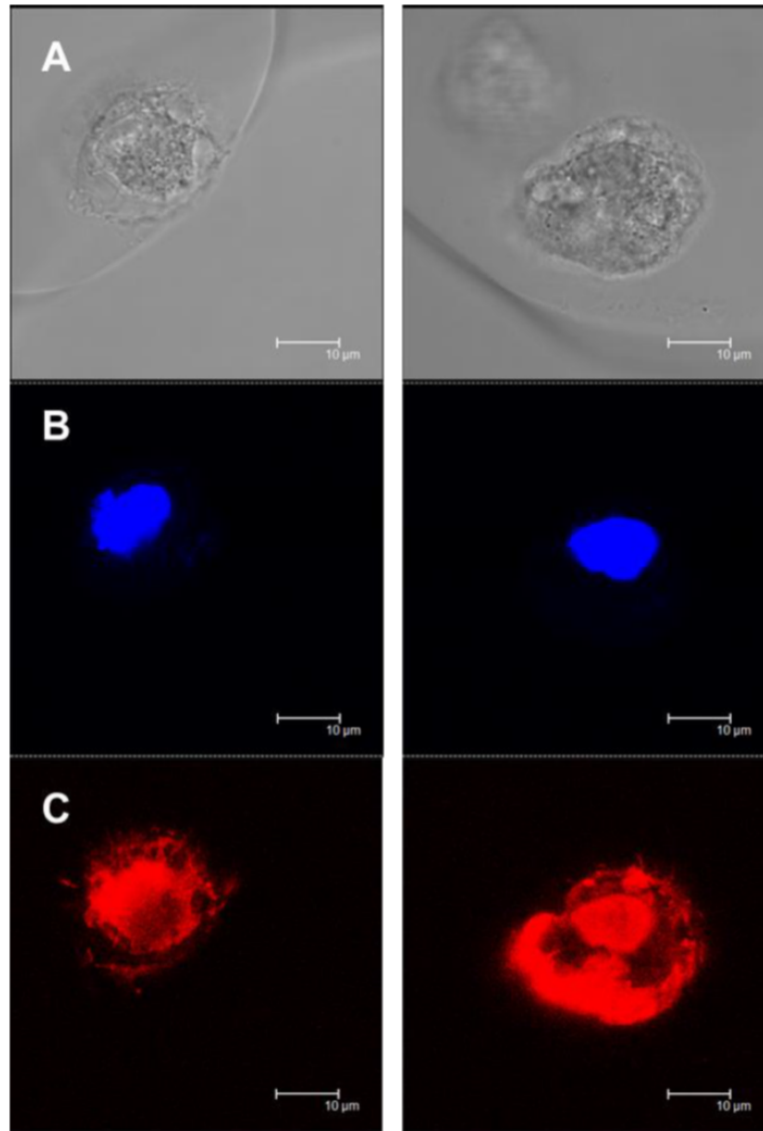


Figure 7.13. Confocal laser scanning micrographs on cell and nucleus morphologies of encapsulated hMSCs in microniches without FBNG. The HASH concentration used in this case is 2%. DIC images are shown in A. DAPI (B: blue) and TRITC-phalloidin (C: red) were used to stain the F-actin cytoskeleton and the nucleus, respectively. Almost all cells show a rounded morphology and some with micrometer-sized cortical protrusions on the cells towards the surrounding matrix. Scale bars are 10 μm for all images.

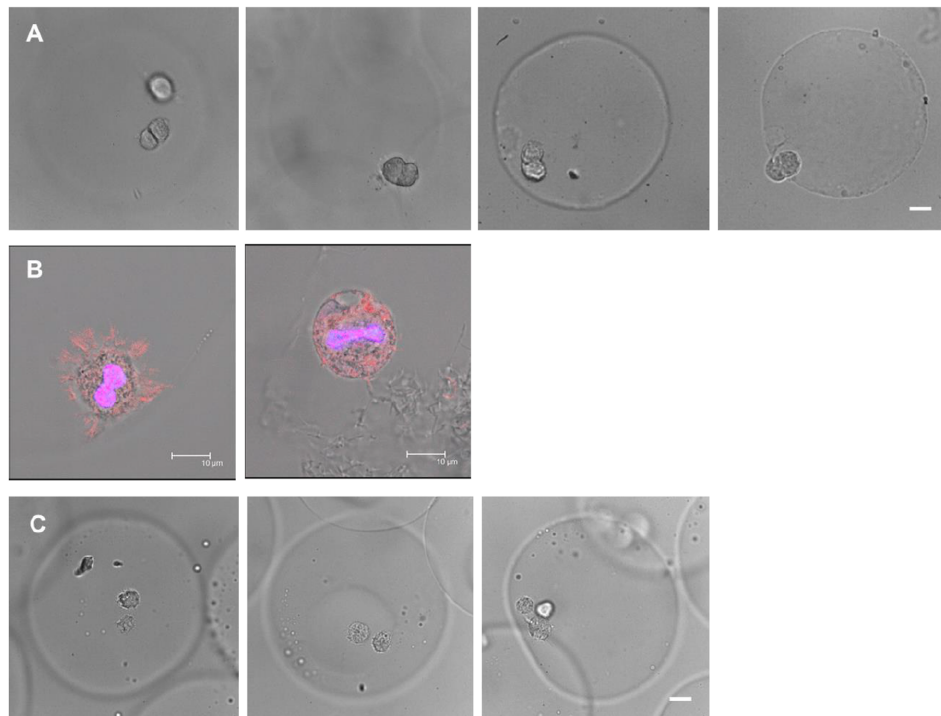


Figure 7.14. Micrographs showing dividing cells and multiple cells in hydrogel microbeads. (A) Cells in their (late) mitotic phases captured by bright-field microscopy. (B) cells in their (early) mitotic phases captured by confocal microscopy, DAPI (blue) and TRITC-phalloidin (red) were used to stain the the nucleus and the F-actin cytoskeleton, respectively and the overlay image is shown here. (C) Multiple cells encapsulated in one hydrogel microbead. Scale bars are 10 μm for all images.

References

- (1) Chambon, F.; Petrovic, Z. S.; MacKnight, W. J.; Winter, H. H. *Macromolecules* **1986**, *19*, 2146–2149.

8

Formation and mechanical characterization of aminoplast core/shell microcapsules

Melanie Pretzl, Martin Neubauer, Melanie Tekaath, Carmen Kunert, Christian Kuttner, Géraldine Leon, Damien Berthier, Philipp Ernie, Lahoussine Ouali and Andreas Fery; *ACS Applied Materials & Interfaces* **2012**, 4:2940-2948. Reprinted with permission. ©2012 American Chemical Society.

Abstract

This work aims at establishing a link between process conditions and resulting micromechanical properties for aminoplast core/shell microcapsules. The investigated capsules were produced by the in situ polymerization of melamine formaldehyde resins, which represents a widely used and industrially relevant approach in the field of microencapsulation. Within our study, we present a quantitative morphological analysis of the capsules' size and shell thickness. The diameter of the investigated capsules ranged from 10 to 50 μm and the shell thickness was found in a range between 50 and 200 nm. As key parameter for the control of the shell thickness, we identified the amount of amino resin per total surface area of the dispersed phase. Mechanical properties were investigated using small deformations on the order of the shell thickness by atomic force microscopy with a colloidal probe setup. The obtained capsule stiffness increased with an increasing shell thickness from 2 to 30 N/m and thus showed the same trend on the process parameters as the shell thickness. A simple analytical model was adopted to explain the relation between capsules' geometry and mechanics and to estimate the elastic modulus of the shell about 1.7 GPa. Thus, this work provides strategies for a rational design of microcapsule mechanics.

Introduction

Microcapsules are of broad interest not only in fundamental science^{1,2} but also in a wide range of applications. Whenever the functionality of an active substance needs to be protected and/or a controlled release is demanded, microencapsulation is a frequently used solution.³⁻¹⁰ Industrially relevant wall materials are amino resins, like melamine formaldehyde (MF), because this class of resins is produced from cheap raw materials, widely applicable, and economical to use.¹⁰ In particular, aminoplast core/shell microcapsules are suitable for the encapsulation of pressure sensitive recording materials,¹⁰ perfume fragrances,^{11,12} phase change materials,^{13,14} self-healing composites,^{15,16} agrochemicals,¹⁷ or analytes in biosensor applications.¹⁸ All these applications require a particular me-

chanical stability, compliance, release, shelf life, and adhesion of the microcapsules.^{19,20} Therefore, a rational process design of microcapsules is desired to individually tailor their mechanical properties.²¹ To establish correlations between process parameters and the resulting capsule mechanics, methods are favored that allow an investigation of microcapsule mechanics on the single-particle level.²⁰

So far, reported mechanical characterizations on aminoplast microcapsules were focused on compression experiments with the single capsule compression apparatus described by Keller and Sottos²² and the micromanipulation technique described by Zhang and co-workers.²³ With both setups, individual microcapsules were deformed in the range of micrometers under applied force loads of millinewtons. Thus, the authors were able to access a deformation regime where rupture forces and the failure of microcapsules can be successfully determined.²⁴⁻²⁸ To understand how our approach differs from the ones used in previous studies, the definition of the terms "small deformation" and "large deformation" is crucial. In general, the mechanical response of a material can be elastic or plastic. In brief, an elastic response is characterized by a full recovery of the material's original shape, whereas a plastic response is accompanied by a permanent change of the material's shape (*e.g.*, buckling or capsule failure). In material sciences, small deformations are often referred to compression tests carried out in the elastic regime. We stress that for our approach, the critical parameter used for the definition of small and large deformations is the microcapsule's shell thickness and not the yield point, which describes the transition between the elastic and plastic regime. Hence, small deformations are understood in this publication as compressions below or on the order of the shell thickness and large deformations as compressions larger than the shell thickness. There is one pioneering paper by Mercadé-Prieto²⁹ where finite element modeling has been used to estimate the wall thickness to radius ratio and the elastic modulus of individual capsules from compression experiments in the elastic regime. We appreciate the approach of the authors because it offers the possibility to estimate the critical mechanical parameters for individual capsules. However, for this publication, the included experimental data concentrates on fractional deformations between small deformations on the order of the

shell thickness and very high deformations.²⁹ In contrast to previous studies, our interest is concentrated on the mechanical response of capsules in the small deformation regime, which refers to a compression of the capsule on the order of the shell thickness. This regime has not yet been explored for aminoplast microcapsules, which is unfortunate, because it offers the possibility to link the capsules' mechanical response to its geometric design. For polyelectrolyte multilayer capsules it has been shown³⁰ that this regime is also relevant for adhesion properties. Atomic force microscopy (AFM) is an ideal tool to carry out deformations of capsules on the order of the shell thickness, because it offers a displacement resolution of nanometers and a force resolution of piconewtons. The compression apparatuses used in previous studies show with a resolution of a few hundred nanonewtons a sufficient resolution to investigate the elastic response of many capsule systems. Indeed the limiting factor for small deformation experiments is also often not the force resolution but the resolution of the induced deformation.

Several strategies exist for the synthesis of aminoplast core/shell microcapsules,^{10,31} but the most applied and industrially relevant is the *in situ* polymerization,^{32,33} which sometimes is also referred to as phase separation method.¹² In this emulsion-templated process, the hydrophobic core material is dispersed in form of small oil droplets in the aqueous continuous phase, where the MF prepolymer is dissolved. The polycondensation of the prepolymers starts under acidic conditions and elevated temperatures. Formed oligomers are deposited at the oil/water interface, where they polymerize to a three-dimensional shell around the oil droplet.^{13,34} To control capsule mechanics process parameters are interesting that affect size, shell thickness and the elastic modulus of the wall material. Typically, a polydispersity in size is observed for capsules manufactured with the *in situ* polymerization. These size distributions are determined by the produced emulsion droplets, which serve as soft templates for the buildup of the shell. Key parameters for the adjustment of the emulsion droplet size are the interfacial tension between core and continuous phase and the energy dissipation of the stirrer.^{13,27} In general, the *in situ* polymerization yields aminoplast core/shell microcapsules between 5 and 50 μm ,³² where smaller capsules show narrower size distributions than larger

capsules.³⁵ The shell thickness is expected to be between 30 and 300 nm³² and can be adjusted by the ratio of melamine to formaldehyde,¹² the reaction time,²⁴ pH,³⁴ and the core to shell mass ratio per created surface area of the emulsion droplets.¹³ The elastic modulus of the shell depends on the used wall material³⁶ and can be changed through chemical modifications and/or the cross-linking density.

In this paper, we investigate aminoplast core/shell microcapsules and strategies to rationally design their mechanical properties. The motivation to focus on aminoplast microcapsules is based on their regular application in different industrial fields.^{5,11} Challenging for the presented work was the polydispersity of the studied capsules that is very well reflecting the actual industrial situation for amino resin microcapsules produced by an emulsion-templated *in situ* polymerization. Structure property relations are often not efficiently resolved by standard methods employed during industrial quality assurance. Therefore, the characterization on the single particle level is crucial for such size-dispersed systems. For this reason, we have chosen methods that are able to resolve and quantify the geometry and mechanics of single microcapsules. In particular, we used transmission electron microscopy (TEM) to determine the shell thickness from ultrathin sections of Epon-embedded microcapsules. With AFM and a colloidal probe setup we studied the mechanical response of single capsules in the small deformation regime, which refers to a capsule compressions on the order of the shell thickness. Subsequently, we correlated the obtained shell thickness with the process parameters and then via a simple analytical model with the resulting capsule mechanics. The full correlation between process parameters and resulting mechanical properties suggests strategies to rationally tailor microcapsules produced by an industrial relevant process.

Experimental section

Materials

The key ingredients for the microcapsules synthesis are the melamine-formaldehyde resin (Urecoll SMV, BASF); a colloidal stabilizer (Poly(acrylamide 20%, acrylic acid 80%))

sodium salt, Sigma Aldrich); a formaldehyde scavenger (ethylene urea, Fluka); acetic acid and sodium hydroxide for pH adjustments. The core liquid is a mixture of a 5-"model" fragrance compound, as described previously:⁵ hexyl salicylate 20% w/w, (+-)-methyl 2,2-dimethyl-6-methylene-1-cyclohexanecarboxylate 20% w/w (Romascone), 3-(4-tert-butylphenyl)-2-methylpropanal 20% w/w (Lilial), cis/trans-4-tert-butyl-1-cyclohexyl acetate 20% w/w (Vertenex), and (+-)-2-tert-butyl-1-cyclohexyl acetate 20% w/w (Verdox). As dispersant, we used demineralized water.

Synthesis of microcapsules

Standard core/shell capsules were synthesized according to protocols described previously.^{12,32,33} The specified amounts of the resin, colloidal stabilizer, and water were introduced into a 250 mL reactor at room temperature (pH 7.50). The reaction mixture was sheared at 800 rpm with an anchor stirrer. A resin to oil mass ratio of 0.149 g/g was chosen for the standard core/shell capsules. Then acetic acid (0.78 g) was added for the adjustment of the pH (pH 5.14). The perfume oil (95.00 g) containing Rhodamine (0.1% w/w, Fluka) was added, and the reaction mixture was warmed up to 40 °C and stirred for 1 h. Afterward the reaction mixture was stirred at 55 °C for 3 h. Finally, ethylene urea (50% in water w/w, 16.00 g) was added, and the reaction mixture was stirred at 60 °C for 1 h. Then, the mixture was cooled to room temperature (pH 5.65) and neutralized with NaOH (30% in water w/w, 0.92 g) to give a final pH of 6.57 in the aqueous dispersion.

Morphological characterization

Size distributions were determined with a flow particle image analyzer FPIA (Sysmex FPIA-300, Malvern Instruments). Zeta potential measurements (Zetasizer, Malvern) of the diluted capsule slurries yielded negative values, which typically range from -30 to -50 mV (see Table 8.1). With TEM (Zeiss CEM 902) thin sections of about 50 to 60 nm,

Table 8.1. Microcapsules prepared with different amounts of resin and the obtained results from the morphological and mechanical characterization: average diameter d , zeta potential ζ , measured shell thickness h_i , correction factor f , corrected shell thickness h , and capsule stiffness F/D ; the standard deviation σ of the thickness and stiffness distributions refers to the fit coefficient width w by the following relation $\sigma = w/(2^{1/2})$.

Amino resin [%]	Perfume [%]	d [μm]	ζ [mV]	h_i [nm]	f	h [nm]	F/D [N/m]
100	43.5	34	-48	285 ± 71	0.64	182	29 ± 11
100	45.5	31	-50	214 ± 61	0.57	122	19 ± 7
75	43.5	18	-48	122 ± 16	0.63	77	5.2 ± 2
50	44.8	28	-46	103 ± 38	0.63	65	1.7 ± 3
50	46.4	28	-56	103 ± 38	0.63	65	1.7 ± 3
25	47.9	43	-28				

produced by an ultracut microtome (Leica EM UC7), were imaged at 80 eV. The shell thickness was obtained from TEM images by extracting cross-sectional gray value profiles that were analyzed with ImageJ software. The start/end of the shell was determined at 50% decrease/increase of the gray value intensity. TEM samples were prepared by mixing the capsule solution in a 1:1 ratio with 2% aqueous solution of agar (Agar Noble, Difco). After curing, the flexible gel was cut with a scalpel into small cubes. Next, the agar-embedded capsules were solidified by 1 h incubation with a 2 % glutaraldehyde solution (Serva Electrophoresis GmbH) in phosphate buffer (0.05 M phosphate buffer, pH 7.4 Merck). Afterward three washing steps with phosphate buffer (0.05 M, pH 7.4, Merck) were used to remove the excess of glutaraldehyde. Then the samples were dehydrated in ethanol-water mixtures with increasing ethanol content (30%/50%/70%/95%) and three times to pure ethanol (VWR International). The dehydration exposure time was 15 min for each step. Then the dried samples were mixed with Epon 812 (Serva Electrophoresis GmbH): Epon 812/ethanol mixture (1:1) for 12 h, followed by an Epon 812/ethanol

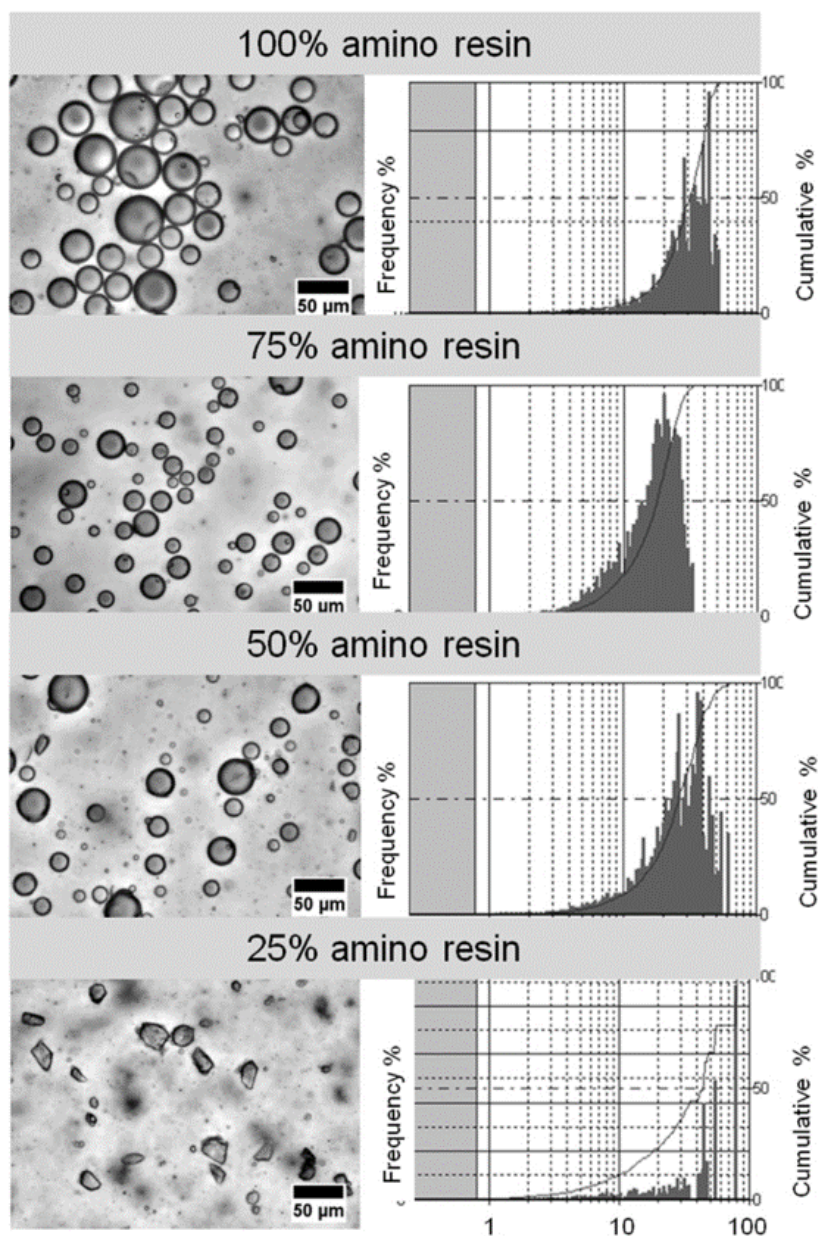


Figure 8.1. Optical micrographs and size distributions of the produced aminoplast core/shell microcapsules. For a 25% level of amino resin, the encapsulation process failed and microcapsules with a deformed capsule shape were produced that were not able to form a stable shell around the dispersed oil droplets.

mixture (3:1) for 3-4 h and finished with three immersion steps (3-4 h) in 100% Epon

812.

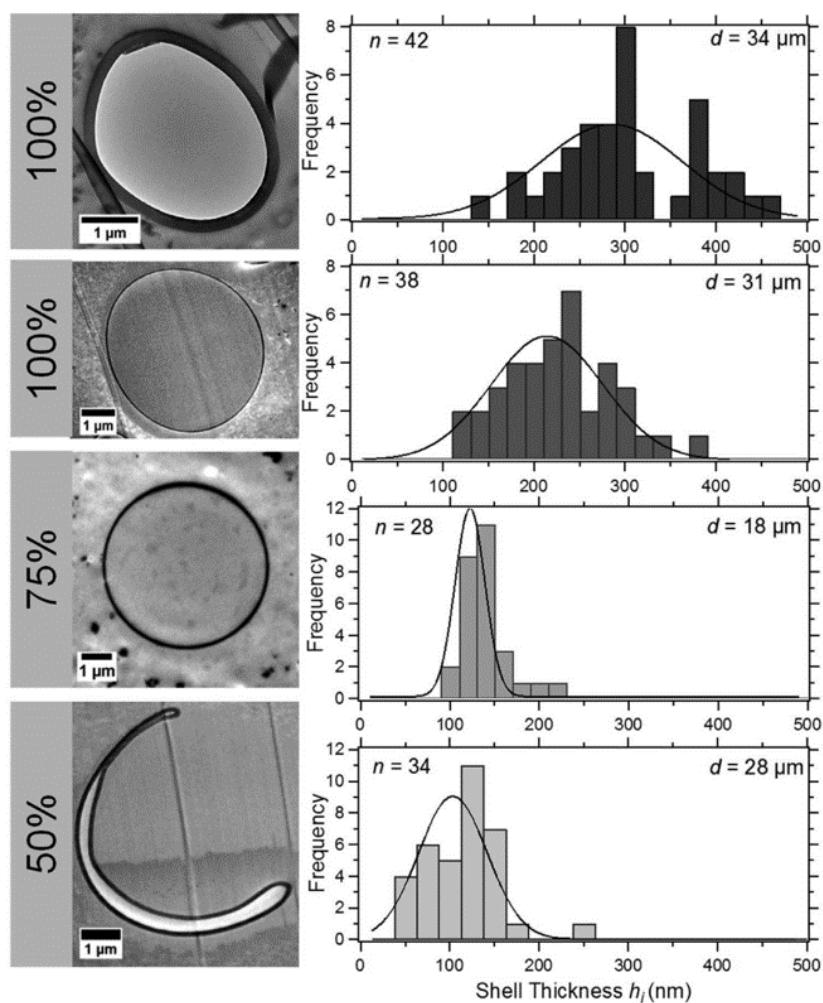


Figure 8.2. TEM images of embedded microcapsules sectioned with an ultra microtome and the quantified distribution of the measured shell thickness. The number of analyzed sections n is indicated along with the used amount of resin in percentage and the average diameter d .

Mechanical characterization

Force spectroscopy experiments were performed in aqueous environment with a commercial AFM setup: Nanowizard[®] (JPK Instruments, Germany) combined with an inverted

optical microscope Axiovert 200 (Zeiss, Germany). The optical microscope was used to determine the size of the microcapsule before the deformation experiment and to align the cantilever probe with the center of the immobilized microcapsule. During the capsules' compression we used the microinterferometry³⁷ mode of the microscope to follow in situ the change of the apparent contact area between microcapsule and substrate. Only elastic and uniform capsule deformations were used for evaluation. The deformations were performed using the colloidal probe technique,^{38,39} in which silica particles (diameter 30-40 μm ; Polysciences Inc., USA) were attached to tipless silicon cantilevers (ACT-TL, $k_c = 25\text{-}75$ N/m, $f_c = 200\text{-}400$ kHz, AppNano). The colloids were attached using a micromanipulator (MP-285; Sutter Instruments) and two-component epoxy glue (UHU Plus Endfest 300, UHU GmbH & Co. KG, Germany). After attachment, the colloidal probe cantilevers were cleaned by exposure to atmospheric plasma (5 min, high intensity, Plasma Technology). Spring constants of the cantilevers were determined with the thermal noise method,^{40,41} which is implemented in the commercial JPK software. Only cantilevers were used that were in accordance with the frequency and spring constant range reported by the manufacturer. The experiments in aqueous solution were carried out in liquid cells, made of a plastic ring (diameter 24 mm, height 5 mm) and a coverslip (diameter 24 mm, thickness 0.13-0.16 mm, Menzel). The liquid cells were cleaned with an isopropanol/ethanol/water mixture (1:1:1) and through exposure to an atmospheric plasma (5 min, high intensity, Plasma Technology). To keep the negatively charged microcapsules immobilized in the liquid cell we used branched polyethyleneimine (PEI, M_W 25.000 g/mol, 1 g/L aqueous solution, Sigma Aldrich) as surface coating. To obtain individual and separated microcapsules for force spectroscopy experiments and to remove nonimmobilized capsules the sample was washed several times with purified water (Millipore Advantage) in the liquid cell. Reference curves on hard substrates were obtained before and after each capsule deformation to ensure a constant optical lever sensitivity, which is necessary for reliable and comparable force deformation curves.⁴²

Results and discussion

Morphology of aminoplast core/shell microcapsules

Size, shell thickness and the used wall material are important parameters for the mechanics of microcapsules. A possible parameter to adjust the shell thickness of aminoplast microcapsules is the resin concentration.¹³ For the microcapsules production the fragrance oil is dispersed by emulsification in the continuous aqueous phase. The melamine formaldehyde prepolymer, which is dissolved in the continuous phase, will start to form oligomers under acidic conditions and elevated temperatures. These oligomers then deposit at the oil/water interface of the emulsified droplets and form under further condensation an impermeable shell around the fragrant oil. The typical amount of MF resin¹¹ used for this encapsulation will be referred to as "100 %" or "standard amount" in the following discussion. The amount of resin was decreased from 100 to 75 to 50 and 25% to obtain microcapsules with thinner shells. All other process parameters were kept constant.

The dispersity in size of the studied microcapsules is typical for an emulsion droplet based *in situ* polymerization. Microcapsules with smaller average diameters show a narrower size distribution than capsules with larger average diameters.^{43,44} Figure 8.1 presents the optical micrographs and size distributions of the produced capsules with a corresponding average diameter d for each sample size distribution summarized in Table 8.1. The size distributions of two additional samples produced from 100 and 50% amount of amino resin are indicated in the Table 8.1, but not shown in Figure 8.1. In particular, we observed for the produced capsules a mean diameter d_{mean} of about 30 μm . Samples that significantly deviated from this mean diameter were microcapsules produced from 75 and 25% amino resin with an average diameter of 18 and 43 μm respectively. Such variations in size are well-known and reflect the actual situation of the industrial production, which already has been reported previously.^{13,44} The success and/or failure of the encapsulation process are clearly indicated in the optical micrographs in Figure 8.1. Spherically shaped capsules with an amino resin level of 100, 75, and 50% indicate a successful encapsulation

of the oil phase. The shape of the microcapsules produced from a 25% level of amino resin was in contrast to the other batches strongly deformed. Here the encapsulation process was not successful, and the formed shell was not stable enough to encapsulate the oil phase.

To access the shell thickness of the microcapsules we used ultrathin sections of Epon-embedded microcapsules, which we analyzed with TEM. In Figure 8.2 examples of such sections are shown for capsules produced from different amount of amino resin. For all investigated samples, we observed a smooth shell with uniform density and rather uniform thickness. For microcapsules produced from 25% amino resin we were not able to obtain any ultrathin sections of the embedded capsules. The measured shell thickness of one section is denoted h_i and refers to an average of six analyzed cross sections, which were extracted from one TEM image. With this method, we were able to determine the shell thickness h_i with an accuracy of 12%. For each microcapsule batch, we used n number of sections to quantify the shell thickness indicated in the histograms displayed in Figure 8.2. From this thickness distributions we were able to determine a mean measured shell thickness h_i from the maximum of the gauss fit.

In general, we observed a decrease of h_i from 285 to 103 nm when we reduced the amount of amino resin from 100% to 50%. The observed mean shell thickness for each batch is summarized in Table 8.1. In Figure 8.2, we grouped our results according to the employed amount of amino resin and the average capsule diameter. The size distribution of the produced capsules is as important as the resin concentration for the final shell thickness of the capsules. If the volume of the dispersed phase and the resin concentration were constant, thinner shells would be expected for batches with smaller capsules compared to those with larger capsules.¹³ The change in thickness is caused through an alteration of the total surface area of the dispersed phase available during the polymerization reaction, which will be larger for smaller emulsion droplets than for larger droplets. We observed this trend as well for the two samples produced from 100% amino resin, where the mean shell thickness was reduced from 285 to 215 nm, when the average diameter of the capsules decreased from 34 to 31 μm , as indicated in Figure 8.2. For samples

whose average diameter was reproduced, as for capsules made of 50% amino resin and average diameter of 28 μm , no significant difference in the shell thickness was observed. Therefore, we combined h_i values of both batches in one diagram, shown in Figure 8.2. When spherical particles are sectioned at random distance from the center, the measured diameter r_i will be smaller than the true diameter r and the measured thickness h_i will be larger than the true thickness h . On average, we obtained a standard deviation of the mean measured shell thickness of about 26%. This deviation is higher than the accuracy of the method of 12% and reflects the uncertainty of the random sectioning process. Smith and co-workers⁴⁵ introduced a correction factor accounting for the thickness artifacts produced by the random slicing process. They described the shell thickness h as a function of the slicing angle, the measured radius, and the measured shell thickness. With an estimated limit for the slicing angle about 80° , we determined the correction factor f to be about 0.62. The obtained correction factor for each batch and the corresponding corrected shell thickness h can be found in Table 8.1.

To estimate the available mean total surface area, a mean diameter of 30 μm , mean mass of 95 g and a density of 0.96 g/mL for the fragrance composition was used. For a constant volume of the dispersed phase, the total surface area of the emulsion droplets will decrease with increasing particle radius. In eq 8.1, the change of the total surface area A_{total} of microcapsules is shown when their radius is changed from r_1 to r_2 . The index 1 refers to capsules characterized by the radius r_1 and index 2 to the capsule characterized by the radius r_2 . A_{total} of the dispersed phase can be described by the surface area A_1 of the individual oil droplets multiplied by the number n of droplets. The number n of particles is obtained by the volume of the dispersed phase V divided by the volume of the dispersed particles V_1 . With regard to the application the volume of the dispersed phase V can be easily controlled at the start of the synthesis and the mean radius of micrometer-sized capsules that is determined by the emulsion droplet size can be assessed by standard techniques for quality assurance. As eq 8.1 shows, the ratio of the total surface area for microcapsules with different diameters is the same like the ratio between the two capsule radii when the volume of the dispersed phase is constant

$$\frac{A_{1,total}}{A_{2,total}} = \frac{n_1 A_1}{n_2 A_2} = \frac{\frac{V}{V_1} A_1}{\frac{V}{V_2} A_2} = \frac{r_2}{r_1} \quad (8.1)$$

with $V_1 = V_2 = V$; $V_i = 4/3\pi r_i^3$; and $A_i = 4\pi r_i^2$, it follows that $A_i/V_i = (4\pi r_i^2)/(4/3\pi r_i^3) = 3/r_i$.

For the production of the studied capsules, the volume of the dispersed phase was constant for the different amounts of amino resin. For microcapsules that showed a deviation from the expected mean radius of 30 μm the average total surface area could be corrected by the ratio of the capsule radii, where r_1 refers to the expected mean capsule radius and r_2 to the radius of the actual produced microcapsules. Figure 8.3 describes the shell thickness as a function of the amount of amino resin per total surface area. Both results of the measured and the corrected shell thickness are displayed. As a trend, we can observe an increase of the shell thickness with an increase of the MF amount per total surface area, which was already reported for MF microcapsules by Sgraia *et al.*¹³ In view of the complex nature of the manufacturing process inherent to the application-oriented study and the characterization method, the observed error margins are to be expected. We are confident that our analysis of a relatively large number of sections and the performed correction of the random sectioning process takes these variations into account. The morphological characterization and the correlation to simple and accessible process parameters showed that it is possible to adjust and predict the thickness for the investigated process. Both analysis and correlation provide strategies to realize an adjustment of the shell thickness for microcapsules produced by *in situ* polymerization.

Mechanical properties

The mechanical response of immobilized microcapsules was studied by force-deformation experiments with atomic force microscopy (AFM). We used cantilevers modified with a colloidal probe to ensure an axisymmetric and uniform compression of the microcapsules.

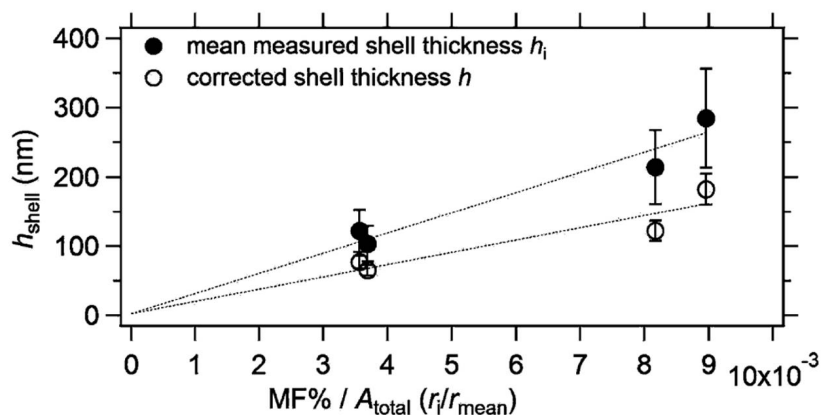


Figure 8.3. Shell thickness is a function of the ratio of resin amount (MF %) per total surface area of the dispersed phase. The lines were added as a guide to the eye.

An AFM mounted on an optical microscope ensures optical control over the alignment of probe and sample. Immobilized capsules are recognized by the presence of an apparent contact area by using the microscope in microinterferometry mode.³⁹ In Figure 8.4, the typical change of the apparent contact area for an elastic response of the microcapsule is shown. The time in seconds displayed on the x-axis corresponds to the length of the video that can be found in the Supporting Information. The apparent contact area refers to the dark spot in the middle of the interference pattern, shown in the insets in Figure 8.4. During the first 5 s, there is no compression of the capsule and the contact area shows the immobilized capsule in uncompressed state. After 5 s, the cantilever reaches the capsule and the contact area linearly increases with further compression until the maximum deformation is reached. The cantilever retraction ends the deformation cycle and indicates the same curve progression as for the compression. The apparent contact area returns to its initial state before it is deformed again. The constant and periodic change of the apparent contact area during the presented three consecutive load-unload cycles clearly indicates a uniform and elastic compression of the capsule and the recovery of its original contact area and shape. This optical control is crucial to ensure the correct alignment between probe and sample and to carry out a reproducible capsule deformation.

To assess the mechanical properties of the shell we performed all compression experiments in the small deformation regime. For our approach as already highlighted in the introduction, the critical parameter to distinguish between small and large deformations is the shell thickness. In Figure 8.5A the deformation process of a thick-shelled and a thin-shelled microcapsule is illustrated. As expected for capsules with comparable size, the thin-shelled capsule deforms stronger than the thick-shelled capsule under the same force load. In this example, the thick-shelled capsules synthesized from the standard amount of amino resin show a mean shell thickness about 185 nm. The thin-shelled microcapsules were produced from 50% level of amino resin and refer to a thin shell with a thickness about 65 nm. The capsule with the thick shell deforms less than 10 nm, whereas the capsule with a thin shell deforms by 50 nm. In both cases, we observe a linear increase of the deformation with increasing force load, which represents a typical scaling behavior for a capsule deformation in the small deformation regime.⁴⁶

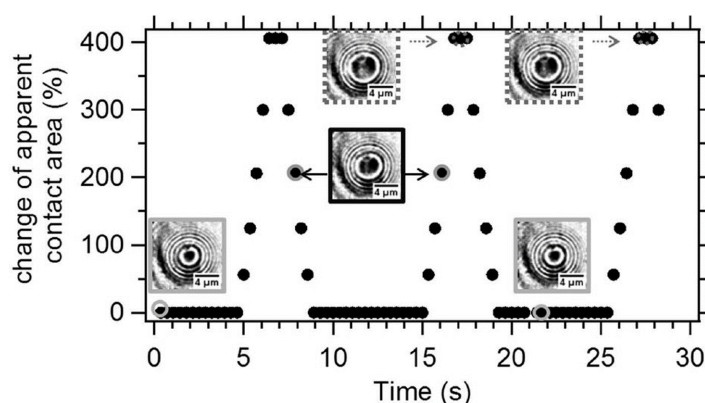


Figure 8.4. Uniform and elastic deformation of a microcapsule observed with an optical microscope using micointerferometry (corresponds to the video in the Supporting Information file, available online). The investigated capsule with a diameter of $30\ \mu\text{m}$ was deformed by 870 nm, corresponding to a relative deformation of 2.91%.

The slope of the force-deformation curves reflects the compression of the capsule under the applied force load, referred to as the capsule's stiffness in units of N/m. In Figure

8.5B,³⁰ repeated force deformation cycles of the thin- and thick-shelled capsules are shown. The observed stiffness values are constant for both capsules throughout the repeated compression, illustrating that no altering of the capsules' stiffness is obtained through consecutive deformation. We also investigated the influence of fast and slow deformation rates on the microcapsules' stiffness. The used deformation rates of $10 \mu\text{m/s}$ and $0.625 \mu\text{m/s}$ did not significantly affect the mechanical response of thick-shelled microcapsules. For thin-shelled capsules, we observed an increase of the stiffness about 12% for faster deformations.

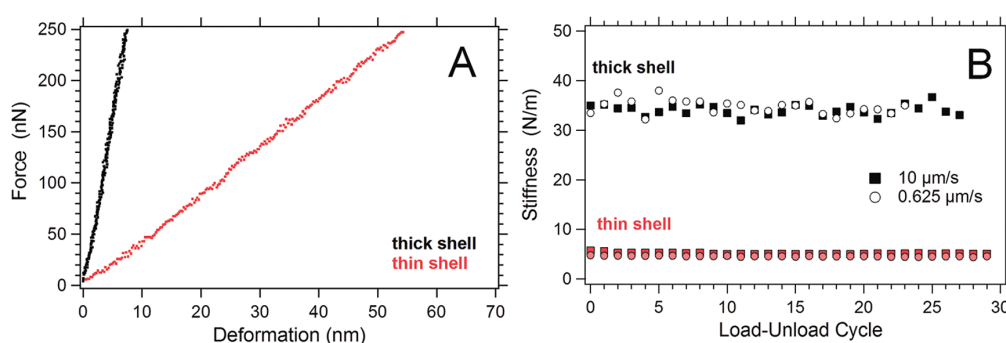


Figure 8.5. (A) Compression of capsules under the same force will yield larger deformations for thin-shelled capsules compared with thick-shelled capsules. (B) Microcapsules compression is elastic and the stiffness is constant over thirty load-unload cycles.

To quantify the stiffness of the capsules produced from different amount of amino resin, we measured a representative number n of aminoplast microcapsules with a slow deformation rate of $0.5 \mu\text{m/s}$. In Figure 8.6, the distributions of the measured stiffness values present a decrease of the mean stiffness from about 30 N/m to 2 N/m for a change of the shells thickness from 285 to 103 nm , respectively. The capsules' stiffness strongly depends on the capsules' diameter. Hence, smaller microcapsules will be stiffer than larger capsules, if they were produced from the same batch and have the same shell thickness. For example, standard core/shell microcapsules with a mean shell thickness of 214 nm showed an increase in the capsule stiffness from 14 N/m to 35 N/m when the diameter of the

capsule was decreased from 30 to 14 μm . Therefore, the width of the stiffness histograms is also reflecting the size distribution of the investigated capsules within one batch. The mean stiffness value determined from the histogram for each capsule batch can be found in Table 8.1.

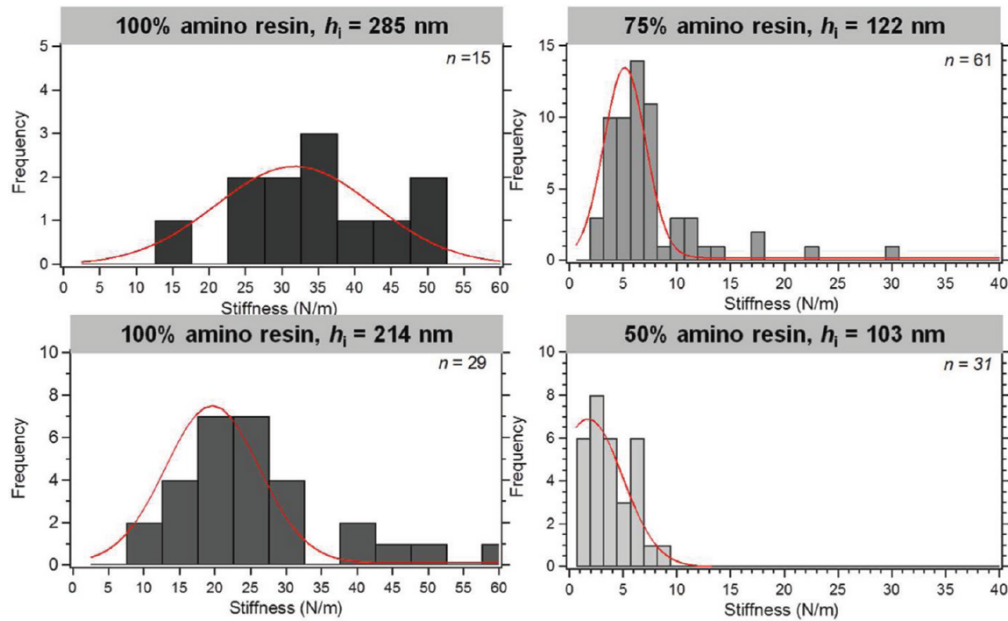


Figure 8.6. Capsules become softer with thinner shells, shown by the decrease of the mean stiffness for capsules with reduced shell thickness.

In Figure 8.7, all results obtained from the morphological and mechanical characterization of the aminoplast capsules are displayed in relation to the used process parameters. Both shell thickness and capsule stiffness increase with the amount of amino resin per total surface area. It already has been shown³⁰ that properties determined in the small deformation regime play an important role for macroscopic properties such as the capsule's adhesion. In the case of MF-shelled microcapsules, with a uniform, closed, and rather strong shell, it would be interesting to link the results gained from the small deformation regime with the already well investigated rupture force of aminoplast microcapsules.^{22,23} Zhang and co-workers^{23,29} showed that the deformation at burst is one of the key parameters for the rupture of aminoplast microcapsules. As discussed before the deformation

behavior of microcapsules is strongly linked to the thickness of their shell, as shown in Figure 8.5A, where thin-shelled capsules deform much more under an applied load than thick-shelled capsules. Microcapsules burst when a critical compression is reached, which was for MF capsules reported about 70% relative deformation at burst.³⁶ The force loads needed for a burst will be reached for smaller force loads in the case of thin-shelled capsules compared with thick-shelled capsules. Therefore, the observed correlations present a potential strategy to be further linked with the reported macroscopic rupture forces. Such a relation would be beneficial for the tailoring of aminoplast microcapsule mechanics used in various applications with very different requirements.

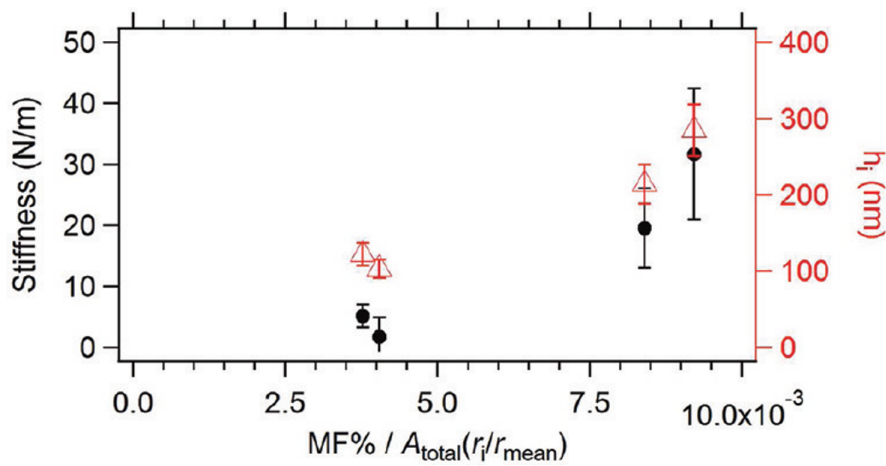


Figure 8.7. Summary of the morphological and mechanical characterization of aminoplast core/shell capsules and the influence of used process parameters.

The tendency observed in Figure 8.7 can be further analyzed to understand how the shell thickness influences the microcapsule mechanics. The mechanical response obtained from the small deformation regime can be used to understand structure property relations, because the mechanical response can be linked to the capsule's geometry and the shell's material properties.²⁰ According to Reissner, the measured stiffness F/D is a function of the capsules geometric parameters, radius R and the shell thickness h and the properties of the shell material, elastic modulus E and Poisson ratio ν :

$$\frac{F}{D} = \frac{h^2}{R} \frac{4E}{\sqrt{3(1-\nu^2)}} \quad (8.2)$$

As described in a previous study⁴⁶ the regime valid for Reissner's prediction^{47,48} of a linear scaling behavior of the applied force F with the resulting deformation D can be easily estimated based on the shell thickness h and the radius r of the capsule:

$$\varepsilon_{crossover} \approx \sqrt{\frac{h}{4\pi r}} \quad (8.3)$$

A critical relative deformation ε is obtained that refers to the crossover of the linear deformation regime with the deformation caused by volume forces, which scales proportional to D^3 . Thus, the morphological characterization can be used to estimate the deformation regime where Reissner's prediction is valid (see Table 8.2 in the Supporting Information). In Figure 8.8A, the measured stiffness is displayed in relation to the capsule radius. All samples show an increase in the stiffness with decreasing capsule diameter, which is in accordance with Reissner's model. The linear relation is then described by the proportionality factor, which is the square of the shell thickness and the material constants E and ν . The stiffness of microcapsules with comparable diameters increases with increasing shell thickness as Figure 8.8A clearly indicates. The stiffness normalized by the size plotted versus the shell thickness shows a linear relation that can be used to estimate Young's modulus of the microcapsules' shell (Figure 8.8B).^{41,49}

The Poisson ratio ν is expected to be between 0.33 for a solid-like material and 0.5 for rubber-like materials. Equation 8.2 describes the impact of Poisson's ratio on the resulting elastic modulus. In order to make the impact of ν transparent, we calculated the elastic modulus for both extremes. From Figure 8.8B, we are able to estimate the elastic modulus of the shell material of about 1.7 GPa for a Poisson ratio of 0.5, which is

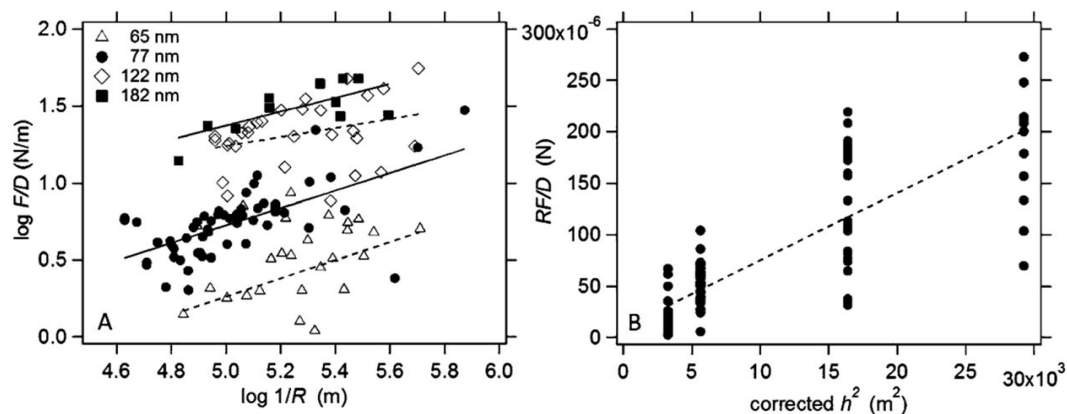


Figure 8.8. (A) Stiffness displayed in relation to the reciprocal radius clearly indicates an increase in the stiffness for capsules with thicker shell and comparable radius. (B) Linear relationship displayed in this graph can be correlated to the material constants of the shell material and an elastic modulus of 1.7 GPa can be estimated.

in good agreement with the elastic modulus reported recently by Mercadé-Prieto *et al.*,²⁹ and for a Poisson ratio 0.33 of about 2.2 GPa.

However, as Figure 8.8B displays a certain spread of the individual data remains even after the normalization of the data by size and shell thickness. One reason for this spread can be due to differences in the shell density caused by kinetic differences during the shell formation. Salaun and co-workers⁵⁰ showed that different surface morphologies of the capsules shell are dependent on the formation of the MF precondensate. They concluded that a rather rapid shell formation will yield higher oligomers or even small MF particles in the continuous phase, which will be deposited at the oil/water interface.^{32,50} The melamine to formaldehyde ratio, pH and temperature were identified as important parameters to affect the kinetics of the precondensate formation. Based on the formed oligomers, which represent the building blocks of the shell, a rougher or smoother capsule shell is obtained.¹² From this perspective and based on the results of our mechanical characterization, we think that the size of the formed oligomers and their assembly to a shell is an important aspect for shell mechanics that would be of interest for further studies.

Conclusion

In conclusion, we showed how mechanical properties of aminoplast microcapsules correlate with process parameters for an industrially relevant microencapsulation process, the *in situ* polymerization of amino resins. With the help of a thorough morphological analysis we were able to determine the microcapsule's geometric parameters, radius and shell thickness. The mechanical response of the microcapsules was investigated in form of small deformations on the order of the shell thickness, using an AFM and the colloidal probe technique. Both results, from geometrical and micromechanical characterization, were explained in the framework of a simple analytical model for microcapsule deformation, the Reissner shell theory. On the basis of the results, we identified the ratio of amino resin to total emulsion surface area as key parameter for controlling the microcapsules geometry and mechanical properties. Thus, a rational design of mechanical properties of aminoplast microcapsules is in reach.

References

- (1) Sukhorukov, G.; Fery, A.; Mohwald, H. *Progress in Polymer Science* **2005**, *30*, 885–897.
- (2) Becker, A. L.; Johnston, A. P. R.; Caruso, F. *Small* **2010**, *6*, 1836–1852.
- (3) Nelson, G. *International Journal of Pharmaceutics* **2002**, *242*, 55–62.
- (4) Madene, A.; Jacquot, M.; Scher, J.; Desobry, S. *International Journal of Food Science and Technology* **2006**, *41*, 1–21.
- (5) Jacquemond, M.; Jeckelmann, N.; Ouali, L.; Haefliger, O. P. *Journal of Applied Polymer Science* **2009**, *114*, 3074–3080.
- (6) Rokka, S.; Rantamaki, P. *European Food Research and Technology* **2010**, *231*, 1–12.
- (7) Sanchez, L.; Lacasa, E.; Carmona, M.; Rodriguez, J. F.; Sanchez, P. *Industrial & Engineering Chemistry Research* **2008**, *47*, 9783–9790.
- (8) Mauldin, T. C.; Kessler, M. R. *International Materials Reviews* **2010**, *55*, 317–346.
- (9) Quellet, C.; Schudel, M.; Ringgenberg, R. *Chimia* **2001**, *55*, 421–428.
- (10) Dietrich, K.; Herma, H.; Nastke, R.; Bonatz, E.; Teige, W. *Acta Polymerica* **1989**, *40*, 243–250.
- (11) Haefliger, O. P.; Jeckelmann, N.; Ouali, L.; Leon, G. *Analytical Chemistry* **2010**, *82*, 729–737.
- (12) Lee, H. Y.; Lee, S. J.; Cheong, I. W.; Kim, J. H. *Journal of Microencapsulation* **2002**, *19*, 559–569.
- (13) Sgraja, M.; Bloemer, J.; Bertling, J.; Jansens, P. J. *Journal of Applied Polymer Science* **2008**, *110*, 2366–2373.
- (14) Su, J.-F.; Wang, L.-X.; Ren, L.; Huang, Z. *Journal of Applied Polymer Science* **2007**, *103*, 1295–1302.

- (15) Yuan, Y. C.; Rong, M. Z.; Zhang, M. Q. *Polymer* **2008**, *49*, 2531–2541.
- (16) Balazs, A. C. *Materials Today* **2007**, *10*, 18–23.
- (17) Sliwka, W. *Angewandte Chemie International Edition in English* **1975**, *14*, 539–550.
- (18) Roitman, D. B. Microcapsule Biosensors and Methods of Using the Same. pat., 07312040, 2007.
- (19) Esser-Kahn, A. P.; Odom, S. A.; Sottos, N. R.; White, S. R.; Moore, J. S. *Macromolecules* **2011**, *44*, 5539–5553.
- (20) Fery, A.; Weinkamer, R. *Polymer* **2007**, *48*, 7221–7235.
- (21) Chen, P. W.; Erb, R. M.; Studart, A. R. *Langmuir* **2012**, *28*, 144–152.
- (22) Keller, M. W.; Sottos, N. R. *Experimental Mechanics* **2006**, *46*, 725–733.
- (23) Zhang, Z.; Saunders, R.; Thomas, C. R. *Journal of Microencapsulation* **1999**, *16*, 117–124.
- (24) Hu, J. F.; Chen, H. Q.; Zhang, Z. B. *Materials Chemistry and Physics* **2009**, *118*, 63–70.
- (25) Long, Y.; York, D.; Zhang, Z. B.; Preece, J. A. *Journal of Materials Chemistry* **2009**, *19*, 6882–6887.
- (26) Sun, G.; Zhang, Z. *Journal of Microencapsulation* **2001**, *18*, 593–602.
- (27) Yang, J.; Keller, M. W.; Moore, J. S.; White, S. R.; Sottos, N. R. *Macromolecules* **2008**, *41*, 9650–9655.
- (28) Caruso, M. M.; Blaiszik, B. J.; Jin, H.; Schelkopf, S. R.; Stradley, D. S.; Sottos, N. R.; White, S. R.; Moore, J. S. *Acs Applied Materials & Interfaces* **2010**, *2*, 1195–1199.
- (29) Mercade-Prieto, R.; Nguyen, B.; Allen, R.; York, D.; Preece, J. A.; Goodwin, T. E.; Zhang, Z. B. *Chemical Engineering Science* **2011**, *66*, 2042–2049.
- (30) Elsner, N.; Dubreuil, F.; Fery, A. *Physical Review E* **2004**, *69*, 6.

- (31) Arshady, R.; George, M. H. *Polymer Engineering & Science* **1993**, *33*, 865–876.
- (32) Dietrich, K.; Bonatz, E.; Geistlinger, H.; Herma, H.; Nastke, R.; Purz, H. J.; Schlawne, M.; Teige, W. *Acta Polymerica* **1989**, *40*, 325–331.
- (33) Hong, K.; Park, S. *Materials Chemistry and Physics* **1999**, *58*, 128–131.
- (34) Alic, B.; Sebenik, U.; Krajnc, M. *Journal of Applied Polymer Science* **2011**, *119*, 3687–3695.
- (35) Yuan, L.; Liang, G.; Xie, J.; Li, L.; Guo, J. *Polymer* **2006**, *47*, 5338–5349.
- (36) Sun, G.; Zhang, Z. *International Journal of Pharmaceutics* **2002**, *242*, 307–311.
- (37) Dubreuil, F.; Elsner, N.; Fery, A. *European Physical Journal E* **2003**, *12*, 215–221.
- (38) Butt, H. J. *Biophysical Journal* **1991**, *60*, 1438–1444.
- (39) Ducker, W. A.; Senden, T. J.; Pashley, R. M. *Nature* **1991**, *353*, 239–241.
- (40) Hutter, J. L.; Bechhoefer, J. *Review of Scientific Instruments* **1993**, *64*, 1868–1873.
- (41) Elsner, N.; Dubreuil, F.; Weinkamer, R.; Wasicek, M.; Fischer, F.; Fery, A. *Progr Colloid Polym Sci* **2006**, *132*, 117–123.
- (42) Butt, H. J.; Cappella, B.; Kappl, M. *Surface Science Reports* **2005**, *59*, 1–152.
- (43) Yuan, L.; Gu, A.; Liang, G. *Materials Chemistry and Physics* **2008**, *110*, 417–425.
- (44) Wang, N.; Tytell, J. D.; Ingber, D. E. *Nature Reviews Molecular Cell Biology* **2009**, *10*, 75–82.
- (45) Smith, A. E.; Zhang, Z.; Thomas, C. R. *Chemical Engineering Science* **2000**, *55*, 2031–2041.
- (46) Fery, A.; Dubreuil, F.; Mohwald, H. *New Journal of Physics* **2004**, *6*, 13.
- (47) Reissner, E. *Journal of Mathematics and Physics* **1946**, *25*, 80–85.
- (48) Reissner, E. *Journal of Mathematics and Physics* **1946**, *25*, 279–300.
- (49) Zoldesi, C. I.; Ivanovska, I. L.; Quilliet, C.; Wuite, G. J. L.; Imhof, A. *Physical Review E* **2008**, *78*, 8.

- (50) Salaun, F.; Vroman, I. *European Polymer Journal* **2008**, *44*, 849–860.

Supporting information

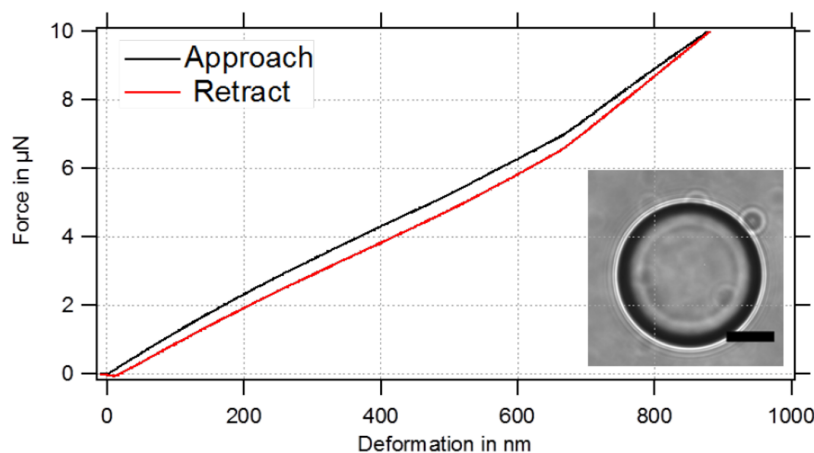


Figure 8.9. Force-deformation curve of a standard core/shell microcapsule with $30\ \mu\text{m}$ diameter and a shell thickness of about $185\ \text{nm}$.

Figure 8.9 displays the force-deformation curve of a standard core/shell microcapsule, which was obtained during the elastic compression shown in the video. The observed deformation is fully elastic, which was additionally shown with an independent optical method that allows the observation of the capsule's shape during its compression (Figure 8.4 manuscript). However, a closer look to the force deformation curve allows the identification of different regimes within the elastic response. From $0\ \text{nm}$ to $200\ \text{nm}$ compression the observed deformation scales proportional with the applied force. This regime shows a linear relationship and is considered in the context of the publication as small deformation regime and compressions on the order of the shell thickness. To analyze the structure-property relations with the analytical solution from Reissner the linear deformation response of the shell is crucial. Compressions on the order of the shell thickness and below were investigated in this publication. After the linear compression phase a non-linear increase (smooth changeover due to the colloidal probe setup) and a kink in the curve at about $\sim 700\ \text{nm}$ deformation and a force load of $\sim 6\ \mu\text{N}$ is observed. This non-linear regime referred to as large deformation regime indicates that volume forces become dominant for the observed deformation behavior.

As shown in previous studies¹ the crossover between the Reissner and the volume regime can be estimated based on the capsules geometry:

$$\varepsilon_{crossover} \approx \sqrt{\frac{h}{4\pi r}} \quad (8.4)$$

The critical relative deformation ε indicates the crossover with the contributions of volume forces that scale proportional to D^3 . The crossover between the Reissner and the volume regime is estimated for the studied capsules and presented in the following Table:

Table 8.2. Small deformation regime estimated from the corrected shell thickness h , the radius r , and the critical deformation ε .

Sample	Corrected shell thickness [nm]	Capsule radius [μm]	ε at crossover	Small deform. regime up to [nm]
100 %	182	17	0.029	248
75 %	77	9	0.082	371
50 %	65	14	0.060	425

References

- (1) Fery, A.; Dubreuil, F.; Mohwald, H. *New Journal of Physics* **2004**, *6*, 13.

9

Mechanics of pH-responsive hydrogel capsules

James P. Best, Martin P. Neubauer, Sameen Javed, Henk H. Dam, Andreas Fery and Frank Caruso; *Langmuir* **2013**, 29:9814-9823. Reprinted with permission. ©2012 American Chemical Society.

Abstract

While soft hydrogel nano- and microstructures hold great potential for therapeutic treatments and *in vivo* applications, their nanomechanical characterization remains a challenge. In this paper, soft, single-component, supported hydrogel films were fabricated using pendant-thiol-modified poly(methacrylic acid) (PMASH). The influence of hydrogel architecture on deformation properties was studied by fabricating films on particle supports and producing free-standing capsules. The influence of the degree of thiol-based cross-linking on the mechanical properties of the soft hydrogel systems (core-shell and capsules) was studied using a colloidal-probe (CP) AFM technique. It was found that film mechanical properties, stability, and capsule swelling could be finely tuned by controlling the extent of poly(methacrylic acid) thiol modification. Furthermore, switching the pH from 7.4 to 4.0 led to film densification due to increased hydrogen bonding. Hydrogel capsule systems were found to have stiffness values ranging from 0.9 to 16.9 mN m⁻¹ over a thiol modification range of 5 to 20 mol%. These values are significantly greater than those for previously reported PMASH planar films of 0.7-5.7 mN m⁻¹ over the same thiol modification range (Best *et al.*, *Soft Matter* 2013, 9, 4580-4584). Films on particle substrates had comparable mechanical properties to planar films, demonstrating that while substrate geometry has a negligible effect, membrane and tension effects may play an important role in capsule force resistance. Further, when transitioning from solid-supported films to free-standing capsules, simple predictions of shell stiffness based on modulus changes found for supported films are not valid. Rather, additional effects like diameter increases (geometrical changes) as well as tension buildup need to be taken into account. These results are important for research related to the characterization of soft hydrogel materials and control over their mechanical properties.

Introduction

Soft nanostructured planar and particle hydrogel systems are promising for biomedical applications due to their low cytotoxicity and tunable hydration and rigidity.¹⁻⁴

Increasingly, research is focusing on the influence of advanced material physicochemical properties on cellular and biological interactions.^{5,6} While this is primarily directed to the delivery of therapeutics for *in vivo* systems, its scope extends as far as the understanding of basic cellular function and activity. In a recent example, Giasson and co-workers investigated the effect of hydrogel nanoparticle uptake by RAW 264.7 murine macrophage cells.⁷ The mechanical properties of the hydrogel particles were controlled through the cross-linking degree, and it was found that both the rate and endocytosis mechanism utilized by the cells were governed by the rigidity of the particles studied. In addition to particle systems, the influence of hydrogel film mechanical properties on cellular adhesion, migration, proliferation, and growth has also been studied.⁸ We recently reported that by tuning the stiffness of the thiolated hydrogel films presented here, cervical cancer cell adhesion was able to be mediated.⁹ Such studies are likely to influence the design of future hydrogel materials for tissue engineering and targeted drug delivery applications. However, our current understanding of the properties of free-standing capsule systems is largely based on studies extrapolated from films assembled on planar supports.

Atomic force microscopy (AFM) force spectroscopy is a useful technique for the mechanical analysis of soft nanostructured materials. AFM has been used for the characterization of planar thin films,¹⁰⁻¹² particles,^{7,13} and hollow polyelectrolyte capsules¹⁴⁻¹⁶ with great precision. One of the advantages of such a technique is that single capsules (or particles) can be independently measured, offering considerable mechanical information. However, collecting sufficient data for a reasonable statistical analysis can be time-consuming. Furthering the single particle measurement technique, in 1991 Ducker *et al.* developed a colloidal probe method for higher sensitivity force measurements.¹⁷ Useful for especially soft materials, a colloidal probe (CP) is attached to the end of a cantilever to increase the interaction area when compared to a sharp tip probe.¹⁸ This also offers the advantage of having a well-defined interaction geometry, tailored surface roughness and chemistry, and reduced localized axial strain during measurement.^{18,19} The latter is particularly important, as for large applied axial strains, material nonlinearity can be observed.¹⁹ The CP-AFM technique has been used for the characterization and Young's modulus

(E_Y) determination of polyelectrolyte multilayer films²⁰ and capsules^{21,22} and has been successfully utilized to investigate large hydrogel capsules undergoing pH cycling in buffer under low applied forces.²³ However, apart from the latter study, the tuning and analysis of extremely soft free-standing hydrogel particles has received sparse attention. It is also important to note that while the swelling behavior of planar film and capsule poly(methacrylic acid) (PMA) systems has been investigated,^{24,25} no study has compared the mechanical properties of materials on various substrates with different dimensionalities.

Thiol-modified poly(methacrylic acid) (PMA_{SH}) can be used to form tunable hydrogel systems that have been the focus of recent studies.²⁶⁻²⁸ Single-component films and hydrogel capsules (HCs) can be formed using the layer-by-layer (LbL) assembly technique, through cooperative hydrogen-bonding interactions between PMA and poly(N-vinylpyrrolidone) (PVPON). PMA_{SH} can be then cross-linked through oxidation of the pendant thiol groups into disulfide linkages and the PVPON removed at physiological pH by disrupting the hydrogen bonding network. As the pKa of PMA is $\sim 6-7$, carboxylic acid groups are deprotonated at pH 7.4, leading to intermolecular charge repulsion and capsule swelling. Crosslinked PMA_{SH} systems, however, are able to form highly hydrated and stable networks at high pH. In addition, the disulfide cross-links between adjacent polymers may be cleaved under reducing conditions, such as for intracellular environments, which may facilitate material degradation and cargo release *in vivo*. Specifically, PMA_{SH} systems have been shown to be degradable in simulated intracellular conditions^{29,30} while demonstrating stability at bloodstream pH.³⁰ PMA_{SH} capsules can be antibody-functionalized for enhanced cell binding and association³¹ and can also encapsulate proteins,³⁰ oligonucleotides,³² and double-stranded linear DNA or plasmid DNA.³³ These characteristics demonstrate the considerable promise of PMA_{SH} hydrogel materials for future therapeutic treatments.

In this paper, we quantify the extent of 2-(2-pyridinyldithio)-ethaneamine (PDA) modification of PMA (PMA-PDA), which allows for disulfide cross-link formation, for four different PDA target percentages using UV-vis spectrophotometry. We then examine the

structure and LbL assembly of the constituent PMA_{SH} polymers on particle substrates and quantify the mechanical properties. In particular, we investigate how the degree of cross-linking in these systems affects HC film stability and system stiffness, using CP-AFM. This approach allows for the investigation of free-standing shell mechanics in hollow capsule systems, which can then be compared to soft hydrogel planar films previously reported.⁹ This provides insights into the effects of hydrogel architecture on mechanical resistances at deformations on the nanoscale.

Experimental methods

Materials

The pH of all solutions was measured with a Mettler-Toledo MP220 pH meter. High-purity (Milli-Q) water with a resistivity of >18 MΩ cm was obtained from an inline Millipore RiOs/Origin water purification system. Dialysis tubing (68035-35FT) with a MWCO of 3500 Da was obtained from Thermo Scientific. SiO₂ particles (1.11 ± 0.05 μm diameter) were purchased from Microparticles GmbH (Berlin, Germany) as a 50 g L⁻¹ suspension. Poly(methacrylic acid, sodium salt), (PMA-Na, $M_W = 15\,000\text{ g mol}^{-1}$) was purchased from Polysciences, while PVPON ($M_W = 10\,000\text{ g mol}^{-1}$), 1-ethyl-3-(3-dimethylaminopropyl)carbodiimide (EDC), dithiothreitol (DTT), polyethyleneimine (PEI, $M_W = 25\,000\text{ g mol}^{-1}$), phosphate-buffered saline (PBS), 3-(N-morpholino)propanesulfonic acid (MOPS), 2-(N-morpholino)ethanesulfonic acid (MES), sodium acetate (NaOAc), N-chloro-p-toluenesulfonamide sodium salt (CaT), hydrofluoric acid (HF), and PDA were obtained from Sigma-Aldrich. All chemicals were used as received. Mica (grade V-4) substrates of 22 mm diameter were sourced from SPI Chem. PMA-PDA was synthesized and characterized using nuclear magnetic resonance spectroscopy (¹H NMR, 500 MHz Varian INOVA system at 25 °C) as previously reported.⁹

Prior to LbL assembly, the PMA-PDA precursor was reduced to PMA_{SH} through cleavage of the PDA group. The reduction required a 0.5 M DTT solution in 50 mM MOPS buffer (pH 8) for 30 min at 37 °C with constant agitation. The resultant PMASH solution was

then diluted with 100 mM NaOAc buffer (pH 4) to 0.5 mg mL^{-1} for planar films or 2 mg mL^{-1} for HC LbL assembly. The resultant concentration of cleaved 2-pyridinethione was then measured using UV-vis spectrophotometry against a calibration curve for 2-pyridinethione ($\lambda_{max} = 343 \text{ nm}$).

Fabrication of PMA_{SH} architectures

Planar PMA_{SH} films were fabricated using a previously described method.⁹ For film fabrication on particle templates, a SiO₂ ($100 \text{ }\mu\text{L}$, 50 g L^{-1}) suspension was first washed in ethanol and Milli-Q water, before being dispersed in 100 mM NaOAc buffer (pH 4). Three wash cycles (centrifugation followed by resuspension in $100 \text{ }\mu\text{L}$ NaOAc) were performed after the deposition of each polymer layer. For polymer deposition, $50 \text{ }\mu\text{L}$ of NaOAc buffer was first added and the washed pellet resuspended via mixing. PMA_{SH(x)} and PVPON polymer solutions ($50 \text{ }\mu\text{L}$, 2 mg mL^{-1}) were then added, the solution mixed vigorously, and the polymer allowed to adsorb under mild agitation for 15 min. This process was repeated until five PMA_{SH(x)} layers were deposited. The resulting core-shell particles were then oxidized using CaT (2.5 mM) in MES buffer (10 mM, pH 6) for 60 s, resulting in the formation of disulfide cross-links. The particles were suspended in $20 \text{ }\mu\text{L}$ of NaOAc, to which $80 \text{ }\mu\text{L}$ of HF (5 M, pH 1) was added. *Caution! Hydrofluoric acid is very toxic. Extreme care should be taken when handling HF solution, and only small quantities should be prepared.* The resulting capsules were washed four times via centrifugation (4 min, 4500g) and suspended in $100 \text{ }\mu\text{L}$ of NaOAc solution, followed by three centrifugation/wash cycles in $100 \text{ }\mu\text{L}$ of PBS solution (10 mM, pH 7.4). The resulting single-component PMA_{SH} HCs were characterized using differential interference contrast (DIC) microscopy (Olympus IX71 microscope, Olympus $100\times/1.40$ Oil objective) and processed using ImageJ software and algorithms (NIH).³⁴

AFM cantilever preparation

Both intermittent contact (IC) mode and CP cantilevers were cleaned to remove salt depositions and organics prior to use. The cantilevers were immersed in a 30 vol%

2-propanol solution, followed by Milli-Q water, and then further cleaned using oxygen plasma for 180 s (Harrick Plasma, 0.1 L min⁻¹ O₂ flow rate, 29.6 W, 300 mTorr). Glass substrates for cantilever spring constant calibration and capsule measurements were cleaned using the same method.

AFM intermittent contact mode imaging

For IC mode imaging of collapsed HC structures in air, standard tapping mode cantilevers with a spring constant of 40 N m⁻¹ (Tap300-G, Budget Sensors, Bulgaria) were used. Images were recorded using a JPK Nanowizard II (JPK Instruments AG, Berlin, Germany). Images were post-treated using accompanying JPK image processing software and algorithms. A three-point first-degree polynomial fit was first subtracted, and then a polynomial fit was subtracted from each scan line independently, excluding capsule regions.

AFM force spectroscopy

Force spectroscopy measurements were carried out in PBS (140 mM NaCl, pH 7.4) buffer using a JPK Nanowizard II (The University of Melbourne) for planar film and core-shell particles and a JPK Nanowizard I (Bayreuth University) for HC measurements. Force measurements on planar PMA_{SH} films and CP cantilever calibration and preparation have been described previously.^{9,35} For HC and core-shell particle measurements, PMA_{SH} particles were immobilized onto a PEI-coated glass substrate. The glass substrate was cleaned with 30 vol% 2-propanol and oxygen plasma prior to PEI adsorption. The sample was positioned above an Axiovert 200 microscope (Carl Zeiss MicroImaging, Jena, Germany) with Zeiss objectives (20× and 63× oil). Measurements were conducted by aligning the probe over the center of the visualized colloid, approaching the surface, and then engaging in a "push-pull" cycle with the center axis. This was achieved by lowering the cantilever, until a predetermined force set-point was reached, and then raising the piezo back to its original position. For each measurement, the InvOLS of the PEI-coated glass substrate in working buffer was first determined to allow for accurate

postprocessing of the force data. Approach speeds ranging from 0.3 to 1.5 $\mu\text{m s}^{-1}$ were employed; however, the slopes of the HC force/deformation (F/δ) curves were seen to be independent of approach speed in this range. Each push-pull cycle generated a force-displacement curve for treatment and analysis. Raw AFM data was processed using as-received JPK software to subtract the zero-force baseline during cantilever approach, to set the origin to the initial contact point, and to extract data. The effect of cantilever bending during sample compression was removed using eq 9.1 to give true sample deformation data

$$\delta = \text{displacement} - (F/k_c) \quad (9.1)$$

where k_c is the spring constant of the cantilever. For an incompressible material, the force increases with no observable change in deformation, while for softer samples the gradient reduces due to the compliance of the material. Due to possible viscoelastic effects and associated hysteresis, only the approach force curve was analyzed. The stiffness was evaluated to be the linear gradient of the force/deformation curve in the small-deformation regime, corresponding to deformations in the range of the wall thickness (approximately 40 nm), as to negate the effects of capsule permeability.¹⁸ Reported stiffness values are an average of at least 20 measurements on separate capsules, with the error equating to one standard deviation of the data set. For the colloidal probe cantilevers used there was only a small variation in probe radius ($16.5 \pm 2.0 \mu\text{m}$ for planar measurements and $15.7 \pm 0.2 \mu\text{m}$ for capsule measurements), and the effect of differences in contact area between samples was discounted. For the PMA_{SH(20)} core/shell particles a probe of radius 16.2 μm was used.

For investigating the force spectroscopy of films and capsules at variable pH, the same experimental methodology was used as previously described. After measurement on the respective systems, ca. 50% of the pH 7.4 buffer was carefully removed via micropipet aspiration to prevent drying, and an equal volume of 100 mM NaOAc buffer (pH 4.0) was gently administered. This was repeated 10 times so that the resulting solution was

at pH ~ 4.0 . The force measurements were then repeated at the new pH value.

Debye-Hückel screening length

The screening length (κ^{-1}) was calculated to justify that negligible long-range interactions occur between the colloidal silica probe and the sample. This can be evaluated using eq 9.2,

$$\kappa^2 = 4\pi\lambda_B n \quad (9.2)$$

where n is the concentration of monovalent ions and λ_B is the Bjerrum length, which can be approximated as 0.7 nm, the value for water at room temperature. Formally, λ_B can be calculated using eq 9.3

$$\lambda_B = \frac{e^2}{4\pi\epsilon_0\epsilon_r k_B T} \quad (9.3)$$

where e is the elementary charge, ϵ_0 the vacuum permittivity, ϵ_r the relative dielectric constant of the medium, T the absolute temperature of the solution, and k_B Boltzmann's constant. As we use a PBS buffer (140 mM NaCl, $\lambda_B = 0.7$ nm), we obtain a value for the Debye-Hückel screening length of approximately 0.9 nm. As the range of indentations used for our measurements and analyses varied between 20 and 100 nm, we can assume that nonzero range interactions in our buffered systems will be negligible. This result aligns with findings in literature for similar experiments.²⁰

Applied probe axial strain

As the cantilever probe applies a force to the material, it also exerts an intrinsic axial strain. It is important regarding linear elastic theory that an applied axial strain of 0.2 is not exceeded; otherwise, material nonlinearity becomes an important factor.¹⁹ The axial

strain (ε_{zz}) can be evaluated using the active contact radius (a) during compression, where

$$a = \left(\frac{3FR_{eff}(1-\nu^2)}{4E_Y} \right)^{1/3} \quad (9.4)$$

for the Poisson's ratio (ν), effective probe radius (R_{eff}), and the Young's modulus (E_Y). This can then be substituted into the equation below, which is developed from the differentiation of the axial displacement field (u_z), where $\varepsilon_{zz} = \delta u_z / \delta z$ and

$$\varepsilon_{zz}(0,0) = \frac{2a}{\pi R_{eff}(1-\nu)} \quad (9.5)$$

$$u_z(r,z) = \int \int P_z(r_s)G(s)dA \quad (9.6)$$

which can be evaluated according to the approach set out by Landau and Lifshitz. Here P_z is the pressure distribution and $G(s)$ is the Green's function in A , the contact region.³⁶ We can then model our colloidal probe and capsule system to check the magnitude of the axial strain. When the applied axial strain is modeled for both planar films and capsule systems, it is most sensitive for low Young's modulus and high Poisson's ratio systems. As it is important to only analyze data for applied forces that allow for an axial strain less than 0.2, data collected for both planar and HC samples were only modeled to a maximum force of 1.0 nN. In the case of the low E_Y PMA_{SH(5)} samples, the maximum force studied regarding mechanical properties was 0.7 nN.

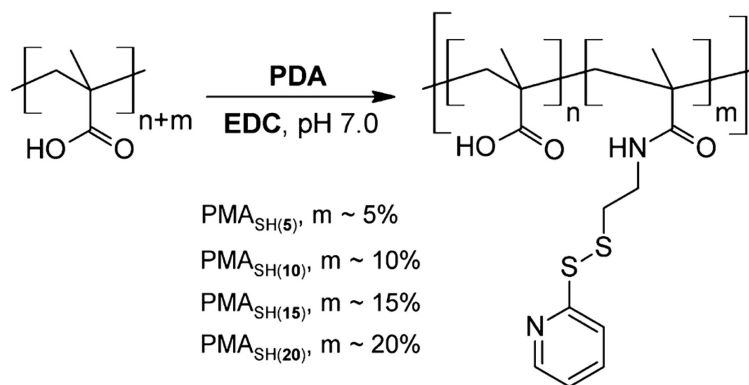


Figure 9.1. Preparation of PMA-PDA. The extent of pendant PDA modification was quantified using both ^1H NMR and UV-vis spectrophotometry (m is the target thiol percentage).

Results and discussion

PMA-PDA characterization

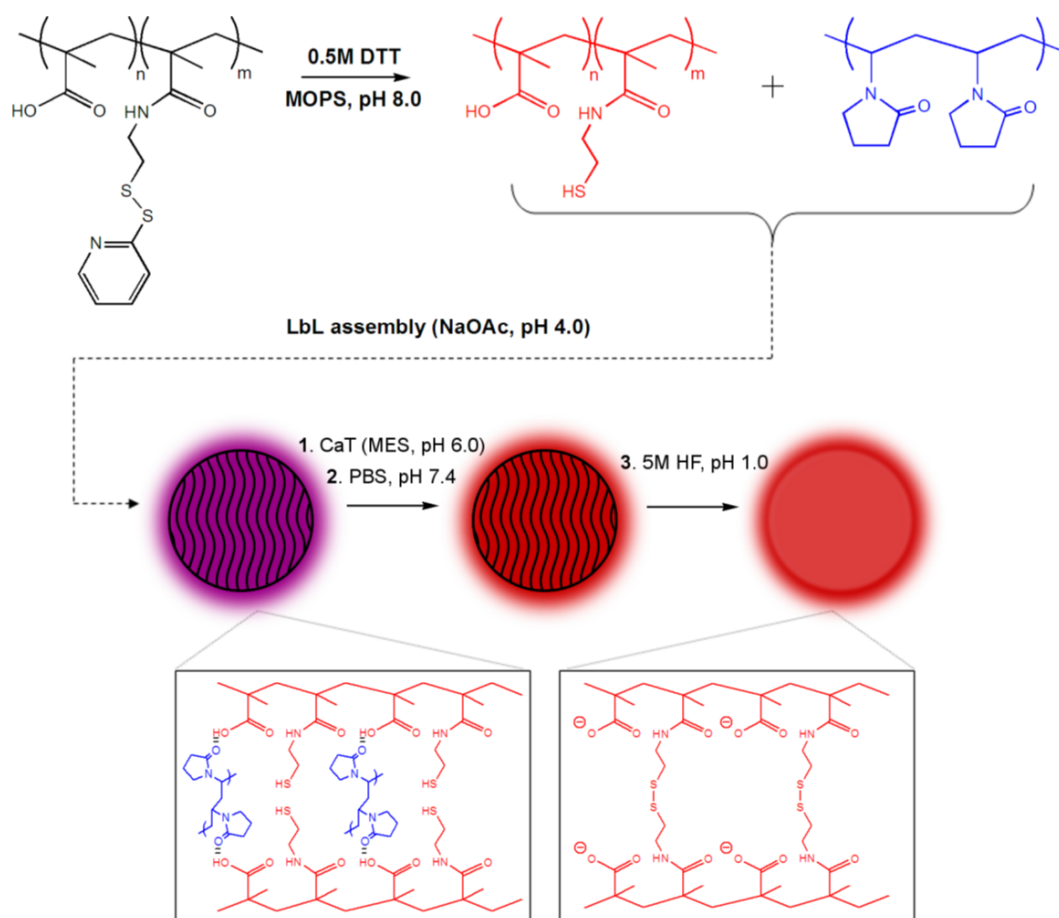
The extent of cross-linking between neighboring PMA_{SH} layers is governed by the number of thiol groups that are present in the polymer, which is equivalent to the number of PDA groups per PMA chain (Figure 9.1). PMA-PDA was synthesized using EDC-activated amide coupling chemistry.³⁰ Target mole percentages of PMA-PDA of 5, 10, 15, and 20 % were prepared, and the resulting modified polymers are denoted as PMA_{SH(5)}, PMA_{SH(10)}, PMA_{SH(15)}, and PMA_{SH(20)}, respectively (PMA_{SH(x)}). The extent of PMA functionalization with PDA has been previously determined by comparing the integrals of the aromatic peaks with the peaks from the backbone of PMA-PDA in corresponding ^1H NMR spectra.⁹ The amount of PDA present here was additionally quantified using UV-vis spectrophotometry by measuring the concentration of 2-pyridinethione (343 nm) that is released after reducing the PDA groups with DTT (pH 8) (Figure 9.8, Supporting Information). For all measured samples the UV-vis characterization yields lower values by 30-40% of the PMA-PDA modification percentage, when compared to the values that were previously obtained using ^1H NMR spectroscopy (Figure 9.9, Supporting Information). It is likely that the PDA groups of PMA-PDA in aqueous solution are situated in the

more hydrophobic regions of the polymer. This diminishes their reactivity and can lead to the mentioned quantification differences, while additionally affecting the actual degree of cross-linking occurring in PMA_{SH} systems. Further, the contribution to the measured differences from small errors in the NMR integration cannot be excluded. However, it is clear from both measurements that there is an increase in PDA substitution with target thiol modification.

Free-standing PMA_{SH} capsules

We then investigated the formation of stable, free-standing, hydrogel capsules at physiological pH. PMA_{SH(x)} polymers were used for LbL assembly of films on particle templates (Scheme 9.1). After the assembly of the planar multilayers, the thiol groups were crosslinked with CaT. Fabrication of free-standing PMA_{SH} capsules was achieved through removal of the silica core using HF, resulting in hollow shells for all modification percentages. Further washing into PBS solution at pH 7.4 resulted in removal of the PVPON by disrupting the H-bonds, as has been experimentally demonstrated previously,²⁸ to yield single-component PMA systems. Furthermore, it was observed that all HC systems fabricated were stable over a period of at least 1 week at physiological pH. The resulting swollen capsules were characterized using DIC microscopy in PBS buffer. AFM imaging was used for air-dried capsules immobilized onto a PEI-coated substrate (Figure 9.2). DIC images in Figure 2 show that with increasing cross-linking degree the optical density of the HCs increases, along with a reduction in the degree of capsule swelling. AFM height image analysis using JPK-SPM data processing software showed that the shell thickness for the dried HCs increased with increasing thiol modification. If we assume that the shell volume is conserved for HC swelling, as proposed by Köhler *et al.*,³⁷ then the difference between theoretical shell thickness and measured dry thickness indicates a partial loss of material from the shell wall (Figure 9.2). Decreasing the number of cross-links leads to less stable hydrogel films, and non-cross-linked material may be lost from the system; this aids capsule expansion at pH 7.4. A general trend was also

Scheme 9.1. Fabrication of hydrogel architectures; top: reduction of PMA-PDA to PMA_{SH(x)} (red). PMA_{SH(x)} and PVPON (blue) are then assembled onto particulate silica templates at pH 4.0 (purple). PMA_{SH(x)} is then oxidized to form stable disulfide cross-links, followed by removal of the PVPON with PBS at pH 7.4. Silica templates were then removed by dissolution using 5 M HF [magnifications show structure before cross-linking (left) and after resuspension in PBS at pH 7.4 (right)]. Five PMA_{SH(x)} layers were deposited.



observed from the AFM scans, where higher cross-linked HCs tended to display more folding features as a result of buckling than less cross-linked HCs. This indicates that higher cross-linked capsules are more rigid.

AFM force spectroscopy measurements were then performed to quantify the mechanical

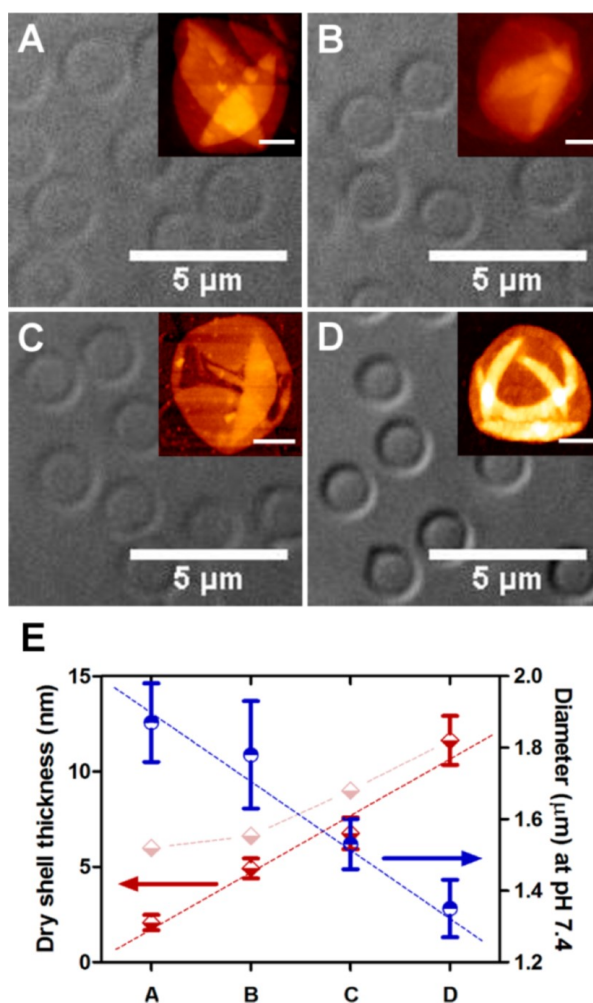


Figure 9.2. DIC microscopy images of HCs dispersed at pH 7.4. Insets show IC AFM scans of dried HCs immobilized onto a PEI-treated substrate (height range from 0 to 50 nm and scale bar 500 nm, for all images). Images A, B, C, and D represent $PMA_{SH(5)}$, $PMA_{SH(10)}$, $PMA_{SH(15)}$, and $PMA_{SH(20)}$ HCs, respectively. HC diameter at pH 7.4 from DIC microscopy analysis (blue circles), air-dried HC shell thickness (red diamonds) from AFM imaging analysis, and theoretical air-dried shell thickness assuming conservation of shell volume (transparent red diamonds) (E). Error bars represent one standard deviation, and dotted lines are used to guide the eye only.

properties of the soft hydrogel materials using CP-AFM and to observe tuning of these properties through variation in cross-linking. In CP-AFM measurements, indentation of

hydrogel systems is achieved through controlled piezo movement in the z-direction, with great precision (Figure 9.3A). As the probe is sensitive to force due to its large surface area, it is important to note that, on the basis of calculations for the Debye-Hückel screening length for the colloidal silica probe in PBS, with 140 mM NaCl, negligible long-range interactions occur between the probe and sample. For all force measurements, there was negligible variation in the radius of the probe used for indentation, and axial strains were kept below 0.2 by analyzing forces <1.0 nN (Figure 9.9, Supporting Information), allowing us to treat deformations as being linearly elastic. A CP cantilever with a spring constant of 6.8 mN m^{-1} was used for $\text{PMA}_{\text{SH}(5)}$, while a cantilever with a constant of 66.4 mN m^{-1} was employed for the measurement of all other HCs. It was seen when collecting the AFM force data that approach and retract curves for the $\text{PMA}_{\text{SH}(10)}$, $\text{PMA}_{\text{SH}(15)}$, and $\text{PMA}_{\text{SH}(20)}$ capsule systems all showed considerable hysteresis.

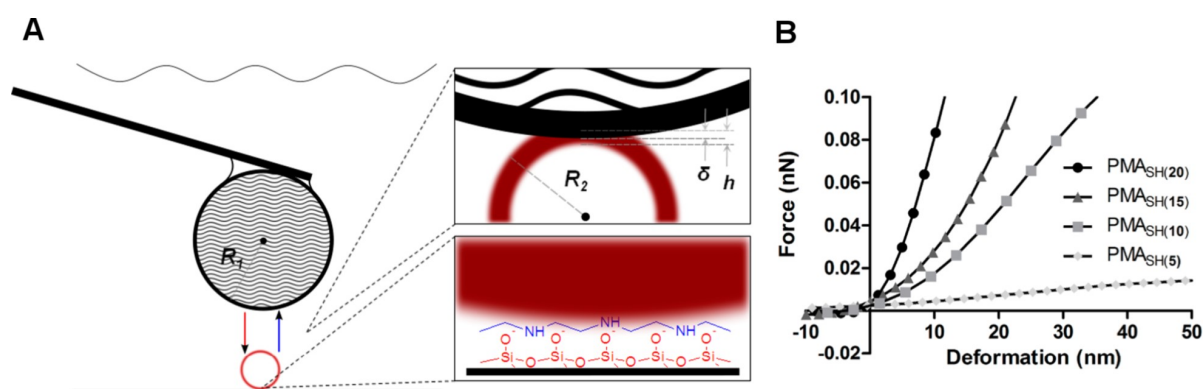


Figure 9.3. Schematic representation of the CP-AFM technique (A) and representative small-deformation F/δ curves for immobilized HCs (B). An attached glass microsphere (radius R_1) is positioned above an immobilized HC in PBS buffer, from where approach (red arrow) and retract (blue arrow) force curves are generated (A). Top inset depicts deformation (δ) of the HC (shell thickness h , radius R_2) by the CP, while the bottom inset illustrates surface immobilization of the HC using PEI (blue).

It was previously observed that the deformation of melamine formaldehyde capsules generates hysteresis features, which generally occur for shell-based systems undergoing

buckling transitions.²² The force response for PMA_{SH(5)} HCs was primarily elastic, owing to the extremely soft and compliant nature of the system. Although the stiffer capsules demonstrated a shell-bending behavior, HCs were also compressed multiple times to ca. 50% of their diameter, and it was seen that the force response was unchanged after at least 12 cycles, using a retracted delay time of 1.0 s. This indicates that the HC compressions are elastic to at least 12 deformations and that they retain their original shell conformation after each compression event.

An important requirement for performing force measurements on shells is that the deformation of the shell by the probe is performed uniaxially.²³ This means that the capsule senses the force normal to its center axis. As the diameter of the colloidal bead is approximately 30 times that of the HC, it was expected that the capsule would experience a force similar to a parallel plate compression, thereby achieving uniaxial deformation over quite a large radial area. To test this, a 12 × 12 force map was performed over a 4 × 4 μm² area where a single PMA_{SH(20)} HC was immobilized. From Figure S4 (Supporting Information), the force curves collected at points A, B, C, and D give equivalent overall spectra with comparatively equal stiffness values (14.0 mN m⁻¹) over 40 nm of indentation and are constant to 65 nm for spectra A, C, and D. It can therefore be assumed that, due to the relative sizes of the probe and capsule, uniaxial deformation can be achieved over a radius of approximately 2-3 μm.

Analyzing the small-deformation gradient for the HCs (Figure 9.3B) allowed for determination of the shell stiffness. While the HCs could be tuned between 0.9 and 16.9 mN m⁻¹ for 5-20 mol% PDA modification, we previously reported that planar hydrogel films could be tuned between 0.7 and 5.7 mN m⁻¹ over the same range.⁹ A quadratic increase was observed for the HC structures, whereas the planar film stiffness increased linearly. The basis of this relationship for the HC results can be observed in the Reissner model for thin spherical shells, where the capsule stiffness is proportional to the square of the shell thickness for an isotropic elastic material (eq 9.7).³⁸

$$E_{Y,Reissner} = \frac{FR_{eff}\sqrt{3(1-\nu^2)}}{4\delta h^2} \quad (9.7)$$

This relationship is evident in the data contained in both Figures 9.2 and 9.3, where a quadratic relationship must exist between HC stiffness and dry shell thickness, similar to trends observed in the literature.²³ The hydrated shell thickness of low-cross-linked HCs is difficult to quantify accurately. As shown in previous work,⁹ low-cross-linked films that experience contraction during dehydration are fragile and lose material. Collapsing a low-cross-linked HC in air and then washing and rehydrating in buffer would result in removal of a portion of the wall material, leading to inaccuracies in determining the wall thickness. In addition, once a capsule collapses, there is increased electrostatic interaction between the PMA_{SH} and surface-bound PEI.

For estimation of the Young's modulus, we assumed that all HCs had an equal hydrated shell volume and that the shell thickness would reduce as the capsules swell with decreasing cross-linking degree. This relationship was demonstrated by Köhler *et al.* for the thermal shrinking of polyelectrolyte capsules, where it was shown that conservation of the shell volume occurred.³⁷ We also employed the Reissner relationship for thin shells (eq 9.7), which has been used previously for modeling the E_Y of polyelectrolyte capsule shells.³⁹ The applicability of thin shell theory, assumed in the Reissner model, is often limited to a shell thickness to radius ratio of less than 1/20.⁴⁰ Collapsed PMA_{SH(20)} HCs have a hydrated shell thickness in PBS buffer of roughly 40 nm (data not shown), with a diameter of 1.35 μm in free suspension. This is equivalent to $h/R \sim 0.06$, greater than the 1/20 limit discussed. Indeed, Mercade-Prieto *et al.* utilized finite element modeling to demonstrate that eq 9.7 only applies to thin shells dependent on bending deformations and that thicker shells require corrections due to considerable Green and Hencky strains.⁴¹ For E_Y evaluation using the Reissner model, R_{eff} was calculated as a function of both CP and HC radial components. As it was not possible to accurately measure the hydrated shell thickness, h was estimated on the basis of shell volume conservation. More weakly cross-linked HCs expanded at pH 7.4, thereby decreasing the shell thickness, assuming an equal initial mass of polymer adsorbed to the surface for all systems. Using these assumptions, the thickness for the PMA_{SH(20)} system was estimated, and the shell

thickness for the other HC systems was based on this. With these values, the Young's modulus of the HCs was found to increase from 0.70 to 2.56 MPa. In the literature, comparable free-standing systems were shown to exhibit elastic moduli typically in the low GPa range.²¹ For instance, Glynos *et al.* found that polylactide microspheres with a cross-linked albumin outer skin had a shell stiffness of 3.8 N m^{-1} , while the E_Y was evaluated to be 2.5 GPa using the Reissner relationship.¹⁵ In contrast, our HCs prove to be remarkably soft and of a similar magnitude to reported collapsed cross-linked PMA capsules evaluated using a Hertz model.²⁵

Influence of pH on film mechanics

Next, we investigated the potential effect of net shell "pressurization" on the observed enhanced force resistance of the HCs. As this effect would be due to PMA_{SH} charge repulsion in the shell, we studied the swelling behavior and stiffness characteristics of $\text{PMA}_{SH(15)}$ capsules at both pH 7.4 and 4.0. As shown in Figure 9.4, the capsule stiffness increases considerably when the pH is dropped to 4.0. It is postulated that if the shell demonstrated a pressurization effect, decreasing the pH and removing the charge repulsion would soften the capsules. As an increase in stiffness is observed with reduced HC swelling, the effect of shell pressurization on force resistance is negligible when compared to other factors.

We then correlated this finding to the pH behavior of PMA_{SH} films fabricated on solid-supported planar structures. $\text{PMA}_{SH(20)}$ was used for this experiment as it has previously demonstrated a high degree of stability, so any differences in mechanical properties of the film at different pH values is a function of film behavior rather than possible film disruption during buffer change. Force experiments were performed as per the other PMA_{SH} film measurements;⁹ however, after the initial measurement, the pH 7.4 buffer was replaced with buffer at pH 4.0, and the force map was repeated. It was observed that the film thickness decreased to ca. 35 nm and that the stiffness and E_Y both increased roughly 20-fold (Figure 9.5). We had previously observed a general film thickness of

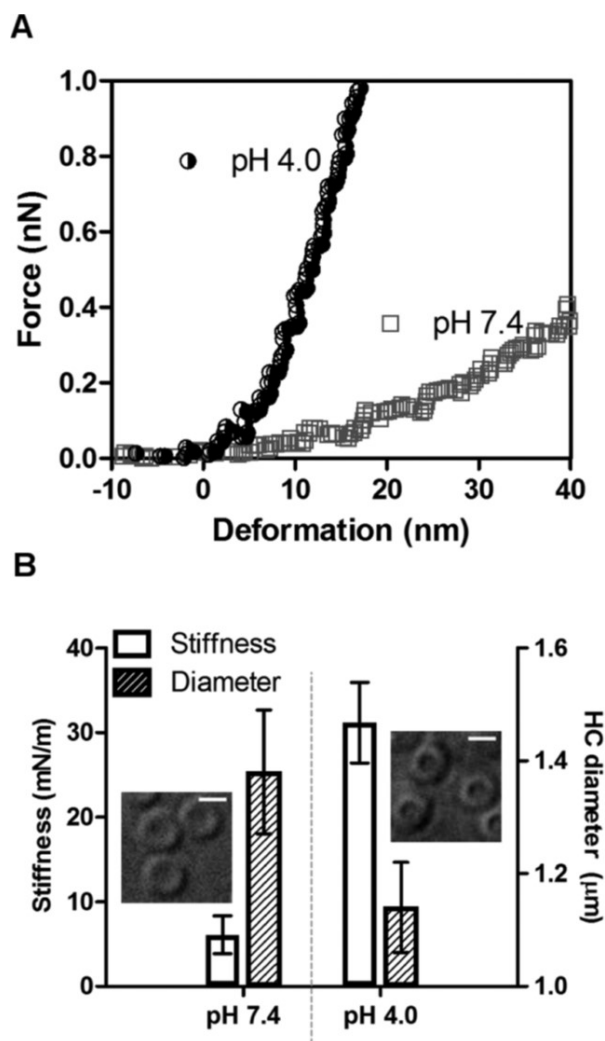


Figure 9.4. Influence of pH on PMA_{SH(15)} HC stiffness. Representative force curves (A) and DIC microscopy images and stiffness and diameter results (B) for PMA_{SH(15)} capsules at both pH 7.4 and 4.0. Error bars in B correspond to one standard deviation, while scale bars for the DIC images equal 1 μm .

130 \pm 50 nm for all PMA_{SH(x)} films,⁹ where the film thickness was evaluated as the deformation distance of the probe, from initial contact to substrate incompressibility, on the basis of a literature technique.⁴² Sukhishvili and co-workers previously found that EDC-cross-linked PMA films also contracted greatly when the pH was reduced.²⁴ This can also be related to results published by Elsner *et al.* for PMA capsules, where it was found that, as the solution pH decreased below the pK_a of the polymer system, the stiffness

increased dramatically due to the formation of hydrogen-bonding interactions.⁴³ These reports are consistent with our observations that a reduction of the solution pH below the pKa of PMA_{SH} increases the film density due to the carboxyl group protonation on the polymer backbone.

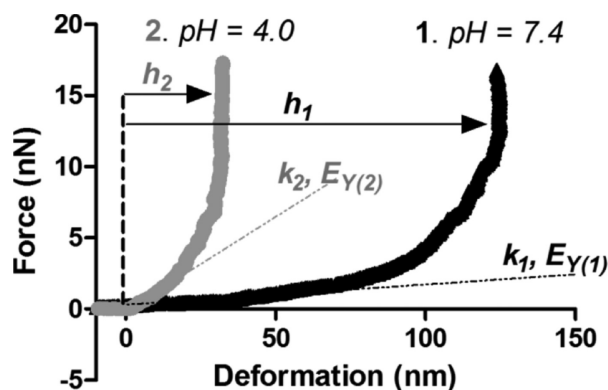


Figure 9.5. The effect of in situ pH variation on PMA_{SH(20)} film thickness (h) and mechanical properties (k , E_Y) measured using CP-AFM.

PMA_{SH} films anchored on particulate supports

As an intermediate step to the production of free-standing hollow capsules, we examined whether mechanical differences between HCs and planar films may occur due to film formation on particle substrates. The LbL technique was used to adsorb alternating layers of PVPON and PMA_{SH(20)} onto particulate silica templates ($d = 1.11 \mu\text{m}$) in NaOAc buffer. The hydrogel core-shell particles were cross-linked, dispersed into PBS buffer, and then immobilized onto a PEI-coated glass substrate. Measurements were performed on immobilized colloids visualized optically; the probe was positioned above the center axis of the colloid to achieve uniaxial deformation, and an approach/retract cycle was initiated to measure small material deformations of the film as a function of the applied force. Immobilization is an important aspect of the measurement, as insufficient immobilization can lead to lateral movement during force application and result in poor or misleading spectra. The material stiffness in the small deformation

regime was determined from the treated spectra and found to be $2.1 \pm 0.4 \text{ mN m}^{-1}$, approximately half that of $\text{PMA}_{SH(20)}$ planar films on mica, as shown in Figure 9.6. This is an interesting observation, as we would expect core-shell particles to be deformed at two contact points when under an applied force: at both the substrate and colloidal probe surfaces. This would lead to a material stiffness half that of the planar hydrogel films, as an incompressible spherical substrate allows for no bending resistance. A further explanation for this was given by Fytas and co-workers when they observed that poly(methyl methacrylate) (PMMA) capsules had different mechanical properties to SiO_2 -PMMA core-shell particles.⁴⁴ Using light-scattering techniques, it was postulated that these differences arose due to differences in the system architecture.

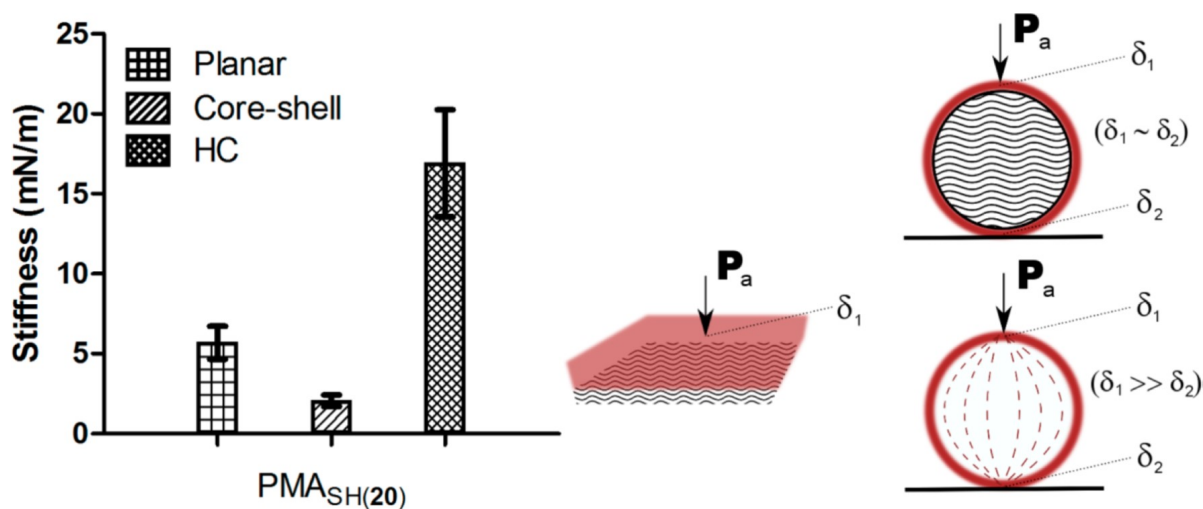


Figure 9.6. Stiffness values for $\text{PMA}_{SH(20)}$ hydrogels confined in planar film, core-shell, and HC architectures. An applied force (P_a) affects a deformation (δ) of the film surface. Error bars represent one standard deviation (planar film data reproduced from ref [9]).

Transition from planar films to hollow capsules

We previously reported on the mechanical properties of PMA_{SH} planar films on atomically flat mica substrates.⁹ It was found that the stiffness of the hydrogel films could be

effectively tuned through adjustment of the degree of disulfide-based crosslinking and that all films were mechanically homogeneous over a $50 \mu\text{m}^2$ area. From 5 to 20 mol% PDA modification, we reported that the stiffness of the films was found to increase from 0.7 to 5.7 mN m^{-1} , while the E_Y increased from 0.4 to 2.1 kPa using a Hertz model or from 1.0 to 2.3 kPa evaluated using the Johnson-Kendall-Roberts (JKR) model for adhesive contact.⁹ All mechanical results were observed to increase linearly with increasing PDA modification. Comparable materials in literature characterized using CP-AFM measurements demonstrate that planar PMA_{SH} films are extremely soft. Using Hertz modeling, soft gelatin films were found to have an E_Y of 20 kPa to 1 MPa,¹⁰ while both the Picart and Singer groups found that, using EDC as a cross-linker, thin hydrogel films could have their modulus tuned between 3 kPa and 1 MPa.^{20,45}

In this paper we have shown that the elastic modulus determined for HCs based on Reissner's theory is 3 orders of magnitude greater than those for planar films of the same material. It would generally be assumed that these ranges would be similar, as the material is constant. A possible explanation for these differences was provided by Glynos and co-workers, based on their observation that thick-shelled polymer microspheres had an E_Y approaching that of the bulk material, whereas thinner shelled spheres had a dramatically increased E_Y .⁴⁶ They postulated that morphological and molecular restructuring may occur due to confinement in thinner shells and that, as the dimensions approach the nanoscale, surface effects such as surface tension and gradient elasticity can have a profound influence on material properties.⁴⁶ In addition, the Reissner model is not directly applicable to the PMA_{SH} HC systems studied. The shell thickness and small diameter of the HCs dictates that they are at, or above, the limit of thin shell theory required for use of the Reissner model. Above this limit, estimates of E_Y are reliant on significant corrections, and accuracy is dependent on accurate shell thickness information.⁴¹ Other assumptions in these models were met, however, as uniaxial deformation and low applied axial strains were achieved during measurement. In addition, this result highlights the requirement of contact mechanics models for soft, viscoelastic, nanostructured hydrogel shells.

The increased HC stiffness observed when compared to planar films fabricated using the same $\text{PMA}_{SH(x)}$, as is seen in Figure 9.7, is of inherent interest. During HC compression, system deformation may occur at the two contact points on the shell surface; however, this will occur predominantly at the CP contact point due to finite energy dissipation through the shell structure via bending resistances. The CP cantilever measures resistance to applied force through both the film and shell bending resistances, if we assume that the HC is not instantaneously permeable to the encapsulated solvent. This would increase the stiffness experienced by the cantilever when compared to the single contact point indentation for films, which allow for increased energy dissipation, as they can be viewed as essentially an infinite plane. Geometrically, spheres have the smallest surface area for a given volume and have a maximized moment of inertia increase around the shell bending axis. This gives a spherical shell structure an increased apparent stiffness when compared to an immobilized membrane of the same material and shell thickness. Further, to our knowledge, planar materials with a system stiffness $<5 \text{ mN m}^{-1}$ have not been characterized in the literature, and only one example of similarly soft HCs has been shown,⁴³ demonstrating the applicability of CP-AFM for this task.

As shown in Figure 9.7, the planar film stiffness increases linearly with cross-linking degree, as the network becomes increasingly dense and robust to external force. HC stiffness increases at a greater rate with cross-linking, as both the shell becomes more robust and the capsules resist expansion. The increase in stiffness observed for the HCs is a combination of both enhanced material stiffness (shown through increases in film stiffness) and consolidated shell structure (verified based on the observed increases in shell thickness). Previous analyses of PSS/PAH multilayers in planar and capsule configurations demonstrated that capsules tend to have a greater E_Y (1.5-2.0⁴⁷ and 1.3-1.9 GPa¹⁴) when compared to planar films (0.30-0.59 GPa) measured using an elastic buckling technique.⁴⁸ Bathe and co-workers were able to show through finite element analysis that the ratio of membrane to bending energies stored within a shell system was highly sensitive to the shell thickness.⁴⁹ These results support the argument that the

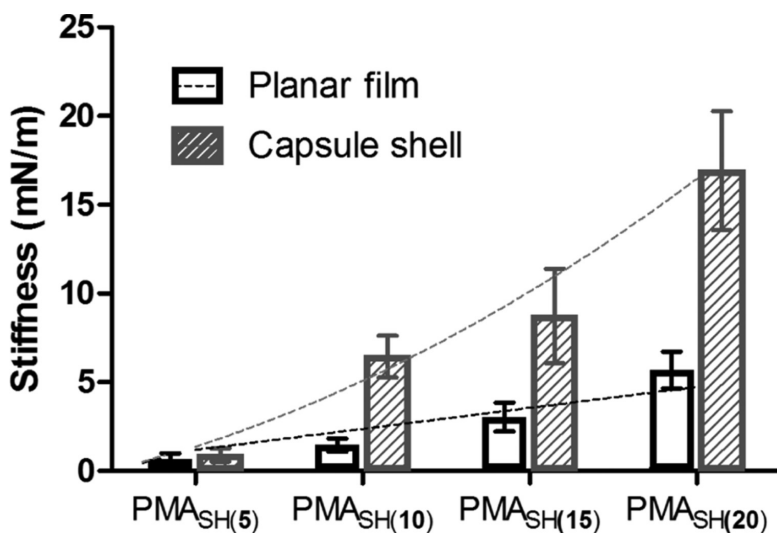


Figure 9.7. Stiffness comparison results for planar hydrogel films on mica substrates (planar film data reproduced from ref [9]) and PEI immobilized HCs. Planar film data are fit with a linear regression, while capsule shell stiffness data are fit with a second-order polynomial. Error bars represent one standard deviation.

shell structure of PMA_{SH} HCs aids in improving the mechanical stiffness of the system. This finding can be reasoned when considering the bending energies of thin shells and spherical vessels under an applied pressure. On the basis of the Kirchhoff-Love plate theory for elastic shells, the energy change derived from a differential shell geometry is made up of both membrane and bending strains.⁵⁰ Due to increased stiffness values for the HCs, we were able to observe these shell resistances for micrometer-sized soft hydrogel capsules when compared to planar films of the same material.

Conclusion

The mechanical properties of PMA_{SH(x)} free-standing hollow capsules with varying degrees of cross-linking were investigated. The stability of these constructs was analyzed using optical and AFM techniques, and it was found that introducing a higher degree of disulfide cross-linking improved both network density and stability. The material

compliance was quantified using CP-AFM, and it was found that a hollow capsule architecture offers a greater force resistance when compared to substrate-supported (planar and particulate) films of the same material. It was postulated that this was due to the transfer of the applied force to bending energies within the capsule structure, geometric effects, and shell densification. The mechanical properties of the PMA_{SH} systems were quantified using the highly sensitive CP-AFM technique, and the results indicated that they were extremely soft and tunable via network density.

We envisage that these results will be useful for researchers involved in the study and characterization of soft and tunable hydrogel shells, in particular for studies where particle material parameters are assumed on the basis of planar film studies. Future work will examine the biological interaction of these materials and the effect that compliance has upon effects such as cellular association and uptake, *in vivo* clearance rates, cellular adhesion strength, and modulation of biomolecule/conjugate interactions.

Acknowledgments

This work was supported by the Australian Research Council under the Australian Laureate Fellowship (F.C., 120100030) and Discovery Project (F.C., 130101846) schemes, and the European Union-funded Nanosirna Project (A.F., F.C.).

References

- (1) Hoare, T. R.; Kohane, D. S. *Polymer* **2008**, *49*, 1993–2007.
- (2) Becker, A. L.; Johnston, A. P. R.; Caruso, F. *Small* **2010**, *6*, 1836–1852.
- (3) Nguyen, K. T.; Shukla, K. P.; Moctezuma, M.; Braden, A. R. C.; Zhou, J.; Hu, Z.; Tang, L. *Journal of biomedical materials research. Part A* **2009**, *88*, 1022–30.
- (4) Stuart, M. A. C.; Huck, W. T. S.; Genzer, J.; Mueller, M.; Ober, C.; Stamm, M.; Sukhorukov, G. B.; Szleifer, I.; Tsukruk, V. V.; Urban, M.; Winnik, F.; Zauscher, S.; Luzinov, I.; Minko, S. *Nature Materials* **2010**, *9*, 101–113.
- (5) Best, J. P.; Yan, Y.; Caruso, F. *Advanced Healthcare Materials* **2012**, *1*, 35–47.
- (6) Yan, Y.; Such, G. K.; Johnston, A. P. R.; Best, J. P.; Caruso, F. *Acs Nano* **2012**, *6*, 3663–3669.
- (7) Banquy, X.; Suarez, F.; Argaw, A.; Rabanel, J. M.; Grutter, P.; Bouchard, J. F.; Hildgen, P.; Giasson, S. *Soft Matter* **2009**, *5*, 3984–3991.
- (8) Georges, P. C.; Janmey, P. A. *Journal of Applied Physiology* **2005**, *98*, 1547–1553.
- (9) Best, J. P.; Javed, S.; Richardson, J. J.; Cho, K. L.; Kamphuis, M. M. J.; Caruso, F. *Soft Matter* **2013**, *9*, 4580–4584.
- (10) Domke, J.; Radmacher, M. *Langmuir* **1998**, *14*, 3320–3325.
- (11) Kovalev, A.; Shulha, H.; Lemieux, M.; Myshkin, N.; Tsukruk, V. V. *Journal of Materials Research* **2004**, *19*, 716–728.
- (12) Markutsya, S.; Jiang, C. Y.; Pikus, Y.; Tsukruk, V. V. *Advanced Functional Materials* **2005**, *15*, 771–780.
- (13) Schmidt, S.; Zeiser, M.; Hellweg, T.; Duschl, C.; Fery, A.; Mohwald, H. *Advanced Functional Materials* **2010**, *20*, 3235–3243.
- (14) Dubreuil, F.; Elsner, N.; Fery, A. *European Physical Journal E* **2003**, *12*, 215–221.
- (15) Glynos, E.; Sboros, V.; Koutsos, V. *Materials Science and Engineering B-Advanced Functional Solid-State Materials* **2009**, *165*, 231–234.

- (16) Ye, C.; Drachuk, I.; Calabrese, R.; Dai, H.; Kaplan, D. L.; Tsukruk, V. V. *Langmuir* **2012**, *28*, 12235–12244.
- (17) Ducker, W. A.; Senden, T. J.; Pashley, R. M. *Nature* **1991**, *353*, 239–241.
- (18) Fery, A.; Dubreuil, F.; Mohwald, H. *New Journal of Physics* **2004**, *6*, 13.
- (19) Dimitriadis, E. K.; Horkay, F.; Maresca, J.; Kachar, B.; Chadwick, R. S. *Biophysical Journal* **2002**, *82*, 2798–2810.
- (20) Francius, G.; Hemmerle, J.; Ohayon, J.; Schaaf, P.; Voegel, J. C.; Picart, C.; Senger, B. *Microscopy Research and Technique* **2006**, *69*, 84–92.
- (21) Pretzl, M.; Neubauer, M.; Tekaat, M.; Kunert, C.; Kuttner, C.; Leon, G.; Berthier, D.; Erni, P.; Ouali, L.; Fery, A. *Acs Applied Materials & Interfaces* **2012**, *4*, 2940–2948.
- (22) Lulevich, V. V.; Andrienko, D.; Vinogradova, O. I. *Journal of Chemical Physics* **2004**, *120*, 3822–3826.
- (23) Elsner, N.; Dubreuil, F.; Weinkamer, R.; Wasicek, M.; Fischer, F.; Fery, A. In: Grundke, K., Stamm, M., Adler, H. J., Eds.; Springer: 2006; Chapter Mechanical properties of freestanding polyelectrolyte capsules: a quantitative approach based on shell theory, pp 117–123.
- (24) Kozlovskaya, V.; Kharlampieva, E.; Mansfield, M. L.; Sukhishvili, S. A. *Chemistry of Materials* **2006**, *18*, 328–336.
- (25) Drachuk, I.; Shchepelina, O.; Lisunova, M.; Harbaugh, S.; Kelley-Loughnane, N.; Stone, M.; Tsukruk, V. V. *Acs Nano* **2012**, *6*, 4266–4278.
- (26) Becker, A. L.; Zelikin, A. N.; Johnston, A. P. R.; Caruso, F. *Langmuir* **2009**, *25*, 14079–14085.
- (27) Chong, S.-F.; Lee, J. H.; Zelikin, A. N.; Caruso, F. *Langmuir* **2011**, *27*, 1724–1730.
- (28) Zelikin, A. N.; Li, Q.; Caruso, F. *Chemistry of Materials* **2008**, *20*, 2655–2661.
- (29) Saito, G.; Swanson, J. A.; Lee, K. D. *Advanced Drug Delivery Reviews* **2003**, *55*, 199–215.

- (30) Zelikin, A. N.; Quinn, J. F.; Caruso, F. *Biomacromolecules* **2006**, *7*, 27–30.
- (31) Shimoni, O.; Postma, A.; Yan, Y.; Scott, A. M.; Heath, J. K.; Nice, E. C.; Zelikin, A. N.; Caruso, F. *Acs Nano* **2012**, *6*, 1463–1472.
- (32) Zelikin, A. N.; Li, Q.; Caruso, F. *Angewandte Chemie-International Edition* **2006**, *45*, 7743–7745.
- (33) Zelikin, A. N.; Becker, A. L.; Johnston, A. P. R.; Wark, K. L.; Turatti, F.; Caruso, F. *Acs Nano* **2007**, *1*, 63–69.
- (34) Abramoff, M. D.; Magalhaes, P. J.; Ram, S. J. *Biophotonics Int* **2004**, *11*, 36–42.
- (35) Attard, P. *J. Phys.: Condens. Matter* **2007**, *19*, 473201–473233.
- (36) Landau, L. D.; Lifschitz, E. M., *Theory of Elasticity*; Pergamon Press Ltd, Oxford: 1959, pp 30–36.
- (37) Kohler, K.; Shchukin, D. G.; Mohwald, H.; Sukhorukov, G. B. *Journal of Physical Chemistry B* **2005**, *109*, 18250–18259.
- (38) Reissner, E. *Journal of Mathematics and Physics* **1946**, *25*, 80–85.
- (39) Fery, A.; Weinkamer, R. *Polymer* **2007**, *48*, 7221–7235.
- (40) Gregory, R. D.; Milac, T. I.; Wan, F. Y. M. *Studies in Applied Mathematics* **1998**, *100*, 67–94.
- (41) Mercade-Prieto, R.; Thomas, C. R.; Zhang, Z. *European Biophysics Journal with Biophysics Letters* **2013**, *42*, 613–620.
- (42) McNamee, C. E.; Yamamoto, S.; Higashitani, K. *Langmuir* **2007**, *23*, 4389–4399.
- (43) Elsner, N.; Kozlovskaya, V.; Sukhishvili, S. A.; Fery, A. *Soft Matter* **2006**, *2*, 966–972.
- (44) Still, T.; Sainidou, R.; Retsch, M.; Jonas, U.; Spahn, P.; Hellmann, G. P.; Fytas, G. *Nano Letters* **2008**, *8*, 3194–3199.
- (45) Boudou, T.; Crouzier, T.; Auzely-Velty, R.; Glinel, K.; Picart, C. *Langmuir* **2009**, *25*, 13809–13819.

- (46) Glynos, E.; Koutsos, V.; McDicken, W. N.; Moran, C. M.; Pye, S. D.; Ross, J. A.; Sboros, V. *Langmuir* **2009**, *25*, 7514–7522.
- (47) Gao, C.; Donath, E.; Moya, S.; Dudnik, V.; Mohwald, H. *European Physical Journal E* **2001**, *5*, 21–27.
- (48) Nolte, A. J.; Rubner, M. F.; Cohen, R. E. *Macromolecules* **2005**, *38*, 5367–5370.
- (49) Bathe, K. J.; Chapelle, D.; Lee, P. S. *International Journal for Numerical Methods in Engineering* **2003**, *57*, 1039–1052.
- (50) Love, A. E. H. *Philosophical Transactions of the Royal Society of London* **1888**, *179A*, 491–546.

Supporting information

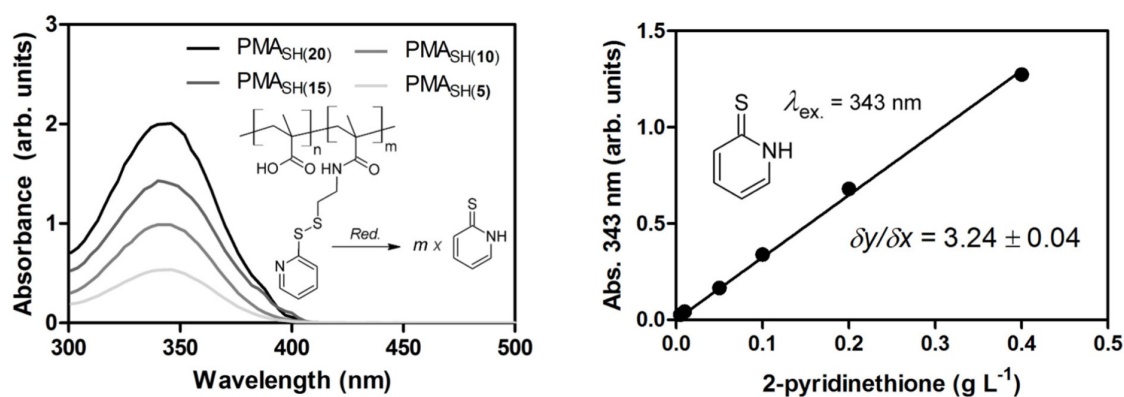


Figure 9.8. UV-Vis spectra for the PMA-PDA polymers under reducing conditions (*left*, $\lambda_{2\text{-pyridinethione}} \approx 343 \text{ nm}$), and resulting 2-pyridinethione calibration curve (*right*).

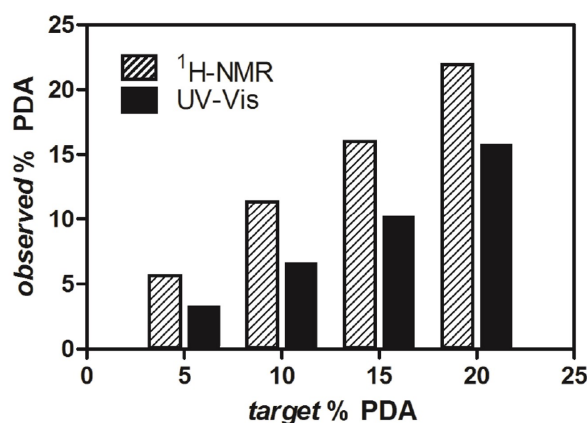


Figure 9.9. Quantification of the amount of pendant PDA attached to PMA using ¹H-NMR (NMR results reproduced from ref. [1]) and UV-Vis spectrophotometry.

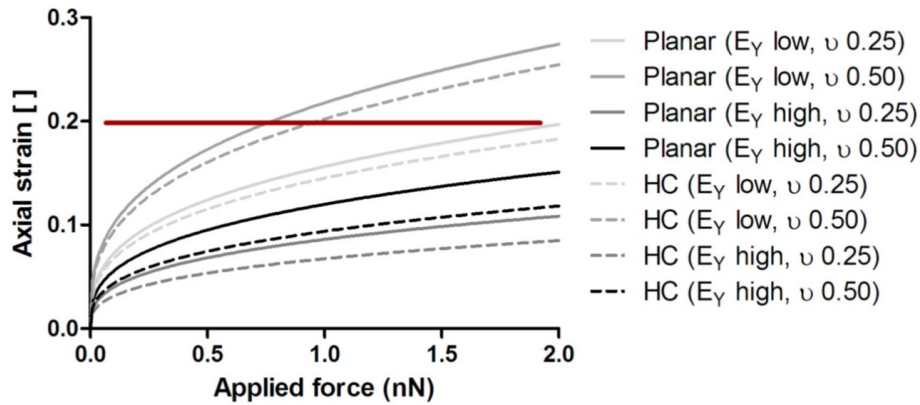


Figure 9.10. Theoretical axial strain plots for boundary conditions of material parameters. The red line indicates the maximum allowable axial strain for linear elastic theory to be valid ($\varepsilon_{zz} = 0.2$). It was assumed that a glass bead probe of radius $15 \mu\text{m}$ was used while varying the Poisson ratio from 0.25 (low) to 0.50 (high).

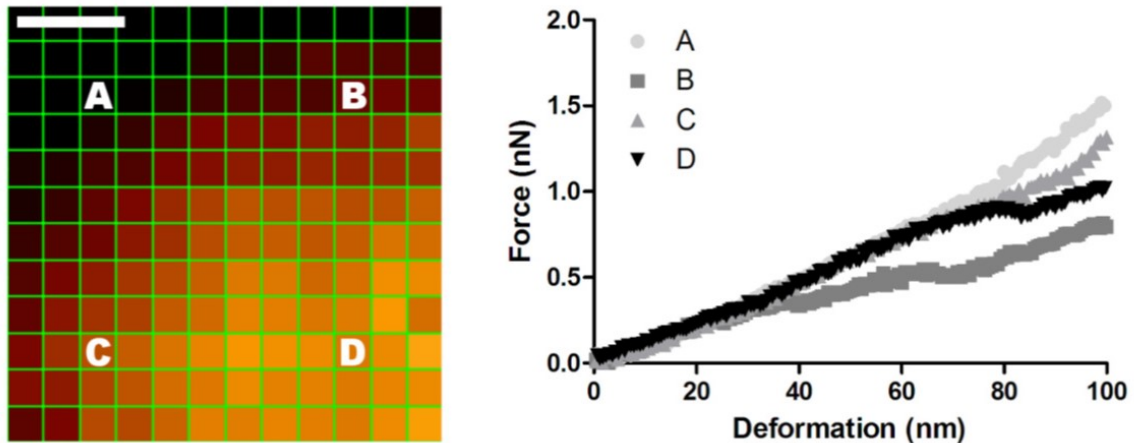


Figure 9.11. Force map (*left*) showing the piezo height distribution (scale bar $1 \mu\text{m}$, vertical color scale 0 to 500 nm) over a $4 \times 4 \mu\text{m}^2$ grid for a single $\text{PMA}_{SH(20)}$ HC. Spectra A, B, C and D (*right*) correspond to the approach-retract curves labeled on the force map.

References

- (1) Best, J. P.; Javed, S.; Richardson, J. J.; Cho, K. L.; Kamphuis, M. M. J.; Caruso, F. *Soft Matter* **2013**, *9*, 4580–4584.

10

Stiffness-dependent *in vitro* uptake and lysosomal acidification of colloidal particles

Raimo Hartmann, Marcel Weidenbach, Martin Neubauer, Andreas Fery and Wolfgang J. Parak; *Angewandte Chemie International Edition* **2014**, DOI:10.1002/anie.201409693.
Reprinted with permission. ©2014 John Wiley and Sons.

Abstract

The physico-chemical properties of colloidal particles determine their uptake into cells. For a series of microparticles only one parameter, the mechanical stiffness, was varied, whereas other parameters such as size, shape, and charge were kept constant. The uptake was monitored *in situ* by analyzing individual particle trajectories including the progress of endocytosis, derived from local pH measurements around each particle. Evidence is presented that soft particles with low stiffness are transported faster to lysosomes than stiffer ones.

Full text

The number of applications based on the interaction of colloids with cells has been increasing steadily over the past few years, mostly for sensing or delivery based applications. As most of the approaches require particle internalization, cellular uptake mechanisms have been heavily studied.¹ Unfortunately, the ultimate goal, to entirely correlate the uptake process with the physico-chemical parameters of the particles, is not trivial, in particular as many of these properties are interrelated.² Thus, it is extremely challenging to obtain consistent studies, in which only one particular parameter of the particles is varied, while all other properties are held constant. Properties that have been studied systematically comprise particle size,^{3,4} shape,⁵ and charge.^{6,7} While size, shape, and charge are the "standard" well investigated parameters influencing *in vitro* particle incorporation by cells, there are many additional well-defined physical properties, for instance particle stiffness, which might also play an important role. Dependent on their stiffness hollow microparticles are compressed and deformed upon cellular internalization.^{8,9} Based on theoretical considerations Yi *et al.* claimed that cellular processing of deformable particles might be different to that of stiffer counterparts, because these particles are less prone to membrane wrapping.¹⁰ Hydrogel-based nanoparticles with a Young's modulus between 30 and 140 kPa were found to be internalized more efficiently by RAW 264.7 macrophages than softer (<30 kPa) or stiffer (>140 kPa) nanoparticles.¹¹ Liu *et al.* reported that the

uptake rate of flexible micron-sized hydrogel particles (15-35 kPa) was higher than that of less elastic ones (75-160 kPa) by HepG2 cells.¹²

Polymer capsules, for example, hollow microparticles synthesized by layer-by-layer assembly of oppositely charged polyelectrolytes,¹³ are a well-suited model system for systematic investigations, since their various physico-chemical properties can be tuned independently.¹⁴ Size^{15,16} and shape¹⁷⁻¹⁹ can be varied by using different template cores, and the sign of the surface charge is simply determined by the charge of the outermost layer. Stiffness can be tuned by variation of the number of polymer layers or by the polymer materials used.²⁰⁻²² Thus, polyelectrolyte capsules are a convenient particle system to investigate stiffness-dependent *in vitro* uptake by cells, in a way such that particle size, shape, charge, and surface chemistry remain constant, while stiffness is varied. Most important, with this system it is possible to change exclusively one parameter, whereby the outer surface remains the same, and physicochemical parameters other than stiffness are fully maintained.

Upon internalization, capsules (*i.e.* particles) are taken up *via* endocytic processes and are transferred from the neutral extracellular medium to increasingly acidic intracellular vesicles of different maturity, and finally end up in the lysosome.²³ The local pH around each particle can be used as read-out that describes its present stage of uptake. For this purpose particles can be loaded with pH-sensitive fluorophores such as fluorescein-based dyes^{24,25} and seminaphtharhodaffluor (SNARF),^{25,26} which allow for time-resolved detection of the local pH around the capsules in extra- and intracellular environments.^{8,26,27} Based on LbL assembly¹³ around sacrificial $CaCO_3$ template cores we synthesized pH-sensitive capsules with a different number of layers to vary capsule stiffness with two frequently used polymer systems (nondegradable polymers: poly(sodium 4-styrenesulfonate) (PSS) and poly(allylamine hydrochloride) (PAH); degradable polymers: dextran sulfate sodium salt (DextS) and poly-l-arginine hydrochloride (PLArg));^{23,28} *cf.* Figure 10.1a). Two batches of template cores with resulting diameters of 4.1 μm (size "S") and 4.7 μm (size "L") were used. The pH sensitivity was achieved by embedding SNARF-1^{25,26}-labeled dextran into the cavity of the capsules. Response curves relating the ratio of red

(I_r ; 615-700 nm) to yellow (I_g ; 560-615 nm, shown in green) fluorescence $I_r/I_g(\text{pH})$ were obtained for each type of capsule (Figure 10.1b). With this setup changes in pH could be monitored down to values around 4.5. However, SNARF-1 embedded in biodegradable DextS/PLArg capsules was slightly less sensitive at lower pH values.

The stiffness of the capsules in solution was determined by atomic force microscopy (AFM) for each type of capsule^{21,22} (Figure 10.1c). As expected, the stiffness of the capsules increased with the number of polyelectrolyte layers. Presumably this is a direct consequence of the shell thickness, which increases with the number of polyelectrolyte layers. In particular, in case of the DextS/PLArg capsules there were batch-to-batch variations of the absolute stiffness values (*cf.* the Supporting Information (SI), Figure 10.8).

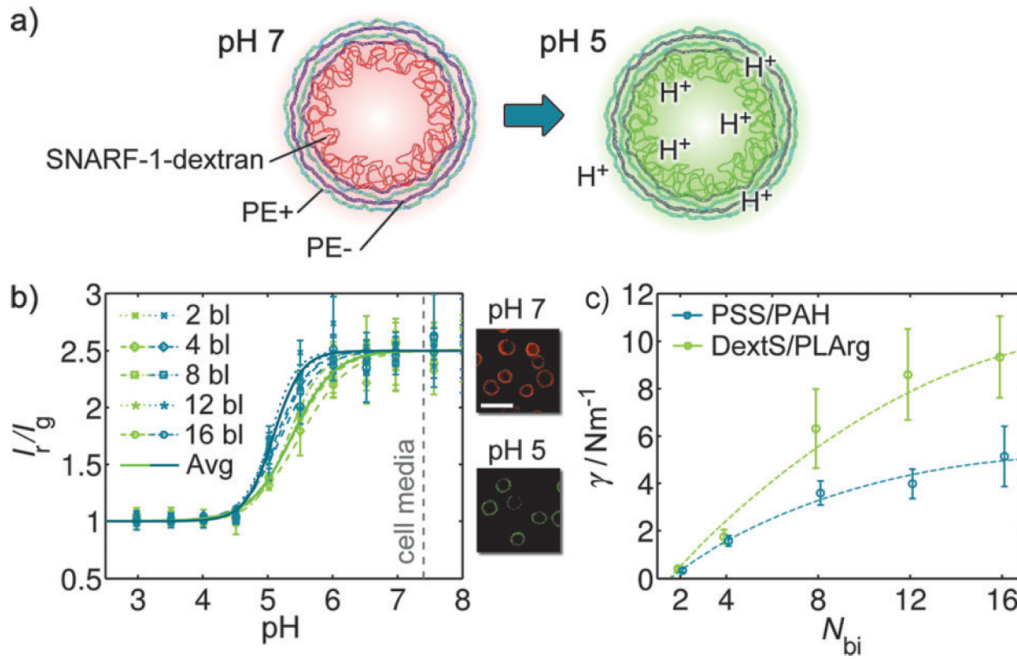


Figure 10.1. a) Sketch of one polyelectrolyte capsule, which comprises $N_{bi} = 2$ bilayers, each composed out of one negatively charged (PE- (purple), PSS or DextS) and one positively charged (PE+ (light blue), PAH or PLArg) polyelectrolyte layer. Due to the positively charged outermost layer the whole particle is positively charged (*cf.* Figure 10.9). pH-sensitive fluorophores SNARF-1 conjugated to dextran are located inside the cavity. b) The red-to-green ratio (false colors) of the fluorescence signal I_r/I_g from the capsule cavity depends on the local pH around each capsule. Response curves are shown for capsules of 2-16 bilayers (bl) of size "S" (green: DextS/PLArg, blue: PSS/PAH) and are normalized to pH 7.4 (cell media). The solid lines (labeled "Avg") show the average response curves for both types. The insets (scale bar: $2 \mu\text{m}$) show fluorescence microscopy images of capsules at neutral (red fluorescence) and acidic pH (green fluorescence). c) The dependence of the mechanical stiffness γ for the different capsules ($d \approx 4.1 \mu\text{m}$) as determined by AFM is plotted *versus* the number of bilayers N_{bi} making up the capsule shell. The dashed lines are guides to the eye only.

The uptake process was monitored in different adherent cells (cell lines as well as primary

cells). Upon internalization, the local environment of the capsules changed from neutral (cell medium) to strongly acidic (lysosome), which can be seen by the ratiometric readout of the pH-sensitive fluorophores embedded in the capsules^{26,27} (Figure 10.2a). First (image A), each capsule is located in neutral/slightly alkaline cell medium, thus leading to high, constant I_r/I_g values. At one point in time, here defined as t_C , the particle touches the cell surface (image B) and then it moves along the outer plasma membrane, as visible by the red emission which demonstrates extracellular location. It is then engulfed by the cell, as visualized by the change in fluorescence, and subsequently passed to more and more acidic compartments (images C and D), until at one point the pH seems to remain constant. At this point (image E) the capsule reaches its final destination, the lysosome.²³ If the pH decreases below 4.5 changes to an even more acidic environment are no longer observable due to the limited sensitivity of the pH-indicator used (Figure 10.1b). Figure 10.2b shows that the pathway of uptake is not necessarily continuous, as can be seen by the jump of the pH-values along the trace in image D at $t = 525$ min. We speculate that at this point in time the capsule-containing vesicular compartment may have fused with a vesicle of potentially much lower pH. (A correlation of fusion events of acidic vesicles with the pH values of the capsule-containing compartment can be found in Figure 10.19.) In order to derive quantitative data from the $I_r/I_g(t)$ traces we define t_A as the acidification time and $t_{P10\%}/t_{P50\%}$ as the processing time. The processing time is the duration from the first contact t_C (membrane attachment) of the capsule with the cell, following its incorporation and finally partial acidification (10% or 50%). The acidification time describes the duration of acidification from high to low pH following the sigmoidally shaped time-dependent $(I_r/I_g)(t)$ curve (Figure 10.2b, for more details see Figure 10.12).

The uptake of microcapsules can differ significantly between different cell types and capsule materials.^{8,23} In most previous studies research focused on quantifying the amount of incorporated capsules *versus* time, while in this work the acidification and

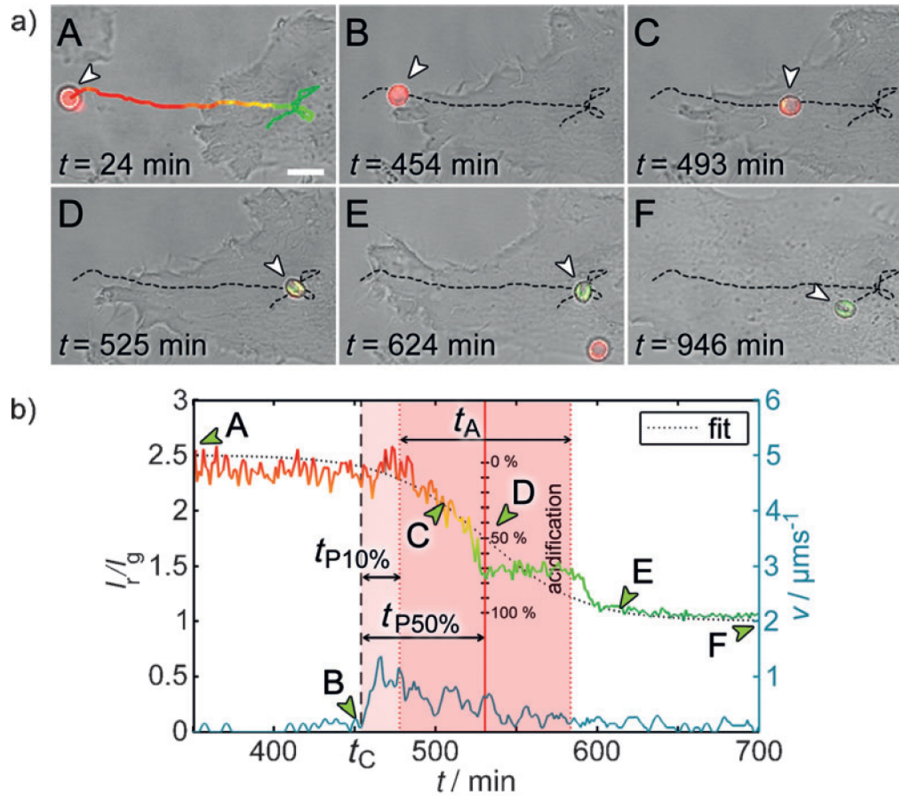


Figure 10.2. a) Typical timelapse recording of one PSS/PAH capsule ($N_{bi} = 8$, size "L") during its uptake by a HeLa cell. The images (overlay of green and red fluorescence and the brightfield micrograph) recorded at a temporal resolution of 120 s are used to determine the trajectory of the capsule (scale bar: $5 \mu\text{m}$). b) The ratio of red-to-green fluorescence I_r/I_g of the capsule has been determined for each image and is plotted *versus* the incubation time t . The time points corresponding to the images in a) are labeled A-F. A ratio of $I_r/I_g \approx 2.5$ corresponds to a pH 7.4, while $I_r/I_g \approx 1$ corresponds to local pH < 4.5 (Figure 10.1b). The acidification time t_A reflects the duration of the acidification process while the processing time $t_{P10\%}$ is determined as the period from the first contact of the capsule with the cell (B, high velocity) until the beginning of the acidification process (red area) and $t_{P50\%}$ as the period until the point of inflection of the readout curve (D).

processing time of individual capsules was quantified during uptake. Whereas PSS/PAH and DextS/PLArg capsules are differently processed by cells (nondegradable *versus* degradable),²⁸ both are internalized in a similar way and are ultimately located in the lysosomes.²³ It has to be noted that the acidification time and processing time, t_A and $t_{P50\%}$, respectively, depend on the cell line used (see Figure 10.17). There is also a significant difference between the capsule types (PSS/PAH *versus* DextS/PLArg, and batch "S" *versus* "L") regarding t_A , while the values for $t_{P50\%}$ are comparable for both materials. The differences are more distinct for HeLa cells than for phagocytes such as monocyte-derived macrophages (MDM) and monocyte-derived dendritic cells (MDDC), which are known for rapid phagocytosis of micron-sized particles.

In the following we focused on HeLa cells in order to probe for the dependence of uptake on the stiffness of the capsules (as calibrated in Figure 10.1c). The data shown in Figure 10.3a demonstrate that independent of the particle size of the non-degradable PSS/PAH capsules the acidification time t_A increases linearly with capsule stiffness γ , whereas for degradable DextS/PLArg capsules there is no such dependence. In other words, for the degradable capsules the transition from neutral/slightly alkaline extracellular pH to the highly acidic pH of lysosomes is faster. In comparison, for the non-degradable capsules the duration of this process is longer and in addition becomes even slower with increasing capsule stiffness. The dwelling time for the capsules in the cascade of intracellular vesicles during internalization thus may be different for the two types of capsules. In contrast, the processing time $t_{P10\%}$ increases with the stiffness for both capsules, for $\gamma < 5Nm^{-1}$ in a first approximation even linearly (Figure 10.3b). Hence, $t_{P10\%}$ is universally determined by γ . The acidification time only reflects the duration of the event where the local pH of the particle-containing vesicle is lowered, whereas the processing time also comprises the full uptake process. This involves the duration of engulfment by the cellular plasma membrane, pinching-off into an endocytic vesicle and subsequent processing to more acidic environments. While t_A is fully derived from a sigmoidal fit to the response function $I_r/I_g(t)$, it is not biased. In contrast, the processing time requires the determination of the time of first contact t_C with the cellular plasma

membrane for each capsule. Hence, this parameter is less robust, as t_C is difficult to determine accurately especially if the substrate is very crowded and particles are passed between cells before they are fully endocytosed. From our results we conclude that the uptake itself and the subsequent endosomal trafficking is strongly dependent on the stiffness of the particle, while further processing and acidification is governed mainly by the particle chemistry.

After contact with cells up to their internalization, particles undergo a cascade in which the particle-containing intracellular vesicles grow steadily in size, for example by fusion with other (smaller) vesicles.²⁹ From a mechanistic point of view one can regard this cascade as an intracellular sorting mechanism. Particles are passed from one vesicle to a subsequently larger one by fusion. Upon each fusion step the pH is lowered, which has been observed by fluorescence staining of acidic vesicles while the pH value around the capsule is recorded (see Figure 10.19). In a simplified view one can imagine that upon such sorting the stiffness plays a decisive role. The more flexible the particle, the better it can adopt its shape and allow evolution of vesicular containers. Thus, less deformable, that is, stiffer particles that can follow shape fluctuations to a lesser degree are more prone to delay their processing within this cascade. The same has been observed for particles that are agglomerated and therefore less "flexible" towards well dispersed particles.²⁹ Our data clearly demonstrate that the transport of particles from the outer cellular membrane to the lysosome is determined by the mechanical properties of the particles, that is, by the stiffness of the particles.

One might speculate that these findings could be reciprocal. This would lead to a situation in which cells with higher deformability would be better at incorporating a given type of particle. For such an analysis the data shown in Figure 10.3b would need to be related with the stiffness of cells. It is clearly known from the literature that cell stiffness can differ significantly for different cells types. For instance, cancerous cells are softer

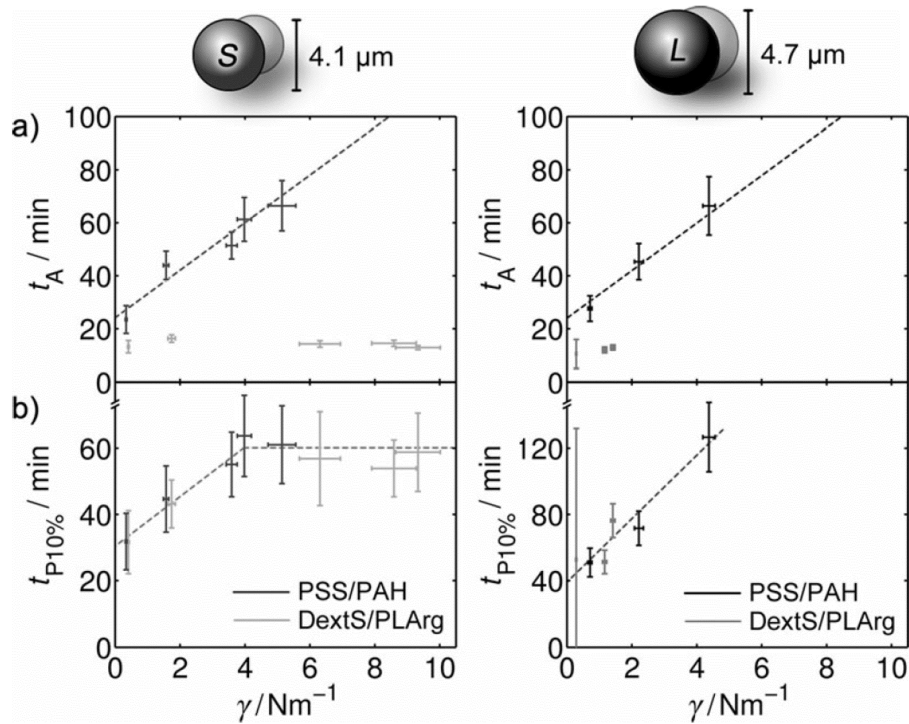


Figure 10.3. a) Acidification time t_A and b) processing time $t_{P10\%}$ of PSS/PAH and DextS/PLArg capsules with variable number of bilayers N_{bi} and different average diameters as recorded upon incubation with HeLa cells. For each number of bilayers N_{bi} the stiffness γ was taken from Figure 10.1c and then t_A and $t_{P10\%}$ were plotted against γ . Each data point corresponds to the median t_A or $t_{P10\%}$ value including the confidence intervals (y-axis) versus the mean stiffness γ value \pm standard error (x-axis), as obtained from at least 80 capsules (time values) and 40 capsules (stiffness values). The dashed lines are guides to the eye only. Please note that the large error bars in b) for $t_{P10\%}$ and DextS/PLArg capsules ($N_{bi} = 1$, size "L") result from the fact that these capsules are extremely fragile and thus the determination of t_C (membrane attachment) is challenging.

than their noncancerous counterparts (MCF7 versus MCF10).³⁰ While measurements of cell stiffness as obtained with optical tweezers indicate the global stiffness of cells in suspension,³⁰ measurements with AFM indicate the local stiffness of adherent cells.^{31,32} The softest part of a cell is the nuclear region and the cell becomes stiffer towards its

exterior regions.³² Concerning the cells as investigated in this study the following elastic moduli are known from the literature: HeLa: (105 ± 17) kPa³³ and (13 ± 7) kPa,³⁴ A549: (12 ± 5) kPa,³⁵ MDM: (44 ± 9) kPa (podosome-containing regions) *versus* (8 ± 2) kPa (podosome-free regions)³⁶ and HUVEC: (6 ± 5) kPa.³² If we compare these values with our data shown in Figure 10.18 no direct correlation of processing times t_P with the elastic moduli E of cells can be concluded, which is likely because these values cannot be compared directly to those from other studies. For such data future AFM experiments would be required, in which the elastic moduli are recorded under controlled conditions. Our study demonstrates how the cellular uptake of particles indeed is controlled by basic physico-chemical parameters such as low stiffness. A comprehensive picture about such dependencies will make it possible to synthesize particles with defined cellular interaction patterns. In addition the introduced system might improve our understanding of specific endocytic mechanisms related to lysosomal acidification.

Experimental section

Polyelectrolyte capsules composed out of different polymers (biodegradable/non-biodegradable) and having different stiffnesses (adjusted by varying the number of adsorbed layers) loaded with SNARF-1 were synthesized according to procedures described in the literature.^{23,27,28} Force spectroscopy measurements in aqueous solution were performed with a Nanowizard I device from JPK Instruments. The capsule uptake by cells (HeLa, A549, MDM, MDDC, SH-SY5Y, and HUVEC) was monitored by confocal laser scanning microscopy (LSM Meta 510, Zeiss) with a temporal resolution $\Delta t < 2$ min. Image processing and capsule tracking was performed with Matlab (MathWorks). A detailed description can be found in the Supporting Information.

Acknowledgements

This work was supported by LOEWE (project Synchembio to W.J.P). We thank Dr. Andreas Schaper for his kind introduction into ultrasectioning and Dr. Pilar Rivera Gil for stimulating technical discussions at the initial stages of this work.

References

- (1) Parveen, S.; Misra, R.; Sahoo, S. K. *Nanomedicine-Nanotechnology Biology and Medicine* **2012**, *8*, 147–166.
- (2) Rivera-Gil, P.; Jimenez De Aberasturi, D.; Wulf, V.; Pelaz, B.; Del Pino, P.; Zhao, Y.; De La Fuente, J. M.; Ruiz De Larramendi, I.; Rojo, T.; Liang, X.-J.; Parak, W. J. *Accounts of Chemical Research* **2013**, *46*, 743–749.
- (3) Jiang, W.; Kim, B. Y. S.; Rutka, J. T.; Chan, W. C. W. *Nature Nanotechnology* **2008**, *3*, 145–150.
- (4) Zhang, S.; Li, J.; Lykotrafitis, G.; Bao, G.; Suresh, S. *Advanced Materials* **2009**, *21*, 419.
- (5) Stoehr, L. C.; Gonzalez, E.; Stampfl, A.; Casals, E.; Duschl, A.; Puntès, V.; Oostingh, G. J. *Particle and Fibre Toxicology* **2011**, *8*.
- (6) Javier, A. M.; Kreft, O.; Alberola, A. P.; Kirchner, C.; Zebli, B.; Susha, A. S.; Horn, E.; Kempter, S.; Skirtach, A. G.; Rogach, A. L.; Radler, J.; Sukhorukov, G. B.; Benoit, M.; Parak, W. J. *Small* **2006**, *2*, 394–400.
- (7) Huehn, D.; Kantner, K.; Geidel, C.; Brandholt, S.; De Cock, I.; Soenen, S. J. H.; Gil, P. R.; Montenegro, J.-M.; Braeckmans, K.; Muellen, K.; Nienhaus, G. U.; Klapper, M.; Parak, W. J. *Acs Nano* **2013**, *7*, 3253–3263.
- (8) Javier, A. M.; Kreft, O.; Semmling, M.; Kempter, S.; Skirtach, A. G.; Bruns, O. T.; del Pino, P.; Bedard, M. F.; Raedler, J.; Kaes, J.; Plank, C.; Sukhorukov, G. B.; Parak, W. J. *Advanced Materials* **2008**, *20*, 4281–4287.
- (9) Palankar, R.; Pinchasik, B. E.; Schmidt, S.; De Geest, B. G.; Fery, A.; Mohwald, H.; Skirtach, A. G.; Delcea, M. *Journal of Materials Chemistry B* **2013**, *1*, 1175–1181.
- (10) Yi, X.; Shi, X. H.; Gao, H. J. *Physical Review Letters* **2011**, *107*, 5.
- (11) Banquy, X.; Suarez, F.; Argaw, A.; Rabanel, J. M.; Grutter, P.; Bouchard, J. F.; Hildgen, P.; Giasson, S. *Soft Matter* **2009**, *5*, 3984–3991.

- (12) Liu, W. J.; Zhou, X. Y.; Mao, Z. W.; Yu, D. H.; Wang, B.; Gao, C. Y. *Soft Matter* **2012**, *8*, 9235–9245.
- (13) Borges, J.; Mano, J. *Chemical Reviews* **2014**, *114*, 8883–8942.
- (14) Donath, E.; Sukhorukov, G. B.; Caruso, F.; Davis, S. A.; Mohwald, H. *Angewandte Chemie-International Edition* **1998**, *37*, 2202–2205.
- (15) Zhu, H. G.; Stein, E. W.; Lu, Z. H.; Lvov, Y. M.; McShane, M. J. *Chemistry of Materials* **2005**, *17*, 2323–2328.
- (16) Peyratout, C. S.; Dähne, L. *Angewandte Chemie International Edition* **2004**, *43*, 3762–3783.
- (17) Shchepelina, O.; Kozlovskaya, V.; Kharlampieva, E.; Mao, W. B.; Alexeev, A.; Tsukruk, V. V. *Macromolecular Rapid Communications* **2010**, *31*, 2041–2046.
- (18) Yashchenok, A.; Parakhonskiy, B.; Donatan, S.; Kohler, D.; Skirtach, A.; Moe-hwald, H. *Journal of Materials Chemistry B* **2013**, *1*, 1223–1228.
- (19) Shimoni, O.; Yan, Y.; Wang, Y.; Caruso, F. *Acs Nano* **2013**, *7*, 522–530.
- (20) Gao, C.; Donath, E.; Moya, S.; Dudnik, V.; Mohwald, H. *European Physical Journal E* **2001**, *5*, 21–27.
- (21) Fery, A.; Weinkamer, R. *Polymer* **2007**, *48*, 7221–7235.
- (22) Dubreuil, F.; Elsner, N.; Fery, A. *European Physical Journal E* **2003**, *12*, 215–221.
- (23) Kastl, L.; Sasse, D.; Wulf, V.; Hartmann, R.; Mircheski, J.; Ranke, C.; Carregal-Romero, S.; Antonio Martinez-Lopez, J.; Fernandez-Chacon, R.; Parak, W. J.; Elsasser, H.-P.; Rivera Gil, P. *Acs Nano* **2013**, *7*, 6605–6618.
- (24) Reibetanz, U.; Chen, M. H. A.; Mutukumaraswamy, S.; Liaw, Z. Y.; Oh, B. H. L.; Venkatraman, S.; Donath, E.; Neu, B. *Biomacromolecules* **2010**, *11*, 1779–1784.
- (25) Del Mercato, L. L.; Abbasi, A. Z.; Parak, W. J. *Small* **2011**, *7*, 351–363.
- (26) Kreft, O.; Javier, A. M.; Sukhorukov, G. B.; Parak, W. J. *Journal of Materials Chemistry* **2007**, *17*, 4471–4476.

- (27) Rivera-Gil, P.; Nazarenius, M.; Ashraf, S.; Parak, W. J. *Small* **2012**, *8*, 943–948.
- (28) Rivera-Gil, P.; De Koker, S.; De Geest, B. G.; Parak, W. J. *Nano Letters* **2009**, *9*, 4398–4402.
- (29) Brandenberger, C.; Muehlfeld, C.; Ali, Z.; Lenz, A.-G.; Schmid, O.; Parak, W. J.; Gehr, P.; Rothen-Rutishauser, B. *Small* **2010**, *6*, 1669–1678.
- (30) Lincoln, B.; Erickson, H. M.; Schinkinger, S.; Wottawah, F.; Mitchell, D.; Ulvick, S.; Bilby, C.; Guck, J. *Cytometry Part A* **2004**, *59A*, 203–209.
- (31) Domke, J.; Dannohl, S.; Parak, W. J.; Muller, O.; Aicher, W. K.; Radmacher, M. *Colloids and Surfaces B-Biointerfaces* **2000**, *19*, 367–379.
- (32) Kuznetsova, T. G.; Starodubtseva, M. N.; Yegorenkov, N. I.; Chizhik, S. A.; Zhdanov, R. I. *Micron* **2007**, *38*, 824.
- (33) Berquand, A.; Holloschi, A.; Trendelenburg, M.; Kioschis, P. *Microscopy Today* **2010**, *18*, 34–37.
- (34) Ren, J.; Yu, S.; Gao, N.; Zou, Q. *Physical Review E* **2013**, *88*.
- (35) Xiao, L.; Tang, M.; Li, Q.; Zhou, A. *Analytical Methods* **2013**, *5*, 874–879.
- (36) Labernadie, A.; Thibault, C.; Vieu, C.; Maridonneau-Parini, I.; Charriere, G. M. *Proceedings of the National Academy of Sciences of the United States of America* **2010**, *107*, 21016–21021.

Supporting information

Cell Culture

Adenocarcinomic human alveolar basal epithelial (A549) cells and Human cervical cancer (HeLa) cells were maintained in Dulbecco's Modified Eagles Medium (DMEM, Sigma-Aldrich, Germany, # D6546) with 4.5 g/L glucose supplemented with 10% fetal bovine serum (FBS, Biochrom, Germany, # S0615), 1% penicillin/streptomycin (P/S, Sigma-Aldrich, # P4333) and 2 mM L-glutamine (Sigma-Aldrich, # G7513) at 5% CO_2 and 37 °C.

Neurons (SH-SY5Y cells) were maintained in Dulbecco's Modified Eagles Medium/Ham's Nutrient Mixture F12 (DMEM/F-12, Sigma-Aldrich, # D6421) supplemented with 15% FBS, 1% P/S, and 2 mM L-glutamine at 5% CO_2 and 37 °C.

Human umbilical vein endothelial cells (HUVEC) were cultured in Endothelial Cell Growth Medium (ECGM, PromoCell, Germany, # C22010) at 5% CO_2 and 37 °C.

Monocyte derived macrophages (MDMs) and monocyte derived dendritic cells (MDDCs) were obtained from peripheral blood monocytes following the protocol from Sallusto *et al.*¹ Briefly, monocytes were isolated from buffy coats (blood donation service Universitätsklinikum Giessen Marburg, Giessen, Germany) by using density gradient centrifugation in Ficoll-Paque (GE Healthcare, Germany, # 17-1440-02) and matured in RPMI 1640 (Sigma-Aldrich, # R0883) supplemented with 5% heat-inactivated (pooled) human serum (blood donation service, Zentrum für Klinische Transfusionsmedizin, Tübingen, Germany), 1% P/S and 2 mM L-glutamine at 5% CO_2 and 37 °C. Monocytes were matured in the presence of 34 ng/mL human IL-4 (New England Biolabs, Germany, # 8919SC) and 50 ng/mL human GM-CSF (New England Biolabs, # 8922SF) for 7-9 days to obtain MDDCs, whereas for the generation of MDMs no additional supplements were used.

Polyelectrolyte multilayer capsules

Synthesis

pH-sensitive capsules with a different number of layers to vary capsule elasticity (1, 2, 4, 6, 8, 12 and 16 bilayers, N_{bi}) were synthesized with 2 frequently used polymer systems (non-degradable polymers: poly(sodium 4-styrenesulfonate), $M_W \approx 70$ kDa, PSS and poly(allylamine hydrochloride), $M_W \approx 56$ kDa, PAH, degradable polymers: dextran sulfate sodium salt, $M_W \approx 40$ kDa, DextS and poly-L-arginine hydrochloride, $M_W \approx 15$ -70 kDa, PLArg). Based on layer-by-layer assembly polyelectrolytes of alternating charge were adsorbed around sacrificial template cores according to published protocols.^{2,3} The pH-sensitivity was achieved by embedding SNARF-1⁴-labeled dextran into the cavity of the capsules following the co-precipitation method.⁵ For all capsules of the same class of polyelectrolytes but different wall thickness core templates from the same batch (having all the same size distribution) were used to minimize artifacts due to different sizes. For each class of polyelectrolytes two different batches "S" and "L" with different size ("S": smaller, "L": larger) and unequal mechanical properties were prepared to cover a broad range of elasticity values, *cf.* Figure 10.8.

Chemicals

Poly(sodium 4-styrenesulfonate) (PSS, $M_W \approx 70$ kDa, # 243051), poly(allylamine hydrochloride) (PAH, $M_W \approx 56$ kDa, # 283223), dextran sulfate sodium salt (DextS, $M_W \approx 40$ kDa, # 42867), poly-L-arginine hydrochloride (PLArg, $M_W \approx 15$ -70 kDa, # P7762), calcium chloride dehydrate (CaCl_2 , # 223506), sodium carbonate (Na_2CO_3 , # S7795) and ethylene-diamine-tetraacetic acid disodium salt dihydrate (EDTA disodium salt, # E5134) were purchased from Sigma-Aldrich (Germany), SNARF-1 dextran ($M_W \approx 70$ kDa, # D3304) from life technologies (USA) and sodium chloride (NaCl , # HN00.2) was obtained from Roth (Karlsruhe, Germany). Ultrapure water (ddH_2O) with a resistance greater than $18.2 \text{ M}\Omega \text{ cm}^{-1}$ was used for all experiments.

Procedure

CaCO₃ microparticles were prepared at room temperature (RT) from solutions of CaCl₂ and Na₂CO₃ under vigorous stirring in the presence of SNARF-1 dextran. 1 mL of aqueous solution of CaCl₂ (0.33 M), 1.4 mL SNARF-1 dextran 70 kDa (0.5 mg mL⁻¹) were mixed in a glass vial. During magnetic stirring (1000 rpm) 1 mL of aqueous solution of Na₂CO₃ (0.33 M) solution was added quickly. After 30 s the stirrer was turned off and particle growth was stopped after additional 2 min by centrifugation. The particles were washed three times with ddH₂O and then directly used for the layer-by-layer assembly of polyelectrolytes.

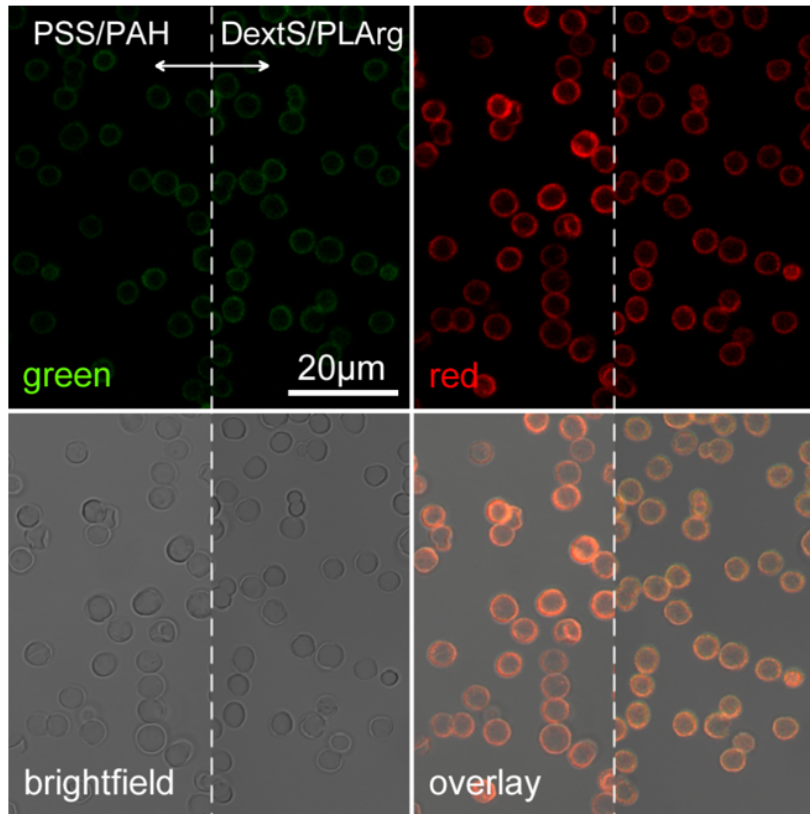


Figure 10.4. Fluorescent micrographs of pH-sensitive microcapsules. The fluorescence images of PSS/PAH (left) and DextS/PLArg (right) capsules ($N_{bi} = 4$, size "L") as recorded between 560 and 615 nm ("green" channel, in false colors) and >615 nm ("red" channel), brightfield images, and the corresponding overlays are shown. Images were taken at pH 7 in DMEM. It can be seen that most of the SNARF-dextran is attached to the inner membrane of the capsules instead of being homogeneously distributed in the capsule cavity.⁶

Biodegradable capsules were obtained by depositing alternating layers of negatively charged DextS (2 mg/mL in 0.5 M NaCl) and positively charged PLArg (2 mg/mL in 0.5 M NaCl) onto the charged microparticles as described previously.^{7,8,2,9} For coating with each layer the microparticles were suspended in 1 mL of polyelectrolyte solution. The dissolution of the cores was carried out by Ca^{2+} ion complexation with EDTA (1 mL, 0.2 M, pH 6.5).

Non-biodegradable capsules were obtained by using PSS as negatively and PAH as positively charged polymers.

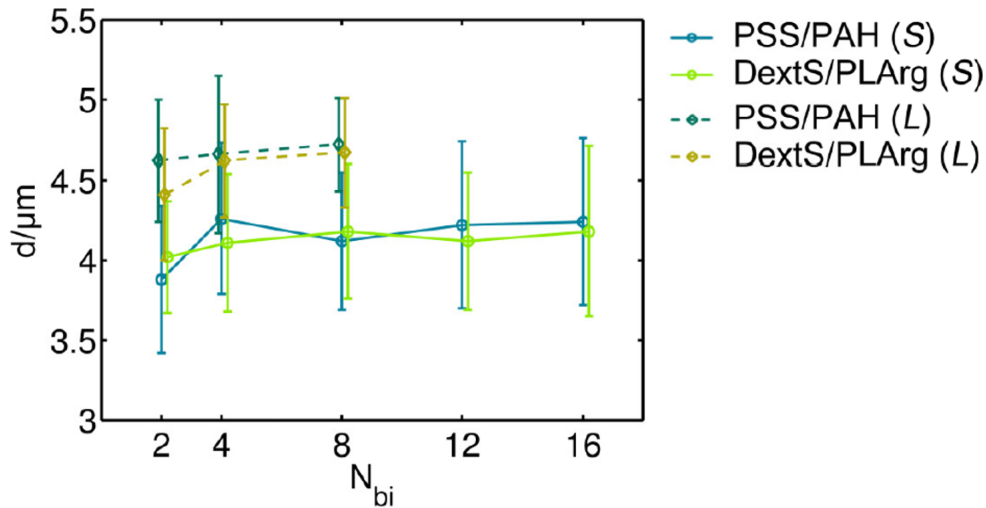
Samples carrying 1, 2, 4, 6 and 8 bilayers were synthesized in both cases.

Characterization

The size distributions of the PEM capsules were derived from confocal laser scanning fluorescence (cLSM) micrographs (*cf.* Figure 10.4). The shell thickness and structure was examined by transmission and scanning electron microscopy (TEM and SEM), while the mechanical properties were investigated by atomic force microscopy (AFM) measurements.

Size distribution

Size distributions (*cf.* Figure 10.5) were derived from fluorescent micrographs of PEM capsules (*cf.* Figure 10.4) taken at pH 7 in DMEM. For details regarding the image acquisition see below. Capsules being in focus were automatically segmented and quantified with respect to size (see below for details). More than 200 capsules were analyzed in each case.



“S” (small)

“L” (large)

N_{bi}	$d/\mu\text{m}$	
	<i>PSS/PAH</i>	<i>DextS/PLArg</i>
2	3.88 ± 0.46	4.02 ± 0.35
4	4.26 ± 0.47	4.11 ± 0.43
8	4.12 ± 0.43	4.18 ± 0.42
12	4.22 ± 0.52	4.12 ± 0.43
16	4.24 ± 0.52	4.18 ± 0.53

N_{bi}	$d/\mu\text{m}$	
	<i>PSS/PAH</i>	<i>DextS/PLArg</i>
2	4.62 ± 0.38	4.41 ± 0.41
4	4.66 ± 0.49	4.62 ± 0.35
8	4.72 ± 0.29	4.67 ± 0.34

Figure 10.5. Size distribution of microcapsules. The size distributions of the capsule diameters d were obtained from fluorescent micrographs of capsules with $N_{bi} = 2$ -16 bilayers at pH 7 in DMEM.

Shell thickness

The shell thickness was determined from TEM images of 70 nm thin capsule cross-sections (*cf.* Figure 10.6) and derived from AFM height-measurements of dried (collapsed) capsules (*cf.* Figure 10.7).

1) obtained from ultrathin cross-sections

PEM capsules were embedded in resin as described by Pretzl *et al.*¹⁰ The sectioning was

performed with an ultramicrotome (EM UC7, Leica, Germany) and the sections were imaged using a JEM-3010 (Jeol, Japan). The shell thickness was derived by extracting cross-sectional intensity profiles that were analyzed with Matlab (MathWorks, USA).

The capsule wall can be segmented into two distinct structures (Figure 10.6): The outer membrane (d_1) is most likely the polyelectrolyte shell, while the porous structure (d_2) is SNARF-dextran adhering to the inner surface of the polyelectrolyte shell. The thickness of d_2 increases with increasing thickness of d_1 . We assume that during dissolution of the CaCO_3 -templates with EDTA in the case of thinner capsules with less bilayers the leakage of SNARF-dextran out of the capsules is higher due to higher porosity of the shell. Shell-attached dextran might influence the capsule stiffness. As the fluorescence which is attributed to SNARF-labeled dextran is also higher in the capsule shell in fluorescence micrographs in aqueous solution (*cf.* Figure 10.4) the observed phenomenon is not an artifact caused by the ethanol-drying of the capsules during sample preparation for embedding into epoxy resin.

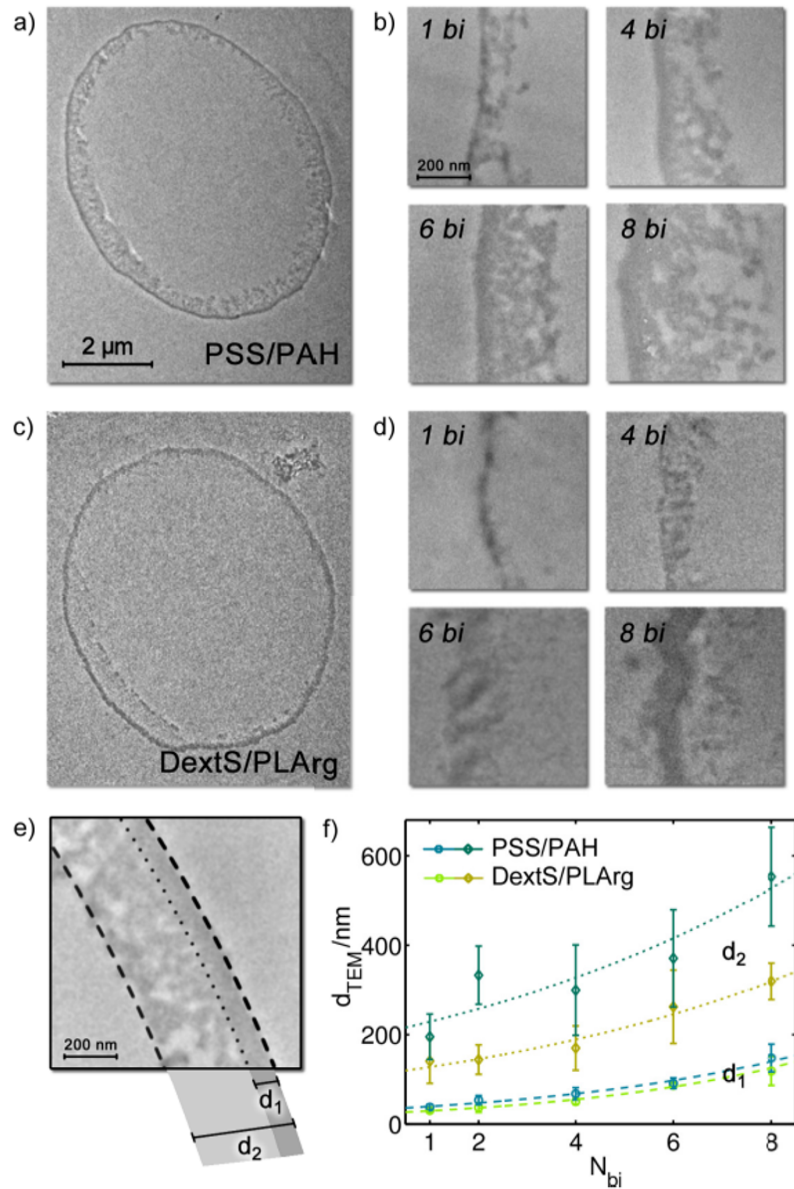


Figure 10.6. a) TEM micrograph of a 70 nm thick cross-section of a PSS/PAH capsule composed of 4 bilayers ($N_{bi} = 4$, size "L") embedded in epoxy resin. b) Cross-section of PSS/PAH-capsule membranes for $N_{bi} = 1, 4, 6$, and 8 bilayers in higher magnification. c) TEM micrograph of DextS/PLArg capsules with 4 bilayers. d) Cross-section of DextS/PLArg-capsule membranes for $N_{bi} = 1, 4, 6$, and 8 bilayers in higher magnification. e) The thickness of only the outer layer d_1 which is supposed to be composed of polyelectrolytes measured from TEM images and d_2 included also a porous structure which is probably SNARF adhering to the inner surface of the polyelectrolyte shell. f) Thickness values for d_1 and d_2 for non-biodegradable PSS/PAH and biodegradable DextS/PLArg capsules measured for $N_{bi} = 1-8$ (size "L").

II) derived from collapsed capsules by atomic force microscopy (AFM)

AFM imaging of collapsed capsules was carried out in intermittent contact mode at the MFP-3D (Asylum Research, Santa Barbara, CA, USA) which was combined with the optical microscope Axiovert 200 (Zeiss, Jena, Germany). Silicon nitride cantilevers (NSC 36, no Al coating, MikroMasch, Tallinn, Estonia) with a nominal spring constant of 0.6 N/m were used. Measurements were performed in the MFP liquid cell filled with deionized water (MilliQ[®] Academic, Millipore, Billerica, USA). To ensure adhesion of the capsules the glass substrate was coated with one bilayer of polyethylenimine (PEI) and PSS. Collapse of the capsules was achieved through drying the capsules directly on the substrate. More rigid capsules (4 to 8 bilayers) were treated with ultrasound for 1 min in an ultrasonic bath prior to drying.

The thickness of the capsules measured by AFM (d_{AFM}) (*cf.* Figure 10.7), is between d_1 and d_2 (*cf.* Figure 10.6). SNARF-dextran present in d_2 might be compressed during drying of the capsules.

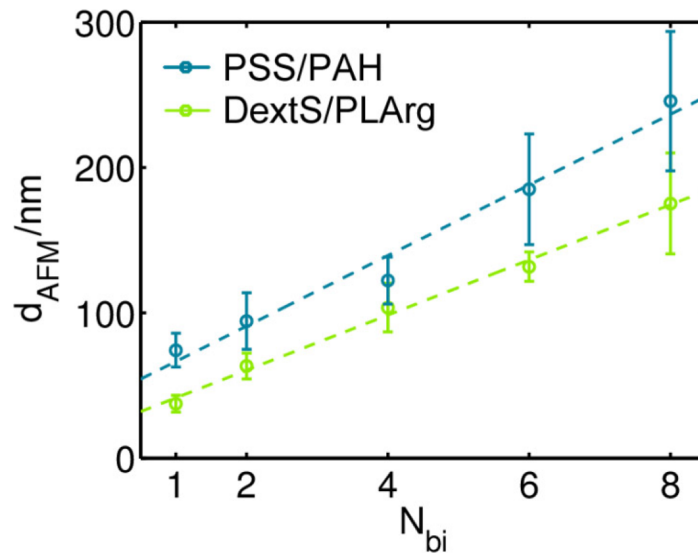


Figure 10.7. Shell thickness of PSS/PAH and DextS/PLArg capsules, respectively composed of 1-8 bilayers (size "L") obtained from AFM measurements.

Mechanical properties

Force spectroscopy measurements were carried out at the Nanowizard I[®] (JPK Instruments, Berlin, Germany) which was combined with the inverted optical microscope Axiovert 200 (Zeiss, Jena, Germany). As a probe we used tip-less silicon nitride cantilevers (NSC 12, no Al coating, MikroMasch, Tallinn, Estonia) with nominal spring constants of 0.65 and 14 N/m. These cantilevers were modified by gluing a glass sphere of colloidal dimensions (diameter 30-40 μm , Polysciences Europe GmbH, Eppelheim, Germany) with two component epoxy glue (UHU Endfest 300, UHU GmbH & Co. KG, Buhl, Germany) under their very front (colloidal probe). The exact spring constant of the employed cantilevers was determined prior to any modification from their thermal vibration spectrum (thermal noise method¹¹). Before probing the microcapsules, the cantilever's optical lever sensitivity was determined by pressing the cantilever against the non-deformable glass substrate. All measurements were performed in home-built Petri dishes (diameter 2 cm, height 0.5 cm) filled with deionized water (MilliQ[®] Academic, Millipore, Billerica, USA). To promote capsule adhesion the glass bottom of the dishes was coated with one layer of each PEI and PSS. The stiffness of the capsules' shell was obtained as the slope of the linear part of the recorded force *vs.* deformation curves for small deformations in the order of the shell thickness. A representative force-deformation characteristic is displayed in Figure 10.9. Obtained results are shown in Figure 10.8.

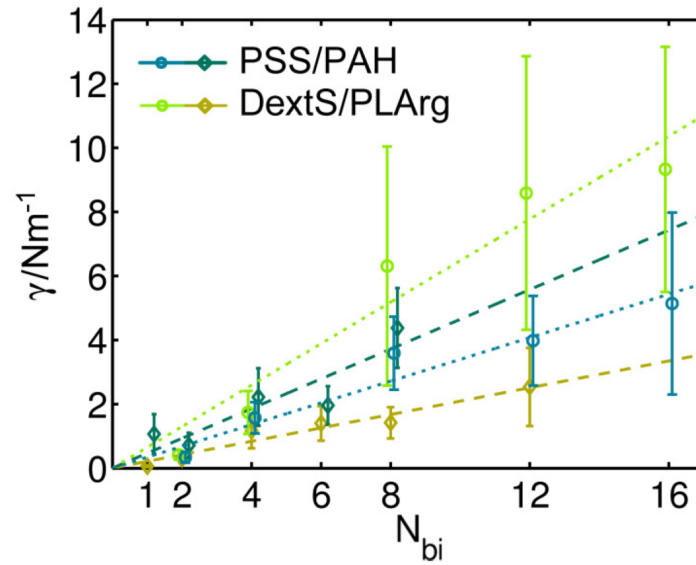


Figure 10.8. Stiffness γ of PSS/PAH and DextS/PLArg capsules, respectively (size "S": dashed line, size "L": dotted line).

The leakage of SNARF-dextran out of the capsules during dissolution of the sacrificial core-templates¹² strongly depended on the thickness of the polyelectrolyte shell and decreased with increasing numbers of polymer layers. As the encapsulated SNARF-dextran was attached rather to the inner membrane of the capsules instead of being homogeneously distributed inside the cavities⁶ (*cf.* Figure 10.4 and Figure 10.6) it might have also influenced the stiffness of the capsules.

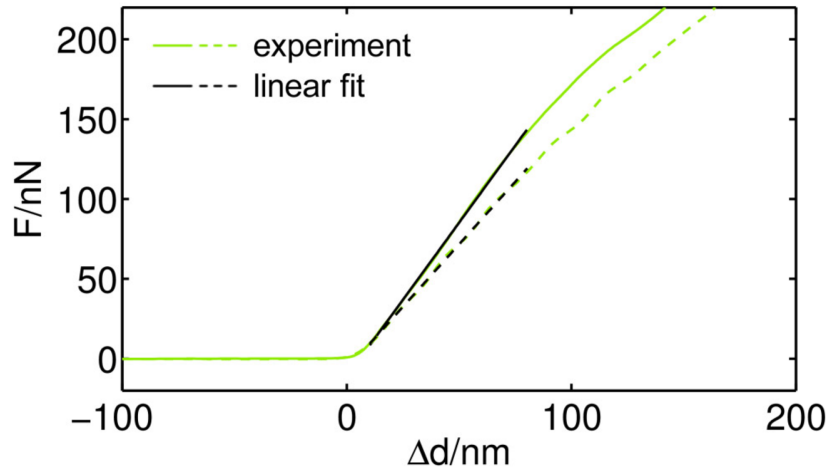


Figure 10.9. Representative force-deformation characteristics of 4-bilayer DextS/PLArg microcapsules and linear fits in the small deformation regime (deformation: Δd) yielding the capsule's stiffness (size "S": solid line, size "L": dashed line).

pH response

The fluorescence response of the SNARF-capsules to changes in pH was measured by adding a drop containing capsules to cell culture medium samples with differently adjusted pH-values (*cf.* Figure 10.1b, main part). The fluorescent readout was measured using confocal laser scanning microscopy as described below with the difference that the capsules in pH-adjusted cell media were imaged on top of a conventional glass slide. For each pH-value approximately 200 capsules were imaged to obtain the average red/green ratio at a specific ionic concentration. We note again that in images fluorescence is displayed in false colors.

Zeta-potential

The Zeta potential (ζ) was measured in ddH₂O by dynamic light scattering (DLS) using a Zetasizer Nano ZS (Malvern Instruments, UK). Biodegradable DextS/PLArg PEM

capsules turned out to carry a higher positive potential than their non-biodegradable counterparts made from PSS/PAH (*cf.* Figure 10.10).

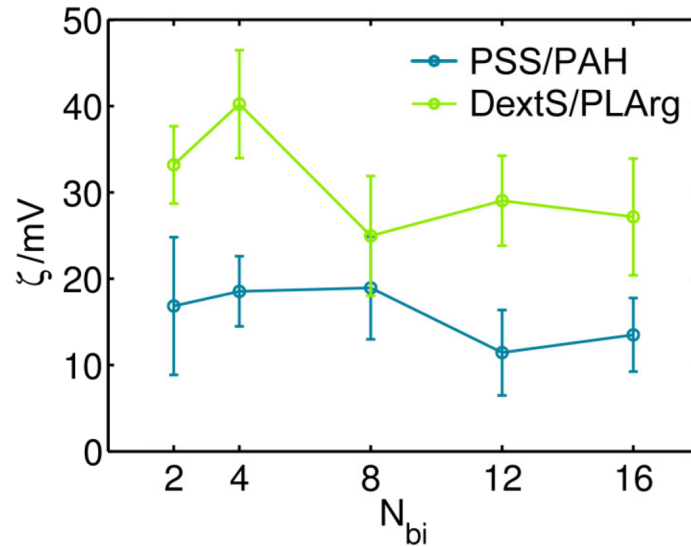


Figure 10.10. Zeta potential (ζ) of PSS/PAH and DextS/PLArg capsules, respectively, composed of 2-16 bilayers (size "S") derived from DLS measurements.

Uptake studies

For tracking the internalization of the different PEM capsule systems 15,000 cells/well were seeded into each well of an 8-well μ -slide (Ibidi, Germany, # 80826), whereby the growth area of each well was 1 cm^2 , filled with $300 \mu\text{L}$ medium. Imaging was performed on the next day.

Live confocal fluorescence microscopy

The capsule uptake was studied using a confocal laser-scanning fluorescence microscope (CLSM 510 Meta, Zeiss) equipped with a portable incubator (Pecon, Germany) to maintain the μ -slides at $37 \text{ }^\circ\text{C}$ with $5\% \text{ CO}_2$. Prior to image acquisition approximately

7 capsules/cell were added and time lapse image series were acquired using a Plan-Apochromat 63x/1.40 Oil DIC M27 objective. SNARF-1 was excited at 543 nm (with a HeNe-laser) and its fluorescence was recorded between 560 and 615 nm ("green" channel, false color) and >560 nm ("red" channel). To minimize bleaching the acquisition parameters were tuned to detect fluorescence at very low excitation power. The lateral sampling frequency was set to $0.32 \mu\text{m}$ while the temporal resolution was set to 45-150 s, depending on the acidification rate during uptake of each cell type. The absolute axial position of the boundary layer μ -dish substrate/medium was determined by detecting the z-position of the increased level of scattered photons in this boundary layer. Two images of the same lateral position were acquired: To catch internalized capsules, one slice was imaged $2.2 \mu\text{m}$ above the substrate which was typically located in the cell interior. Another slice was obtained $3 \mu\text{m}$ higher to resolve capsules located on top of cells. The pinhole of the confocal system was adjusted to image $2 \mu\text{m}$ thick sections in both cases. This alignment was recovered before each time point by a software-based autofocus routine. After acquisition the dimension was reduced by calculating the projection along the z-axis of both slices for further analysis.

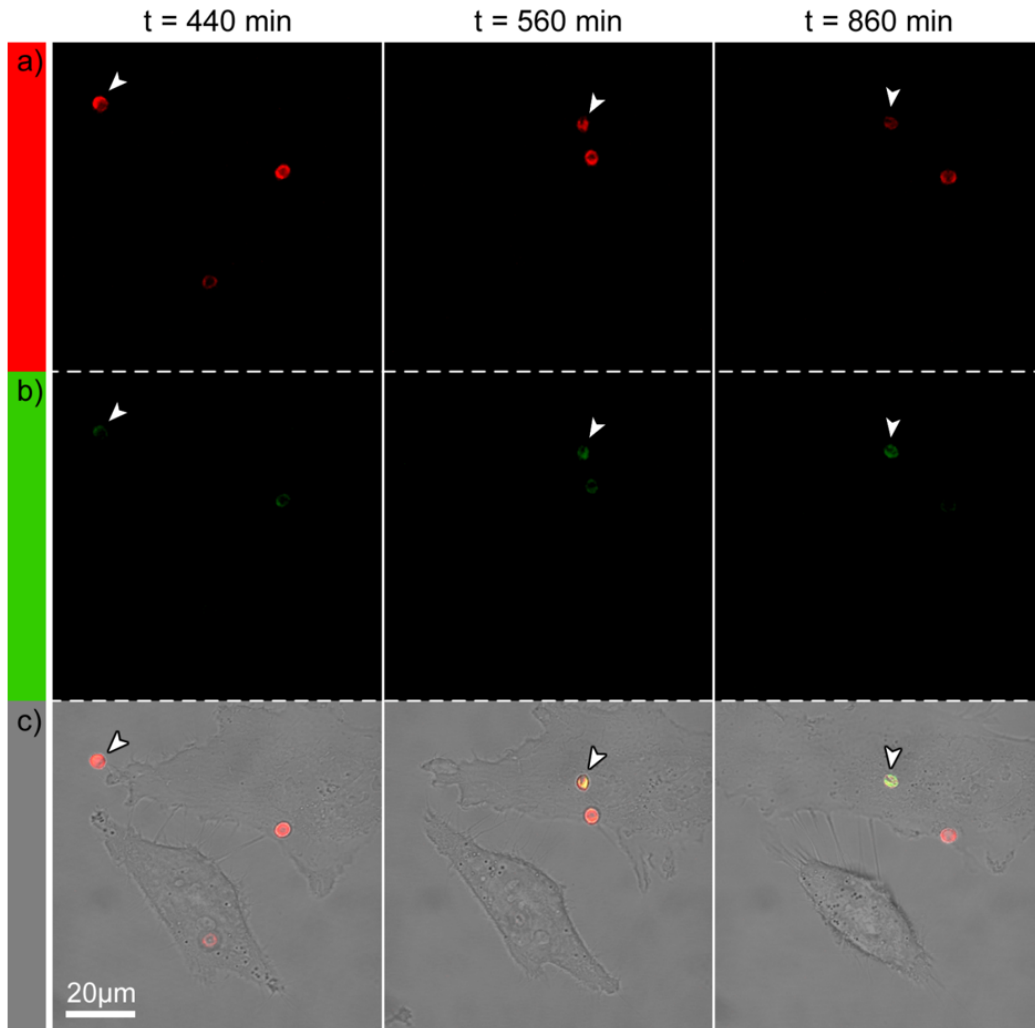


Figure 10.11. Time lapse image series of capsule uptake. Three representative time points of a typical image series tracing PSS/PAH capsules ($N_{bi} = 8$, size "L") during their uptake by HeLa cells are displayed. a) shows the fluorescence of the SNARF-filled capsules in the red channel (>615 nm), b) shows their fluorescence in the green channel (560 - 615 nm), and c) shows the overlay of both channels with the corresponding brightfield image. The white arrows highlight a capsule which shows a transition from red to green, indicating its transfer into an acidic lysosomal compartment.

Image processing

For automated image processing, capsule segmentation, tracking and visualization a toolbox was developed using Matlab (Mathworks, USA). In the following the workflow (Figure 10.12) is described briefly. First, photon shot noise in the red and green channel was reduced by median-filtering and the background was completely removed by defining a threshold (Figure 10.12b1). As a microcapsule typically appears as a slightly filled circle in a confocal fluorescence image a modified Hough transformation¹³ was computed to identify all capsules positions and their corresponding radii automatically to create masks for further intensity value readout (Figure 10.12). It turned out that in the case of several clustered capsules or image regions with high capsule density this segmentation method performed better than object identification by thresholding strategies. Each pixel was considered as the origin of a parameterization of a circle with similar radius as the structure to be found. The sum of all pixel intensities which were hit by the circle was calculated and assigned to the origin pixel of the circle. Basically each pixel was tested if its position was likely to be the origin of a circle of given radius. By doing so the center positions of all circles were identified. A classical Hough transform does not yield the radius of the round features it is finding. To identify the position and the dimension of each capsule a parameterization of a donut-shaped structure with a shell thickness of $0.64 \mu\text{m}$ was used. For each pixel the radius r of this structure was varied within given boundaries (derived from the size distribution of the capsules), and the underlying pixel intensities were summed up as a function of r . The position of the first maximum of this function was identified as the capsule radius, and the corresponding maximum was assigned to the initial pixel. For each pixel in the original image a number representing the probability to be the center of a capsule with radius r was obtained. The local maxima in this probability depiction were identified as the centers of all capsules being present in the current frame. To reduce computational time the transformation was only calculated for image regions in which capsules were present. These regions were obtained by a morphological area opening to remove structures smaller than the capsules, morphological closing with a disk-shaped structuring element to fill dark gaps in the

capsule walls, and finished by filling all holes in the image (*i.e.* filling "empty" capsules). The local maxima (*i.e.* capsule center positions) generated by the modified Hough transform were emphasized by image dilation and stored. Finally, the segmentation performance was evaluated for each detected capsule to reduce artifacts. The coordinates and the radius (x position, y position, radius) were used to create a mask for each capsule (ROI) in the red and green channel, respectively. Within this mask the average pixel intensity ratio red/green (I_r/I_g) was calculated from the noise-corrected raw data (Figure 10.12b1) indicating the local pH. To obtain the progression of I_r/I_g *versus* time for each capsule during uptake and cellular trafficking (further referred to as "trajectory") a capsule-tracking routine was applied, which was inspired by the particle tracking algorithms developed by John Crocker *et al.*,¹⁴ and provided for Matlab by Danial Blair and Eric Dufresne. The described procedure resulted in almost gap-less two-dimensional capsule trajectories. Finally, each trajectory was checked manually and erroneous lateral displacements were corrected by adjusting the capsules ROIs if needed.

Trajectory processing

For illustration a typical trajectory is shown in Figure 10.2 (*cf.* the main part). From each trajectory the processing times $t_{P10\%}$ and $t_{P50\%}$, respectively, and the acidification time t_A were derived. The processing time is the time from the first contact t_C (membrane-attachment, as visible from the brightfield images) of the capsule with the cell, which is taking up the microcapsule until its acidification. The acidification time describes the duration of acidification from high to low pH following the sigmoidal curve. Consequently, the experimental data were fitted with the following curve: $(I_r/I_g)(t) = (R_a - R_b)/(1 + \exp((t - t_{50\%})/\Delta t)) + R_b$.

Hereby, the acidification time is defined as $\Delta t_A = t_{90\%} - t_{10\%} = 2\Delta t \cdot \ln(9)$. The time points $t_{90\%}$ and $t_{10\%}$ are derived from the equations $(I_r/I_g)(t_{10\%}) = 0.9 \cdot (R_a - R_b) + R_b$ and $(I_r/I_g)(t_{90\%}) = 0.1 \cdot (R_a - R_b) + R_b$. In other words: Δt_A is the duration of the acidification process of a single particle, *cf.* Figure 10.2b (main part). The processing times

for different endpoints $t_{P10\%}$ and $t_{P50\%}$ are derived from these data as $t_{P10\%} = t_{10\%} - t_C$ and $t_{P50\%} = t_{50\%} - t_C$. In this way each uptake trajectory is defined by two quantitative parameters: t_A and $t_{P10\%}$ or $t_{P50\%}$, respectively.

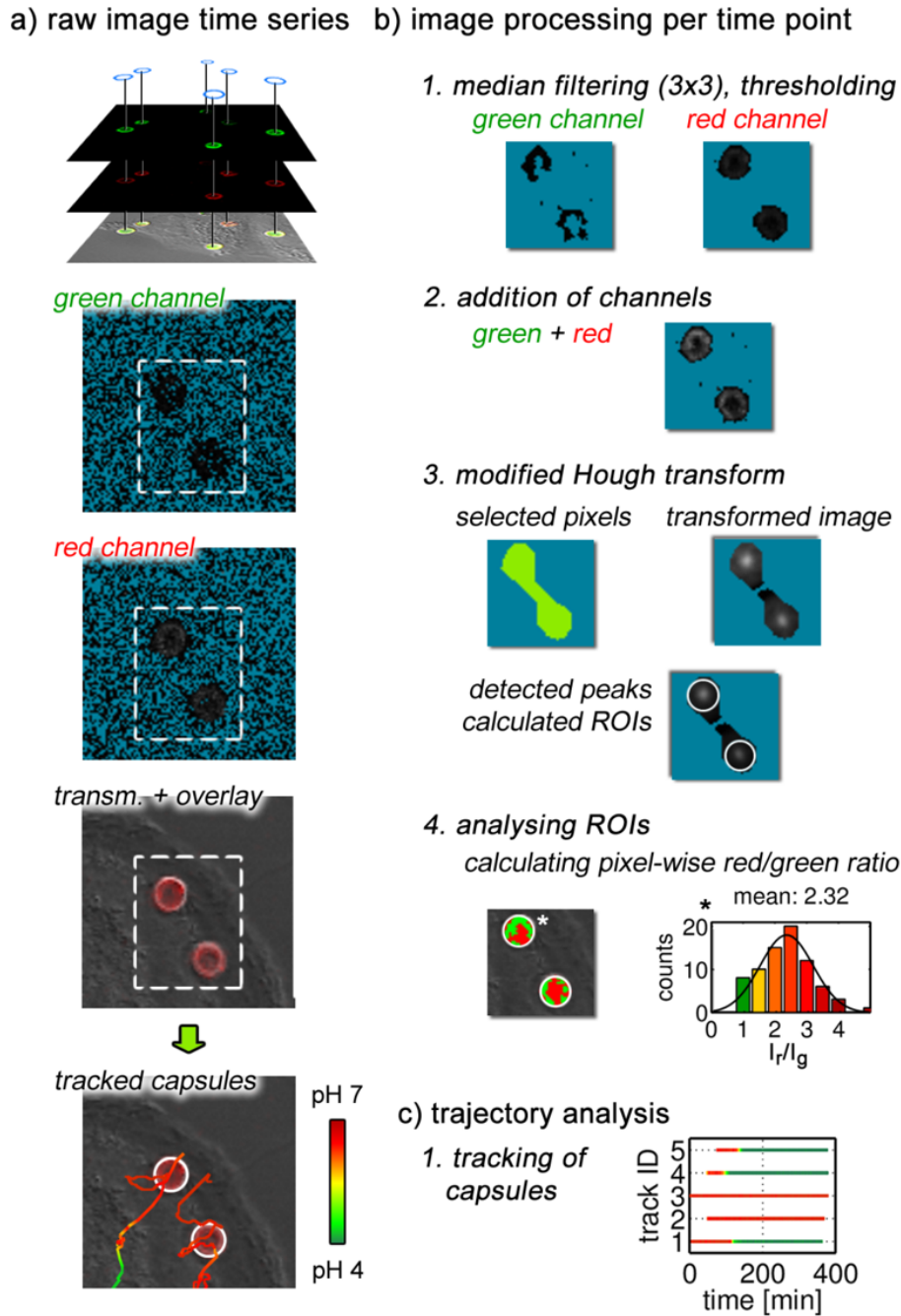


Figure 10.12. Overview over the image processing workflow. Time lapse image series of cellular capsule uptake were acquired with an automated confocal fluorescence microscope. To derive capsule-trajectories the indicated image processing routines were applied. Pixels with zero intensity are colored in blue. For calculating the per-pixel red/green ratio only pixels with intensity values above a certain threshold in both channels were considered (colored in green in b.4).

Elasticity dependent intracellular processing

In this section additional figures are provided which show the influence of the capsule shell thickness and the used polyelectrolytes (non-biodegradable PSS/PAH *vs.* biodegradable DextS/PLArg) on the endocytic processing during uptake by HeLa cells. In Figure 10.13 and Figure 10.14 typical trajectories from capsules of different shell thickness ($N_{bi} = 2, 4$ and 16, size "S") were selected and the pH-response during internalization is plotted. For each trajectory the duration of acidification is displayed (acidification time t_A) and the processing time is shown ($t_{P10\%}$). Typical events are marked in the pH-response curve (A: first appearance of capsule, B: first contact with cell which internalizes the capsules later, C: partial acidification, D: capsule is fully acidified) and the corresponding microscopic images are given showing the particular point in time. In Figure 10.15, Figure 10.16 and Figure 10.17 the acidification times t_A and the processing times $t_{P10\%}$ and $t_{P50\%}$ are shown and correlated with the particle stiffness γ .

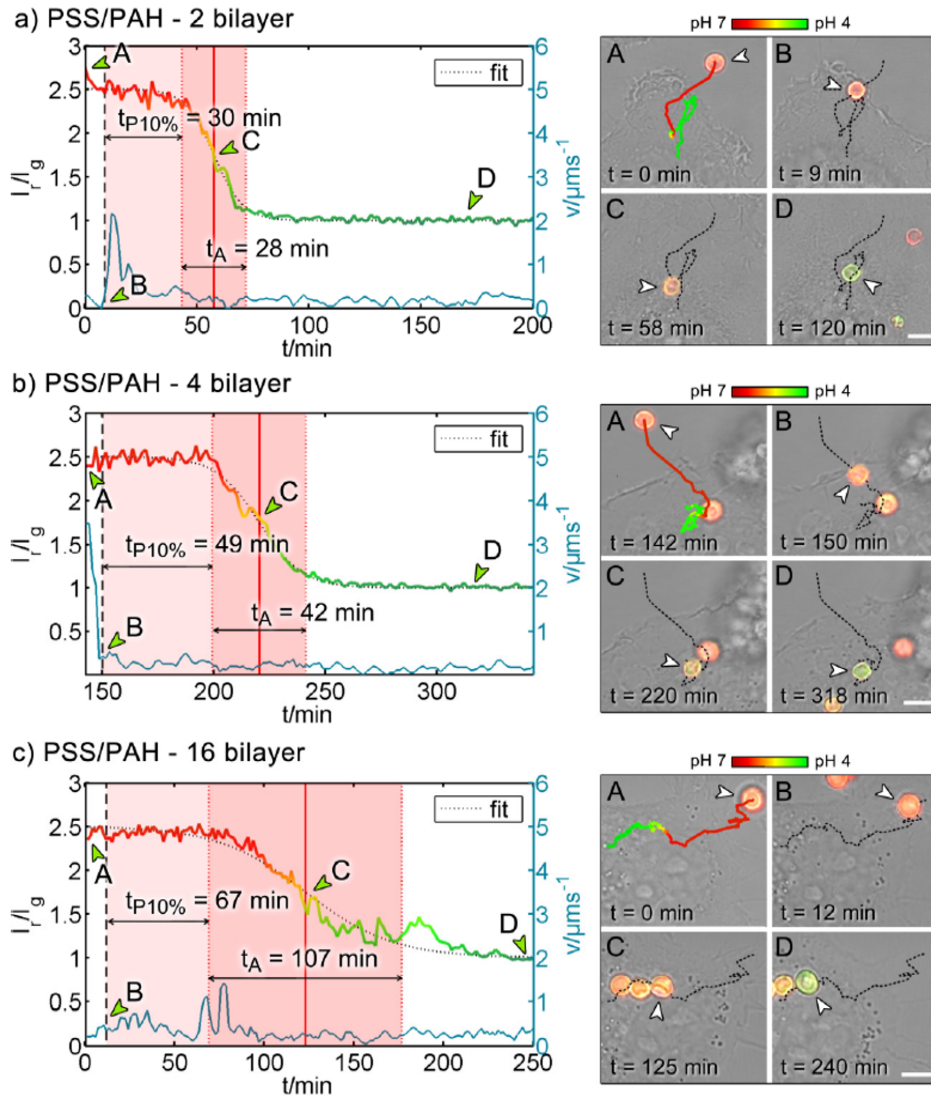


Figure 10.13. Example trajectories of PSS/PAH capsules of different thickness in HeLa cells. On the left side typical SNARF-response curves of 2, 4 and 16 bilayer thick (*cf.* a, b and c) non-biodegradable PSS/PAH capsules (type "S") are shown during uptake by HeLa cells. $I_r/I_g \approx 2.5$ corresponds to neutral pH while capsules with $I_r/I_g \approx 1$ are located inside acidic vesicles. On the right side corresponding microscopic images are shown for the time points A-D marked with a green arrow inside the graph. The respective tracked capsule is highlighted with a white arrow. The scale bar length is $5 \mu\text{m}$.

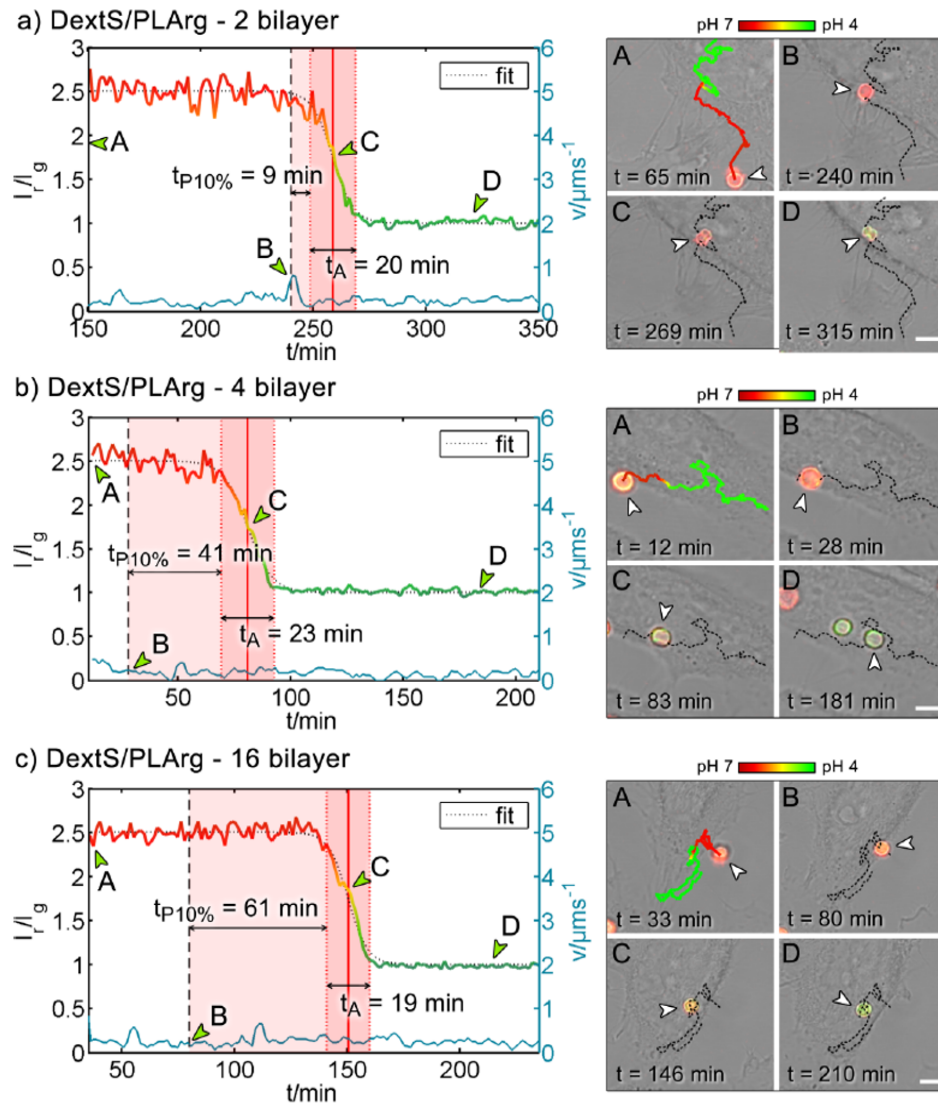


Figure 10.14. Example trajectories of DextS/PLArg capsules of different thickness in HeLa cells. On the left side typical SNARF-response curves of 2, 4 and 16 bilayer thick (*cf.* a, b and c) biodegradable DextS/PLArg capsules (type "S") are shown during uptake by HeLa cells. $I_r/I_g \approx 2.5$ corresponds to neutral pH while capsules with $I_r/I_g \approx 1$ are located inside acidic vesicles. On the right side corresponding microscopic images are shown for the time points A-D marked with a green arrow inside the graph. The respective tracked capsule is highlighted with a white arrow. The scale bar length is 5 μm .

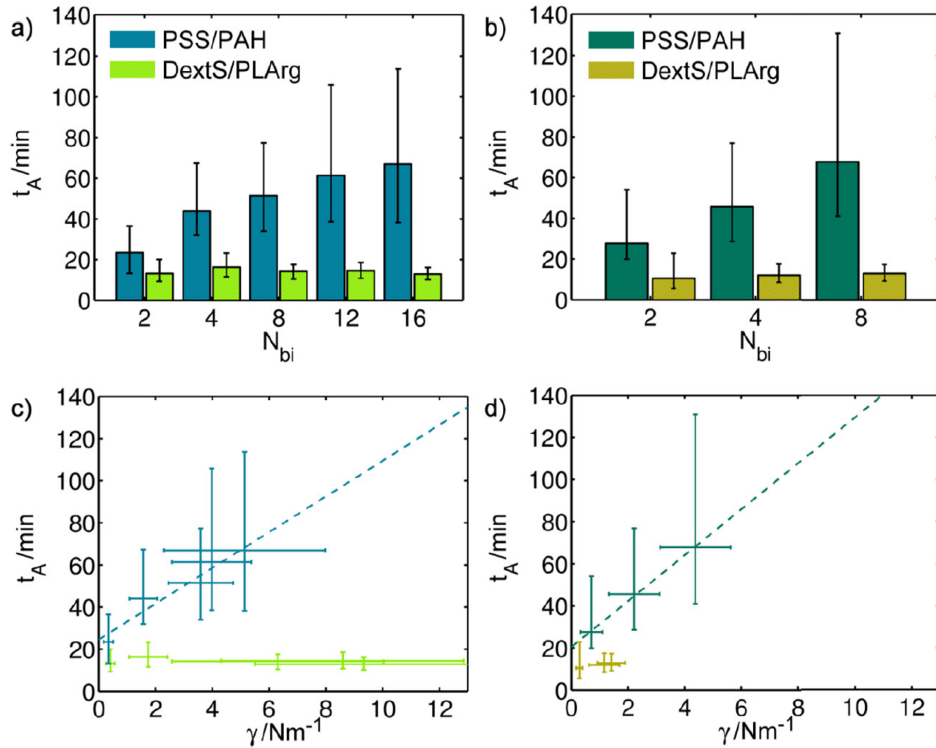


Figure 10.15. Acidification time t_A for capsules of different stiffness in HeLa cells. The time period t_A is reflecting the duration of acidification during endocytosis for non-biodegradable PSS/PAH and biodegradable DextS/PLArg capsules of batch "S" (a) and batch "L" (b). In c-d) the obtained t_A -values are displayed *versus* the average stiffness γ of the respective capsule type. Each data point corresponds to the median acidification time t_A value \pm upper and lower quartile (y-axis) *versus* the mean stiffness γ value \pm standard deviation (x-axis), as obtained from at least 80 capsules (time values) and 40 capsules (stiffness values).

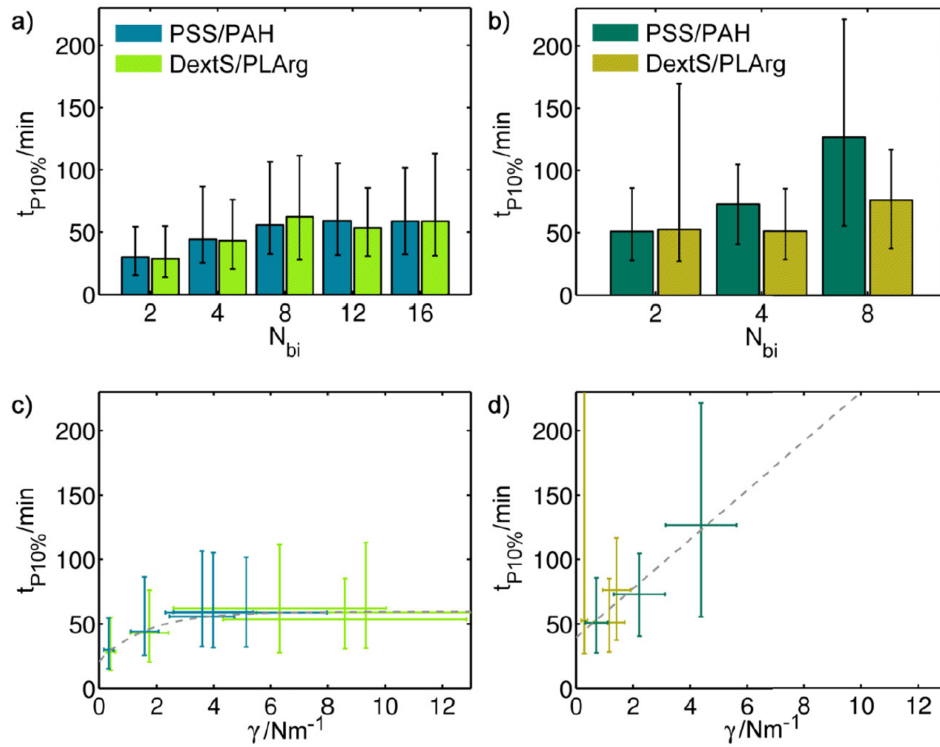


Figure 10.16. Processing time $t_{P10\%}$ for capsules of different stiffness in HeLa cells. The time period $t_{P10\%}$ is measured between first contact and the beginning of the acidification process upon internalization of non-biodegradable PSS/PAH and biodegradable DextS/PLArg capsules of batch "S" (a) and batch "L" (b). In c)-d) the obtained $t_{P10\%}$ -values are displayed *versus* the average stiffness γ of the respective capsule type. Each data point corresponds to the median processing time $t_{P10\%}$ value \pm upper and lower quartile (y-axis) *versus* the mean stiffness γ value \pm standard deviation (x-axis), as obtained from at least 80 capsules (time values) and 40 capsules (stiffness values).

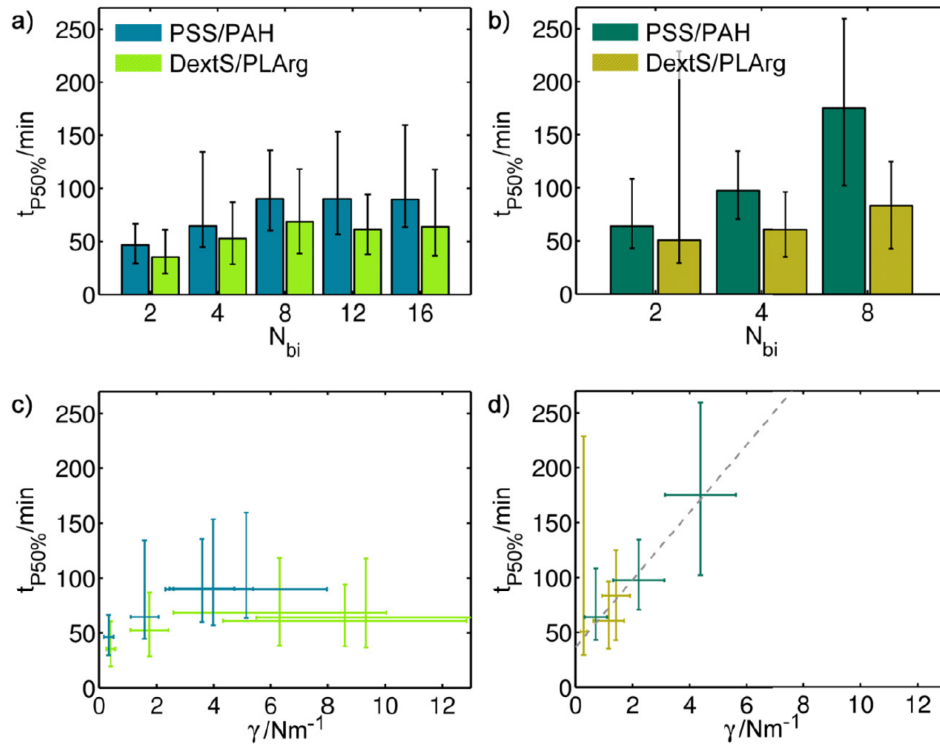


Figure 10.17. Processing time $t_{P50\%}$ for capsules of different stiffness in HeLa cells. The time period $t_{P50\%}$ is measured between first contact and 50% acidification during internalization of non-biodegradable PSS/PAH and biodegradable DextS/PLArg capsules of batch "S" (a) and batch "L" (b). In c)-d) the obtained $t_{P50\%}$ -values are displayed *versus* the average stiffness γ of the respective capsule type. Each data point corresponds to the median processing time $t_{P50\%}$ value \pm upper and lower quartile (y-axis) *versus* the mean stiffness γ value \pm standard deviation (x-axis), as obtained from at least 80 capsules (time values) and 40 capsules (stiffness values).

Acidification and processing in different types of cells

Capsule acidification and processing was investigated in various types of cells including cell lines and primary cells such as HeLa cells, A549 cells, MDMs, MDDCs, SH-SY5Y neurons and HUVECs. Biodegradable and non-biodegradable capsules with 4 bilayers of

type "L" were used. The corresponding data is shown in Figure 10.18.

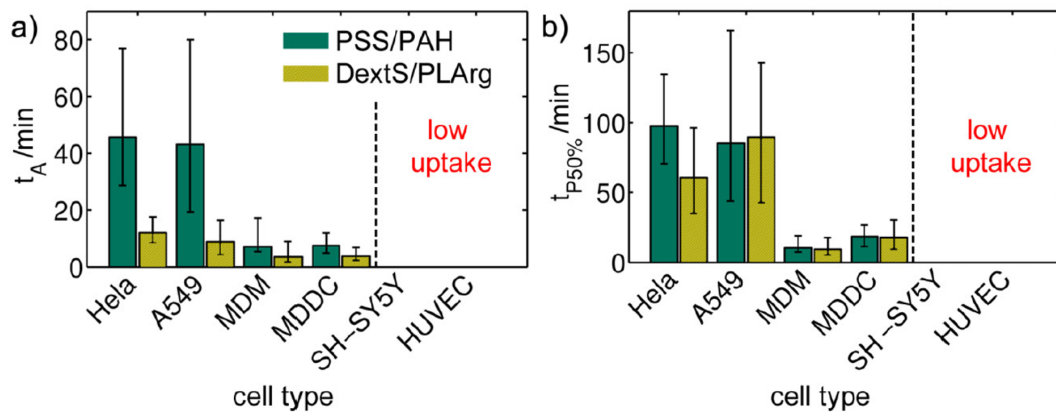


Figure 10.18. Acidification and processing in different types of cells. The acidification time t_A (a), and processing time $t_{P50\%}$ (b) of PSS/PAH and DextS/PLArg capsules ($N_{bi} = 4$, size "L") as recorded upon incubation with different types of cells. For neurons (SH-SY5Y) and human umbilical vein endothelial cells (HUVECs) under the present conditions only few uptake events were observed. Each data point corresponds to the median value \pm upper and lower quartile.

Distribution of LAMP1 during processing and acidification

Lysosomal associated protein 1 (LAMP1) is a glycoprotein, mostly situated at the luminal membrane of late endosomes and lysosomes and commonly used as a marker for acidic vesicles.^{11,15,16} To correlate the trafficking of acidic vesicles during capsule uptake HeLa were transfected to express LAMP1 labeled with green fluorescent protein (GFP) to allow live-imaging of lysosomes and the capsule acidification in parallel.

For cell culture hereby approximately 5,000 cells per well were seeded into an 8-well Ibidi μ -slide. After 12 hours 2 μ L of CellLight Lysosomes-GFP BacMam 2.0 (Invitrogen, # C10596) were added corresponding to 20 virus particles per cell. After 24 h capsule

uptake experiments were performed as described above. In addition to the capsule fluorescence GFP was excited at 488 nm using an Argon-laser and emitted photons were recorded between 505 and 550 nm. For each time point the intensity of LAMP1-GFP was measured along the capsule area to detect the amount of LAMP1 being incorporated into the endocytic vesicle containing the internalized capsule. In addition the fusion frequency of LAMP1-positive vesicles was monitored. Fluorescent micrographs and a corresponding trajectory are shown in Figure 10.19.

Immediately after capsule uptake no fluorescent signal of LAMP1-GFP could be associated with the capsules (*cf.* Figure 10.19a). After several minutes of incubation the first fusion of LAMP1-positive vesicles with the capsule-containing vesicles could be observed (*cf.* Figure 10.19b). With increasing fusion frequency the local pH around the capsules dropped (*cf.* Figure 10.19c) and the mean fluorescence of LAMP1-GFP ($I_{LAMP1-GFP}$) associated with the endocytic vesicles in which capsules were contained continued to rise until both measures (pH and LAMP1-GFP-fluorescence) reached a plateau and kept constant.

We speculate that the fusion of LAMP1-positive vesicles which should be acidic mediate the decrease in pH of the larger capsule-containing vesicles.

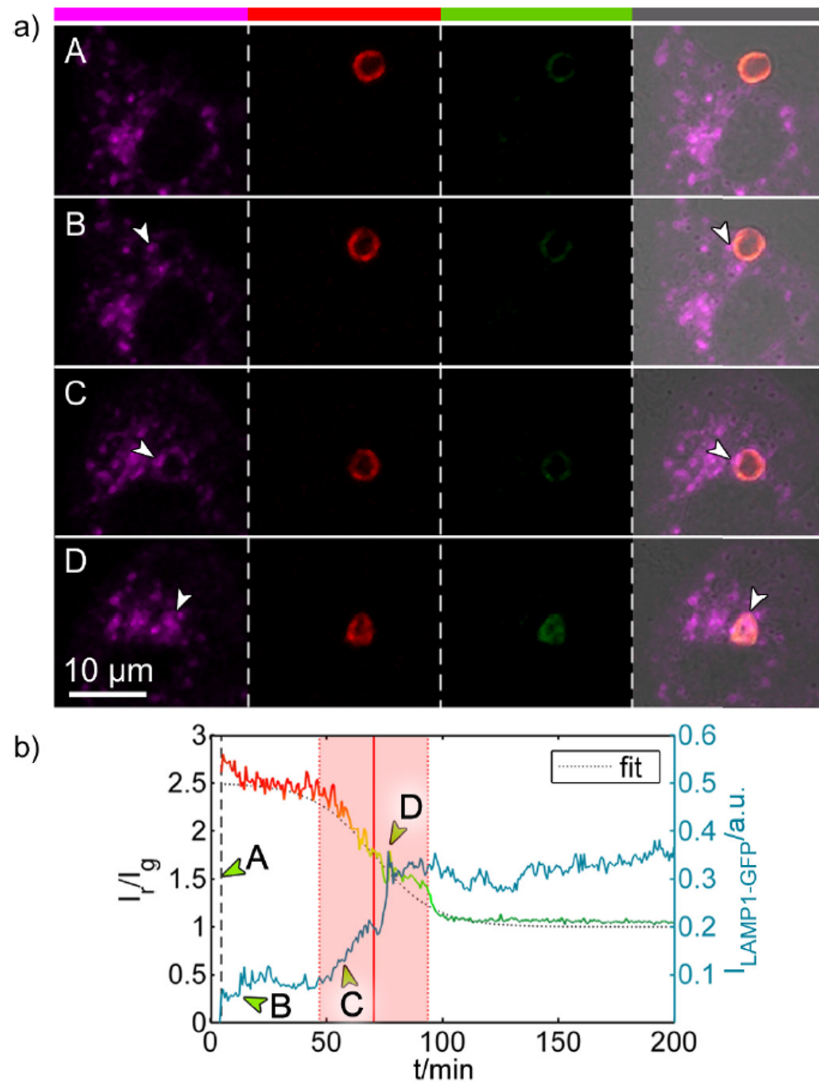


Figure 10.19. Distribution of LAMP-1 during capsule uptake in HeLa cells. In a) a time lapse recording is displayed showing the fluorescent signal of LAMP1-GFP (magenta), the red and green fluorescence channel of the capsule ($N_{bi} = 4$) pH-readout and an overlay of all fluorescent channels with a brightfield image. In b) for each image the ratio of red-to-green fluorescence I_r/I_g of the capsule has been determined and is plotted versus the incubation time t . The time points corresponding to the images shown in a) are labeled as A - D. A ratio of $I_r/I_g \approx 2.5$ corresponds to a pH value of 7.4, while $I_r/I_g \approx 1$ corresponds to local pH values below 4.5, *cf.* Figure 10.1b (main text). In addition the mean fluorescence of LAMP1-GFP ($I_{LAMP1-GFP}$) over the capsule area is plotted in blue.

Integrity-investigations of capsules

To investigate possible reasons for the fast elasticity-independent acidification of biodegradable DextS/PLArg capsules the integrity within the first 46 h upon contact with cells was examined. To be able to spot capsule fragmentation or release of cargo the conjugate DQ-ovalbumin (DQ-OVA) was encapsulated into 2-16 bilayer thick capsules being either composed out of PSS/PAH or DextS/PLArg following the protocol described by Rivera Gil *et al.*² DQ-OVA is composed out of BODIPY dye-saturated protein ovalbumin. Due to the close proximity of the dye molecules the green fluorescence of the BODIPY dye is almost completely self-quenched¹⁷ and forming dye excimers are showing a light red fluorescence signal. Upon enzymatic degradation inside cells the fluorescence is dramatically increased independent on pH. Due to these properties internalized capsules filled with DQ-OVA can be easily recognized (bright green fluorescence) and potential released fragments of DQ-OVA or capsule disruption becomes visible.²

For the experiment DQ-OVA loaded capsules with 2-16 bilayers were prepared as described above replacing SNARF-1 by DQ-OVA (1.25 mg mL⁻¹, life technologies, # D12053). Approximately 5,000 cells per well were seeded into an 8-well Ibidi μ -slide. After attachment 7.5 capsules/cell were added and CLSM images were taken after 3 h, 24 h and 46 h. DQ-OVA was excited at 488 nm (emission: 520/30 nm, "green channel") and 543 nm (emission: LP 650, "red channel"). Fluorescent micrographs are shown in Figure 10.20.

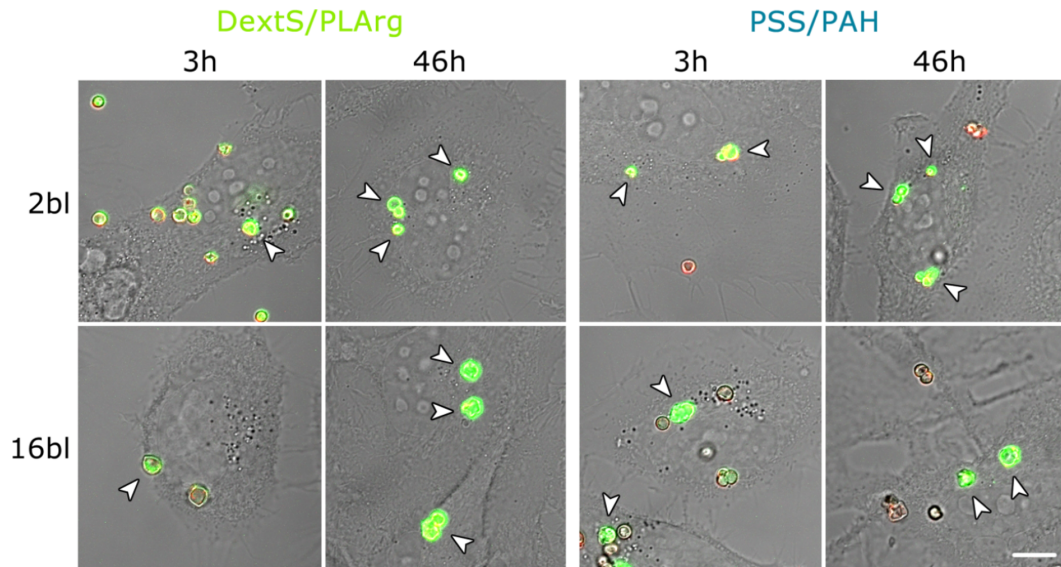


Figure 10.20. Probing proteolytic degradation of microcapsules. DQ-OVA-filled microcapsules show an increase in green fluorescence after internalization by HeLa cells (indicated by white arrows) independent on the number of bilayers ($N_{bi} = 2$ and 16). Even after 46 h no fragmentation occurs. The scale bar corresponds to 10 μm .

In agreement with already published data² the cargo of non-biodegradable PSS/PAH capsules is not completely protected by proteolytic degradation, visible as increased green fluorescence inside the cavity of internalized capsules, even for $N_{bi} = 16$. For bio-degradable DextS/PLArg capsules the increase is much stronger, though. Within the first 46 h no visible evidence was found that either high amount of DQ-OVA was released or capsules became fragmented neither for PSS/PAH capsules nor for DextS/PLArg ones. This is in agreement with the study of Rivera Gil *et al.*² who observed a spreading into the cytoplasm of the cells after 3-5 days.

References

- (1) Sallusto, F.; Lanzavecchia, A. *Journal of Experimental Medicine* **1994**, *179*, 1109–1118.
- (2) Rivera-Gil, P.; De Koker, S.; De Geest, B. G.; Parak, W. J. *Nano Letters* **2009**, *9*, 4398–4402.
- (3) De Koker, S.; Hoogenboom, R.; De Geest, B. G. *Chemical Society Reviews* **2012**, *41*, 2867–2884.
- (4) Whitaker, J. E.; Haugland, R. P.; Prendergast, F. G. *Analytical Biochemistry* **1991**, *194*, 330–344.
- (5) Petrov, A. I.; Volodkin, D. V.; Sukhorukov, G. B. *Biotechnology Progress* **2005**, *21*, 918–925.
- (6) Del Mercato, L. L.; Abbasi, A. Z.; Parak, W. J. *Small* **2011**, *7*, 351–363.
- (7) De Geest, B. G.; Vandenbroucke, R. E.; Guenther, A. M.; Sukhorukov, G. B.; Hennink, W. E.; Sanders, N. N.; Demeester, J.; De Smedt, S. C. *Advanced Materials* **2006**, *18*, 1005.
- (8) De Koker, S.; De Geest, B. G.; Cuvelier, C.; Ferdinande, L.; Deckers, W.; Hennink, W. E.; De Smedt, S.; Mertens, N. *Advanced Functional Materials* **2007**, *17*, 3754–3763.
- (9) Carregal-Romero, S.; Ochs, M.; Rivera-Gil, P.; Ganas, C.; Pavlov, A. M.; Sukhorukov, G. B.; Parak, W. J. *Journal of Controlled Release* **2012**, *159*, 120–127.
- (10) Pretzl, M.; Neubauer, M.; Tekaat, M.; Kunert, C.; Kuttner, C.; Leon, G.; Berthier, D.; Erni, P.; Ouali, L.; Fery, A. *Acs Applied Materials & Interfaces* **2012**, *4*, 2940–2948.
- (11) Hutter, J. L.; Bechhoefer, J. *Review of Scientific Instruments* **1993**, *64*, 1868–1873.
- (12) Kreft, O.; Javier, A. M.; Sukhorukov, G. B.; Parak, W. J. *Journal of Materials Chemistry* **2007**, *17*, 4471–4476.

- (13) Gonzalez, R., *Digital image processing*; Pearson Edition: 2008.
- (14) Crocker, J. C.; Grier, D. G. *Journal of Colloid and Interface Science* **1996**, *179*, 298–310.
- (15) Eskelinen, E. L.; Tanaka, Y.; Saftig, P. *Trends in Cell Biology* **2003**, *13*, 137–145.
- (16) Carlsson, S. R.; Fukuda, M. *Journal of Biological Chemistry* **1990**, *265*, 20488–20495.
- (17) Mansour, M. K.; Latz, E. *J. Immunology* **2006**, *176*, 3053.

Part III

Synopsis

The present thesis puts mechanical properties of microparticles in the center of investigations.

Mechanics is seen as one key parameter for the functionality of particulate systems. Functionality manifests in application perspectives for drug delivery, cell biology and consumer products.

With these premises let me summarize and guide through the essence of my work, including motivations, experimental results and prospects.

Particle mechanics has attracted increasing interest and relevance mainly for one distinct field of application within the past decade, namely for particles serving as delivery agents either for pharmaceutical ingredients or for flavors. In both applications it is mandatory to find the right balance between stability (*e.g.*, for reasons of processing and storage) and fragility (*e.g.*, for release). In other words, tailored mechanical properties are required, ideally combined with smart particle features such as remote control.

For some applications the importance of mechanical properties is obvious. For instance, in carbonless copy paper, the first commercial use of microcapsules, the capsules shall burst only under the pressure of the pen. Another example are fragrance filled microcapsules which are included in conditioners to give long-term scent from the fabric. These capsules have to mechanically survive processing, storage and the washing process. Only then, attached to the fabric, they may release their cargo upon friction.

For other applications the importance of particle mechanics has been recognized only recently. During the past years some evidence has been found that cellular uptake of delivery particles is not only depending on particle size, shape and surface chemistry but also on their mechanical properties. These may determine whether uptake takes place at all and, if so, by which mechanism. In addition, it is crucial to know, especially in the case of microcapsules, which forces act during uptake and how mechanics affect engulfment and further intracellular processing. The advent of advanced optical and force spectroscopy techniques in combination with well defined capsule architectures

allowed for first investigations and remarkable insights in this direction.

Finally, for almost twenty years it is known that substrate stiffness influences the behavior of cells cultured thereon. It is time to make the transition to biologically more relevant three-dimensional matrices with tunable mechanics. To date only few studies have covered this issue, most of them examining an ensemble of cells in a common scaffold. The progress in microfluidic techniques allows for the construction of spherical hydrogel beads well defined in size and composition. These can serve as single-cell micro-environments to study the effect of a range of parameters including mechanical properties on separate cells. Again, particle mechanics move to the focus of interest.

Let's stay with that last topic. Two of our publications deal with it. In both works single cells were included in monodisperse hydrogel beads produced from a microfluidics approach.

In one case the beads were made of a collagen/gelatin mixture gently cross-linked upon blue-light irradiation and had sizes of about 80 micron. Using colloidal probe atomic force microscopy (CP-AFM) I determined the elastic modulus of the beads, which was found to mainly depend on gelatin concentration and to a minor degree on chemical crosslinking. This and the almost constant mesh size was attributed to the internal structure of gelatin which forms triple helices during gelation. Consequently, these helices govern the mechanical properties and the network structure. Still, the mesh size I calculated with Flory-Rehner theory based on swelling data corresponded well with mesh values from experimental studies. In general, cell encapsulation was successful as demonstrated by high viability rates. Interestingly, we could establish a correlation between the stiffness of the matrix and the behavior of the encapsulated 3T3 fibroblast cells. In our study we saw a clear preference for the softer environment where cell spreading sets in earlier and proceeds faster as compared to a less flexible gel.

In the other case the matrix material mainly consisted of thiolated hyaluronic acid (HASH) and poly-ethylene-glycol di-vinylsulfone (PEG-DVS) which were crosslinked by mild thiol-ene click chemistry. The beads were slightly larger (about 150 micron)

but, again, this cultivation platform could be shown to successfully encapsulate and host cells with high viability. This time, human mesenchymal stem cells (hMSCs) were used to study the suitability of the micro-niches for their differentiation. Indeed, their multipotency and differentiation potential within the beads was demonstrated. I characterized the mechanical properties of the beads which fall in the range of several kPa, typical for soft solid tissue. Interestingly, we find again an indication for the effect of matrix mechanics on cell behavior. As the matrix rather resembles soft tissue the cells preferentially differentiate into adipocytes. However, a certain percentage already develops into osteoblasts. Generally, in the stiffer environment the amount of differentiated stem cells is much higher after two weeks culture as compared to the softer matrix.

In conclusion, the presented hydrogel microenvironments can be regarded as powerful tools to study cell-matrix interactions. Concerning the effect of matrix elasticity first important results were obtained which may serve as a basis for future work.

Remaining within the biologic domain, it was stressed in the beginning that particle mechanics matters for cellular uptake and processing. In our work on the uptake of poly-electrolyte multilayer capsules (PEMCs) this is outlined impressively. Two types of PEMCs were constructed, one biodegradable, the other not. For both of them I could show that the shell stiffness generally increases with the number of adsorbed layers. This increase in stiffness corresponds to an increase in shell thickness as determined from AFM imaging and electron microscopy. Cellular uptake was followed optically and evaluated by particle tracking software. Therefore, the capsules were filled with pH-sensitive dye which changes color under lysosomal acidification. Presenting the capsules to different types of cells we find that both the acidification time of internalized capsules and the overall processing time of the capsules (engulfment, intracellular migration and acidification) vary depending on cell and capsule type. Moreover, focusing on one distinct cell type (HeLa cells) we could reveal a striking correlation between capsule mechanics and uptake. The stiffer the shell the longer was the processing time. Thus, by adjusting one sole parameter,

i.e. capsule stiffness, we are able to control the cellular uptake of particles. Furthermore, it can be envisaged that a combination of tailored mechanics, size, morphology and surface chemistry will provide target specific delivery vehicles.

In a more fundamental study, we investigated the mechanical properties of very compliant and pH-responsive hydrogel capsules. These were built from five layers of poly-methacrylic acid (PMA) modified with varying amounts of pendant thiol groups. These were crosslinked to stabilize the assembly. It was found that both shell thickness and capsule size were affected by the different modifications. In terms of mechanics it could be shown that the stiffness increases with thiol content at a given pH. However, changing pH from neutral to acidic resulted in a manifold increase in stiffness while the capsules were contracting. This observation is attributed to arising H-bonding which could be interpreted as an additional physical crosslinking. For corresponding films similar trends were observed, yet, absolute stiffness values were inferior to hollow capsules. This is an interesting outcome as it confirms the superior mechanical properties of shell structures compared to planar assemblies. For the studied capsules of colloidal dimensions additional effects like surface tension may further contribute to the geometrical stiffening.

The correlation between synthesis, morphology and mechanics was in the focus of our work on fragrance filled melamine formaldehyde (MF) capsules. As this system is very common in industrial encapsulation the development of rational design criteria is not only advantageous for process enhancement and improving performance but can also bring benefits in terms of reduced materials consumption. Here, we could show how the variation of MF amount in the initial reaction mixture translates into shell thickness and, consequently, into mechanical stability. Experimentally, shell thickness was determined by examining thin sections of embedded capsules with transmission electron microscopy (TEM) and mechanics were again characterized by CP-AFM (partly carried out by myself). Increasing the amount of MF results in thicker shells with higher stiffness. Applying the Reissner model for linear elastic shells we could also determine the elastic

modulus of the capsule material which compares well with literature data on bulk MF.

Finally, one major focus of my PhD work was on the structural and mechanical characterization of microparticles from engineered spider silk. Apart from further, extensive yet unpublished work, the article on eADF4(C16) particles and modifications thereof provides first remarkable results. Using AFM imaging and force spectroscopy techniques I could reveal fundamental aspects of particle morphology, swelling and mechanics as well as establish relationships between structural modifications and mechanical properties.

The particles are obtained by a simple salting-out process. They are spherical with smooth surfaces and a homogeneous interior, as proven by AFM and electron microscopy. This is an important prerequisite for the modeling of deformation experiments with Hertz theory. Indeed, force-deformation curves (as obtained from CP-AFM on single particles) follow the predicted scaling. Passing from swollen to dried particles the elastic modulus increases by orders of magnitude from few MPa to almost GPa. Furthermore, I could show that the particles' elasticity can be tuned both by variations in protein chain length (molecular weight) and covalent crosslinking.

AFM imaging of individual C16 particles in dried and hydrated state revealed uniform swelling and moderate volume increase. In addition, swelling is reversible which is crucial for possible applications as delivery agents.

In conclusion, as different as the investigated systems may be it has always turned out that mechanical properties are tightly connected to structural features and the functionality of the particles. In all cases colloidal probe AFM proved to be a valuable tool to study and quantify particle mechanics, while optical, electron and force microscopy techniques contributed indispensable insights into the particles' geometry and morphology, which are the key to model deformation experiments and thoroughly comprehend mechanical properties. In revealing structure-mechanical property relationships my work has contributed to the understanding of fundamental principles in colloid and interface science and to exploring the application perspectives of microparticles for (drug) delivery and

the study of cell behavior.

Part IV

Zusammenfassung

Die vorliegende Arbeit stellt die Untersuchung mechanischer Eigenschaften von Mikropartikeln in den Mittelpunkt.

Mechanik wird als ein Schlüsselparameter für die Funktionalität von partikulären Systemen aufgefasst.

Funktionalität manifestiert sich in Anwendungsperspektiven in den Bereichen Wirkstofftransport, Zellbiologie und Konsumgüter.

Nach diesen Prämissen möchte ich im Folgenden einen Überblick geben über die wesentlichen Ergebnisse meiner Arbeit.

Im vergangenen Jahrzehnt hat das Interesse an der Mechanik von Partikeln deutlich zugenommen wie auch allgemein die Bedeutung dieses Themas, insbesondere aber im Bereich des Wirkstofftransports, sei es für pharmazeutische Formulierungen oder für Duft- und Geschmacksstoffe. Bei beiden Anwendungen kommt es darauf an, das richtige Verhältnis von Stabilität (etwa in Hinblick auf Verarbeitung und Lagerung) und Instabilität (etwa zur Freisetzung) zu finden. In anderen Worten: es werden maßgeschneiderte mechanische Eigenschaften benötigt, idealerweise in Kombination mit "smarten" Partikeleigenschaften wie beispielsweise kontrollierter Fernsteuerung.

Für einige Anwendungen liegt die Bedeutung mechanischer Eigenschaften auf der Hand. So etwa bei kohlefreiem Durchschreibepapier - der erste kommerzielle Einsatz von Mikrokapseln -, wo die Kapseln genau dann aufbrechen sollen, wenn der Stift darüberfährt. Ein weiteres Beispiel sind Parfüm-gefüllte Mikrokapseln wie sie häufig in Weichspülern eingesetzt werden, damit der behandelte Stoff über einen längeren Zeitraum duftet. Diese Kapseln müssen mechanisch stabil genug sein, um die Verarbeitung, Lagerung und schließlich den Waschvorgang zu überdauern. Erst danach sollen sie ihren Inhalt durch Reibung freisetzen.

Für andere Anwendungen wurde die Bedeutung der Partikel-Mechanik erst in letzter Zeit erkannt. In den vergangenen Jahren wurden einige Hinweise gefunden, dass die Aufnahme von (etwa mit Wirkstoff beladenen) Partikeln durch Zellen nicht nur von

Größe, Aussehen und Oberflächenchemie dieser Partikel abhängt, sondern auch von deren mechanischen Eigenschaften. Diese können dafür Ausschlag gebend sein, ob überhaupt eine Zellaufnahme stattfindet und, wenn ja, über welchen Mechanismus. Darüber hinaus ist es wichtig, insbesondere im Fall von Mikrokapseln, die Kräfte zu kennen, die während der Zellaufnahme wirken, und wie die Mechanik den Aufnahmeprozess und die weitere intrazelluläre Verarbeitung beeinflusst. Erst die Weiterentwicklung optischer Analyseverfahren und der Kraftspektroskopie sowie die Etablierung neuer Synthesestrategien zur kontrollierten Herstellung von Kapseln haben es ermöglicht, fundierte Untersuchungen durchzuführen und erste bemerkenswerte Einblicke zu erhalten.

Schließlich weiß man seit rund zwanzig Jahren, dass die Steifigkeit des Nährbodens das Verhalten von darauf kultivierten Zellen beeinflusst. Es ist an der Zeit, den Übergang zu biologisch relevanteren drei-dimensionalen Kulturmedien mit steuerbaren mechanischen Eigenschaften zu machen. Bisher haben sich relativ wenige Studien mit diesem Thema befasst, die meisten von ihnen behandeln Ensembles von Zellen in einem gemeinsamen Medium. Mit Hilfe der Mikrofluidik können sphärische Hydrogel-Partikel hergestellt werden, deren Größe und Zusammensetzung präzise eingestellt werden kann. Solche Partikel können als Mikroumgebungen für einzelne Zellen dienen, um die Auswirkungen verschiedener Parameter inklusive mechanischer Eigenschaften auf individuelle Zellen zu untersuchen. Auch hier gewinnt also die Mechanik von Partikeln zunehmendes Interesse und Bedeutung.

Bleiben wir bei diesem Thema. Zwei unserer Veröffentlichungen beschäftigen sich hiermit. In beiden Arbeiten wurden einzelne Zellen in monodisperse Hydrogel-Partikel eingebettet, die mittels Mikrofluidik hergestellt wurden.

In dem einen Fall bestanden die Partikel (Durchmesser rund 80 Mikrometer) aus einer Mischung von Kollagen und Gelatine, die in einem milden Verfahren, induziert durch blaues Licht, quervernetzt wurden. Mit Hilfe der "Colloidal Probe"-Technik (CP) konnte ich am Rasterkraftmikroskop (AFM) den E-Modul der Partikel bestimmen. Dieser hing hauptsächlich von der Gelatine-Konzentration ab, sowie, in geringerem Ausmaß, vom Grad

der Vernetzung. Dies und die beinahe unveränderte Maschenweite des Netzwerks wurden auf die interne Struktur der Gelatine zurückgeführt. Diese bildet dreifache Helices während der Gelierung. Folglich dominieren diese Helices die mechanischen Eigenschaften und die Struktur des Netzwerkes. Dennoch stimmte die Maschenweite, die ich basierend auf Quelldaten nach der Flory-Rehner-Theorie berechnete, gut mit experimentell ermittelten Werten überein. Das Einkapseln von Zellen war im Allgemeinen erfolgreich, da die meisten Zellen diesen Prozess unbeschadet überlebten. Interessanterweise konnten wir einen Zusammenhang herstellen zwischen der Steifigkeit der Matrix und dem Verhalten der darin eingebetteten 3T3-Fibroblasten. Diese zeigten eine deutliche Präferenz für die weichere Umgebung, wo die Ausbreitung der Zellen früher beginnt und schneller voranschreitet als bei härteren Gelen.

In dem anderen Fall bestand das Matrixmaterial hauptsächlich aus mit Thiolen modifizierter Hyaluronsäure (HASH) und Poly-Ethylenglycol Di-Vinylsulfon (PEG-DVS), die Zell-schonend durch die milde Thiol-en Click-Chemie vernetzt wurden. Die Partikel waren etwas größer (um die 150 Mikrometer), aber Zellen wurden auch hier erfolgreich eingebettet bei hoher Überlebensrate. Diesmal wurden menschliche mesenchymale Stammzellen (hMSCs) verwendet, um die Eignung der Mikro-Nischen für deren Differenziation zu untersuchen. In der Tat konnte auch nach der Verkapselung die Multipotenz der Stammzellen und deren Fähigkeit zur Weiterentwicklung nachgewiesen werden. Ich habe die mechanischen Eigenschaften der Partikel charakterisiert. Der E-Modul liegt bei einigen kPa, was vergleichbar ist mit weichem Gewebe. Interessanterweise sehen wir auch für dieses System Anhaltspunkte für einen Einfluss der Mechanik auf das Verhalten der Zellen. Da die umgebende Matrix weich ist, entwickelt sich eine Mehrzahl der Stammzellen zu Adipozyten. Jedoch bildet ein kleinerer Teil bereits Osteoblasten. Allgemein wurde beobachtet, dass sich nach zwei Wochen Kultivierung in der härteren Umgebung ein weit größerer Anteil der Zellen differenziert hat als in der weicheren Matrix.

Zusammenfassend lässt sich sagen, dass sich die vorgestellten Hydrogel-basierten Mikro-Umgebungen als hervorragend geeignet erwiesen haben, um Wechselwirkungen zwischen einzelnen Zellen und der sie umgebenden Matrix zu untersuchen. In Hinblick auf

den Einfluss mechanischer Eigenschaften auf das Zellverhalten wurden erste wichtige Ergebnisse erzielt, die als Grundlage für weitere Arbeiten dienen können.

Bleiben wir im Bereich der Biologie. Eingangs wurde betont, dass die Mechanik von Partikeln eine Rolle spielt bei der Zellaufnahme und -verarbeitung. In unserer Arbeit über die Aufnahme von Polyelektrolyt-Multischicht-Kapseln (PEMCs) wird dies in beeindruckender Weise dargelegt. Zwei Arten von PEMCs wurden hergestellt, eine bioabbaubar, die andere nicht. Für beide konnte ich zeigen, dass die Steifigkeit der Kapselschale mit der Zahl an adsorbierten Schichten zunimmt. Diese Zunahme entspricht einer Erhöhung der Schalendicke, wie durch abbildendes AFM und Elektronenmikroskopie nachgewiesen wurde. Die zelluläre Aufnahme wurde optisch verfolgt und mit Hilfe einer "particle-tracking"-Software ausgewertet. Dazu wurden die Kapseln mit einem pH-sensitiven Farbstoff befüllt, der seine Farbe während der lysosomalen Ansäuerung verändert. Schaut man sich die Interaktion mit verschiedenen Zelltypen an, so fällt auf, dass sowohl die Ansäuerungszeit als auch die komplette Verarbeitungszeit (also vom Kontakt der Partikel mit der Zellwand bis hin zur Ansäuerung) variieren, je nach Art der Zellen und der Kapseln. Um den Einfluss der Kapselmechanik genauer zu studieren, wählten wir eine bestimmte Zellart (HeLa-Zellen) aus. So konnten wir einen deutlichen Zusammenhang zwischen Mechanik und Zellaufnahme aufdecken: je steifer die Schale war, umso länger war die Verarbeitungszeit. Das heißt, durch die Veränderung eines einzigen Parameters, nämlich der Steifigkeit, können wir die Zellaufnahme von Partikeln steuern. In Zukunft könnten also durch eine geschickte Einstellung ihrer Eigenschaften maßgeschneiderte Wirkstofftransporter entwickelt werden.

In einer mehr grundlagenorientierten Studie haben wir die mechanischen Eigenschaften von sehr weichen und pH-responsiven Hydrogel-Kapseln untersucht. Diese bestanden aus fünf Schichten von Poly-Methacrylsäure (PMA), die unterschiedlich stark mit freien Thiolgruppen modifiziert war. Diese wurden kovalent miteinander verknüpft, um den

Aufbau zu stabilisieren. Der unterschiedliche Anteil an Thiolgruppen hatte einen Einfluss auf die Schalendicke, Kapselgröße und auch die Mechanik. Die Steifigkeit stieg mit dem Thiolgehalt an. Eine Veränderung des pH von neutral zu sauer bewirkte einen vielfachen Anstieg der Steifigkeit bei gleichzeitigem Schrumpfen der Kapseln. Dies kann einer Zunahme an Wasserstoff-Brückenbindungen zugeschrieben werden, die eine Art zusätzliche, physikalische Vernetzung darstellen. Für Filme aus demselben Schichtmaterial wurden ähnliche Trends beobachtet, allerdings war deren Steifigkeit deutlich niedriger. Dies ist ein interessantes Ergebnis, da es die erhöhte mechanische Stabilität von Kugelschalen gegenüber flachen Architekturen bestätigt. Im Falle der hier untersuchten kolloidalen Kapseln dürften zusätzlich zu dieser geometrischen Stabilisierung weitere Effekte wie etwa Grenzflächenspannung zu der gemessenen Steifigkeit beitragen.

Die Korrelation von Synthese, Morphologie und Mechanik stand im Mittelpunkt unserer Arbeit zu Parfüm-gefüllten Melamin-Formaldehyd (MF) Kapseln. Diese werden häufig zur Verkapselung im industriellen Maßstab eingesetzt. Dementsprechend trägt die Entwicklung rationaler Designkriterien nicht nur zur Prozessoptimierung und Verbesserung der Eigenschaften bei, sondern kann auch dabei helfen den Verbrauch von Ressourcen zu minimieren. Wir konnten zeigen, dass und, vor allem, wie über die Veränderung des MF-Gehaltes in der Reaktionsmischung die Schalendicke der Kapseln und damit auch deren mechanische Stabilität direkt steuerbar sind. Experimentell wurde die Schalendicke mit Hilfe von Transmissions-Elektronenmikroskopie (TEM) aus Dünnschnitten eingebetteter Kapseln bestimmt und die Mechanik wurde wieder mit CP-AFM untersucht (unter meiner Beteiligung). Erhöht man die Menge an MF, führt dies zu dickeren Schalen mit größerer Steifigkeit. Mit Hilfe des Reissner-Modells zur Beschreibung der Deformation linear elastischer dünner Schalen konnten wir überdies den E-Modul des Schalenmaterials bestimmen. Dieses stimmte gut mit Literaturwerten überein.

Schließlich bildete die Charakterisierung von Struktur und Mechanik von Mikropartikeln aus rekombinant hergestellter Spinnenseide einen weiteren Schwerpunkt meiner

Arbeit. Abgesehen von einer Reihe weiterführender, jedoch noch nicht publizierter Untersuchungen, hält der Artikel über eADF4(C16)-Partikel und deren Modifikationen erste bemerkenswerte Ergebnisse bereit. Mit Hilfe von Rasterkraftmikroskopie (Abbildung und Kraftspektroskopie) konnte ich fundamentale Aspekte der Morphologie, des Quellverhaltens und der Mechanik der Partikel ergründen und Verbindungen zwischen strukturellen Modifizierungen und mechanischen Eigenschaften aufzeigen.

Die Partikel werden durch das Aussalzen des Proteins aus Lösung erhalten. Sie sind kugelförmig, homogen und zeigen eine glatte Oberfläche, wie durch AFM und Elektronenmikroskopie bestätigt wurde. Dies ist eine wichtige Voraussetzung für die Beschreibung der Deformationsexperimente mit der Hertz-Theorie. Tatsächlich folgen die Kraft-Deformation-Kurven (aus CP-AFM-Messungen an individuellen Partikeln) der vorhergesagten Skalierung. Beim Übergang von gequollenen zu trockenen Partikeln ändert sich der E-Modul um Größenordnungen von wenigen MPa zu annähernd GPa. Weiterhin konnte ich zeigen, dass die Elastizität der Partikel sowohl über die Länge der Proteine (also über das Molekulargewicht) als auch über kovalentes Quervernetzen gesteuert werden kann. Abbildendes AFM an getrockneten und hydrierten Partikeln zeigte gleichförmiges Quellen bei moderater Volumenzunahme. Außerdem ist das Quellen reversibel, was eine wichtige Voraussetzung ist für eine mögliche Verwendung der Partikel als Wirkstofftransporter.

Zusammenfassend lässt sich festhalten: so unterschiedlich die untersuchten Systeme auch sein mögen, es zeigte sich stets, dass die mechanischen Eigenschaften dieser Partikel eng mit ihrem strukturellen Aufbau und ihrer Funktionalität verknüpft sind. In allen Fällen erwies sich die "Colloidal Probe"-AFM-Technik als wertvolles Werkzeug, um die Mechanik von Partikeln zu untersuchen und zu quantifizieren. Gleichzeitig lieferten optische, Elektronen- und Kraftmikroskopie unverzichtbare Einblicke in die Geometrie und Morphologie der Partikel, die der Schlüssel sind zur Modellierung von Deformationsexperimenten und zum tiefergehenden Verständnis mechanischer Eigenschaften. Indem wichtige Beziehungen zwischen Struktur und Mechanik von partikulären Systemen aufgedeckt wurden hat meine Arbeit einen wesentlichen Beitrag geleistet zum Verständnis

fundamentaler Prinzipien in der Kolloid- und Grenzflächenforschung sowie zur Erkundung von Anwendungsperspektiven der Mikropartikel für den Wirkstofftransport und die Untersuchung von Zellen.

Part V

Annex

List of Figures

1.1	Substrate stiffness and differentiation	5
1.2	Cellular uptake of PEMCs with varying stiffness	8
2.1	Stress-strain schematic	24
2.2	"Adhesion map" showing which model applies best for a given combination of dimensionless load \bar{F} and elasticity parameter λ . For more details see [19]. Reprinted with permission from [19], ©1997 Elsevier.	27
2.3	Schematic representation of basic requirements in thin shell theory.	29
2.4	Graphical representation of bending and stretching contributions in capsule deformation	32
2.5	Particle in shear flow	35
2.6	Schematic representation of an atomic force microscope (AFM) probing a particle.	39
2.7	Schematic representation of a deformation experiment with AFM force spectroscopy	41
2.8	Schematic representation of the different probes/measurement geometries in AFM based force spectroscopy	42
2.9	Example for the large deformation of an MF capsule with an AFM-based NanoIndenter.	44
2.10	Overview measurement techniques to probe particle mechanics	45

3.1	Schematic representation of layer-by-layer assembly	54
3.2	Morphologies of engineered spider silk	55
3.3	Schematic representation of loading of and release from C16 microparticles	56
4.1	Silk particle morphology and crosslinking	86
4.2	Microfluidic production of hydrogel beads	88
4.3	Microfluidic production of microniches for stem cells	90
4.4	Basic parameters for the design of melamine formaldehyde microcapsules	93
4.5	TOC-figure hydrogel capsule mechanics	96
4.6	TOC-figure stiffness dependent cellular uptake	98
5.1	C16 particles - morphology, dry mechanics, thermal behavior	105
5.2	C16 particles - swelling and mechanics in hydrated state	106
5.3	Silk particle mechanics and swelling as a function of molecular weight and crosslinking	109
5.4	Colloidal probe technique and Hertz modeling	118
5.5	C16 particles - fatigue test	118
5.6	Schematic of C16 particle-formation and crosslinking	119
6.1	Col-gela beads production and photo-crosslinking	128
6.2	Homogeneity control of col-gela beads	129
6.3	Elastic modulus of col-gela beads as function of concentration and crosslinking	132
6.4	Fraction of non-degraded col-gela beads with incubation time in varied environments	135
6.5	On the embedding of cells into hydrogel beads	137
6.6	Matrix elasticity-dependent cell behavior	139
6.7	On the mechanical characterization of microbeads	145
6.8	SEM images of microbeads	146
6.9	Riboflavin adsorption and bead morphology	147
6.10	Log-log plot of hydrodynamic diameter against different molecular weights	149
6.11	Experimental mesh size determination	150

6.12	Swelling ratios of microbeads at different gelatin concentrations	151
6.13	Live/dead assay of encapsulated cells	154
7.1	Microfluidic fabrication of hydrogel based microniches	167
7.2	Rheology on bulk HASH hydrogels	171
7.3	Chemical and physical characteristics of the prepared microniches	173
7.4	Viability of hMSCs in HASH based microniches	175
7.5	CLSM on cell and nucleus morphologies of encapsulated hMSCs	177
7.6	Multipotency of hMSCs embedded in microniches	179
7.7	Examination of hMSC differentiation in microniches	181
7.8	NMR spectrum of thiolated hyaluronic acid	188
7.9	Time-dependent rheology on bulk HASH hydrogels	189
7.10	Evaluation of microniche mesh size	190
7.11	Typical force-deformation curves on HASH microbeads	191
7.12	Poisson distribution of cell encapsulation	192
7.13	CLSM on cell and nucleus morphologies of encapsulated hMSCs	194
7.14	Micrographs showing dividing cells and multiple cells in hydrogel microbeads	195
8.1	Optical micrographs and size distributions of MF capsules	203
8.2	TEM images of microcapsules and shell thickness	204
8.3	Shell thickness as function of MF amount	210
8.4	Elastic deformation of MF microcapsules	211
8.5	Compression of MF capsules	212
8.6	Stiffness as function of shell thickness	213
8.7	Conclusive figure MF capsule characterization	214
8.8	Correlation stiffness and geometric parameters	216
8.9	Typical force-deformation curve, MF capsule	222
9.1	Preparation of PMA-PDA	234
9.2	Size and shell thickness of hydrogel capsules	237

9.3	Schematic representation of CP-AFM technique and representative deformation curve	238
9.4	Influence of pH on capsule size and stiffness	242
9.5	pH effect on film thickness and mechanics	243
9.6	Comparison of the stiffness of different hydrogel architectures	244
9.7	Comparison of the stiffness of hydrogel films and capsules	247
9.8	UV-Vis spectra for the PMA-PDA polymers and calibration curve	253
9.9	Quantification of thiol modification	253
9.10	Theoretical axial strain plots	254
9.11	Force map on single hydrogel capsule	254
10.1	Architecture, pH-response and mechanics of multilayer capsules	260
10.2	Example for particle tracking analysis	262
10.3	Correlation of cellular acidification and processing time of multilayer capsules with their stiffness	265
10.4	Fluorescent micrographs of pH-sensitive microcapsules	274
10.5	Size distribution of microcapsules	276
10.6	TEM analysis of capsule shell thickness	278
10.7	AFM analysis of capsule shell thickness	279
10.8	Stiffness results	281
10.9	Force-deformation characteristic of a 4-bilayer microcapsule	282
10.10	Zeta-potential	283
10.11	Time lapse image series of capsule uptake	285
10.12	Overview over the image processing workflow	289
10.13	Example trajectories PSS/PAH	291
10.14	Example trajectories DextS/PLArg	292
10.15	Acidification time overview	293
10.16	Processing time $t_{P10\%}$ overview	294
10.17	Processing time $t_{P50\%}$ overview	295
10.18	Comparison different cells	296

10.19	Distribution of LAMP-1 during capsule uptake	298
10.20	Degradation study	300

List of Tables

5.1	Fit parameters from histograms	119
6.1	Comparison of calculated and experimental mesh size	133
6.2	Hydrodynamic diameters of FITC-dextran of different M_W	149
6.3	Parameters for Flory-Rehner calculation	153
7.1	Composition and gelling kinetics of HASH-PEGDVS-FBNG hydrogels. .	170
7.2	Swelling ratios of HASH-PEGDVS-FBNG hydrogel microbeads fabricated in our experiment.	193
8.1	Overview MF capsule parameters	202
8.2	Estimation small deformation regime	223

Erklärung

Hiermit erkläre ich an Eides statt, dass ich die vorliegende Arbeit selbständig und nur unter Verwendung der angegebenen Quellen und Hilfsmittel angefertigt habe.

Weiterhin erkläre ich, dass ich weder an der Universität Bayreuth noch an einer anderen Universität versucht habe, eine Dissertation einzureichen oder eine Promotionsprüfung abzulegen.

Ich erkläre, dass ich zu keinem Zeitpunkt die Hilfe eines gewerblichen Promotionsberaters oder -vermittlers in Anspruch genommen habe und dies auch in Zukunft nicht tun werde. Schließlich erkläre ich mein Einverständnis, dass die elektronische Fassung der Dissertation unter Wahrung meiner Urheberrechte und des Datenschutzes einer gesonderten Überprüfung hinsichtlich der eigenständigen Anfertigung der Dissertation unterzogen werden kann.

Bayreuth, 06.05.2014

Martin Peter Neubauer

"I cannot doubt but that these things, which now seem to us so mysterious, will be no mysteries at all; that the scales will fall from our eyes; that we shall learn to look on things in a different way - when that which is now a difficulty will be the only common-sense and intelligible way of looking at the subject."

(Lord Kelvin)